Three Dimensional X-ray Diffraction analysis of polycrystalline thin-films

Lucas, Mariana Mar

Publication date:
2020

Document Version
Publisher's PDF, also known as Version of record

Three Dimensional X-ray Diffraction analysis of polycrystalline thin-films

PhD Thesis

Mariana Mar Lucas

December 2020

Author:
Mariana Mar Lucas

Title:
Three Dimensional X-ray Diffraction analysis of polycrystalline thin-films

Supervisor:
Professor Jens Wenzel Andreasen

Co-supervisors:
Professor Henning Friis Poulsen
Dr. Christian Rein

Assessment committee:
Professor Poul Ægidius Norby
Professor Susan Schorr
Dr. Jonathan J. S. Scragg

Sponsorship:
This study was supported by the H2020 European Research Council through the SEEWHI Consolidator grant, ERC-2015-CoG-681881

DTU Energy
Department of Energy Conversion and Storage
Technical University of Denmark

Anker Engelunds Vej
2800 Kgs. Lyngby, Denmark
Phone +45 46 77 58 00
www.energy.dtu.dk

Abstract

This project explores polycrystalline photovoltaic thin-film microstructure through three-dimensional X-ray diffraction (3DXRD), focusing on the absorber layer of Cu_2ZnSnS_4 (CZTS) thin-film solar cells.

CZTS is a promising non-toxic, earth-abundant, and inexpensive material for third-generation solar cells. Through the CZTS formation process, secondary phases may arise, which cannot be identified with conventional methods such as powder diffraction because of the significant overlap of diffraction peaks. Hence, the motivation to apply 3DXRD is to reveal the thin-film structural properties, texture, and effect on solar cell efficiency.

In this work, the implementation of 3DXRD analysis on a CZTS solar cell and other types of photovoltaic thin-films provides the structural characterization of the grains composing the film, such as grain size, orientation, strain, and twin boundaries. The study of the microstructure of an Ag-alloyed CZTS and a CIGS solar cell are examples of how 3DXRD can be applied to other chalcogenide thin-films. Additionally, to compare the microstructure variations of different processing methods, kesterite samples prepared by sputtering, solution-processed, and Pulsed Laser Deposition (PLD) were measured.

Multiple setups of 3DXRD are employed according to the capabilities of the beamlines visited at APS, ESRF, and SPring-8. These setups allow the following analyses:

- Statistical analysis on an ensemble of grains to obtain sizes and orientations
- Determination of sample texture through the orientation of grains
- Characterization of twin boundaries to improve grain growth models and reveal their influence on device performance
- Determination of strain in the sample
- Reconstruction of a grain map by employing the scanning modality 3DXRD

In general, 3DXRD can advance the microstructural characterization of polycrystalline thin-films with a grain size of about 1 μm.

Resumé

Dette projekt studere polykrystallinske fotovoltaik tyndfilms mikrostrukturer ved hjælp af tredimentionel røntgenstrålings diffraktion (3DXRD) med fokus på absorberings laget på Cu_2ZnSnS_4 (CZTS) tyndfilms solceller.

CZTS er et lovende materiale. Det er billigt og består af ufarlige, hyppigt forekommende grundstoffer som kan benyttes til fabrikering af tredje generations solceller. I formations processen af CZTS, kan sekundære faser opstå. Disse kan ikke identificeres ved hjælp af konventionelle metoder såsom pulverdiffraktion, grundet et signifikant overlap af diffraktionstoppe. I stedet anvendes her 3DXRD til at afdække tynd-filmens strukturelle egenskaber, teksturer og effekten af solcellen.

I denne afhandling udarbejdes en 3DXRD analyse af en CZTS solcelle samt andre typer fotovoltaik solceller. Analysen resulterer i en strukturel karakterisering af de korn der udgør tyndfilmen. Herunder korn størrelse, orientering, tøjning og tvillinge grænser. Et studie af mikrostrukturerne af en sølvlegeret CZTS og en CIGS solcelle præsenteres som eksempler på hvordan 3DXRD kan anvendes til andre chalcogenide tyndfilm. Yderligere anvendes teknikken til at måle og sammenligne de mikrostruktur variationer der fremkommer ved forskellige fremstillingsmetoder. Herunder sputter deponering, vådkemisk deponering og pulseret laser deponering (PLD).

Varierende opsætninger af 3DXRD anvendes i overensstemmelse med egenskaberne for den enkelte synkrotron ved faciliteterne APS, ESRF og Spring-8. Disse opsætninger muliggøre følgende analyser:

- Statistisk analyse på en gruppe korn med formål at bestemme kornenes størrelse og orientering.
- Bestemmelse af prøvens tekstur ud fra orientering af kornene.
- Karakterisering af tvilling grænser for at forbedre korn vækstmodeller og klarlægge deres indflydelse på solcellens ydeevne
- Bestemmelse af tøjning i prøven
- Rekonstruering af kornmap ved at anvende skanning modalitet 3DXRD

Generelt kan 3DXRD forbedre den mikrostrukturelle karakterisering af polykrystalinske tyndfilm med en korn størrelse på omkring 1 µm.

Preface

This thesis is submitted in candidacy for the PhD degree from the Technical University of Denmark (DTU). The work was carried out at the Department of Energy Conversion and Storage from November 15th, 2017, to December 31st, 2020. The project was supervised by Professor Jens Wenzel Andreasen and co-supervised by Professor Henning Friis Poulsen and Dr Christian Rein. A collaboration with scientist Dr Jonathan Wright during a three-month external stay at the European Synchrotron Radiation Facility was established. The work presented in this thesis is part of the larger project SEEWHI, financed by the H2020 European Research Council through the SEEWHI Consolidator grant, ERC-2015-CoG-681881.

This work aims to characterize the structural properties of thin-film solar cells, which are tightly related to their deposition process. The final film microstructure influences the physical properties of the film. Therefore, characterizing the grains in the film allows a better understanding of the material and leads to the control and optimization of the engineering of these materials. Here, we assess the application of 3DXRD on polycrystalline thin-films with grain sizes in the order of 1 µm.

Research objectives:

- Identify secondary phases
- Characterize grain properties: size, orientation, strain, twinning relations between grains
- Compare different fabrication processes

Structure of the thesis

This thesis advances the characterization of thin-film solar cells and the analysis of the individual grain properties that constitute the polycrystalline thin-films. It envisions the application of this methodology to other polycrystalline thin-films.

Chapter 1 introduces the concepts of microstructure in polycrystalline thin-films and their influence on the film's physical properties. It presents some of the thin-film photovoltaic technologies and the challenges to control the defects that form during the film fabrication. The final section focuses on the promising kesterite solar cells, describing the material properties and fabrication methods. Finally, the crystallographic phases that form during the kesterite device fabrication and the resulting microstructure are also discussed.

In **Chapter 2**, we explain the methodology of this work. We present the principles of 3DXRD and describe the experiments carried out. We also present the samples that were examined. After that, the available analysis tools and the analysis pipeline are explained. In the last

section, we discuss an alternative algorithm for data processing. We show its application on simulated data and the optimistic results.

Chapter 3 is divided into six sections that comprehend the analysis of different samples and different experimental setups. Starting with the kesterite solar cell, we dive into the challenges for analyzing this material, as we discover the unsurprising presence of secondary phases. We determine statistical information about the grain properties and discuss their influence on device performance. Next, we reconstruct a grain map of a kesterite solar cell using the 3DXRD scanning modality. We explain the principles of this technique and the advantages of this approach. The following section includes the analysis of a silver alloyed kesterite thin-film. We implement a similar methodology applied in the analysis of the kesterite solar cell and obtain a statistical report on the grain sizes, orientations, and twin boundaries. Subsequently, we describe an approach to refine the crystal structure of a kesterite grain extracted from the 3DXRD data. Additionally, we also study a different type of solar cell made of Cu(In, Ga)Se_2. In this solar cell, we recognize the chalcopyrite structure of the main material and two secondary phases. We can also distinguish different types of twin boundaries. Finally, we describe the design of the last experiment at SPring 8 and the expected outcome from the samples that were examined.

Chapter 4 concludes this work. It summarizes the results of this thesis and discusses the challenges of analyzing thin-films using 3DXRD.

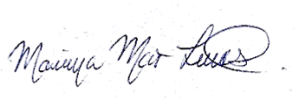

Mariana Mar Lucas

December 2020

Acknowledgements

I had the opportunity to meet many helpful and supportive people who were eager to share their experience and knowledge with me, people committed to their job and with a great passion for science.

I would like to thank my supervisor, Jens Wenzel Andreasen, who introduced me to the exciting business of X-rays and synchrotron radiation. His vision to improve solar cells through structural characterization initiated the SEEWHI project. I am very grateful to Jens for giving me the chance to be part of this group.

I am also very thankful to my co-supervisor, Henning Friis Poulsen. Despite his busy agenda, he always made time for my project, revising beamtime proposals, abstracts for conferences, and answered my emails at the speed of light. He was a great help with drafting the structure of a manuscript and correcting it.

Special thanks to my co-supervisor, Christian Rein, for his support through the PhD, the discussions about kesterite, proofreading the introduction of this thesis, and offering valuable and constructive suggestions.

I am deeply indebted to Jonathan Wright, who taught me all about 3DXRD data analysis at ESRF. During and after my external stay, he supported me in answering all my questions, examining the data with me, discussing indexing strategies, not to forget the acquisition of the scanning-3DXRD data. Many thanks to Carlotta, who helped me with crystal refinement. To Marta, who helped me debugging and coding and took me on a nice excursion to the mountains.

I want to thank Sara Engberg, Filipe Mesquita, and Shagai Gansukh from DTU Photonics, who provided me with samples for my experiments. To Stela Canulescu and Jørgen Schou, I appreciate your support by collaborating and sharing their knowledge about kesterite.

I would like to thank Tiago Ramos, Peter Stanley, Mustafacan Kutsal, and Henning Øsholm. They accompanied me and helped to perform the experiments for this thesis at APS and SPring-8. Their motivation and good spirit made the beamtimes a great experience. Special thanks to Ebtisam, who prepared the samples for the experiments and finish them on time even with short notice.

The experiments would not have been possible without the support of the beamline scientists who work very hard to make every user's investigation a success: Jonathan Almer, Perter Kenesei, Jung-Sang Park, and Hemant Sharma, who assisted us at APS, and Akihisa

Takeuchi, Masayuki Uesugi, and Kentaro Uesugi for their help during the experiment at Spring-8.

I would like to extend my gratitude to Nana Wahlberg and Sepideh Hakim from DTU Physics, who worked on the multigrain indexing algorithm and tested the CZTS simulated data.

I am also grateful to Anders Østergård Madsen from Copenhagen University, who helped with the crystal refinement of the CZTS grain and corrected the writing of the chapter related to this subject.

I also thank Michael Stuckelberger from DESY, who provided the CIGS sample and prepared multiple proposals for beamtimes at PETRA III. I also wish to thank Hergen Stieglitz and Christina Krywka from Helmholtz-Zentrum Geesthacht, who collaborated to compose a proposal for scanning 3DXRD at PETRA III.

I would like to extend my sincere thanks to Luise Theil Kuhn, the head of the ISA section, who always watches over the Ph.D. students and supports us in taking action when it is needed.

Many thanks to my colleagues from the SEWWHI project, with who I shared very good moments and laughs at work, at conferences, and in our free time.

Finally, special thanks to my supportive husband, Jakob, who read most of my thesis and gave me good suggestions to improve it. You kept me going to the last bit of this journey. I am grateful to my parents-in-law, Jens and Annette, who welcome me into their family as their own daughter and make Denmark feel like a second home. Thanks also to my family in Mexico, who always believes in me. To my dad for his unconditional love. To my mom and sister, Euge and Pau, you are my heroes, and you motivate me to work hard and tenaciously. You are always ready to face adversity and never give up. Finally, I want to thank my Tita, a kind-hearted woman who inspired me with her blissful spirit.

List of publications

PUBLICATIONS INCLUDED IN THIS THESIS

Mar Lucas, M.; Ramos, T.; Jørgensen, P.S.; Canulescu, S.; Kenesei, P.; Wright, J., Poulsen, H.F.; Andreasen, J.W. (submitted): **Non-destructive determination of phase, size, and strain of individual grains in polycrystalline photovoltaic materials**

The manuscript is placed in Section 3.1

CONTRIBUTIONS TO CONFERENCES ABROAD

[C.1] M. Mar Lucas, H.F. Poulsen, J.W. Andreasen, *3D Multigrain Crystallography for detection and discrimination of secondary phases in Cu_2ZnSnS_4 for thin-film solar cell applications*. Poster at the 4th International Conference on 3D Materials Science (3DMS 2018), Helsingør, Denmark.

[C. 2] M. Mar Lucas, H.F. Poulsen, J.W. Andreasen, *Characterization of the crystallographic phases in Cu_2ZnSnS_4 thin-film solar cells.* Poster at DESY User's Meeting 2019, Hamburg, Germany.

[C.3] M. Mar Lucas, M. Gansukh, S. Canulescu, S. Engberg, T. Ramos, P. S. Jørgensen, P. Kenesei, J. Wright, H.F. Poulsen, J. W. Andreasen. *Identification of secondary phases in thin-film solar cells by 3DXRD and multigrain crystallography.* Oral presentation at the 25th International Congress on X-ray Optics and Microanalysis (IXCOM-25), 2019, Lombard IL, USA.

[C.4] M. Mar Lucas, P. S. Jørgensen, T. Ramos, M. Gansukh, S. Canulescu, H.F. Poulsen, J. W. Andreasen. *Analysis of polycrystalline Ag-alloyed Cu_2ZnSnS_4 by 3DXRD.* Poster at the 10th European Kesterite Workshop, 2019. Uppsala, Sweden.

[C.5] M. Mar Lucas, P. S. Jørgensen, M. Gansukh, S. Canulescu, J. Wright, H.F. Poulsen, J. W. Andreasen. *Analysis of polycrystalline Ag-alloyed Cu_2ZnSnS_4 by 3DXRD.* Poster at the Virtual chalcogenide conference 2020. Online

Posters and the oral presentation abstract are placed in Annex I.

List of Abbreviations

3DXRD	Three Dimensional X-ray Diffraction
ACZTS	$(Ag,Cu)_2ZnSnS_4$
APS	Advanced Photon Source
AZTS	Ag_2ZnSnS_4
BCS	Bilbao Crystallographic Server
CIGS	$Cu(In, Ga)Se_2$
CSL	coincidence site lattice
CZTS	Cu_2ZnSnS_4
DC	Direct Current
DEG	dyethylenglycol
DL	double layer
EBSD	Electron Backscattered Diffraction
EDX	Energy-dispersive X-ray spectroscopy
EM	Electron microscopy
ESRF	European Radiation Synchrotron Facility
FABLE	Fully automatic BeamLine Experiments
FIB	Focused Ion Beam
GB	grain boundary
HEXRD	High Energy X-ray diffraction
ICSD	Inorganic crystal structure database
PLD	Pulsed Laser deposition
PV	Photovoltaic
RF	Radiofrequency
SLG	Soda Lime Glass
SPring-8	Super Photon ring-8
TCO	transparent conductive oxide
TETA	triethylenetetramine
TFSC	Thin-film solar cells
XANES	X-ray absorption near-edge spectroscopy
XBIC	X-ray Beam Induced Current
XRD	X-ray Diffraction

List of symbols

(hkl), {hkl}	Crystal plane, family of crystal planes
[hkl], <hkl>	Crystal axis, family of crystal axes
$\|\|E\|\|_F$	Frobenius norm of a strain tensor
A	Transformation matrix between Cartesian hkl lattice and direct space
a*, b*, c*	Reciprocal lattice basis
a, b, c	Direct lattice basis
B	Transformation matrix between Cartesian hkl lattice and reciprocal space
d_{hkl}	Interplanar spacing
E_g	Bandgap
η	Azimuthal angle measured in the plane of the image with respect to the rotation axis
η'	Azimuthal angles measured with respect to the horizontal plane
F	deformation matrix
f(Q)	Atomic form factor
F(Q)	Unit cell structure factor
FF	Fill-factor
G	Reciprocal lattice vector
$\boldsymbol{G}_{\omega}$	Reciprocal lattice vector in the rotation coordinate system
$\boldsymbol{G}_{s}$	Reciprocal lattice vector in the sample reference system
$\boldsymbol{G}_{c}$	Reciprocal lattice vector in the crystal reference system
$\boldsymbol{G}_{l}$	Reciprocal lattice vector in laboratory coordinate system
h, k, l	Miller indexes
J_{SC}	Photocurrent
J_{ph}	Flux of absorbed photons
k	Wave vector
L	Lorentz factor
L	Direct space lattice vectors
ω	Rotation angle
P	Polarization factor
Q	Scattering vector
R	Pure rotation derived from polar decomposition
S	Reference system diffractometer
Us	Right stretch tensor derived from polar decomposition
U	Orientation matrix

$\mathbf{V}$	Left stretch tensor derived from polar decomposition
V_{OC}	Open-circuit voltage
α, β, γ	Unit cell angles
$\boldsymbol{\varepsilon}$**, E**	Strain tensor
ε_{ij}	Strain component
λ	Wavelength of X-ray
Σ	Multiplicity, twin index
$\boldsymbol{\sigma}$	Stress tensor
σ_{ij}	Stress components
σ_m	Machine error

Contents

1 Introduction

1.1 THE PROBLEM

The world electricity consumption increments steadily, and projections estimate growth from 18 TW/y in 2012 to 24 TW/y by 2040 [1]. Current technologies based on fossil fuels cannot cover this demand before depleting these resources. Therefore, renewable technologies such as photovoltaics (PV) are ideal candidates to cover the global need for electricity. Solar energy is abundant, and PV technology can transform it into electricity.

Thin-film Solar Cells (TFSC) have many advantages over the dominant silicon solar cells (Si). TSFC requires less material and less energy to fabricate an efficient device. Consequently, production costs are considerably reduced, and the fabrication processes are scalable with a short energy payback time [2]. Ultimately, the device is lighter than Si-cells and can be fabricated on flexible substrates. TFSC can supply power to remote areas with limited electricity access, be an integrated part of buildings, lower installation costs, or be part of portable electronics [3].

Although TSFC technology provides exceptional characteristics, it remains a challenge to master and optimize the fabrication methods. Different variables can change the film properties and microstructure. To make efficient, low-cost, sustainable solar cells, we need to understand the influence of the fabrication parameters on the film microstructure and the correlation between the film microstructure and the film physical properties.

Furthermore, some TFSC technologies utilize expensive, scarce, and sometimes toxic materials. A relatively new type of TFSC that overcomes these challenges is kesterite solar cells. However, the absorber layer has secondary phases, crystals of different sizes and orientations, grain boundaries, and strained grains that affect the device efficiency. Recent reviews about this material mention the lack of studies about kesterite solar cells microstructure, specifically the bulk/absorber layer [4], [5]. Electron microscopy (EM) is typically the chosen technique to characterize the microstructure of TFSC. However, the device is inevitably destroyed to access the buried absorber layer. Despite the high spatial resolution of EM, the sensitivity of the grain strain measurements is lower than X-ray Diffraction methods [6]. EM strain analysis of TFSC fabricated on flexible substrates could be affected by the sample preparation requirements, which unavoidably would alter the finely structured films.

For these reasons, we propose a non-destructive technique that can provide information about the structural properties of the films and that could potentially allow dynamical experiments such as measuring in-operando solar cells or in-situ recrystallization.

The technique here employed is Three-Dimensional X-ray Diffraction, 3DXRD. After analyzing TFSC, our results show a high potential to employ this technique to other types of polycrystalline coatings.

1.2 A GENERAL OVERVIEW OF POLYCRYSTALLINE THIN-FILMS

Thin-films are coatings with a thickness between tenths of nanometers to several micrometres. This technology has steadily been evolving, as narrated in one of the latest reviews about thin-film coating technology [7]. They have several applications providing unique properties in different fields: mechanical, optical, electronic, superconducting, and photovoltaic technologies.

Overall, the fabrication of thin-films is by chemical or physical deposition techniques. In the chemical methods, a fluid precursor (gas or solution) reacts with the substrate surface and solidifies as a thin-film. Some conventional chemical deposition techniques are chemical vapour deposition, chemical bath deposition, and spin coating. In the physical processes, the precursor material transitions from a solid phase (a target) to a vapour phase, and finally to a thin-film as a solid phase onto the substrate. Sputtering and Pulsed Laser Deposition (PLD) are some physical fabrication techniques commonly used in photovoltaic thin-films.

Depending on the chosen fabrication process, the film structural properties vary, such as phase composition, grain size, grain boundaries, stress, and strain. These properties have a direct impact on the performance of the films.

The complexity of polycrystalline thin-films resides in controlling the manufacturing processes to obtain the desired properties and minimize structural defects in the films. Hence, the characterization of their structural properties is vital. Measuring their microstructure can create models that predict critical parameters to optimize the thin-films.

TFSC are not the exception to this rule. Their design consists of several layers, which are illustrated in Figure 1.1. Each layer is fabricated sequentially utilizing different deposition methods and heat treatments. As a result, the absorber layer endures many processing methods that modify its microstructure, improving device performance. Studying the resulting microstructure is necessary to understand the film structural properties linked to their physical properties and improve the engineering of the films. In this work, we present a characterization technique, 3DXRD, that can measure the microstructure of any polycrystalline thin-film with a thickness of about 1µm.

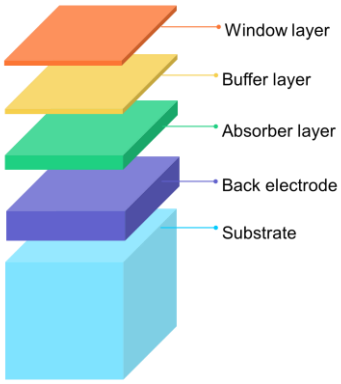

Figure 1.1. Architecture of a thin-film solar cell.

1.3 STRUCTURAL PROPERTIES OF POLYCRYSTALLINE THIN-FILMS

Polycrystalline thin-films are an ensemble of small grains or crystals with different sizes and orientations. Atoms are arranged inside the crystals in three dimensions and are symmetrically associated by rotations, translations, or other symmetry operations. In crystallography, this 3D arrangement of atoms in space is called a crystal lattice. The minimal entity of this arrangement is the unit cell. The geometrical definition of a unit cell is given by three lattice vectors a, b, and c, and the angles between them, α, β, γ. The atoms inside the unit cell occupy positions described by fractional coordinates along the cell edges measured from a reference point. The rest of the atoms are generated by the symmetry operations that characterize the symmetry of the unit cell.

In Figure 1.2, we illustrate a triclinic unit cell to display the unit cell parameters. Moreover, the representation of the most relevant unit cells for this work is shown, the cubic face-centred and the tetragonal body-centred unit cells. The face-centred unit cell has lattice points on the faces of the cube. In contrast, the body-centred unit cell has a point in the centre of the unit cell in addition to the eight corner points.

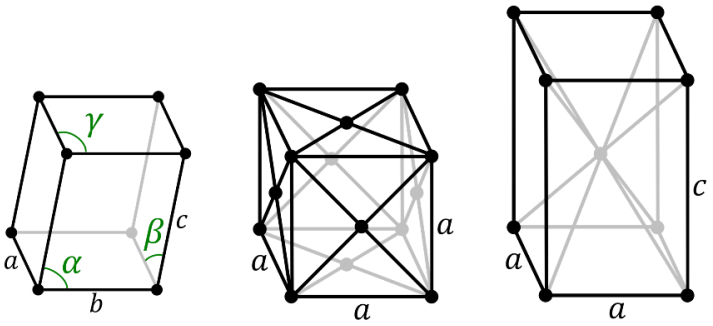

Figure 1.2. Left: Triclinic unit cell [8]. Centre: Cubic face-centred unit cell [9]. Right: Tetragonal body-centred unit cell [10].

The unit cell repeats systematically within a specific volume, forming a grain. Moreover, the unit cell characterized by a symmetric configuration and a specific set of atoms is defined as a crystallographic phase. In a thin-film, one can encounter different crystallographic phases generating a multiphase polycrystalline film.

Optoelectronic, mechanical, and conducting properties vary depending on the crystal structure of the grain, establishing the film properties. Hence, the importance of identifying the crystallographic structure of the individual crystals.

Microstructure variations in the polycrystalline thin-films, such as phase composition, size, shape, grain boundaries, anisotropy, stress, and strain, originate during the annealing and post-treatment processes. As these disparities strongly influence the macroscopic film properties, it is necessary to unveil the detailed structural information of the thin-film. This enables us to master their fabrication processes, for example, controlling the grain size and orientation with respect to the substrate and neighbouring grains.

1.3.1 Recrystallization, grain growth, grain size, and grain boundaries

This section discusses how each microstructure variation evolves during grain growth and its effect on thin-film performance. As described in 1.2, it all starts with the deposition of the material; whether it is a physical or a chemical method, the deposited film undergoes a series of thermal processes that will ultimately define the film microstructure.

After the material deposition onto the substrate, most thin-films are amorphous, with some nuclei of crystals. The transition to grains happens during the annealing step, consisting of heating the material at a high temperature, removing defects, and ordering atoms in lower energy configurations. The annealing step promotes recrystallization (formation of grains with a low density of linear defects such as dislocations) and grain growth (smaller grains are eliminated, larger grains grow, and grain boundaries assume a lower energy configuration) [11]. The result is an ensemble of grain structures and grain boundaries.

The mechanisms involved in the thin-film fabrication start from surface diffusion of the adatoms (adsorbed atoms at the surface) [12] pinned by diverse deposition methods [13], nucleation [14], the kinetics of recrystallization and strain inflicted during the annealing process [11], and the grain growth driven by grain boundary mobility [15].

The grain growth is influenced by different parameters such as temperature, pressure, impurities in the atmosphere. Low-temperature processes are characterized by small columnar grains. As the temperature increases, the size increases, and grain boundary migration is possible [16]. Such variations in microstructure are described in the structure zone model shown in Figure 1.3.

In Figure 1.3, the grain structures change at the various temperatures at increasing film thickness. In Zone I, the substrate temperature, T_s, is lower than the melting point of the film material T_m. A structure with a fine fibre texture develops with random orientations of the nuclei. The columns are generally not single grains but are composed of smaller, more equiaxed grains [17]. Zone T is characterized by $0.2 < T_s/T_m < 0.4$, forming an inhomogeneous structure along the film thickness. The structure is fine crystalline at the substrate while columnar in the upper part of the film. Grain boundary migration is strongly limited. In Zone II, high substrate temperatures are implemented, creating a homogeneous structure along the film thickness composed of columns penetrating from the bottom to the top. The grain boundaries are nearly perpendicular to the film plane [18]. The mechanisms of grain growth can be competitive (different growth rates in different crystallographic directions) or by restructuration (minimisation of the surface and interface energy).

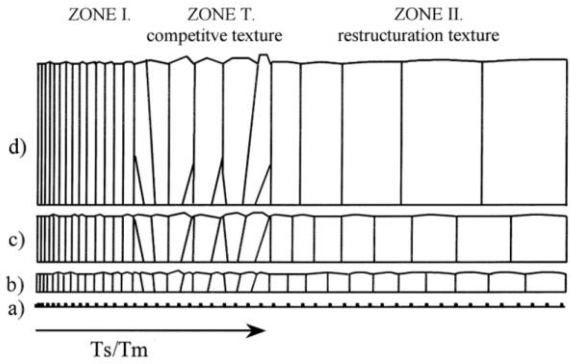

Figure 1.3. Structure zone model at various film thicknesses. Reprinted from [18] with permission from Elsevier.

Complications arise when multi-component films are fabricated as the kinetics of the process change. The grain size is modified, and secondary phases form inevitably once the material reaches an equilibrium. One example is the kesterite solar cell. During the formation of the active layer, secondary phases such as binary and ternary compounds grow. We will discuss this case in detail in section 1.6.2.

Another exciting aspect of grain growth is the formation of grain boundaries, GBs. These are the interface between misoriented grains. The region with overlapping point lattices between the two adjacent grains is called the coincidence site lattice, CSL. The CSL is classified according to the multiplicity Σ, which is the ratio of the unit cell volume of the CSL and the unit cell of the crystal. In Figure 1.4, an example of a CSL with Σ5 is shown [19].

Moreover, symmetry operations such as rotations and translations can transform one grain into another. With the CSL definition, one can identify the rotation axis shared by the two grains with respect to a reference coordinate system, the rotation angle, and the GB plane normal [20].

Grain Boundary Engineering is a recent concept that aims at maximizing the number of favourable GBs. However, GB formation models and evolution mechanisms lack the experimental evidence [15], [21].

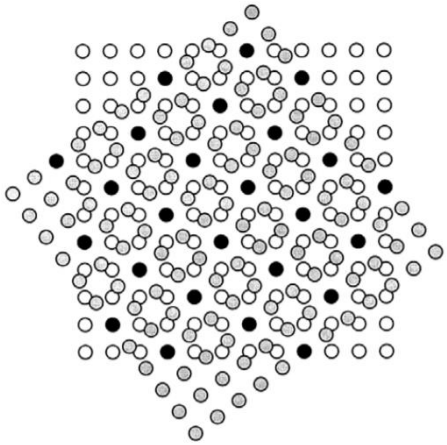

Figure 1.4. Coincidence site lattice (Σ5) formed from two simple cubic lattices rotated by 36.9° about an <001> axis. Filled circles denote sites common to both lattices. Reprinted from [19] with permission from Elsevier.

1.3.2 Strain

One particular aspect of thin-films is the residual stresses that result from their fabrication or that manifest during their lifetime of service. They can be detrimental to the performance of thin-films and even diminish the material lifetime.

Residual stress remains in the material after an original force has been applied, and it remains in equilibrium with the surroundings. As a result, the film structure is in a deformed state or a different configuration from a reference configuration; in other words, the film is strained [22].

The degree of the deformation caused by these remaining internal forces covers different length scales, as shown in Figure 1.5. At the macro-scale level, type I stress provides information on variations larger than the grain size. The mesoscale stresses, type II, describe the average strain of a grain. Type III stresses correspond to the micro-scale and are alterations within the grain, such as dislocations and crystalline defects [23].

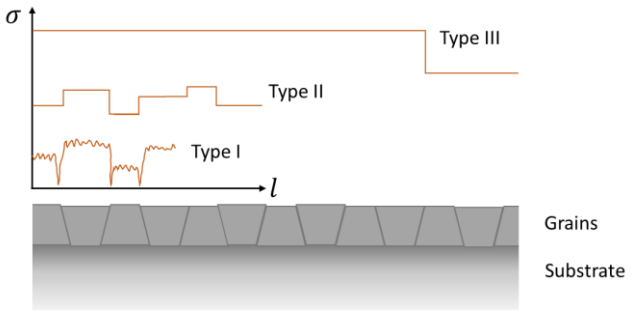

Figure 1.5. Types of residual stress with respect to the length scale of variation. Adapted from [23].

In this study, it is possible to measure strain due to type I and type II stresses using X-rays. For a strained crystal, the interplanar spacing varies, causing a displacement of the diffraction spot position, while peak broadening occurs due to defects within the grain.

In solar cells, the films undergo multiple thermal gradients introducing stresses or relaxation to the films and changing their microstructure. The lattice mismatch between the substrate and the film, or between the multiple layers that constrain one another can also induce strain. In the methodology chapter, we discuss how to obtain the strain measurements from 3DXRD.

1.3.3 Twin boundaries in polycrystalline thin-films

As the grains grow in the film, their orientations evolve accordingly. However, the growth direction can change and start developing a grain with a different orientation. Similar to the CSL model in section 1.3.1, a geometrical operation, called "twin operation," relates these grains by transforming one grain into another. The theory of CSL is used to describe twin operations, and the twin index is the multiplicity of CSL, Σ. A twin boundary is also described by the misorientation angle between the twin grains, the rotation axis, and the GB plane normal.

In chalcogenide thin-films, the occurrence of twin boundaries Σ3 is a common phenomenon. CdTe, with its cubic structure, has Σ3 boundaries characterized by a 60° rotation about axis $<111>_{cubic}$ [24], [25], whereas Cu(In,Ga)$(S,Se)_2$ and Cu_2ZnSnS_4, with tetragonal unit cells, have Σ3 boundaries with a 180° rotation about axis $<221>_{tetragonal}$ [26], [27], as depicted in Figure 1.6. Another recurrent twin boundary in chalcopyrites is the Σ3 with rotation 60° about the axis $<221>_{tetragonal}$, also shown in Figure 1.6. For the latter, two configurations are proposed with anion- or cation-terminated twin boundaries.

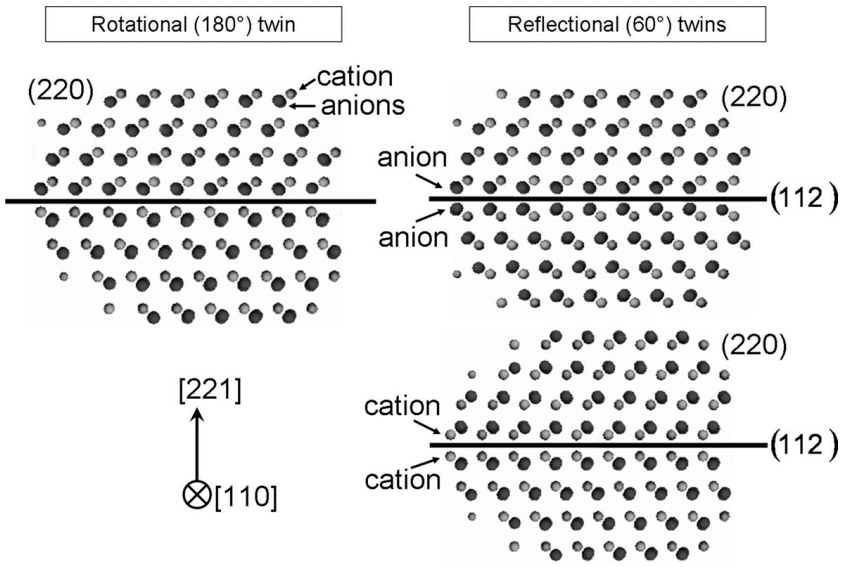

Figure 1.6. Three constellations for 180°−⟨221⟩$_{tetragonal}$ and 60°−⟨221⟩$_{tetragonal}$ twin boundaries in the chalcopyrite-type structure: a 180° rotational (left), and two reflectional, anion- and cation-terminated twin boundaries (right). Reproduced from [26] with permission from the International Union of Crystallography.

Chapter 2 of this thesis demonstrates how to characterize twin boundaries by calculating the angle between grains and the corresponding axis of rotation from the grain orientation matrices.

1.3.4 Pole figures

The grain orientation matrices obtained by 3DXRD can be represented in the form of a stereographic projection. The pole OP intersects the surface of the sphere's northern point P. Then, P is projected to the sphere's equatorial plane, point p, by the line segment PS connecting P to the southern hemisphere, as shown in Figure 1.7.

In general, the pole figures of the crystallographic planes {100}, {110} and {111} are used to describe cubic structures, whereas planes {100}, {110}, {001} describe the tetragonal structure in a xyz reference system. Figure 1.8 shows the pole figure {100} depicting the plane normals of the cube.

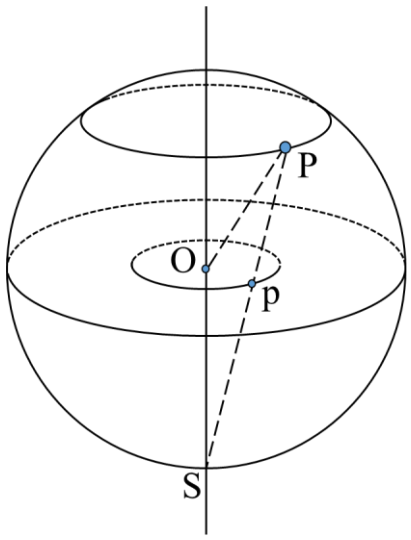

Figure 1.7. Stereographic projection

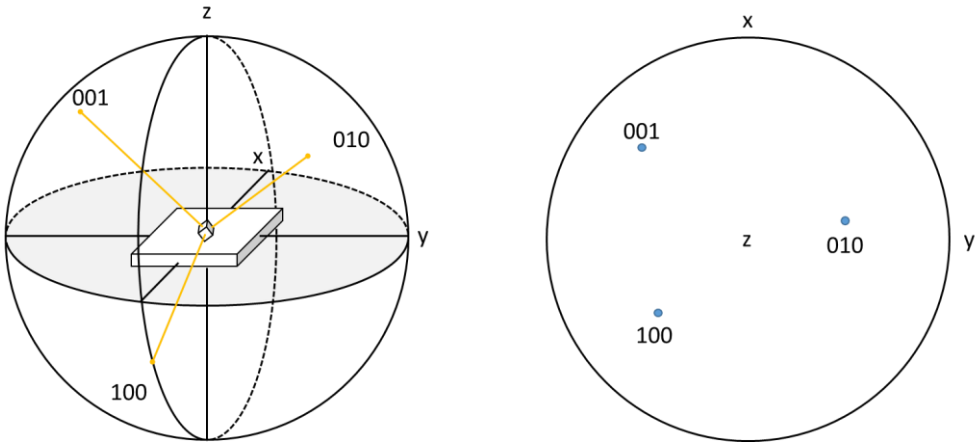

Figure 1.8. Left: Projection plane, reference sphere in the XYZ system, and the points of intersection of the normal to the plane (100), (010), and (001) of the specimen. Right: The three poles 100, 010, and 001, as projected on the basic circle.

1.4 PHOTOVOLTAIC THIN-FILMS

Back in 1939, Edmond Becquerel discovered the photovoltaic effect using an electrochemical cell. In the late 1950s, silicon was already the primary material in solar cells with main applications in satellites and remote sites. Since 2010, the cost of Si-cells has declined dramatically due to the overcapacity of production; this contributed to its wide applications in PV power plants currently covering 95% of the PV market.

Although silicon technology has improved the efficiency of the panels above 20% [28], the production of highly pure silicon wafers requires energy-intensive processes causing the generation of CO_2. Moreover, silicon has an indirect bandgap, which lowers the capacity to

absorb light efficiently. The panel components, such as encapsulation and wiring, make the device rigid and heavy for certain applications that thin-film solar cells could cover.

PV thin-films utilize less material (~ <1 µm thick layers), as the absorber layer has a direct bandgap and a high absorption coefficient. The fabrication processes require less energy than Si-cells and depending on the substrate, modules can also be flexible.

One of the first types of TFSC is amorphous hydrogenated silicon, a-Si:H, with 2.4% efficiency [29]. Their steady development from laboratory to commercial panels, recounted in [30], shows PV thin-films potential in the PV market. This film microstructure is out of the scope of this work, as 3DXRD is limited to the polycrystalline materials.

Meanwhile, chalcogenide[1] materials, CdTe and Cu(In, Ga)Se_2 (CIGS), are other types of semiconductors implemented in PV thin-films. Together with a-Si:H, they belong to the second generation of PV technology.

Nonetheless, the scarcity of indium limits the production capacity of CIGS solar cells, whereas the toxicity of Cadmium imposes restrictions on its use in some countries. As an alternative, third-generation TFSC proposes an organic and new type of chalcogenide semiconductors with promising candidates to overcome these limitations.

In this work, we focus on the chalcogenide film microstructure of Cu_2ZnSnS_4 (CZTS) and solve the challenging task of identifying secondary phases that arise during the film fabrication. As we describe the grain orientations and sizes, we will also analyze the texture and the twin boundaries in the coating.

1.4.1 Principles of operation of a solar cell

- *Photogeneration*. Photons with specific energy are absorbed, generating electron-hole pairs in the material. This energy threshold, called the bandgap, Eg, is particular to the type of semiconductor. For example, silicon has an indirect bandgap (1.1 eV) and a low absorption coefficient (1.5 cm^{-1}), [31], which requires thick wafers (~100 - 150 µm) to absorb useful incident photons. In contrast, thin-film semiconductors such as CdTe (1.5 eV), CIGS (1.0 - 1.7 eV), and CZTS (1.4 eV) have a direct bandgap and high absorption coefficients. Therefore they require less material in the absorber layer (thickness: 1-5 µm).

[1] Common chalcogenides are sulfides, selenides, and tellurides.

- *Charge separation*. Electron-hole pairs separate from each other because of the internal electric field created by the diode structure of the solar cell. The electric field originates at the p-n junction, the region where the p-type semiconductor (acceptor of electrons) and p-type semiconductor (donor of electrons) meet. The basic parameters to characterize the performance of the solar cell are given by:

    - Photocurrent, J_{sc}, which is limited by the flux of the absorbed photons, J_{ph}.
    - Open-circuit voltage, V_{oc}, defined by the Eg/q (q being the charge of an electron).
    - Fill-factor, FF, is determined as the area under the I-V curve of the solar cell.

1.5 SECOND GENERATION THIN-FILM SOLAR CELLS: CdTe, CIGS

CdTe has shown 22.1% and 19% efficiencies for a cell and a module, respectively [32], and because of its binary composition, this film is relatively easy to fabricate. The implementation of some schemes such as the activation treatment with $CdCl_2$ to enlarge the grain size and passivate[2] grain boundaries with Cl have optimized the device [24]. Alloying Se into the absorber layer has recently demonstrated a positive effect on increasing the current density and varying the bandgap [33]. The film microstructure of CdTe, which originates from the zincblende structure of CdTe, consists of grains between 1-40 μm and grains with (111) texture [34]. Interestingly, it has been observed that this texture is not favourable to the device efficiency, and the activation treatment combined with high annealing temperatures can fix this [35]. Moreover, the twin boundaries Σ3 (111) [24], Σ3 (112), and Σ5 (310) are also investigated by density functional calculation to find ways to passivate them [36].

CdTe is typically built in the superstrate configuration, illustrated in Figure 1.9. a). The first layer applied onto the substrate, commonly glass, is the transparent conducting oxide layer (TCO), followed by the window layer (i-ZnO) and the buffer layer (CdS). The absorber layer CdTe and the back contact complete the structure of the cell.

Although CdTe is a stable compound, the toxicity of Cd limits the scalability of this technology. Moreover, disposal at the end-of-life and leaking risk in case of an encapsulation failure may raise concerns about its safety and sustainability.

CIGS comes from the doping of $CuInSe_2$ with Ga, allowing a bandgap variation from 1.04 eV for $CuInSe_2$ and 1.68 eV for $CuGaSe_2$ [37], which enhances the device performance. Reaching 23.4% and 19.5% efficiencies for a cell and a module, respectively [32]. The sodium content in the glass diffuses into the absorber layer during the annealing step,

[2] Inhibition of the defects states in the grain boundaries

producing larger grains with beneficial effects on the device properties [38]. Therefore, a Na-treatment is included in the preparation of flexible substrates, which lack Na-content.

CIGS grains originate from the tetragonal structure, chalcopyrite (I-42d). Electron Backscatter Diffraction, EBSD, studies have shown that the average grain size is below 1 µm, varying according to the fabrication conditions. Twin boundaries Σ3 are the most common with the 180° - $<221>_{tetragonal}$ [26]. For $CuGaSe_2$ absorber layers, the c-axis is preferably aligned to the substrate surface, as well as the Σ3 twin boundary of 60° - $<221>_{tetragonal}$ and 70° - $<110>_{tetragonal}$ [39]. Other studies report preferred orientations (112) and (220) controlling the [Se]/[In + Ga] flux ratio during the deposition of precursors [40].

In contrast to the CdTe solar cells layout, the CIGS cells use an inverted disposition, Figure 1.9. b). The glass is coated by molybdenum, followed by the absorber layer CIGS, the buffer layer (CdS), and the window layer and TCO layer.

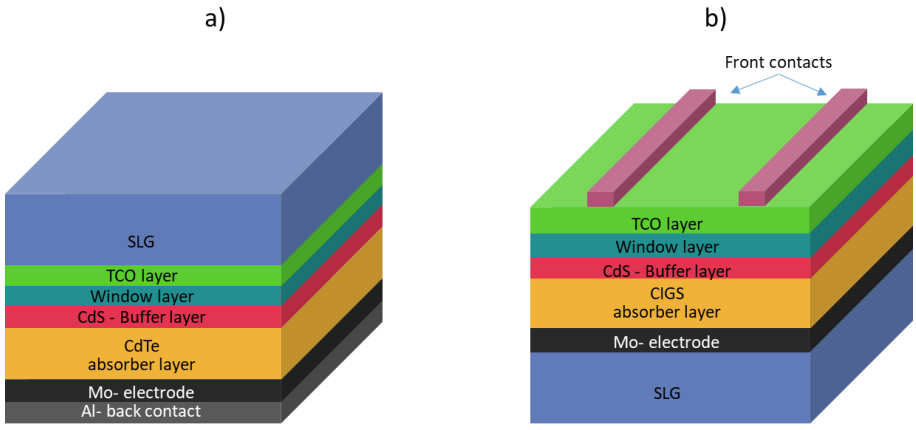

Figure 1.9. Architecture of TFSC. a) CdTe, b) CIGS.

1.6 THIRD-GENERATION SOLAR CELLS: Cu_2ZnSnS_4

Cu_2ZnSnS_4, CZTS, is a promising material that can overcome the CIGS scalability and CdTe toxicity problems. Earth-abundant and non-toxic components form the polycrystalline CZTS absorber layer. Moreover, CZTS has a high absorption coefficient (10^4 cm^{-1}) and a direct bandgap (1.45 eV) suitable for solar cells [41]. Similar to the CIGS cell architecture, CZTS also is deposited on a Molybdenum-coated soda-lime glass, Mo-SLG. The precursor elements are deposited via physical or chemical methods, typically with a Cu-poor, Zn-rich composition, and undergo an annealing step, promoting the CZTS phase formation. The subsequent layers, CdS, ZnO, and TCO, finalize the device.

Nevertheless, CZTS solar cell efficiency has only reached 11% for the sulfide type and 12.6% for the selenized $Cu_2ZnSn(S, Se)_4$ [32]. Some of the challenges regarding structural properties that might affect solar cell electrical properties are discussed in the following sections.

1.6.1 Crystallographic aspects of CZTS

The crystal structure of CZTS has been investigated as a single crystal [42]–[45], and powders [46]–[48], by X-ray and neutron diffraction, X-ray resonant single-crystal diffraction, and X-ray anomalous dispersion. In addition, first-principle calculations examine different structural variations that include kesterite, stannite, and wurtzite-type structures [49]–[51].

There is an established agreement in the literature that CZTS crystallizes in the kesterite structure with space group (I-4). However, changes in the structure occur for thin-films with Cu-poor, Zn-rich composition. For the off-stochiometric CZTS, the stannite structure (I-42m) has been assigned. However, by using neutron diffraction [46] and resonant single-crystal diffraction [44], a third model, the "disordered kesterite" of Cu/ Zn atoms, is proposed.

Kesterite, stannite, and disordered kesterite differ in the cations positions, as shown in Figure 1.10. The kesterite structure alternates layers of CuSn (z = 0, ½) and CuZn (z =¼, ¾). In contrast, the stannite structure has a different cation layer arrangement in which ZnSn (z = 0, ½), Cu_2 (z =¼, ¾) interchange. Additionally, the anion position is different in kesterite (x,y,z) versus stannite (x,x,z). Disordered kesterite has the same cation layer distribution as kesterite, with only disorganized copper and zinc occupying z = ¼ and ¾ atomic planes. Ignoring the anion position in the space group (I-42m), disordered kesterite adopts this configuration with a statistical distribution of copper and zinc on the Wyckoff position 4d. The remaining copper will occupy the 2a site [52].

The atomic scattering factors of Cu^+ and Zn^{2+} are similar; hence it is not possible to distinguish between kesterite, disordered kesterite, and stannite by X-rays. However, this is possible by neutron diffraction [46] or resonant X-ray diffraction [44]. One would expect to find a disordered kesterite structure through these techniques, given the off-stoichiometric and equilibrium conditions in which thin-films are grown.

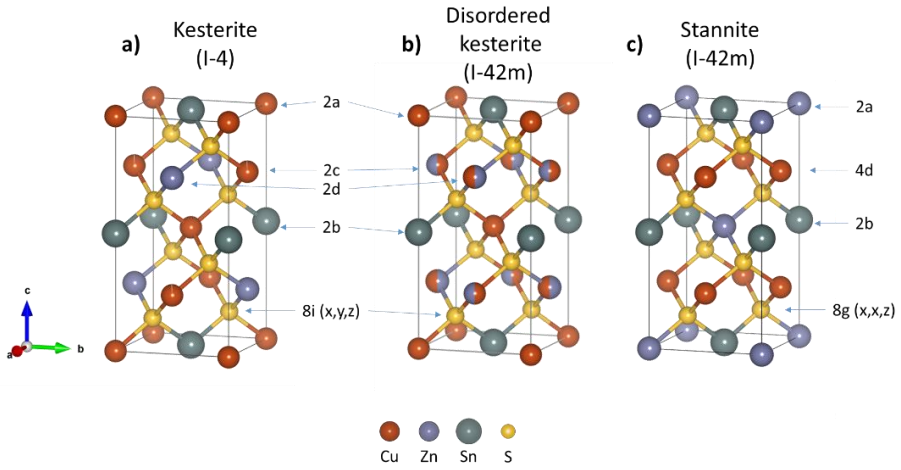

Figure 1.10. Kesterite, Disordered kesterite, and Stannite cation layers viewed from a-b plane at different z-positions along the c-axis, (blue: Cu; orange: Zn; red: Sn) [52]. *The crystal structures were drawn with the VESTA computer program* [53].

When conducting 3DXRD experiments, the phases revealed by the XRD pattern will fit into kesterite, disordered kesterite, or stannite. However, based on the mentioned neutron studies, disordered kesterite should be a good choice to index the film grains. In principle, one can perform a structural refinement on a set of reflections that belong to the grain and determine which structure fits the best.

1.6.2 Secondary Phases in CZTS

CZTS is obtained through an equilibrium reaction in which product formation and decomposition into the initial reactants can happen, as shown in reaction (1.1) and (1.2). The coexistence of secondary phases is difficult to avoid. Moreover, CZTS can only be formed under sufficient partial pressures of S and SnS [54].

$$Cu_2S_{(s)} + ZnS_{(s)} + SnS_{(g)} + \frac{1}{2}\,S_{2(g)} \rightleftarrows CZTS_{(s)} \qquad (1.1)$$

$$SnS_{(s)} \rightleftarrows SnS_{(g)} \qquad (1.2)$$

Figure 1.11 shows the Cu_2S-SnS_2-ZnS equilibrium diagram at 400°C describing all the possible phases that can form. This diagram indicates that CZTS has low thermal stability and is straitened in a narrow single-phase region. The formation of secondary phases originates from an initially non-optimal film composition, outside the single-phase region, or from a film with an initially optimal composition that breaks down due to non-controlled equilibria conditions during the formation process [54].

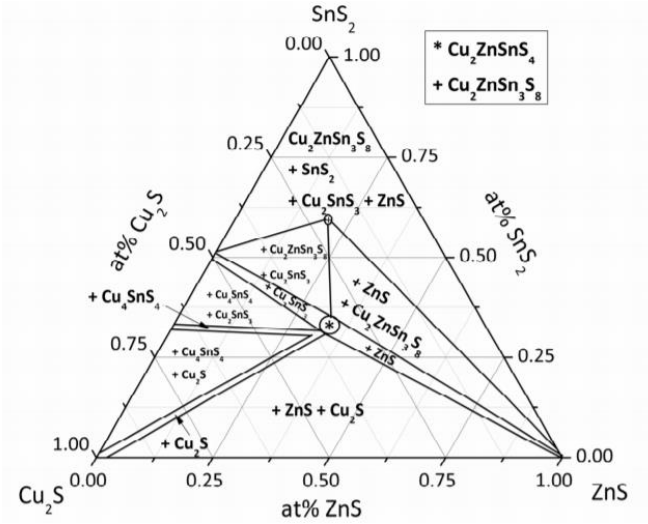

Figure 1.11. Cu_2S-SnS_2-ZnS equilibrium diagram. Reprinted from [55] *with permission from Elsevier.*

Secondary phases can have detrimental effects on the kesterite solar cell performance due to their different optoelectronic properties. The most common secondary phases and their bandgaps are listed in Table 1.1. High bandgaps are responsible for high series resistance when situated close to the back contact. On the other hand, low bandgaps at the p-n junction decrease Voc.

Table 1.1. Bandgap of the secondary phases in CZTS films [54].

Compound	**Cu_2ZnSnS_4**	**Cu_2SnS_3**	**ZnS**	**SnS_2**	**SnS**	**Cu_2S**	**CuS**
Bandgap (eV)	1.5	0.9	3.7	2.5	1-1.3	1.2	1.72 [56]

XRD, Raman scattering, and Energy-dispersive X-ray spectroscopy (EDX) are usually combined to characterize the absorber layer. However, they can only offer qualitative and partial discrimination of phases, especially for ZnS and Cu_2SnS_3 [57]. Structurally, CZTS, Cu_2SnS_3 and ZnS are very similar. The first two phases have a body-centred tetragonal structure, whereas ZnS is a face-centred cubic. Their lattice parameters are also very close, doubling one of the cubic axis results in the tetragonal structure. Hence, X-ray powder Diffraction cannot distinguish among these three phases. The distinction between Cu_2SnS_3 and CZTS is even more convoluted, since the isoelectronic cations Zn^{2+} and Cu^{+} are alike, and their scattering properties are nearly identical.

3DXRD can distinguish between CZTS and ZnS and identify other crystallographic structures. Table 1.2 lists the possible secondary phases and their crystal structures taken from the inorganic crystal structure database (ICSD). These structures are used in the 3DXRD data analysis to identify the crystallographic phases in the diffraction patterns.

Table 1.2. Crystal structures of CZTS and secondary phases from ICSD selected by the data quality

Phase	Crystal Structure	Space group	Lattice parameter (Å)	ICSD	Ref.
Cu_2ZnSnS_4	Tetragonal	I-4	a=5.434* c=10.843* α, β, γ=90°	184358 236246 239674-81,83,85-86 243666-67 253249-50 262388-89	[48] [58] [47] [59] [60] [43]
	Tetragonal (Disorder kesterite)	I-42m	a=5.434*, c=10.843* α, β, γ=90°	192110 192815 239682, 84	[44] [61] [60]
	Tetragonal (Stannite)	I-42m	a=5.434*, c=10.856* α, β, γ=90°	171983	[45]
Cu_2SnS_3	Monoclinic	c1c1	a=6.65, b=11.53, c=6.66 α, γ=90, β=109.39	91762 258981	[62] [63]
	Tetragonal	I-42m	a=5.413 c=10.824 α, β, γ=90°	50965	[64]
$Cu_3SnS_{3.6}$	Tetragonal	I-42m	a=5.426, c=10.838 α, β, γ=90°	237555	[65]
Cu_4SnS_4	Orthorhombic (high temperature)	P n m a	a=10.06, b=13.49, c=10.09 α, γ=90°, β=100.84°	833 432660	[66] [67]
	Monoclinic (low temperature)	P 1 21/c 1	a=13.57, b=7.69, c=6.42 α, β, γ=90°	432661	[67]
$CuSn_{7.5}S_8$	Cubic	F-43m	a=10.393 α, β, γ=90°	32525	[68]
Cu_4SnS_6	Trigonal	R -3 m H	a=3.739, c=32.941 α, β=90°, γ=120°	88972	[69]
$Cu_4Sn_7S_{16}$	Trigonal	R -3 m H	a=7.38, c=36.03 α, β=90°, γ=120°	50964 154696	[69] [70]
ZnS	Cubic	F-43m	a=5.434 α, β, γ=90°	77090	[71]
			a= 5.4032 α, β, γ=90°	230703	[72]
	Hexagonal (Wurtzite)	P63mc	a=3.823, c=6.261 α, β=90°, γ=120°	67453	[73]
SnS_2	Trigonal	P-3m1	a=3.642*, c=5.887* α, β=90°, γ=120°	100610 252197	[74] [75]
SnS	Orthorhombic	Pbnm	a=4.335*, c=3.979* α, β, γ=90°	41739 52108	[76] [77]
Cu_2S	Monoclinic	P121/c1	a=15.246, b=11.884, c=13.494 α, γ =90, β=116.35	100333	[78]
	Hexagonal	P63/mmc	a=4.033, c= 6.739 α, β=90°, γ=120°	95397	[79]
$Cu_{1.78}S$	Cubic	Fm-3m	a=5.582 α, β, γ=90°	106569	[80]
$Cu_{1.8}S$			a= 5.564 α, β, γ=90°	41142	
CuS	Hexagonal	P63/mmc	a=3.788, c=16.333 α, β=90°, γ=120°	67581	[81]

***averaged values of the available structures.**

1.6.3 Fabrication methods of CZTS thin-films

DTU's Department of Photonics Engineering provided the CZTS samples for this project. The absorber layer fabrication involves physical and chemical deposition methods, resulting in films with differences in their microstructures.

- *Pulsed laser deposition*

  This method uses a laser to deposit thin-films via ablation. The extreme energy of the focused beam is absorbed by a small area of the target surface. The chemical bonds break down, and the elements on the surface are removed in the form of an expanding plasma cloud. The components of these layers travel at extreme speed through the vacuum chamber until they impinge on the substrate surface, Figure 1.12.

  A KrF laser beam (248 nm wavelength, 20 ns pulse-width, 15 Hz pulse repetition rate) is focused on a target that consists of sintered binary chalcogenides (2CuS:ZnS:SnS), and the substrate is typically a molybdenum-coated soda-lime glass, Mo-SLG [82]. Subsequently, the obtained film is annealed above 560 °C with a sulfur and SnS atmosphere.

  Alternatively, an oxide route for the production of CZTS is also employed, where a target of sintered oxide and sulfide binaries is used during the deposition [83]. The annealing conditions (temperature and pressure) are also adjusted to optimize the film microstructure.

  For further details about the PLD process for chalcogenide materials and examples of CZTS films, the reader is referred to [82]–[85].

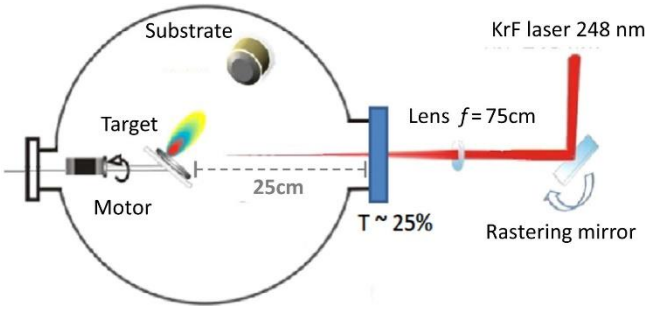

Figure 1.12. PLD setup. Reprinted from [86] *with permission from Elsevier.*

- *Co-sputtering*

  This technique is a physical vapour deposition process in which a plasma, created from an inert gas, is loaded into a vacuum chamber. The plasma bombards the target, made of the coating components, ejecting atoms that will deposit on the substrate and build up a thin-film. Two different types of sputtering were employed in the preparation of CZTS: Direct current (DC) sputtering for the deposition of Cu and radio frequency (RF) sputtering for SnS and ZnS. The DC process is usually for conducting materials, whereas RF is more effective for low-conductivity or insulating materials. It is important to emphasize that the sputtering of the three targets happens simultaneously, as shown in Figure 1.13, hence its name "co-sputtering."

  After the film deposition, the annealing process is carried out in two different ways [87]:

  - Annealing in a single step: Temperature at 575 °C for 45 min, and Sn and S atmosphere at 175 mbar. Cooling is by quenching at 300°C.

  - Annealing in two stages: First, the temperature at 200 °C for 30 min, and Sn and S atmosphere at 660 mbar. Second, the temperature at 575 °C for 30 min, and Sn and S atmosphere at 1000 mbar. Slow cooling for 8 hours.

  Sputtering involves many parameters, and making multi-component materials adds up to the complexity of the technique. For specific details on this process, the reader is referred to Martinho *et al.*, which discusses the resulting solar cell morphology, composition, and optoelectronic properties [87].

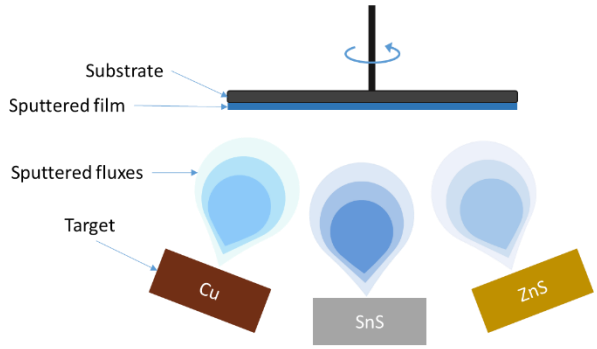

Figure 1.13. Schematic diagram of the CZTS co-sputtering process for the deposition of Cu, SnS, and ZnS.

- *Solution processing*

  Hot-injection is a commonly adopted technique for the fabrication of CZTS [88]. The synthesis consists of mixing $CuCl_2 \cdot 2H_2O$, $Zn(OAc)_2$, and $SnCl_4 \cdot 5H_2O$ with dyethylenglycol, DEG. Secondly, a preheated solution of elemental Sulphur dissolved in triethylenetetramine, TETA, and DEG is injected into the first solution forming the desired CZTS nanoparticles. The nanocrystals are then centrifuged and suspended in a solution of Deionized (DI) water and ethanol. The resulting ink is drop-casted on a Mo-SLG or Silicon substrate, which is then annealed at 600° C in a quartz tube vacuum oven at a nitrogen pressure of 100 mbar [89].

  One of the advantages of using CZTS nanoparticles dispersed in a solution is that they can be deposited on a substrate using printing techniques such as the roll-to-roll process.

  More details about the fabrication and characterization of these nanoparticles are found in [88], [89].

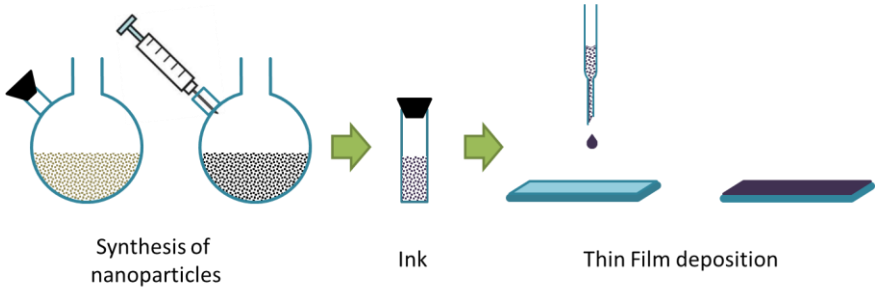

Figure 1.14. Synthesis of CZTS nanoparticles and deposition

1.6.4 The microstructure of CZTS thin-films

The resulting film microstructure differs as the growth mechanisms and conditions of the deposited films vary depending on the deposition method and annealing parameters. Chemical composition, temperature, pressure, processing time are all set to obtain the best possible efficient device.

Apparent differences among the resulting films fabricated by the chemical and physical deposition methods in DTU photonics are shown in Figure 1.15. Besides the evident double layer (DL) formation among all the films, grain sizes, and film thickness fluctuates depending on the fabrication method. Solution processing of nanoparticles results in the smallest grains compared to the other fabrication methods. Meanwhile, the co-sputtered film electrical properties improve as the thickness decreases, and annealing conditions are optimized [87].

Finally, the PLD film fabricated using oxide targets forms a double layer, whereas PLD films created from a sulfur-target form a monolayer.

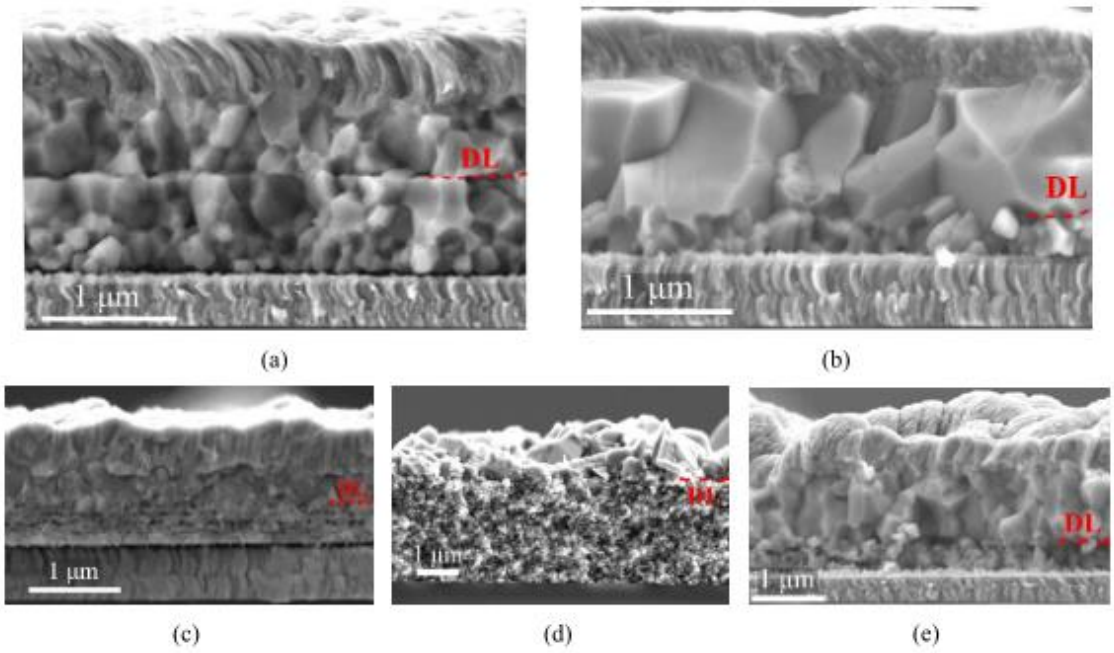

Figure 1.15 SEM cross-sectional images of CZTS solar cells and absorbers exhibiting double-layer structures. (a) and (b) show full devices made by co-sputtering; (c) shows a full device from solution processing of metal salts; (d) shows an absorber from solution processing of nanoparticles; (e) shows a CZTS device from PLD of a single oxide target. In (a), (b), (c), and (e), the solar cell structure consists of Mo/CZTS/CdS/i-ZnO/Al:ZnO, from bottom to top. The red dashed line marks the double-layer (DL) interface. Reprinted with permission from [87]*, Copyright (2020) American Chemical Society.*

A small number of studies are dedicated to the characterization of the CZTS film microstructure, and another handful describes interesting features of CIGS films that could also show in CZTS films [90]–[92]. At first glance, the polycrystalline chalcogenide coatings have grain boundaries with favourable effects, acting as channels for current to flow rather than recombination sites [93]. However, not all grain boundaries have the same properties. Grain boundaries have been classified as twin boundaries of type Σ3, and random boundaries in chalcopyrite films [91], [94]. Likewise, CZTS films have Σ3 type boundaries that correspond to misorientations of 60° [27],[95]. Other experimental and theoretical studies address the electrical properties and passivation methods of GBs [96]–[98].

Hlaing Oo *et al.* observe an out-of-plane (112) fibre texture in CZTS films grown by sputtering [95]. A fibre texture consists of one axis preferentially aligned, whereas the other two are randomly distributed. In another study for co-evaporated CZTS films grown from a

ZnS precursor, Weber *et al.* notice a mixture of fibre texture in the directions $<111>_{cubic}$ and $<100>_{cubic}$ that are perpendicular to the planes $\{111\}_{cubic}$ and $\{200\}_{cubic}$. Kesterite is a distorted superstructure of the cubic sphalerite, so the mentioned planes are equivalent to the tetragonal planes $\{112_{\}tetragonal}$ and $\{200\}/\{004\}_{tetragonal}$ [99].

The strain in co-sputtered CZTS films has been measured by the wafer-curvature method revealing compressive deposition stress of 100 MPa [100]. The study focuses on optimizing the Molybdenum deposition to reduce the stress and improve the adhesion of CZTS on low-stress Mo layers. Moreover, theoretical studies have predicted the elastic constants of CZTS kesterite structure and the Poisson's and Young's modulus. Such magnitudes foresee the lateral deformation and the stiffness of the material [51], [101]. Moreover, the bandgap variations by applying the biaxial strain model are examined, concluding that the bandgap decreases with an increasing tensile biaxial strain [102], [103].

Despite the efforts of many groups to improve CZTS films, open questions remain about the influence of the absorber layer structural properties. For example, how fabrication processes and the resulting different grain sizes, orientations, and grain boundaries are correlated? What is the impact of the film microstructure on the electrical properties during the solar cell operation conditions?

In addition, residual stresses are not studied much in the photovoltaic area, so little is known for the strain effect on the electrical properties. Finally, identifying secondary phases, which can induce bandgap fluctuations in the film, is difficult, and only qualitative assessment by indirect methods is possible.

In summary, texture, identification of twin boundaries, and strain are studied separately. We aim at studying all these structural properties in the CZTS absorber layer by proposing a non-destructive technique to create sustainable and highly efficient TFSC.

2 Methodology

What effect does the CZTS absorber layer microstructure have on the device efficiency?

To answer this question, we need to characterize the grain properties in the polycrystalline film. Different techniques can do it; electron microscopy is notably popular because of the high spatial resolution and accessibility. Electron microscopy studies have examined the structural properties of cross-sections of thin-films extensively [24], [26], [27], [94]. This technique requires a destructive sample preparation that can induce additional structural defects in the specimen. Hence, a need for a non-destructive technique that reveals the internal microstructure of the material is desired.

In this work, we take a different approach to conventional laboratory techniques. We investigate the microstructure of CZTS through a non-destructive technique, three-dimensional X-ray Diffraction. 3DXRD is ideal for studying polycrystalline materials and their microstructure properties, providing the crystallographic orientation, position, morphology, and elastic strains of the grains.

Another critical aspect of 3DXRD compared to other X-ray techniques is that it can illustrate the film heterogeneities by describing individual grain properties. Other X-ray techniques such as Powder X-ray diffraction or Grazing Incident X-ray Scattering probe the average properties of the ensemble of grains.

PV thin-films have crystallites with a size below 3 µm, and in the case of CZTS, below 1 µm. Third-generation synchrotron radiation facilities offer the required resolution to undertake this kind of experiment. We acquire diffraction data from three different radiation facilities, which have distinctive features.

First, we identify secondary phases and correlate these findings to the device performance from previous studies. Secondary phases are not suitable in the absorber layer because of the different electronic properties. Therefore, identifying and quantifying the secondary phases can lead to a better assessment of the causes of failure in the device.

Furthermore, the grain orientations and boundaries present in the final film texture can create better models of the absorber layer growth mechanisms. Moreover, the strain in the film can reveal the stresses that the film has undergone.

In this chapter, we briefly describe the interaction of X-rays with crystals, the principles of 3DXRD, the experimental methods, and the analysis tools employed in this project. Finally, the multigrain indexing approach, an alternative tool for analyzing 3DXRD data, is tested on

simulated CZTS grains. Multigrain is a potential alternative to recognize multiphase materials and grain properties with no *a priori* knowledge of the material.

2.1 X-RAYS AND POLYCRYSTALLINE MATERIALS

X-rays are a form of electromagnetic radiation characterized by short wavelengths ranging from 10^{-11} m to 10^{-9} m, or similarly high energies in the range 100 eV to 100 keV. They can be generated by accelerating electrons towards an anode over an electric field. The spectrum of the impinging electrons on the anode is composed of Bremsstrahlung and sharp lines corresponding to the characteristic X-rays generated by fluorescent radiation[3].

Nevertheless, X-ray tubes have some limitations. It is difficult to obtain high intensities and tune an optimal wavelength for the experiments. Synchrotron facilities can offer this flexibility and a higher brilliance[4] than the laboratory sources. In a synchrotron, a large storage ring keeps electrons circulating at near light speed. The ring is composed of curved and straight sections. From the arced part, X-rays are generated by bending magnets accelerating the electrons. In the straight parts, insertion devices (undulators and wigglers) generate the most intense synchrotron radiation, also by the acceleration of the electrons [104].

X-rays can penetrate solid materials nondestructively, depending on their energy and the electron density of the constituent elements of the material. An X-ray photon can be scattered or absorbed. We will discuss primarily the former interaction, in which X-rays are scattered by the electrons of the atoms in the material. This interaction can be elastic, also known as Thompson scattering, or inelastic, Compton scattering. In the Thompson scattering, the X-ray photon energy is much lower than the energy of the electron and does not change when scattered. In the Compton scattering, energy may be transferred to the electron, and the scattered photon has a lower frequency than the incident one.

The elastic scattering of X-rays is exploited in the investigation of the structure of materials. Diffraction of X-rays can reveal how crystalline matter is build up. It happens when X-ray photons with the propagation direction $\vec{k}$ are deviated by the electron cloud around the atom resulting in the direction $\overrightarrow{k'}$. The magnitude of these vectors $|\vec{k}|$ and $|\overrightarrow{k'}|$ is $2\pi/\lambda$, where lambda is the wavelength of the photons, and the angle between the incident ray and the lattice plane of the crystal is equal to the scattering angle θ. The scattering vector $\vec{Q}$ is defined

[3] Fluorescent radiation is the relaxation of an electron from an outer shell into the vacancy created by the collision of the electrons onto the anode. They may produce an X-ray with a characteristic energy equal to the difference in energy between the two shells.
[4] Brilliance determines how parallel and narrow the X-ray beam is correlated to its intensity.

by the difference of the wave vectors, $\vec{Q} = \vec{k} - \vec{k'}$, and is perpendicular to the scattering planes. From the geometry depicted in Figure 2.1:

$$\left|\vec{Q}\right| = 2\left|\vec{k}\right| sin\,\theta = \frac{4\pi\, sin\,\theta}{\lambda} \tag{2.1}$$

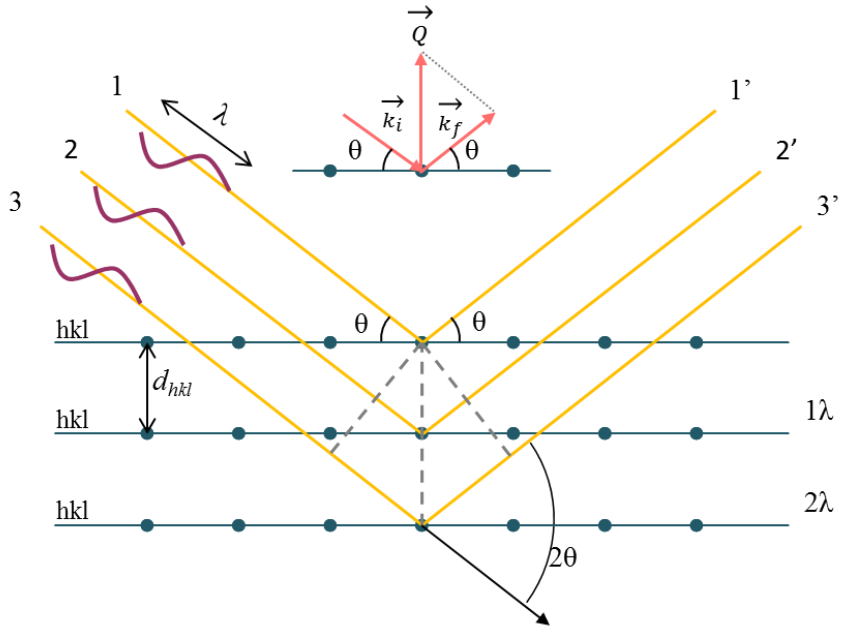

Figure 2.1. Scattering of an X-ray beam of wavelength λ by the lattice planes of a crystal.

The lattice plane of the crystal can be represented by a vector perpendicular to this plane. The reciprocal lattice vector $\vec{G}$ can be parameterized as:

$$\vec{G} = h\overrightarrow{a^*} + k\overrightarrow{b^*} + l\overrightarrow{c^*} \tag{2.2}$$

Where $\overrightarrow{a^*}, \overrightarrow{b^*}, \overrightarrow{c^*}$ are the reciprocal lattice basis vectors and h, k, and l are the Miller indices, integers describing the family of planes within a crystal. The reciprocal lattice vectors care generated using Eqs. (2.3) - (2.5), where $\vec{a}$, $\vec{b}$ and $\vec{c}$ are the lattice vectors in direct space.

$$\overrightarrow{a^*} = 2\pi \frac{\vec{b} \times \vec{c}}{\vec{a} \cdot \left(\vec{b} \times \vec{c}\right)} \tag{2.3}$$

$$\overrightarrow{b^*} = 2\pi \frac{\vec{c} \times \vec{a}}{\vec{b} \cdot \left(\vec{c} \times \vec{a}\right)} \tag{2.4}$$

$$\overrightarrow{c^*} = 2\pi \frac{\vec{a} \times \vec{b}}{\vec{c} \cdot \left(\vec{a} \times \vec{b}\right)} \tag{2.5}$$

When the Laue condition is fulfilled, $\vec{G} = \vec{Q}$, the interplanar distance, d_{hkl}, can be obtained from the scalar product of the normal vector $\vec{n} = \vec{G}/|\vec{G}|$ and a vector describing a point in the lattice plane with respect to the origin, e.g. $\vec{a}/h$:

$$d_{hkl} = \frac{\vec{a}}{h} \cdot \vec{n} = \frac{2\pi}{|\vec{G}|} \tag{2.6}$$

By applying the Laue condition, we can derive Bragg's law using equation (2.1):

$$d_{hkl} = \frac{2\pi}{|\vec{G}|} = \frac{2\pi}{|\vec{Q}|} = \frac{4\pi}{(2\pi/\lambda)\sin\theta} = \frac{\lambda}{2\sin\theta} \Leftrightarrow \lambda = 2d\sin\theta \tag{2.7}$$

The intensity of a given Bragg reflection is described by the scattering amplitude of a crystal. It considers the unit cell structure factor and the sum of the lattice planes, as described in Eq.(2.8). The index j identifies the different atoms, $f_j(\mathbf{Q})$ is the atomic form factor, $\mathbf{r}_j$ is the positions of the atoms in the unit cell, and $\mathbf{R}_n$ represents the lattice vectors:

$$F^{crystal}(\boldsymbol{Q}) = \overbrace{\sum_j f_j(\boldsymbol{Q}) e^{i\mathbf{Q}\cdot\boldsymbol{r}_j}}^{Unit\ cell\ structure\ factor} \overbrace{\sum_n e^{i\mathbf{Q}\cdot\boldsymbol{R}_n}}^{Lattice\ sum} \tag{2.8}$$

The atomic form factor $f_j(\boldsymbol{Q})$ is the scattering from a single atom. $\rho(r)$ represents the electron density of the atom at a position $\boldsymbol{r}$, and $e^{i\boldsymbol{Q}\cdot\boldsymbol{r}}$ the phase factor associated with the total phase-shift experienced by an incoming wave.

$$f(Q) = \int \rho(r) e^{i\boldsymbol{Q}\cdot\boldsymbol{r}}\, d\boldsymbol{r} \tag{2.9}$$

In summary, the theoretical background of X-ray diffraction has been laid out, describing the interaction of X-rays and crystals. Moreover, the sources of X-rays have been described, introducing the synchrotron facilities as the primary instrument in our experiments.

2.2 THREE DIMENSIONAL X-RAY DIFFRACTION, 3DXRD

This technique is suitable for the structural characterization of polycrystalline materials. It was first applied to metals, alloys, and ceramics with millimetre-sized grains [105]. With 3DXRD, it was possible to determine the grain size, morphology, crystallographic orientation, centre-of-mass position, and strain tensor, from which one can obtain stress type II from the average strain of a grain [106].

Different fields have used 3DXRD to recover structural information. Some examples are the determination of a metalorganic compound structure and the identification of nanocrystals in chalk. The review of these cases can be found in [106]–[108].

The overall setup consists of the specimen rotation around an axis perpendicular to the incoming X-ray beam. At every rotation angle, ω, a detector records the diffracted beam and their respective 2θ and η angles (Figure 2.2). An indexing algorithm classifies the spots, characterized by the angles ω, 2θ, and η, into groups that belong to the grain orientation.

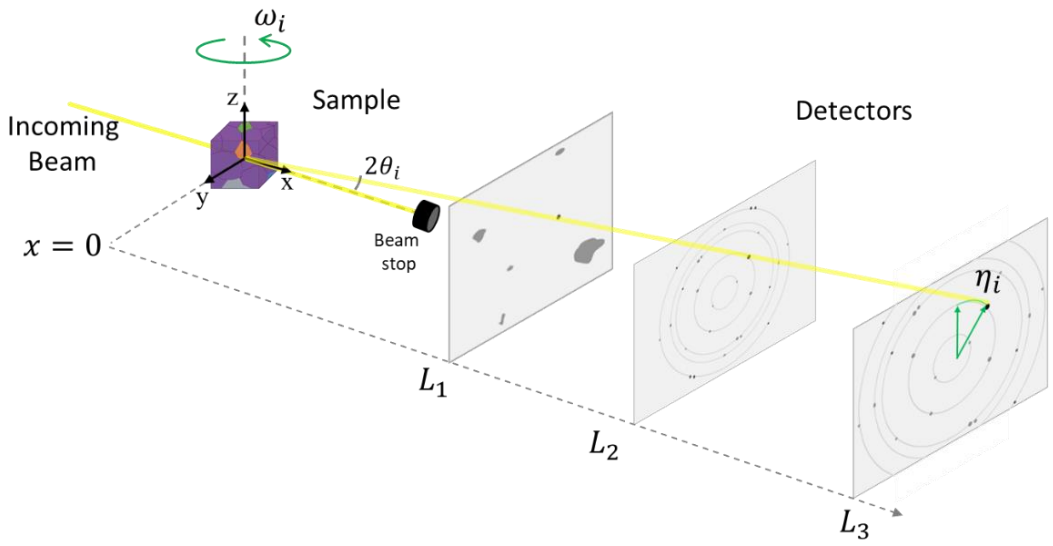

Figure 2.2. 3DXRD setup

In 3DXRD experiments, a trade-off between spatial, angular, and time resolution determines the structural properties that can be studied. In a high angular resolution setup, one compromises the spatial resolution, obtaining a statistical study of grain properties without grain positions and morphologies. In contrast, prioritizing a high spatial resolution will cost time, resulting in a detailed grain map but preventing possible dynamical studies. Following these constraints, 3DXRD operates in four modes (see Figure 2.3):

- Mode I, *Statistical descriptions of the dynamics*, allows statistical studies focusing on the high angular resolution to acquire detailed crystallographic information for each grain [106]. However, the positions of the grains cannot be retrieved. To obtain a statistical dynamical description, one can monitor changes in the volume, and selected orientation/strain components, recording a small ω range [108]. As the rotation range increases, one can acquire sufficient reflections to index grains and determine their full orientation and full strain tensor [106]. In this setup, a far-field detector is employed.

- Mode II, *Centre-of-mass mapping*, focuses on acquiring the phase, centre-of-mass position, volume, average orientation, and average elastic strain tensor of each grain [106]. The result is a low-resolution map made by Laguerre tessellation with the grain centres and volumes [109]. The position accuracy is determined by the grain size and the far-field detector pixel size.

- Mode III, *Grain-by-grain volumetric mapping*, intends to precisely map the grain boundary network, obtaining 3D maps with a resolution of 2 µm [10]. The grain is assumed undeformed with a constant orientation. For this setup, a detector with a high spatial resolution is required.

- Mode IV, *Orientation imaging*, is suitable to study deformed materials with orientation variations within each grain. Here a detector with a high spatial resolution is also employed. In this mode, each voxel in the sample is associated with its orientation. This configuration is comparable to Electron Backscattering Diffraction (EBSD) but non-destructive[108].

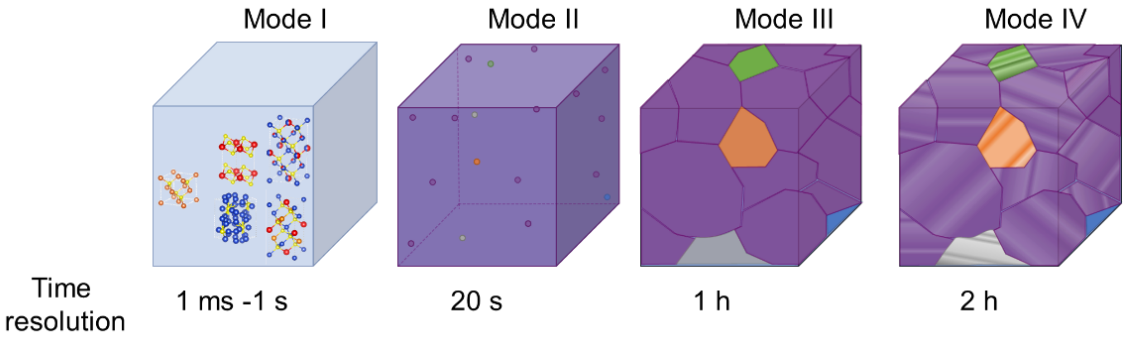

Figure 2.3. Different modes of operation in 3DXRD

In this work, we primarily utilize mode II, optimized for a high angular resolution. However, the grain centre-of-mass positions were not retrieved due to the discrepancy between the detector pixel size (20 - 200 µm) and the grain size (0.5 - 1 µm). One would need a detector with pixels around the grain size to determine their centre-of-mass position. Currently, the spatial resolution of 3DXRD is limited by detector technology to 1.5 to 2 µm, or by the size of the beam in the scanning mode.

2.2.1 3DXRD Principles

The 3DXRD geometry follows the principles outlined in [110] and in the FABLE conventions, a suite of programs to analyze 3DXRD data. For operation mode II, a far-field detector is employed to obtain a full diffraction pattern. The diffraction images display the Debye-Scherrer rings, well known from powder diffraction, conformed by sporadic

diffraction spots. These reflections are associated with the reciprocal space by the reciprocal lattice vector $\vec{G}$ that is described in different reference systems:

- In the laboratory coordinate system ($x_l,\ y_l,\ z_l$), the x-axis is pointing along the incoming X-ray beam. The z-axis is aiming upward parallel to the ω rotation axis. The y-axis results from the cross product $y_l = x_l \times z_l$ to obtain a right-handed system.

- In the rotation coordinate system ($x_\omega,\ y_\omega,\ z_l$), the z-axis coincides with z_l, whereas x and y rotate around z with ω angle. The relation between ($x_l,\ y_l,\ z_l$) and ($x_\omega,\ y_\omega,\ z_\omega$) for a counterclockwise rotation viewed along the z_l-axis is:

$$\begin{pmatrix} x_l \\ y_l \\ z_l \end{pmatrix} = \begin{pmatrix} cos(\omega) & -sin(\omega) & 0 \\ sin(\omega) & cos(\omega) & 0 \\ 0 & 0 & 1 \end{pmatrix} \begin{pmatrix} x_\omega \\ y_\omega \\ z_l \end{pmatrix} \tag{2.10}$$

  The transformation of the reciprocal lattice vector in the laboratory system to the rotation frame is represented as $\overrightarrow{G_l} = \Omega \overrightarrow{G_\omega}$, where Ω is the rotation matrix indicated in equation (2.10).

- The sample coordinate system ($x_s,\ y_s,\ z_s$) is identical to the rotation system unless a different frame (S) is defined. By default, S=I, the identity matrix. The reciprocal lattice vector is expressed as $\overrightarrow{G_\omega} = S\overrightarrow{G_s}$.

- The crystal coordinate system ($x_c,\ y_c,\ z_c$) relates to the sample reference by the orientation of a grain, denoted by $\overrightarrow{G_s} = U\overrightarrow{G_c}$. The orientation matrix (U) is a 3-by-3 rotation matrix. Moreover, the crystal frame is fixed to the reciprocal lattice($a^*,\ b^*,\ c^*, \alpha^*, \beta^*, \gamma^*$) in the grain. Conventionally, the x_c-axis is parallel to a^*, the y_c-axis is in the plane of a^* and b^*, and the z_c-axis is perpendicular to that plane. Finally, the matrix B, described by equation (2.11), is the correspondence between the reciprocal coordinate system (h, k, l) and the orthonormal crystal system represented by the lattice parameters (a, b, c, α, β, γ). Therefore, we obtain the expression: $\overrightarrow{G_c} = B\overrightarrow{G_{hkl}}$.

$$\boldsymbol{B} = \begin{pmatrix} a^* & b^* \cos(\gamma^*) & c^* \cos(\beta^*) \\ 0 & b^* \sin(\gamma^*) & -c^* \sin(\beta^*) \cos(\alpha) \\ 0 & 0 & c^* \sin(\beta^*) \sin(\alpha) \end{pmatrix} \tag{2.11}$$

With,
$$\cos(\alpha) = \frac{\cos(\beta^*)\cos(\gamma^*) - \cos(\alpha^*)}{\sin(\beta^*)\sin(\gamma^*)}$$

With the previous definitions, we obtain the general expression that describes the reciprocal lattice vector:

$$\overrightarrow{\boldsymbol{G_l}} = \boldsymbol{\Omega S}\overrightarrow{\boldsymbol{G_s}} = \boldsymbol{\Omega S U B}\overrightarrow{\boldsymbol{G_{hkl}}} \tag{2.12}$$

The normalized reciprocal lattice vector in the laboratory system and the sample system is:

$$\frac{\overrightarrow{G_l}}{|\overrightarrow{G_l}|} = \Omega S \frac{\overrightarrow{G_s}}{|\overrightarrow{G_s}|} = \boldsymbol{\Omega S U}\vec{h} = cos(\theta)\begin{pmatrix} -tan(\theta) \\ -sin(\theta) \\ cos(\eta) \end{pmatrix} \tag{2.13}$$

Here, $\vec{h}$ is the unit vector defined by Bragg's law as:

$$\begin{pmatrix} h_1 \\ h_2 \\ h_3 \end{pmatrix} = \frac{\lambda}{4\pi\, sin(\theta)} B \begin{pmatrix} h \\ k \\ l \end{pmatrix} \tag{2.14}$$

As shown in equation (2.13), the grain orientation can be obtained from a (ω, 2θ, η)-measurement of the corresponding (hkl) plane.

2.3 EXPERIMENTAL METHODS

In this project, different setups at three facilities were used, which offered different conditions and capabilities for the experiments. Some of the varying aspects were the energy of the X-ray beam, its size and shape, and the type of detectors. In Table 2.1, we present the summary of the distinctive aspects of the measurements at each facility.

Table 2.1. Overview of the 3DXRD experimental conditions at different facilities

Facility	**APS**	**ESRF**	**SPring-8**
Date of the experiment	November 2018	July 2018	July 2019
Energy [kev]	52	40	25
Beam size (h x v) [µm x µm]	200 x 1.5	0.3 x 0.3	19.2 x 11.3
Mode	Scanning z-axis	Scanning y-axis	Full-field
Detector pixel size [µm x µm]	200 x 200	50 x 50	18.9 x 18.9
Detector area [mm x mm]	40.96 x 40.96	10.24 x 10.24	13.312 x 13.312
Sample width [µm]	~ 30-50	~ 600	~ 10
Sample thickness [µm]	~ 4	~ 15	~ 4

At the Advanced Photon Source (APS), a CZTS solar cell fragment was examined with a focused line beam and a flat panel detector area. Additionally, we collected data from a silver-alloyed CZTS absorber layer and a CIGS solar cell.

At the European Radiation Synchrotron Facility (ESRF), another piece of the same CZTS solar cell was tested, reconstructing a map of the scanned area.

Finally, the experiment at Super Photon ring-8 (SPring-8) utilized an imaging detector and a box beam. Compared to the precedent APS investigation, the box beam increases the number of simultaneously illuminated grains.

Besides, samples were prepared in different sizes for each experiment. As the number of simultaneously illuminated grains increases, spot overlap escalates in the diffraction images challenging the indexing process. Therefore, the sample size decreases, reducing the number of grains that the cross-section of the incoming X-ray beam probes. Depending on the beam dimensions, the sample width is modified in each experiment to limit the number of grains.

2.3.1 Line beam scanning at APS

This experiment aims to primarily identify secondary phases in the absorber layer of the thin-film solar cell. As described in Section 1.6.2, the unit cells of ZnS and CZTS are very similar and share many symmetry properties. Moreover, we also investigate a CIGS solar cell to study the absorber layer microstructure and the applicability of this method to other types of solar cells.

The grains are smaller than the detector pixel size, so the exact grain positions cannot be determined. We expect to quantify the primary and secondary phases and obtain the average grain volume, orientations, and strain statistics.

2.3.1.1 Samples description

The description of the samples scanned at APS is presented in Table 2.2. The overall sample size is approximately 30-50 µm wide and 1-2 mm in length. The vertical beam size and the sample width determine the effective studied sample area. Moreover, we reduce the substrate thickness by mechanical polishing to improve the signal to noise ratio. The thinnest part at the tip of the sample is further milled with a Focused Ion Beam (FIB).

The CIGS solar cell is fabricated on a flexible polyimide substrate. The adherence of the films to the substrate is weak, and therefore the absorber layer peels off easily. We took a flake and milled the top edge with a FIB to obtain a 30-50 µm width.

Table 2.2. List of samples scanned at APS

Sample ID	Deposition technique	Solar cell architecture	Description
PLD-CZTS	PLD	Mo (MoS_2)/ CZTS/CdS/ZnO/ Al:ZnO/MgF_2	Ultra-thin solar cell, published in [82]. Sample width: 37 µm
ACZTS	PLD	Mo (MoS_2)/Ag-CZTS	Soda Lime Glass + Mo + annealed CZTS deposited via PLD Sample width: 30 µm
CIGS	Co-evaporation	Mo(MoS_2)/CIGS/ CdS/ZnO/Al:ZnO /MgF_2	Sample width: 51 µm

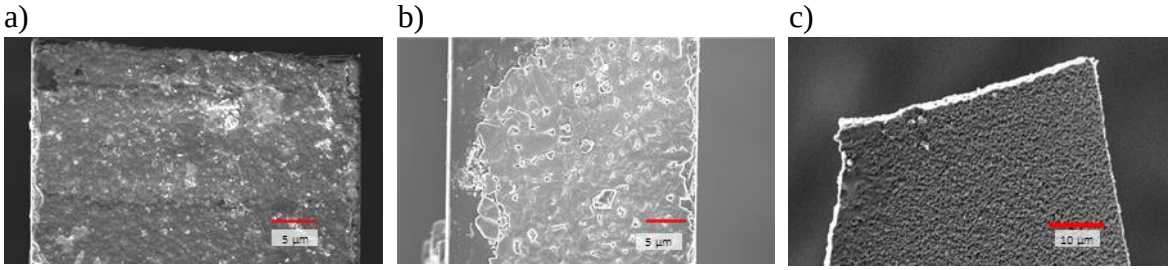

Figure 2.4. SEM images of a) PLD solar cell, b) ACZTS absorber layer, c) flake of a CIGS solar cell.

2.3.1.2 Experimental details

The surface normal of the film is placed parallel to the incoming X-rays. The monochromatic focused line beam (52 keV, 200 µm x 1.5 µm) illuminates the thin-film in transmission mode, and a 2D detector records the diffraction images in the far-field regime. The sample rotates 360° with a 0.1° step while a section of the sample (50 µm (H) x 1.5µm (V)) is continuously in the beam. Each sample was scanned 5 to 7 sections along the z-axis overlapping 0.5 µm, and we repeated the scans at two distances. At 1.4 m, the detector captures as many rings as possible, ensuring enough reflections per grain. At 2.2 m, the angular resolution is increased, the inner rings are separated more, but the outer rings are no longer visible. For the analysis, we use the datasets at 1.4 m.

2.3.2 Scanning 3DXRD at ESRF

While the APS experiment provides statistical information about the absorber layer microstructure, scanning 3DXRD offers the spatial resolution that we were missing due to the discrepancy between grain size and pixel size (1 µm: 200 µm).

The nano-focused beam size (300 nm x 300 nm) at ESRF is comparable to the grain size in the sample. The beam is centred at one position of the specimen while the specimen is rotated. Then the specimen is translated to the next position separated by step size similar to the beamwidth. One advantage of this modality is the reduction of the spot overlap in the diffraction patterns. Moreover, the reconstruction of a grain map with the exact grain positions and shapes is also possible. In this experiment, a scan of the tip of the solar cell was performed, as shown in Figure 2.5.

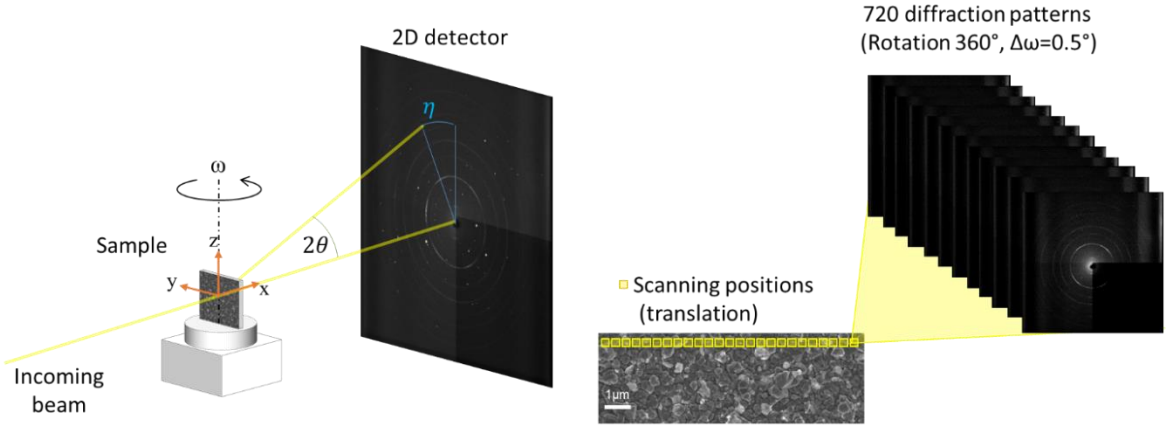

Figure 2.5. Scanning 3DXRD setup. In addition to the typical layout, the sample is translated along the y-axis acquiring diffraction patterns as the sample rotates.

2.3.2.1 Sample description

The sample tested at ESRF serves to assess the experiment viability and ultimately includes the preliminary results in an experiment proposal for future beamtime. Unfortunately, the facility upgrade prevented us from carrying out this experiment in person. Instead, the experiment was carried out as a test by the beam scientist Jonathan Wright.

The collected data at this facility comes from a cut piece of the sister device of the solar cell published in [82]. By decreasing the substrate thickness (~1 mm) to 10 µm using mechanical polishing, the signal to noise ratio improves for the experiment. Figure 2.6 depicts the sample studied in this facility. Some areas at the top edge have been milled using FIB showing the stack of layers. The sample shows a significant strip of the bare substrate due to the poor adherence of the film. This is a common problem during sample preparation for the experiment.

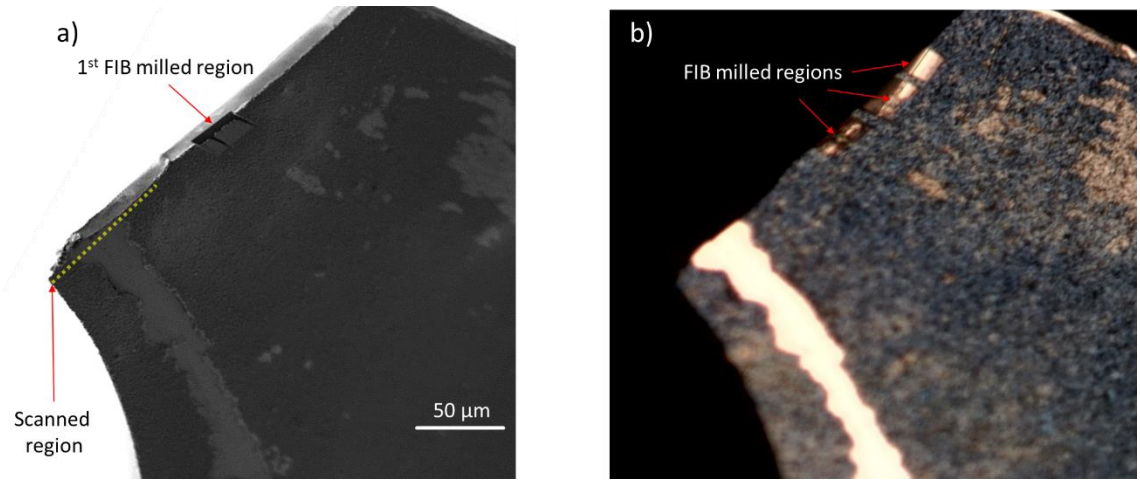

Figure 2.6. a) SEM image of the sample during FIB preparation; at this point, only one region has been milled. b) Optical microscope image of the sample taken at ESRF(courtesy of Jonathan Wright). The top edge shows multiple regions where the FIB milling was performed.

2.3.2.2 Experimental details

A nano-focused beam (40 keV, 300 nm x 300 nm) impinges at the tip of the device whose normal plane is placed parallel to the incoming beam. The sample was aligned with the rotation axis and every y-position (stepping 0.25 µm), rotation scans were performed in the range ω = [-180°, 180°] in steps of 1° clockwise-anticlockwise intercalation. The scans cover the tip of the sample, reconstructing a line of about 75 µm.

2.3.3 Box beam at Spring-8

For this experiment, we focus on the differentiation of secondary phases from the kesterite and the microstructure statistics of larger scanned areas. We studied films deposited by different methods and annealed at two distinctive temperatures to determine specific structural properties depending on the deposition method, precursors, and the annealing stage.

2.3.3.1 Sample description

The preparation of these samples is similar to the procedure described in section 2.3.1.1. The sample size is approximately 10 µm wide and about 1-2 mm long (see Figure 2.7*f*). We reduce the thickness of the substrate by mechanical polishing to improve the signal to noise ratio. The thinnest part at the tip of the sample is further milled about 10-30 µm in length with FIB. Because of the poor PLD film adherence, flakes peeled off easily by scratching

the surface. Peels of 10 µm wide were recovered. The films were prepared at DTU Photonics, as described in Table 2.3.

Table 2.3. List of samples scanned at SPring-8

Sample ID	Precursors	Annealing conditions
PLD-CZTS fully annealed	Sulfides	to 575 °C @20 °C/min, 40min @575C, slow (normal) cooling
PLD-CZTS fully annealed	Oxides	to 575 °C @20 °C/min, 40min @575C, slow (normal) cooling
SP-CZTS 10 min annealed	Oxides	20 °C/min to 600 °C, dwell 10 min, open lid
SP-CZTS 60 min/fully annealed	Oxides	20 °C/min to 600 °C dwell 60 min, natural cooling
Sputtered-CZTS fully annealed	Sulfides	575 °C for 45 min cooling to 60 °C

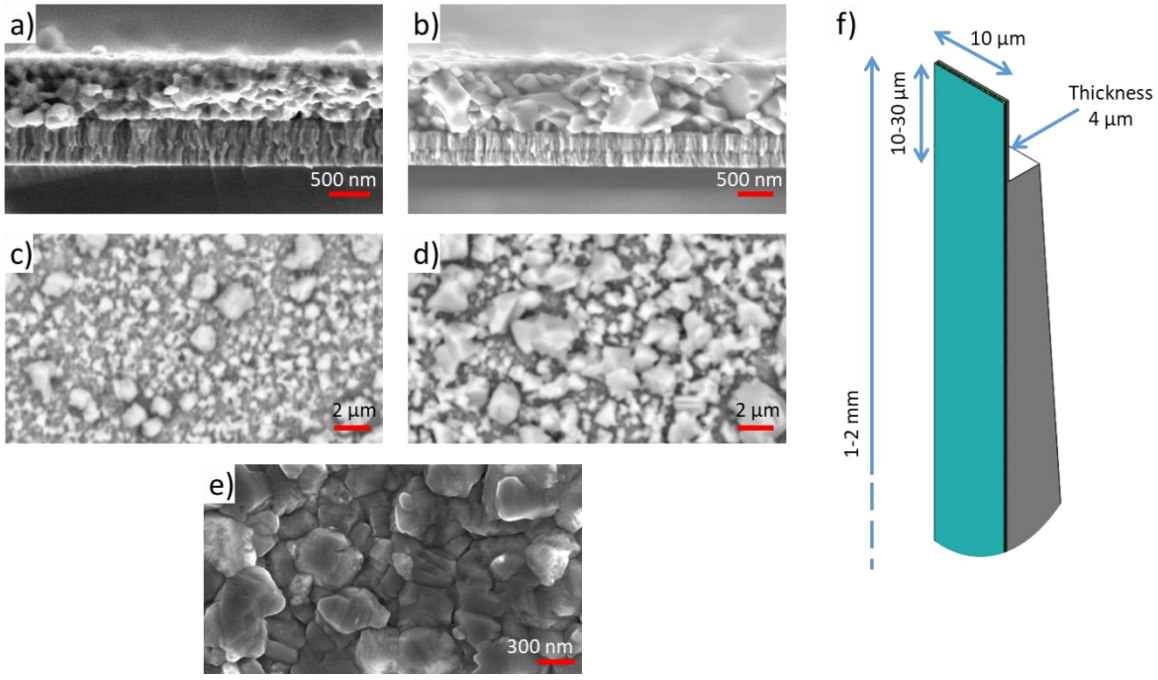

Figure 2.7. Studied samples at SPring-8. a) Cross-section of PLD CZTS fully annealed (sulfide precursors), b) PLD CZTS fully annealed (oxide precursors), c) Solution-Processed CZTS, the first stage of annealing (oxide precursors), c) Solution-Processed CZTS fully annealed (oxide precursors), d) Sputtered CZTS fully annealed (sulfide precursors), f) Approximate dimensions of the cut samples.

2.3.3.2 Experimental details

We used a box beam (25 keV, 19.2 µm (H) x 11.3 µm (V)) and collected diffraction images with an imaging detector at the far-field regime, rotating the samples 360° in 0.1° steps. We recorded the diffraction patterns at three different distances and used short exposure to avoid pixel saturation and prolonged exposure to recover weak reflections. Additionally, we measured a reference sample, the standard powder LaB_6, to calibrate the distance between the sample and the detector.

2.4 DATA ANALYSIS

2.4.1 Analysis tools

There are different available open-source software for the analysis of 3DXRD data. This work utilizes ImageD11, an indexing program for far-field data, developed at ESRF. It is part of FABLE (Fully Automatic BeamLine Experiments), a collection of packages built in collaboration with Risø [111]. Alternatively, GrainSpotter (*Schmidt, 2014)* is another indexing algorithm included in FABLE [112].

The software package available at APS is MIDAS (Microstructural Imaging using Diffraction Analysis Software), which allows the analysis of near-field and far-field data [113]–[115]. Another program developed at Cornell University is HEXRD (High Energy X-Ray Diffraction toolkit), which can index far-field data with a particular focus on strain analysis [116], [117].

In principle, these programs follow a similar methodology. Once the obtained diffraction images are reduced to a list of reflections, the indexing algorithm can identify the grains. Indexing consists of matching reflections to grains with an assumed space group and an orientation. Subsequently, it follows the refinement of the unit cell parameters, in which strain analysis can also be obtained.

During my external stay at ESRF, I had the opportunity to familiarize myself with the software ImageD11. Therefore, it was the chosen program to analyze the diverse experiments during this PhD.

2.4.2 Diffraction Images

In this section, we show an example of the diffraction patterns recorded at the three different facilities. We also discuss the different image formats that each beamline utilizes and how to transform it into a format accepted by FABLE.

The image format of the APS data is converted to be readable by FABLE software. Each file with extension ".ge3" contains a wedge of the tomogram defined by a range of 60°. About 601 images are stored as 16-bit unsigned integers (uint16) with a header of 8192 characters. We split this file into separate images and save them individually with the TIFF format.

The images at ESRF have a format extension EDF and do not need further treatment as they are customized for the analysis on FABLE. The SPring-8 images have the TIFF format, accepted by FABLE.

Figure 2.8 shows the diffraction images acquired in the three facilities. The reflections in the depicted APS data look smaller than in the other experiments because the pixel size (200 µm × 200 µm) is larger than the grain size. Thus, the diffraction spot covers only a few pixels. Moreover, the narrow line beam only illuminates around 100 grains with different orientations, and not all of them might fulfil the Bragg condition at a certain rotation angle. One single image might contain around 20 weak reflections, which makes it difficult to visualize. Therefore, Figure 2.8a is created to give an impression of the diffraction patterns produced in this experiment. Each pixel in this image shows the maximum intensity found in any single image from a set of 200 images. The 200 images correspond to a rotation of 20°. This way, one can appreciate more reflections and the formation of the Debye-Scherrer rings.

Figure 2.8b is generated in the same way as Figure 2.8a to depict a higher number of reflections. In this case, we use a set of 100 images from the ESRF data, which correspond to 50° rotation. In contrast, one single image comes from an illuminated area of 200 nm x 300 nm and contains 20 reflections. Also, the detector had smaller pixels (50 µm x 50 µm). Hence, the diffraction spots spread over more pixels.

Finally, a SPring 8 single exposure illuminates 200 grains (ca. 0.5 µm grain size) per scan with a box beam (11.3 µm (V) x 20 µm (H)). The imaging detector has the smallest pixel size (18.9 µm x18.9 µm) among all the experiments and the smallest area. However, this dataset needs a different segmentation due to the high signal to noise ratio perceived in the background.

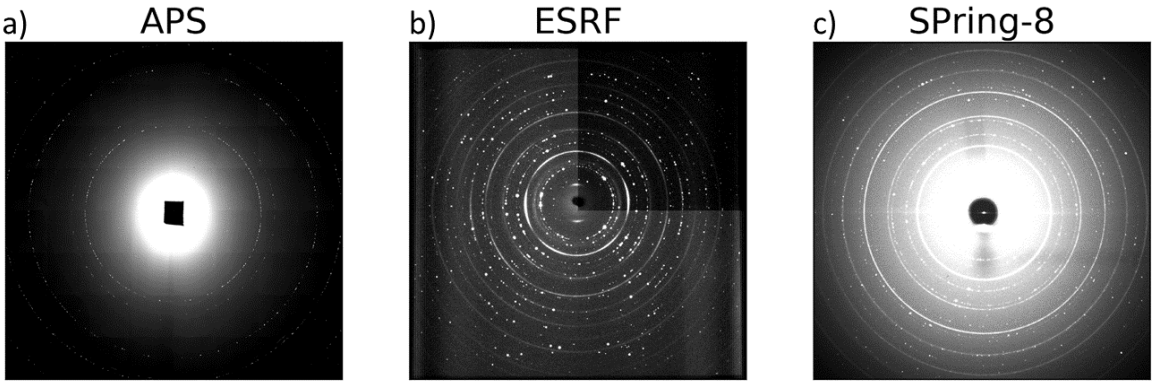

Figure 2.8. Illustration of the diffraction images acquired by three facilities: a) APS scan of a CZTS solar cell (stack of 200 images), b) ESRF scan of a CZTS solar cell (stack of 100 images), c) SPring-8 scan of a CZTS absorber layer (1 image). The corresponding samples were fabricated via PLD.

2.4.3 From peak search to a list of reflections

The analysis begins with the segmentation of the diffraction images. In this step, the diffraction spots are collected into a list containing the rotation angle, ω, the two-theta angle, 2θ, and the azimuthal angle η of each diffraction spot.

The peak search routine in FABLE consists of two steps. First, obtaining a "dark field" image to be subtracted from each frame. Secondly, collecting diffraction spots characterized as connected regions of pixels above a chosen threshold value [118].

The script 'bgmaker.py' creates the dark field image by averaging the minimum values of a series of images. Secondly, the script 'peaksearch.py' identifies the individual reflections once the background has been removed, labelling and storing them in a list. The reflections with a pixel value above a certain threshold (usually defined by the standard deviation of the pixel values) are kept. The application of different thresholds allows the separation of peaks that might have merged when the threshold is too low, whereas a higher threshold value distinguishes two peaks.

However, these procedures do not apply to the SPring-8 images due to the high signal-to-noise ratio background. In the jupyter notebook, 'process_many.ipynb,' reflections are labelled with a watershed algorithm, and the background is removed by applying a Gaussian filter to the image.

2.4.4 Indexing

2.4.4.1 Tuning the detector parameters

The reflection positions in terms of 2θ, η, and ω angles depend on the detector calibration. The calibration of the detector depends on the following parameters:

- sample-detector distance
- tilts in x and y-direction
- detector area
- beam centre coordinates
- pixel size

Usually, one can use the examined sample as a reference to determine those parameters. In our case, we tested a standard powder with known lattice parameters, LaB_6. We recorded a wedge of 10° to collect enough reflections and form the Debye-Scherrer rings.

In this small dataset, the reflections are collected by the routines of 'peaksearch.py.' Then, the program 'ImageD11_gui.py' adjusts the detector parameters to fit the reflections to the LaB_6 unit cell.

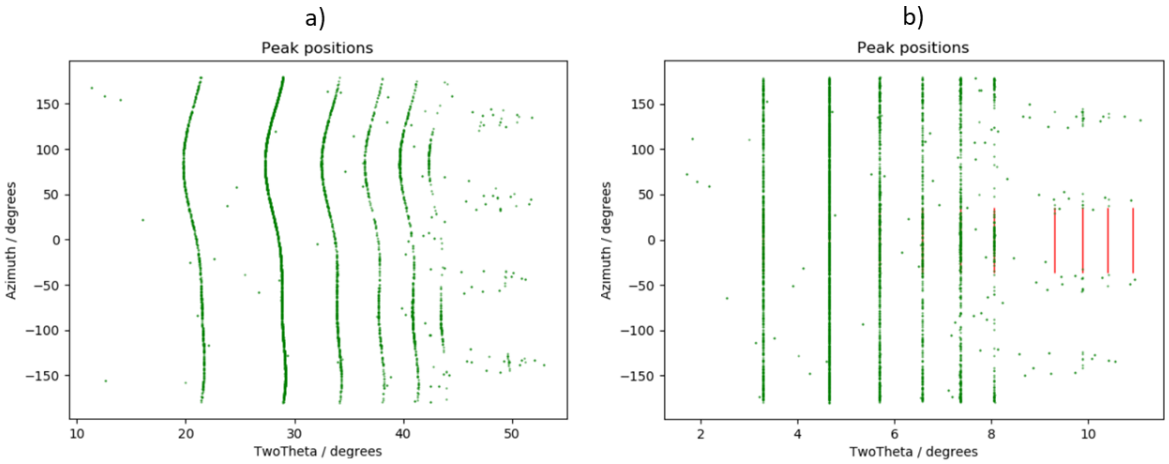

Figure 2.9. Plots of the azimuthal angle vs the two-theta angle: a) LaB_6 reflections without calibration, and b) after the detector parameters have been calibrated.

One important step is to determine the orientation of the image, which varies depending on the detector read-out and the experiment geometry. 'ImageD11_gui.py' includes different orientation matrices that transform the images into the FABLE geometry. The coordinates of the diffraction spots are given as fast (f), and slow (s) coordinates to indicate how the pixel intensities are read from the diffraction image. The f-coordinates traverse the rows of the

images from left to right, whereas the s-coordinates traverse the columns of the image from top to bottom.

In the APS dataset, the first pixel in the file is located in the detector's lower-left corner looking from the X-ray source towards the detector. The pixel reading direction is horizontally towards the right side, then steps up to the next row (see Figure 2.10). While converting the images, the python read-out will allocate the first pixel in the upper left corner reading towards the right side. To orientate an APS image into the FABLE settings, we use equation (2.15).

$$\begin{bmatrix} z_{det} \\ y_{det} \end{bmatrix} = \begin{bmatrix} o_{11} & o_{12} \\ o_{21} & o_{22} \end{bmatrix} \cdot \begin{bmatrix} s \\ f \end{bmatrix} = \begin{bmatrix} 1 & 0 \\ 0 & 1 \end{bmatrix} \cdot \begin{bmatrix} s \\ f \end{bmatrix} \tag{2.15}$$

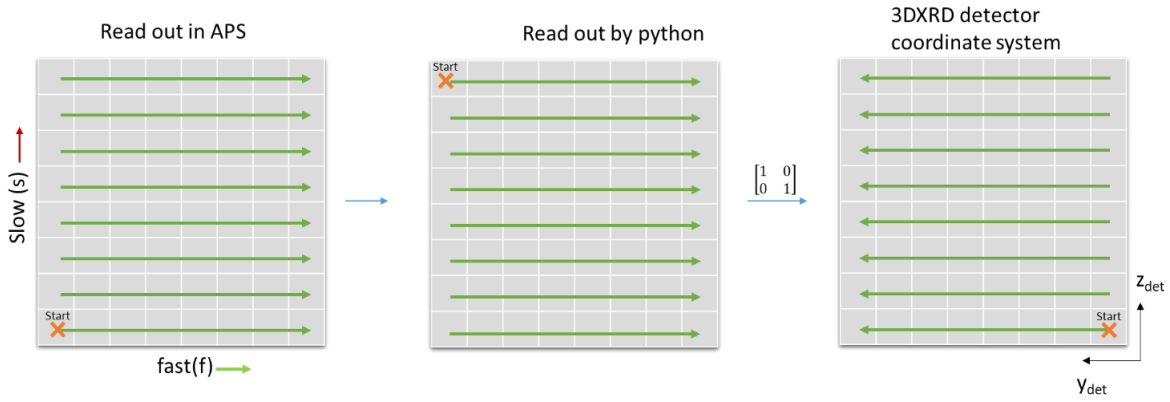

Figure 2.10. Illustration of the orientation matrix determination for the APS data.

Alternatively, one can measure the detector read-out by shadowing a part of the detector and determine how the image is oriented. For the Spring-8 experiment, we covered the detector top right corner when facing the detector with a lead piece. By comparing the obtained image with the lead piece position, we convert the detector coordinates to the FABLE system using the equation (2.16).

$$\begin{bmatrix} z \\ y \end{bmatrix} = \begin{bmatrix} -1 & 0 \\ 0 & 1 \end{bmatrix} \cdot \begin{bmatrix} s \\ f \end{bmatrix} \tag{2.16}$$

2.4.4.2 Indexing strategies

A preliminary step to the indexing of the reflections is to evaluate which crystallographic phases are in the sample. We begin by plotting a histogram of the two-theta positions of the reflections weighted by their intensities. This histogram resembles a powder diffraction pattern where the relative intensity is associated with a lattice reflection. The positions of the reflections and their intensity are indicative of a particular phase and material. We can use

traditional fitting techniques to identify these phases by comparing the obtained powder pattern with available patterns in ICSD.

Figure 2.11 shows the synthetic powder pattern corresponding to the acquired ESRF data with the peaks fitting not only CZTS but also many secondary phases, among them, Cu_2SnS_3, ZnS, indium tin oxide, and molybdenum.

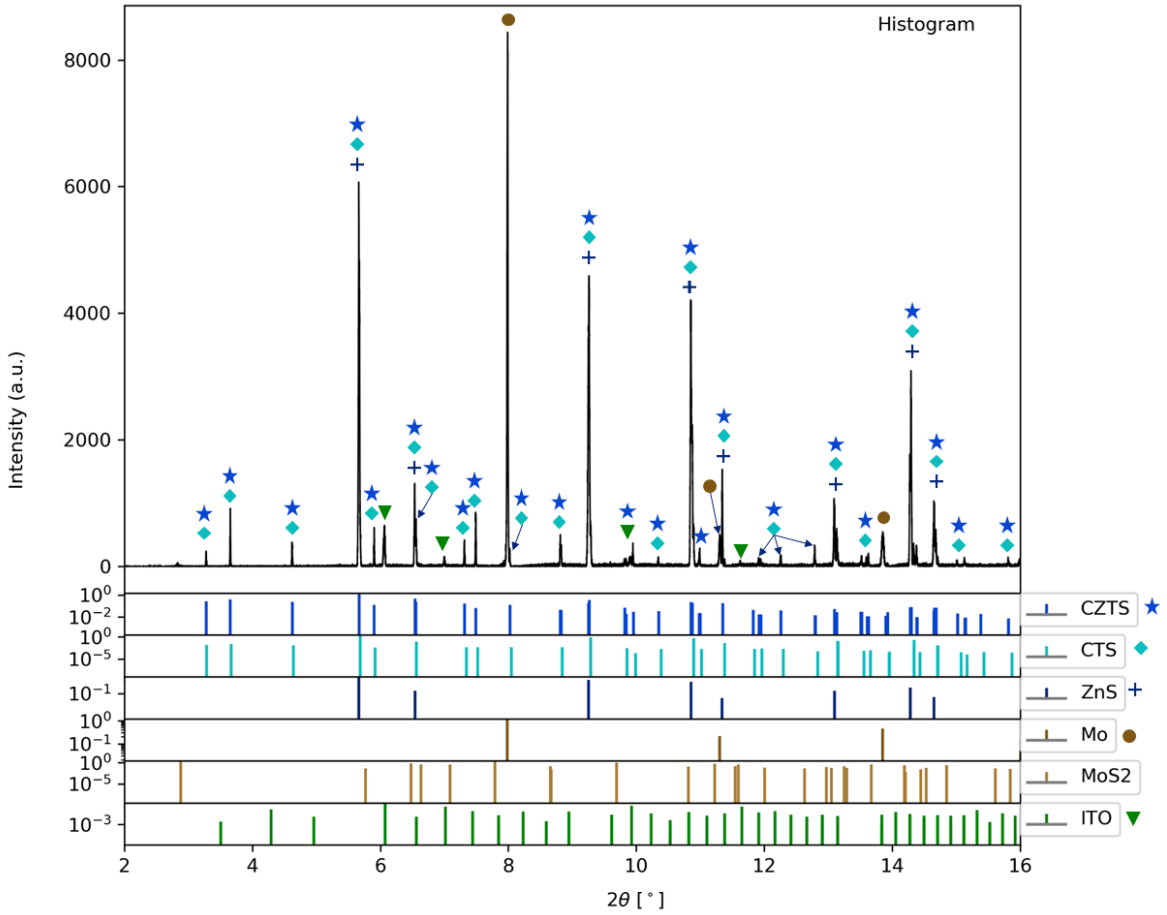

Figure 2.11. Histogram of the two-theta angles weighted by their intensity from the ESRF data set. The bin width is 0.0005°.

ImageD11 can index one phase at a time. Therefore, one needs to choose which phase to index first. The CZTS is derived from the sphalerite ZnS, and therefore they have overlapping peaks. For example, the (112) plane of the tetragonal CZTS phase corresponds to the (111) plane of the cubic ZnS. Moreover, the ternary compound Cu_2SnS_3 also has a tetragonal structure with the same space group as disordered kesterite and similar unit cell lattice parameters. In contrast, the other secondary phases are not overlapping and can be indexed if they have enough peaks.

The peak overlap in powder diffraction patterns makes it hard to distinguish between the CZTS and ZnS phases. We can overcome this problem using the 3DXRD data and assign each peak to a grain.

We encountered that most of the peaks align with the cubic and tetragonal phases in all our experiments. One could start indexing the primary phase, the kesterite. However, indexing the peaks with the tetragonal structure could mislabel cubic peaks and create fake tetragonal grains. On the other hand, indexing the overlapping peaks with the cubic crystal structure would recover all the grains with a cubic unit cell. A verification process to identify tetragonal grains among the indexed "as-cubic" grains is implemented after that.

2.4.4.3 Indexing reflections with the cubic crystal structure

The indexing routine is carried out by the software ImageD11 and consists of matching the peaks in 3D reciprocal space to grain orientations. Each peak/ diffraction spot is associated with a reciprocal lattice vector, **G**.

First, ImageD11 assigns the diffraction spots to powder hkl rings for the known unit cell, in this case, the cubic ZnS. It calculates the cosine angle between two selected hkl rings. When the cosine angle is consistent with the cosine angle between two observed **G** vectors, they are used to compute an orientation matrix. This matrix is used to compute the hkl indices for all observed **G** vectors. The orientation is validated by indexing a minimum number of peaks, "minpks", with a certain tolerance "hkl_tol", which refers to the error between the integer hkl values and the computed hkl indices of the orientation for all observed **G** vectors. If the number of peaks is too low or the tolerance is too large, the algorithm can produce false orientations. In this work, grains were accepted if they have at least 30 out of 50 expected spots and an error below 0.01.

After indexing the peaks, we obtain a list of grains represented by the orientation matrices. These matrices are later refined, together with the grain positions. We also use them to calculate the misorientation angle between twinned grains and strain.

2.4.4.4 From cubic to tetragonal structures

To find the tetragonal grains among the "as-cubic" indexed grains, we follow the next procedure. The cubic unit cell lattice parameters a, b, and c are doubled, creating the supercell with lattice parameters: [2a, 2b, 2c]. One would expect the (hkl) reflections in the supercell to be all even: (2h 2k 2l). If reflections are indexed with h, k, or l being odd, it indicates that a tetragonal subcell is present.

For example, a reflection (h, 2k, 2l) would indicate that the a-axis is twice as long, which means that the a^*-axis is half of the distance in reciprocal space. Similarly, (2h, k, 2l) suggests that the tetragonal grain exists by doubling the b-axis, and (2h, 2k, l) implies doubling the c-axis. By counting the odd miller index of the supercell reflections, one can define the c-axis of the tetragonal unit cell.

In Figure 2.12a, we illustrate the case of one grain showing the supercell reflections and the subcell reflections. In Figure 2.12b, for the same grain, a histogram shows the number of reflections with h, k, or l- odd miller indices and the relative indexing error (hkl indices as 'close enough' to being integers). Reflections in blue with an error above 0.015 do not belong to the grain. The distribution of the total of grain reflections (orange) and the (2h, 2k, l) reflections with the l-odd miller index (purple) overlay and have and have an error below 0.015. It denotes the existence of a tetragonal subcell defining the cubic b-axis as the tetragonal c-axis.

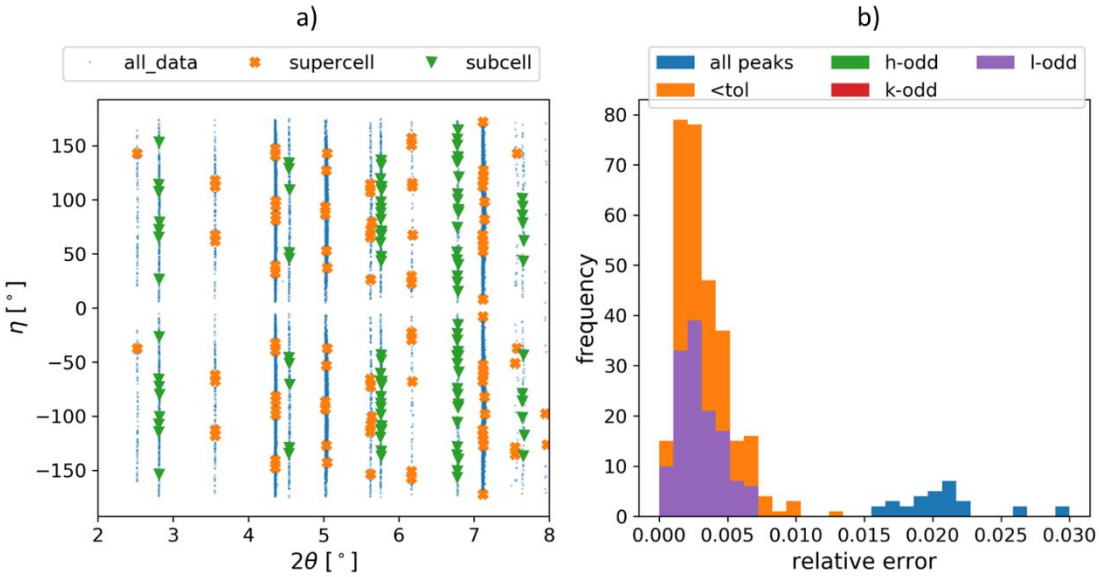

Figure 2.12. Illustration of the tetragonal transformation and assessment of the c-axis in the "as-cubic" grain. a) Plot of the eta vs two-theta angle shows the reflections of the supercell and the subcell. The histogram showing the odd-l miller index with the highest counts indicates that the b-axis should be doubled to retrieve the tetragonal phase.

To summarize, the tetragonal grains are determined under three criteria:

- One of the lengths of the unit cell lattices is shorter than the other two.
- The highest number of counts of odd-h, odd-k, or odd-l coincides with the shortest cubic axis
- The "as-cubic" unit cell volume is larger than 159.6 Å

When the grain is transformed into tetragonal by doubling one of the axes, we compare the new grain against all the equivalent symmetry operations to find the most aligned orientation to the laboratory x, y, z axes.

2.4.5 Determination of grain volume

For determining the grain volume, we assume a proportionality of the volume with the intensities. First, we normalize the intensities by the Lorentz and the polarization factor. Then, we calculate the average of the intensities assigned to the grain without counting the shared reflections, represented with $\bar{I}_g$. The grain volume is given by equation (2.17), where $\sum \bar{I}_g$ is the sum of the average intensities of all indexed grains, and the V_{sample} is the illuminated sample volume. The sample volume is determined by the beam height and the sample width and thickness.

$$V_{grain} = \frac{\bar{I}_g}{\sum \bar{I}_g} \times V_{sample} \tag{2.17}$$

2.4.6 Measuring strain

Crystals in thin-films undergo different fabrication processes that inflict stresses on the lattices of the grains. These stresses create a state of deformation in the grains and eventually the film.

There are different ways to obtain the strain from diffraction data. Ultimately, all these calculations depend on a state before deformation. Here, we explain the methods that were used according to the situation. For example, strain in the scanned volume can be obtained directly from the displacements of the reflections in the diffraction data. In other cases, the deformation matrix is calculated from the unit cell lattices of the indexed grains. The undeformed state is determined based on the average values of the measurements.

2.4.6.1 Strain from Diffraction data

The strain is a perturbation of the local lattice [110]. In diffraction data, the strain can be identified by the shift of the position of the reflections, as expressed in equation (2.18). Here, d_{hkl_0} is the unstrained interplanar distance and θ_{hkl_0} is the unstrained two-theta position of the reference unit cell. The determination of an unstrained state in the material can be defined based on the average values of the ensemble of measured reflections d_{hkl_i} or θ_{hkl_i}.

$$\varepsilon_{hkl_i} = \frac{\Delta d_{hkl}}{d_{hkl_0}} = -\Delta\theta_{hkl_i} \cot \theta_{hkl_0} \tag{2.18}$$

The scalar measured strain, ε_{hkl_i}, is an average property in the direction perpendicular to the Miller planes, $\vec{n}$. The reciprocal lattice vector of the *i* reflection, $\vec{G}_{s_i}$, also perpendicular to the (hkl) planes, can be represented as the difference between a strained and an unstrained vector, $\vec{G}_{s_i} = \vec{s} - \vec{s}_0$. Thus, $\vec{n}_i$ can be defined as:

$$\vec{n}_i = \frac{\vec{G}_{s_i}}{\|\vec{G}_{s_i}\|} \tag{2.19}$$

Each measured peak position can be converted to a corresponding average strain ε_{hkl_i} and strain direction, $\vec{n}_i$ using equations (2.18) and (2.19). We can also deduce the strain tensor, as it is laid out by Poulsen *et al.* (2001) [119]:

$$\varepsilon_{hkl_i} = (n_x \quad n_y \quad n_z)_i \begin{pmatrix} \varepsilon_{11} & \varepsilon_{12} & \varepsilon_{13} \\ \varepsilon_{12} & \varepsilon_{22} & \varepsilon_{23} \\ \varepsilon_{13} & \varepsilon_{23} & \varepsilon_{33} \end{pmatrix} \begin{pmatrix} n_x \\ n_y \\ n_z \end{pmatrix}_i \tag{2.20}$$

To solve equation (2.18) for an ensemble of measured scattering vectors, we introduce matrix D representing the projection of the average strain measurements $\varepsilon_{\mathrm{hkl_i}}$ which are stored in a vector $\vec{m}$. In this linear equation system represented in equation (2.21), we seek the solution for the components of the strain tensor, represented by the vector $\vec{S}$.

$$D_{M\times 6} \times \vec{S}_{6\times 1} = \vec{m}_{M\times 1} \tag{2.21}$$

With,

$$\boldsymbol{D} = \begin{pmatrix} {n_x}^2{}_1 & n_x n_{y_1} & n_x n_{z_1} & {n_y}^2{}_1 & n_y n_{z_1} & {n_z}^2{}_1 \\ & & \vdots & & & \\ {n_x}^2{}_M & n_x n_{y_M} & n_x n_{z_M} & {n_y}^2{}_M & n_y n_{z_M} & {n_z}^2{}_M \end{pmatrix} \tag{2.22}$$

$$\vec{S} = (\varepsilon_{11}\ \varepsilon_{12}\ \varepsilon_{13}\ \varepsilon_{22}\ \varepsilon_{23}\ \varepsilon_{33})^T;\ \vec{m} = \begin{pmatrix} \varepsilon_{hkl_1} \\ \vdots \\ \varepsilon_{hkl_M} \end{pmatrix} \tag{2.23}$$

The strain tensor components correspond to an average strain. In the APS data, all the diffraction peaks were shifted. Therefore, we considered all the peaks to calculate the average strain tensor in the sample. On the other hand, if only the grain reciprocal lattice vectors are taken into account, the strain tensor components correspond to the grain average strain.

APS diffraction data show noticeable displacements of the two-theta positions. Therefore, this method was implemented to correct the unit cell lattice parameters of the indexed grains. The average strain tensor per scanned slice is removed by equation (2.24), improving the lattice parameters closer to the reference unit cell. Here, the reference lattice $(\mathbf{UB})_0$ in reciprocal space is obtained by adding the calculated strain tensor to the deformed lattice **UB**.

$$(\mathbf{UB})_0 = (1 + \mathbf{E})(\mathbf{UB}) \tag{2.24}$$

2.4.6.2 Strain from the grain lattice parameters

Poulsen (2004) describes the strain in terms of the direct space coordinates, not in reciprocal space [110]. By analogy to the B matrix described by equation (2.11), the matrix A represents the transformation between the Cartesian and the crystal reference:

$$\mathbf{A} = \begin{pmatrix} a & b\cos(\gamma) & c\cos(\beta) \\ 0 & b\sin(\gamma) & -c\sin(\beta)\cos(\alpha^*) \\ 0 & 0 & c\sin(\beta)\sin(\alpha^*) \end{pmatrix} \tag{2.25}$$

If a crystal is strained, the atoms have moved compared to a strain-free reference. The strained lattice is described by matrix A and the unstrained state by the matrix A_0. The deformation gradient tensor F is expressed in equation (2.26). Another notation for the deformation gradient tensor is **T**, Poulsen (2004) [12]

$$\mathbf{A} = \mathbf{F}\mathbf{A}_0 \;\; \Rightarrow \mathbf{F} = \mathbf{A}{\mathbf{A}_0}^{-1} \tag{2.26}$$

By definition, the infinitesimal strain tensor ε can be written as:

$$\boldsymbol{\varepsilon} = \frac{1}{2}(\boldsymbol{F} + \boldsymbol{F}^T) - \boldsymbol{I} \tag{2.27}$$

Where *I* is the identity matrix.

Moreover, the **A** matrix is derived from the **B** matrix in FABLE tools. By defining $\boldsymbol{A}^T\boldsymbol{B} = \boldsymbol{I}$, the deformation tensor can be written as:

$$\mathbf{F} = \mathbf{B}_0\mathbf{B}^{-1} \tag{2.28}$$

The previous equations apply to the grain reference system, and the stress components are inscribed in the crystallographic axes ([100], [010], [001]). To calculate the strain in the sample reference system, we apply the grain orientation matrix, as described in equation (2.29).

$$\boldsymbol{\varepsilon}_{sample} = \boldsymbol{U} \cdot \boldsymbol{\varepsilon}_{grain} \cdot \boldsymbol{U}^T \tag{2.29}$$

Another useful definition to calculate the deformation tensor is using the lattice vectors in direct space obtained after indexing, denoted by the matrix $\mathbf{L} = (\mathbf{UB})^{-1}$. In general, the real space lattice **L** is expressed as row vectors, and the representation as column vectors can be done by using the transpose of **L**, indicated by the super index T.

$$\boldsymbol{F} = \boldsymbol{L}^T{\boldsymbol{L}_0}^{-T} = ((\boldsymbol{UB})^{-1})^T((\boldsymbol{UB})_0^{-1})^{-T} \tag{2.30}$$

With, $$\boldsymbol{L} = (\boldsymbol{UB})^{-1} = \begin{pmatrix} x_a & y_a & z_a \\ x_b & y_b & z_b \\ x_c & y_c & z_c \end{pmatrix}$$

This definition is useful, as the L matrix decomposition into the orientation matrix U and the asymmetric Cartesian-reciprocal transformation matrix **B** is avoided. This way, the indexing of the reflections is preserved. Different definitions of the strain tensor can be calculated based on this expression, such as the Lagrangian or Eulerian strain tensors. The reader is invited to learn about the details of the different strain tensor computations by Wright (2020) [120]. Ultimately, this definition is also advantageous for comparing strained grains that are also twinned.

2.4.6.3 From strain to stress

Once the strain is obtained, one can determine the corresponding stresses that caused the deformation in the grains. The stress is calculated using Hook's law, equation (2.31), where σ_{ij} is the second-rank stress tensor and ε_{kl} is the second-rank infinitesimal strain tensor. The fourth-rank elastic stiffness tensor C_{ijkl} describes the stress σ_{ij} induced by the strain ε_{kl}. The constants were calculated by Jamiati *et al.* and are applicable in the crystal reference system [103].

$$\sigma_{ij} = C_{ijkl}\varepsilon_{kl} \tag{2.31}$$

Here, we use the Voight matrix representation, in which the indexes of the tensor components ij or kl become m or n, as follows:

m or n	1	2	3	4	5	6
ij or kl	11	22	33	23	13	12

Using the Voigt matrix representation of Hook's law (equation (2.31) may be written as:

$$\begin{pmatrix} \sigma_1 \\ \sigma_2 \\ \sigma_3 \\ \sigma_4 \\ \sigma_5 \\ \sigma_6 \end{pmatrix} = \begin{pmatrix} C_{12} & C_{12} & C_{13} & C_{14} & C_{15} & C_{16} \\ C_{21} & C_{22} & C_{23} & C_{24} & C_{25} & C_{26} \\ C_{31} & C_{32} & C_{33} & C_{34} & C_{35} & C_{36} \\ C_{41} & C_{42} & C_{43} & C_{44} & C_{45} & C_{46} \\ C_{51} & C_{52} & C_{53} & C_{54} & C_{55} & C_{56} \\ C_{61} & C_{62} & C_{63} & C_{64} & C_{65} & C_{66} \end{pmatrix} \times \begin{pmatrix} \varepsilon_1 \\ \varepsilon_2 \\ \varepsilon_3 \\ 2\varepsilon_4 \\ 2\varepsilon_5 \\ 2\varepsilon_6 \end{pmatrix}$$

Finally, to calculate the stress components in the sample reference system, we apply the grain orientation to the stress tensor:

$$\boldsymbol{\sigma}_{sample} = \boldsymbol{U} \cdot \boldsymbol{\sigma}_{grain} \cdot \boldsymbol{U}^T \tag{2.32}$$

2.4.7 Recovering twin boundaries

Twin boundaries can be described as the domain between two grains joined together according to a specific symmetry operation, i.e., a rotation. The domain between the twinned grains is a single plane of atoms that can be viewed as belonging to the crystal structure of both grains.

Often diffraction spots from twinned grains overlay, complicating the refinement of the structure. In this case, 3DXRD would discern two different orientations for the two grains sharing overlapping reflections, but one grain will get more reflections during the assortment of the reflections than its twinned pair.

To obtain the twin relations between grains, it is necessary to identify the grains that share reflections. We compute the reflections of the grain ‘m’ and compare them against the list of grain orientations. If a different grain orientation indexes some of the ‘m’ grain reflections, these reflections overlap.

Figure 2.13 shows an example of overlapping reflections from two grains that have different orientations. We repeat this comparison for all the grain orientations obtaining the list of the potential twin grains.

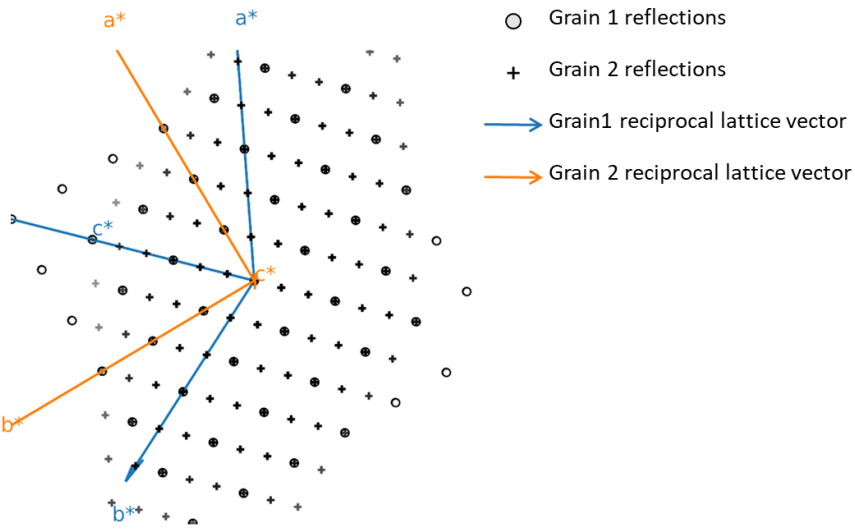

Figure 2.13. Reflections of two twin grains and their reciprocal lattice vectors.

Next, we calculate the misorientation angle between the pair of twinned grains and apply the equivalent symmetry operations. Here, the deformation matrix definition is a powerful tool to compare the lattices of strained grains. Similarly to equation (2.30), we use the direct space

lattices to calculate the deformation matrix. The lattice of grain m is the deformed lattice $(\mathbf{UB})_m^{-1}$, whereas the "unstrained" lattice corresponds to grain "n."

$$\mathbf{F} = ((\mathbf{UB})_m^{-1})^T((\mathbf{UB})_n^{-1})^{-T} = ((\mathbf{UB})_m^{-1})^T((\mathbf{UB})_n)^T \tag{2.33}$$

The deformation matrix can be decomposed using the polar decomposition theorem into a product of two second-order tensors:

$$\mathbf{F} = \mathbf{RU}_S = \mathbf{VR} \tag{2.34}$$

From Eq. (2.34), R is a proper orthogonal tensor representing the pure rotation; whereas U_S is the right stretch tensor, and V is the left stretch tensor. U_S and V describe the deformations and are symmetric tensors and positive definite.

The obtained rotation matrix R is used to calculate the misorientation angle and rotation axis of the two compared grains. The symmetry operations for comparing tetragonal grains of the point group -42m are eight possible transformations. When comparing tetragonal twinned grains, a list with eight twin operations is calculated. In the cubic structure, which belongs to point group -43m, 24 transformations are possible, resulting in 24 possible twin operations.

For each symmetry transformation, a strain tensor is calculated by equation (2.35), defined as the Biot strain tensor[5]. The norm of the strain tensor, $\|\boldsymbol{E}\|_F$, will determine the overall strain magnitude for the symmetry transformation. Finally, we choose the misorientation angle that results from the operation with the lowest strain tensor norm implying the minimal lattice mismatch between the compared grains.

$$\boldsymbol{E} = \boldsymbol{U}_S - \boldsymbol{I} \tag{2.35}$$

[5] Biot strain, also known as the linear strain tensor, is comparable to the infinitesimal strain tensor, described in (2.27) , in the absence of the rotation component. On the other hand, the infinitesimal strain tensor is limited to applications involving small rotations, but not to small strains.

2.5 MULTIGRAIN CRYSTALLOGRAPHY

Multigrain crystallography consists of characterizing polycrystalline materials composed of multiple crystalline phases utilizing 3DXRD [107]. This method proposes a novel approach for simultaneous indexing and identifying diverse crystallographic phases with no *a priori* knowledge of their nature [121].

Frequently, one finds samples with heterogeneities in composition and different crystallographic structures. Notably, in CZTS solar cells, the absorber layer has secondary phases, challenging to identify by X-ray powder diffraction. Therefore, 3DXRD and multigrain crystallography would be an appropriate choice to study this material.

2.5.1 The algorithm

The multigrain algorithm was developed in MATLAB by *Wejdemann et al.* in 2016 [121]. Wahlberg and Hakim, both postdocs from DTU Physics, made later versions written in python in 2017 and 2019, respectively. Finally, the software was acquired by Xnovo for continuing further development.

The input to the algorithm consists of the scattering vectors calculated from the harvested diffraction spots. Briefly described, the multigrain algorithm indexes the scattering vectors to find unit cells and their orientations. The indexing is based on the position of the reflections, not their intensity. It searches for equidistant lattice planes separated by a distance d^* and defined by their normal vector $\vec{u}_1$. It counts the reflections lying on these planes and keeps the planes with the highest number of reflections as a grain candidate. The subset of reflections of the candidate grain is used for the second search in a new direction of the lattice plane normal $\vec{u}_2$ (not parallel to $\vec{u}_1$). The potential grain is determined by the best combination of $\vec{u}_1$ and $\vec{u}_2$, corresponding to the highest number of reflections.

Figure 2.14 a) shows the reflections in reciprocal space, the reciprocal spacing between the tested lattice planes d*, and the corresponding normal vector to the lattice planes. Next, Figure 2.14 b) displays a 2D slice through the centre of reciprocal space. The reflections of two grains are represented with '*' and '+' symbols. Strips of width 2ε separated by the distance d^* are framing some of the reflections. These strips containing the reflections can be visualized as a histogram, counting the number of reflections lying on the planes with the bin width of 2ε, as shown in Figure 2.14 c). In this first step, the reflections of the candidate grain are kept for a second search using a different direction $\vec{u}_2$.

In the next step, the validation of the candidate grain leads to the determination of the unit cell in direct space. Finally, the identified grain reflections are removed from the dataset, and the search for new grains restarts. The details of the algorithm can be found in [121].

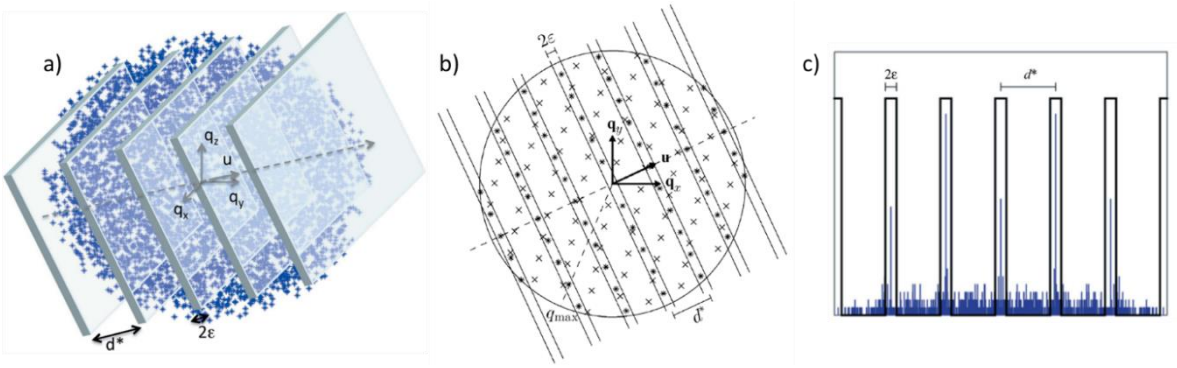

Figure 2.14. a) Illustration of the basic principle of the indexing algorithm, b) Illustration of the first step in the algorithm, c) Illustration of the filter used to count reflections. Reprinted from [121] *CC-BY.*

New parameters were introduced in the later versions to restrict the arbitrariness in the algorithm and reduce computing time. The most relevant ones are listed below:

- **Sort** = True or False; **frac**. The "sort" parameter determines whether the search is random or not, while "frac" dictates the fraction of randomly chosen directions. The non-random normal directions are determined by the shortest scattering vectors combined with the origin (0, 0, 0).
- **Qmin**, **Qmax** are the shortest and the longest d-spacing in reciprocal space.
- **nn**: the number of normal directions kept as candidates to continue with the second search.
- **eps_exp**: Maximum deviation between calculated and observed reflection position.
- **min_ref**: minimum number of reflections assigned to a unit cell
- **max_misses**: Maximum number of unindexed reflections.

In addition to these parameters, the unit cell determination is performed differently from the original version in a four-step process. First, a unit cell is resolved by Duiselberg's algorithm [122], followed by the optimization of the lattice parameters by a least-squares fitting. Here, scattering vectors are calculated according to the retrieved unit cell and are compared to the observed scattering vectors. The lattices of the unit cell are adjusted to fit the observed vectors. Thirdly, the reflections matching the cell vectors are harvested from the full list of reflections. Finally, the unit cell is verified by comparing it against the harvested set of reflections to determine if the grain is accepted or rejected.

The results obtained by the code (2017 version) are:

- Niggli reduced cell[6] with the corresponding lattice parameters
- Orientation matrix, equivalent to $(\mathbf{UB})^{-1}$ provided by ImageD11
- Reciprocal lattice matrix, equivalent to **UB** provided by ImageD11
- Number of matching reflections and list of assigned reflections from the list of g-vectors

2.5.2 Preliminary tests and results

This section tests the multigrain algorithm from 2017 with synthetic data generated by PolyXSim [123]. The simulations parameters are based on the ID11 beamline setup at ESRF, listed in Table 2.4.

Table 2.4. Parameters used for all three simulations.

Parameter	Value
Distance to detector	160 mm
Detector	Channel size 50 x 50 µm Number of channels: 2048 x 2048
ω range: [ω_{min} ; ω_{max}]	[0°; 180°]
ω step	0.5°
Wavelength	0.32628 Å
Grain size **(the same order of the detector size)**	50 µm

Each simulation has a different number of grains and crystallographic phases encountered in the CZTS solar cells. The list of the simulations is as follows:

- "kesterite" simulation

  Phases: CZTS (I-42m), Cu_2SnS_3 (I-42m), ZnS (F-43m), SnS (Pnma), SnS_2 (P-3m1), Cu_2S (P63/mmc) and $Cu_{1.8}S$ (Fm-3m)
  This simulation uses the kesterite phase and secondary phases that could form during solar cell fabrication. In total, seven grains, one of each phase, are created.

[6] A unique primitive unit cell built on the shortest non-coplanar translations [121].

- “CCCm” simulation

  Phases: CZTS (I-42m), Cu_2SnS_3 (c1c1), ZnS (F-43m)
  We explore the reflections of the sphalerite and kesterite phase with the monoclinic Cu_2SnS_3.

- "CCC_30" simulation

  Phases: CZTS (I-42m), CTS (I-42m), ZnS (F-43m)
  A test is carried out with 30 grains containing the three phases that typically overlap. In experimental data, a large number of grains is expected. In a conservative attempt, we simulate ten grains of each phase to study the behaviour of the code, indexing a larger number of reflections and possible spot overlap.

The multigrain indexing algorithm provides the Niggli reduced cell as a result. To compare the standard unit cell, one has to transform it into the primitive unit cell, which can be done in the Bilbao Crystallographic Server (BCS) website, using the toolbox: “Transform Unit cell” [121]. Here, it is required to input the transformation matrices for retrieving the primitive unit cell, which can be found in [124]. BSC calculates the Niggli reduced cells, which are now comparable with the unit cells proposed by Multigrain (see Table 2.5).

Table 2.5. List of the phases used in the simulations with their space group, conventional, primitive, and Niggli reduced unit cells. The unit cell parameters are taken from ICSD. The ICSD collection number and reference are given in the last column.

Phase (Space group)	**Conventional unit cell a, b, c=[Å], α, β, γ=[°]**	**Primitive unit cell a, b, c=[Å], α, β, γ=[°]**	**Niggli reduced unit cell a, b, c=[Å], α, β, γ=[°]**	**ICSD [Ref]**
Cu_2ZnSnS_4 (I-42m)	a, b=5.4334 c = 10.8421 α, β, γ = 90	a, b=5.4334 c = 6.6445 α, β= 65.87 γ = 90	a, b = 5.4334 c = 6.6445 α, β = 114.13 γ = 90	239682 [47]
Cu_2SnS_3 (I-42m)	a, b = 5.413 c = 10.824 α, β, γ = 90	a, b = 5.413 c = 6.629 α, β = 65.9 γ = 90	a, b = 5.413 c = 6.629 α, β = 114.1 γ = 90	50965 [64]
Cu_2SnS_3 Monoclinic (C1 c1)	a = 6.653; b = 11.537 c = 6.665 α, γ = 90; β =109.39	a = 6.653; b = 6.659 c = 6.665 α = 99.55; β = 109.39 γ = 60.03	a = 6.653; b = 6.659 c = 6.665 α = 80.45; β = 70.61 γ = 60.03	91762 [62]
ZnS (F-43m)	a, b, c = 5.433 α, β, γ = 90	a, b, c = 3.842 α, β, γ = 60	a, b, c = 3.842 α, β, γ = 60	77090 [71]
Cu_2S (P63/mmc)	a, b = 4.033; c = 6.739 α, β =90 γ = 120	a, b = 4.033 c = 6.739 α, β = 90 γ = 120	a, b = 4.033 c = 6.739 α, β = 90 γ = 120	95397 [125]
$Cu_{1.8}S$ (Fm-3m)	a, b, c =5.589 α, β, γ = 90	a, b, c = 3.952 α, β, γ = 60	a, b, c =3.952 α, β, γ = 60	95395 [125]
SnS_2 (P-3m1)	a, b=3.638 c=5.88; γ=120	a, b = 3.638 c = 5.88 α, β = 90 γ = 120	a, b= 3.638 c = 5.88 α, β = 90 γ = 120	100610 [74]
SnS (Pnma)	a=11.18; b=3.982; c=4.329 α, β, γ = 90	a = 11.18; b = 3.982 c = 4.329 α, β, γ = 90	a = 3.982; b = 4.329 c = 11.18 α, β, γ = 90	24376 [126]

2.5.2.1 Indexing simulations with multigrain

The study aims to identify the simulated grains with the right unit cell. The applied indexing parameters are the same for the three simulations.

- **nn**: 10
- **ε**: 0.001
- **Nu_1**, **Nu_2**: 10000
- **q_min**: 0.025
- **q_max**: 0.5
- **sort**: True
- **frac**: 0.5
- **eps_exp**: 0.0001
- **min_ref**: 50
- **max_misses**: 10000

The results of each simulation are reported in a table with three columns. Each column describes the following data:

- PolyXSim column includes the information of the simulated grains, the phase, and the number of reflections per grain.
- The multigrain column provides the phase identified from the unit cell parameters and the number of the assigned reflections per grain.
- Average error column. The Niggli reduced unit cell parameters obtained by BCS, $UC_{Bilbao,}$ is compared against the unit cell parameters proposed by multigrain, $UC_{Multigrain}$.

The errors in the lattice constants a, b, c, α, β, and γ are given in Figure 2.15, Figure 2.16, and Figure 2.17. The error corresponds to the absolute difference between the unit cell parameters UC_{Bilbao} and $UC_{Multigrain}$:

$$\%\ \text{error} = \frac{\left|UC_{Bilbao} - UC_{Multigrain}\right|}{UC_{Bilbao}} \times 100 \tag{2.36}$$

"kesterite" simulation

The seven phases are identified correctly, with average percentage errors in the lattice parameters in the order of 10^{-3} %. The average angle error is zero for most of the grains, except for Cu_2SnS_3 and CZTS. The number of assigned reflections by Multigrain is lower than the real number of reflections generated by PolyXSim due to a "cleaning" step in the algorithm to remove duplicated reflections. The origin of the duplicates is unknown, but it already shows the limitations of the code to deal with overlaps and cases of twinning, where reflections tend to lie very close.

Figure 2.15 shows the error in the six unit cell parameters. ZnS cubic structure has the same value error in the three lattices and zero error in the angles. For the tetragonal structures, the

lattices a and b have an error lower than the c-axis, whereas the error in angles α ($\Delta\alpha=2.2\cdot10^{-3}$ %) and β ($\Delta\alpha=2.2\cdot10^{-3}$ %) is higher than γ ($\Delta\gamma=0$). All the grains have zero error in angle γ. Cubic $Cu_{1.8}S$ has lower error values than its polymorph, the hexagonal Cu_2S, whereas orthorhombic SnS lattice errors are higher than the trigonal SnS_2 lattice errors.

Table 2.6. Results of Multigrain indexing kesterite and secondary phases.

PolyXSim			Multigrain output			Average error %	
Grain ID	Phase	Reflect/ grain	Grain ID	Phase	Reflect/ grain	lattice distance	Angles
0	$Cu_{1.8}S$	216	4	$Cu_{18}S$	201	0.005	0
1	SnS	866	3	SnS	811	0.004	0
2	Cu_2SnS_3	809	2	Cu_2SnS_3	761	0.003	0.001
3	CZTS	804	1	CZTS	751	0.005	0.001
4	ZnS	202	5	ZnS	192	0.003	0
5	Cu_2S	430	7	Cu_2S	402	0.011	0
6	SnS_2	348	6	SnS_2	326	0.015	0

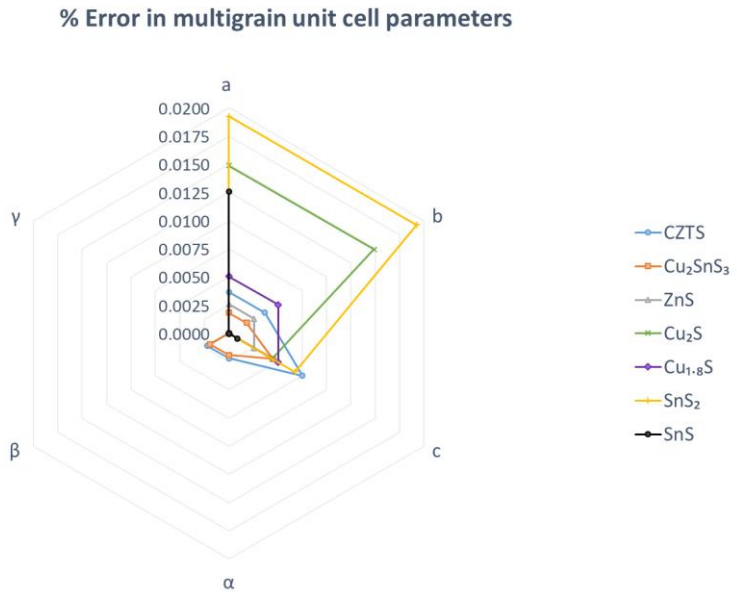

Figure 2.15. Radar chart of the error in the unit cell parameters for CZTS kesterite and secondary phases.

"CCCm" simulation

The three grains are indexed successfully, with a minimal marginal error (10^{-3} %) between the proposed multigrain unit cells and the simulated ones. The Cu_2SnS_3 monoclinic phase

has a lower symmetry order showing additional reflections, which are not present in the tetragonal phase. However, multigrain could identify the monoclinic phase independently of the crystal structure symmetry.

We see that the monoclinic lattice parameters' error is lower than the tetragonal kesterite and the same as the cubic ZnS, whereas the monoclinic angle error is the largest among the three phases (see Figure 2.16).

Table 2.7. Results of Multigrain indexing CZTS, ZnS and monoclinic Cu_2SnS_3.

PolyXsim			Multigrain			Average error %	
Grain ID	Phase	Reflections per grain	Grain ID	Phase	Reflect/ grain	Lattice distances	Angles
2	Cu_2SnS_3	1189	3	Cu_2SnS_3	1114	0.003	0.002
1	CZTS	803	2	CZTS	751	0.005	0.001
0	ZnS	198	1	ZnS	185	0.003	0

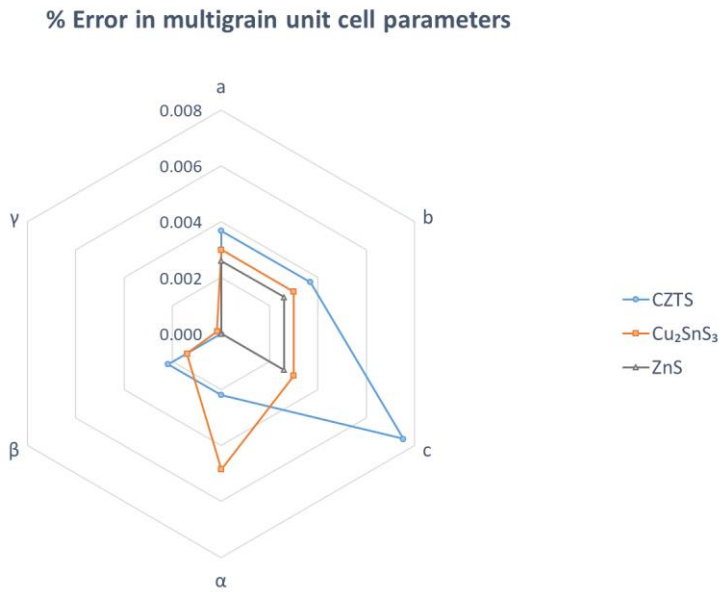

Figure 2.16. Radar chart of the error in the unit cell parameters for CZTS, ZnS, and monoclinic Cu_2SnS_3.

"CCC_30" simulation

The thirty grains were correctly assigned to the three distinct phases. The average error of the unit cell parameters is in the order of 10^{-3} % and higher in the CZTS kesterite unit cell, followed by the tetragonal Cu_2SnS_3 and the cubic ZnS.

Figure 2.17 shows the average errors in the individual lattice parameters. The c-axis has the highest average error in the CZTS with ($\Delta c=7.5\cdot10^{-3}$ %), and Cu_2SnS_3 with ($\Delta c=4.5\cdot10^{-3}$ %). The average errors in the a-axis and the b-axis for CZTS ($\Delta a=3.7\cdot10^{-3}$ %, $\Delta b= 5.5\cdot10^{-3}$ %) are higher than the average errors in Cu_2SnS_3 (Δa, $\Delta b=1.8\cdot10^{-3}$). ZnS error is the same in all the lattice distances (Δa, Δb, $\Delta c= 2.6\cdot10^{-3}$ %), whereas the error angle is zero.

Table 2.8. Results of Multigrain indexing: Unit cell parameters of ten CZTS grains, ten ZnS grains, and ten tetragonal Cu_2SnS_3 grains.

	PolyXSim	Multigrain	Average error %	
Phase	average reflections per grain	average reflections per grain	lattice distances	angles
CZTS	812	759	0.006	0.002
Cu_2SnS_3	804	753	0.003	0.001
ZnS	205	193	0.003	0.000

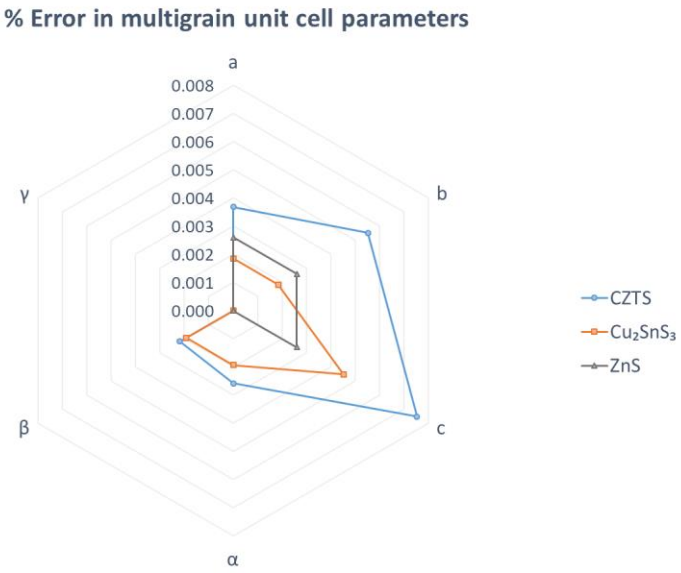

Figure 2.17. Radar chart of the error in the unit cell parameters for ten CZTS grains, ten ZnS grains, and ten tetragonal Cu_2SnS_3 grains.

2.5.3 Conclusions and outlook

The indexing over the synthetic data has shown promising results by identifying all the grains with their corresponding unit cells and the number of reflections.

In general, the higher crystal symmetries have a lower error in their lattices; the cubic ZnS compared to the tetragonal CZTS and Cu_2SnS_3 is an example. When comparing Cu_2SnS_3 tetragonal and monoclinic structures, the former has a lower error in the lattice distances and the angles. An exception to this is the orthorhombic SnS with a lower error in the unit cell parameters than the trigonal SnS_2.

Multigrain can characterize grains and identify their crystallographic space group by providing a Niggli reduced unit cell. It also determines the grain orientation that describes the lattice vectors of the Niggli reduced unit cell in the laboratory coordinate system.

We can identify the crystallographic phases by comparing the Niggli reduced cell lattice parameters with the transformed conventional unit cell into the Niggli cell. We also verify the number of reflections assigned to the Niglli cell with the corresponding number of reflections of the simulated data.

Moreover, one could compare the orientations provided by multigrain with the simulated grain orientations. It would require a transformation of the multigrain Niggli cell lattice vectors to the conventional cell structure. In addition to the transformation, one should apply the symmetry equivalent operations to choose a unique representation of the orientation. For example, the case of a cubic crystal, where the reference crystal could be fixed in 24 different ways to the sample, is determined by choosing the orientation closest to the identity matrix. This principle is implemented in the FABLE packages.

Figure 2.18 depicts the reflections of a cubic ZnS grain, the reciprocal lattice vectors of the simulated unit cell, and the Niggli reduced cell proposed by multigrain. Both unit cells match the reflections, although their orientation matrices are different. The transformation from the Niggli unit cell lattice vectors to the conventional unit cell vectors would allow the comparison of the orientation matrix.

Despite the good results, we identify some challenges in the design of the multigrain algorithm. Further development in the code is needed to be fully operational and be tested on real data.

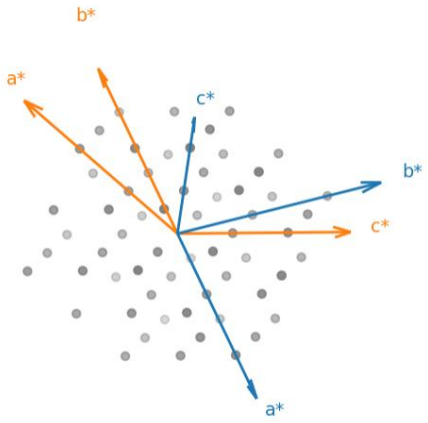

Figure 2.18. Illustration of the reflections of a ZnS grain. The blue vectors are showing the reciprocal lattice vectors of the unit cell proposed by PolyXSim. The orange vectors are the reciprocal lattice vectors of the multigrain unit cell.

3 Experimental section

3.1 NON-DESTRUCTIVE DETERMINATION OF PHASE, SIZE, AND STRAIN OF INDIVIDUAL GRAINS IN POLYCRYSTALLINE PHOTOVOLTAIC MATERIALS

- Mariana Mar Lucas, Tiago Ramos, Peter S. Jørgensen, Stela Canulescu, Peter Kenesei, Jonathan Wright, Henning F. Poulsen, Jens W. Andreasen.

This section comprehends a thorough analysis of the microstructure of the absorber layer of a CZTS solar cell fabricated by pulsed laser deposition. It demonstrates the application of the 3DXRD technique for the study of photovoltaic polycrystalline thin-films.

The manuscript has been submitted to Physical Review Applied.

My contribution:

- Literature review
- Writing the proposal for the experiment
- Establish sample geometry
- Data collection at APS
- Data analysis and interpretation of the results
- Writing the first draft of the manuscript
- Implementation of suggestions and corrections

Non-destructive determination of phase, size, and strain of individual grains in polycrystalline photovoltaic materials

Mariana Mar Lucas[1], Tiago Ramos[1], Peter S. Jørgensen[1], Stela Canulescu[3], Peter Kenesei[4], Jonathan Wright[5], Henning F. Poulsen[2], Jens W. Andreasen[1].

[1.] Department of Energy Conversion and Storage, Technical University of Denmark, 2800 Kgs. Lyngby, Denmark.
[2.] Department of Physics, Technical University of Denmark, 2800 Kgs. Lyngby, Denmark.
[3.] Department of Photonics Engineering, Technical University of Denmark, 2800 Kgs. Lyngby, Denmark.
[4.] X-ray Science Division, Argonne National Laboratory, 9700 S Cass Avenue, Lemont IL 60439
[5.] European Synchrotron Radiation Facility, 71 avenue des Martyrs, 38000 Grenoble, France.

1 Abstract

We demonstrate a non-destructive approach to provide structural properties on the grain level for the absorber layer of kesterite solar cells. Kesterite solar cells are notoriously difficult to characterize structurally due to the co-existence of several phases with very similar lattice parameters.

Specifically, we present a comprehensive study of 597 grains in the absorber layer of a 1.64% efficient Cu_2ZnSnS_4 (CZTS) thin-film solar cell, from which 15 grains correspond to the secondary phase ZnS. By means of three dimensional X-ray diffraction (3DXRD), we obtained statistics for the phase, size, orientation, and strain tensors of the grains, as well as their twin relations. We observe an average tensile stress in the plane of the film of ~ 70 MPa and a compressive stress along the normal to the film of ~ 145 MPa. At the grain level, we derive a 3D stress tensor that deviates from the biaxial model usually assumed for thin films. 41% of the grains are twins. We calculate the frequency of the six types of Σ3 boundaries, revealing that 180° rotations along axis <221> is the most frequent. This technique can be applied to polycrystalline thin film solar cells in general, where strain can influence the bandgap of the absorber layer material, and twin boundaries play a role in the charge transport mechanisms.

2 Introduction

Photovoltaic thin-film technology is increasingly targeting alternative materials to meet the triple challenge of sustainability, low energy payback time, and scalability. Current technologies include polycrystalline CdTe [1] and Cu(In, Ga)Se2 (CIGS) [2], both with power conversion efficiencies that surpass 20%. A relatively new but promising candidate is Cu2ZnSnS4 (CZTS), with an efficiency of 11% [3], and the selenized version, Cu2ZnSn(S, Se)4, where efficiency has reached 12.6% [4]. All of these materials still perform below the Shockley–Queisser limit [5].

The performance of these materials is strongly dependent on their complex microstructures. One limiting factor shared among these semiconductors is the deficient open-circuit voltage (VOC) attributed, among other reasons, to the structural defects in the absorber layer. For example, a small grain size is associated with an increased amount of grain boundaries, which, if poorly passivated, can contribute to carrier recombination [6]-[9]. Secondary phases can cause other deficiencies. For CZTS with a typically Cu-poor and Zn-rich composition, secondary phases with different bandgaps form, such as the high bandgap ZnS, increasing series resistance when situated in the back contact of the solar cell or acting as a barrier to the charge carriers at the p-n

junction [10]-[12]. In CIGS absorbers, which usually have a Cu-poor composition, a Cu(In, $Ga)_3Se_5$ phase can occur at the surface with a high density of indium or gallium appearing as copper antisite (In, Ga)Cu defects and acting as recombination centers [13]. A lattice mismatch between CIGS and Cu(In, $Ga)_3Se_5$ can also create structural defects and an increased density of recombination centers [14]. Moreover, the lattice spacing changes when modifying the material composition while tuning the bandgap e.g., with the variation of Ga/In and Se/S ratios.

Furthermore, the structure of the grains and the local strain change inevitably, as the multicomponent materials undergo different treatments from the deposition and the annealing of the absorber layer to the post-treatment methods for the coating of the subsequent layers of the device. The change in lattice parameters, as a result of fabrication stresses, can affect not only the mechanical properties of the film (adhesion to the substrate, elastic modulus, and deformation [15]) but the electronic properties as well. As an example, theoretical calculations demonstrate the reduction of bandgap due to a tensile biaxial in-plane strain. In contrast, a compressive strain increases the bandgap [16], [17].

CIGS and CdTe exhibit high efficiency, but indium and telluride scarcity is a concern for scaling up module production. Moreover, recycling of systems is complicated because of Cd toxicity. In comparison, CZTS has ideal optoelectronic properties and is made of earth-abundant, non-toxic, and low-cost constituent elements. However, to improve the device efficiency, the structural characterization, such as the identification and quantification of secondary phases, and depiction of grain structural properties, such as strain and twinning, need further work.

An additional complication arising with CZTS is that the crystallographic structures of some of the phases involved have nearly identical lattice parameters, which makes it challenging to identify and quantify the phases. For instance, ZnS with a face-centered cubic crystal structure (F-43m), and the kesterite CZTS with a tetragonal body-centered structure (I-42m), are closely related. Doubling the a, b, or c axis of the cubic ZnS structure yields a unit cell corresponding to kesterite with a small tetragonal deformation $|c/(2a) - 1| < 0.0026$ (with lattice constants from [18]).

A progress beyond the "trial-and-error" approach is vital to visualize the microstructure and local strain within the thin films in 3D and preferably also record their evolution during processing under conditions that are deemed "realistic". Such information can guide theoretical understanding and the development of models for quantitative prediction, thereby accelerating the design efforts. Moreover, physical parameters may be determined by comparing 3D models and 3D experimental data (e.g. [19]). However, the techniques currently employed to characterize the structural properties and the local stress have significant limitations:

- *Electron microscopy* (EM) can provide atomic-scale insight [13] but is confined to studies at the surface or films of a few hundred nanometer thickness. Three-dimensional resolved mapping may be accomplished by a combination of Electron Backscattered Diffraction (EBSD) and serial sectioning using either FIB [20] or laser ablation [21]. However, the destructive procedure prohibits studies of dynamics and direct coupling to functionality. Moreover, the angular resolution achieved by EM makes quantitative stress

determination difficult and does not allow for a distinction between the phases mentioned above with nearly identical lattice parameters.

- *X-ray powder diffraction* (XRD) and *grazing incidence X-ray diffraction* (GIXRD) provide bulk information about phases, orientations, and strain, but only about average properties. Typically these techniques can identify secondary phases at the level of a volume percentage of 1, but the lack of well-separated peaks in the powder diffraction patterns imply that, e.g. quantification of ZnS is not possible [22].

- *X-ray nanoprobe* and forward scattering ptychography methods relying on the use of a synchrotron can reveal the local elemental composition in 3D [23] but does not provide structural information. Moreover, sample must be quite small (<10 μm), and dynamics studies representing bulk conditions are, therefore, excluded.

- *Spectroscopic methods* like X-ray Fluorescence Spectroscopy (XRF), X-ray Absorption Near-Edge Structure analysis (XANES) [24] can reveal the elemental composition but does not reveal anything about the microstructure of the film.

In this paper, we propose three-dimensional X-ray diffraction (3DXRD) as a tool for studying the microstructure and local stress in the photovoltaic polycrystalline films. This non-destructive technique combines highly penetrating hard X-rays from a synchrotron source and the application of 'tomographic' approach to the acquisition of diffraction data [25]-[35]. For grains with a known phase and sizes larger than a few micrometers, 3DXRD can generate 3D maps of several thousands of grains, revealing their shape, orientation, and type II stress (as averaged over each grain) and their variation with time [19]. For grains with a size in the 0.1-1 μm range – as is typical for photovoltaic polycrystals – shape information is not available, but one can still determine the position, size, orientation, and strains of each grain as a function of time, and thereby generate statistics on the dynamics at the grain scale [27], [32]-[35].

However, the application of standard 3DXRD software to thin-film solar cells is hampered by the complication of phase identification. In principle, a standard single crystal crystallographic analysis can be applied to each grain, a method known as multigrain crystallography [29], [36]. Here we present an approach where a priori information about the photovoltaic materials is used to facilitate the generation of comprehensive statistics of phase, grain size, strain, and twinning relations by standard 3DXRD software. We discuss the importance of such data for R&D in photovoltaics and outline how this work can be generalized to the generation of 3D in situ movies of the microstructure.

The method will be presented with reference to and demonstrated on a specific example: a CZTS (kesterite) solar cell device. We examine the crystallographic properties of this semiconductor on the grain level and the mechanical deformation in the film that the experimental data reveal. Moreover, we present approaches to get around the crystallographic challenges that this absorber layer imposes in order to identify and quantify secondary phases, stress values, and twin boundaries in the material. In our view, other chalcogenide thin-film systems such as CIGS and CdTe could also benefit from this type of 3DXRD analysis gathering statistical information about the absorber film microstructure buried in the multilayer device structure.

In the first part of this study, we present the crystallography related to the CZTS absorber layer and the challenges of identifying the secondary phases. Next, we introduce the principles of the 3DXRD technique within the context of the absorber layer microstructure and present an appropriate data analysis pipeline. Subsequently, we present an experimental 3DXRD study of CZTS including the sample details, and the results. In the final part, we discuss the connection of the results to photovoltaics properties and how recent developments of 3DXRD can advance the characterization of thin films even further.

3 Crystallographic aspects of kesterite

First, we must distinguish between kesterite and disordered kesterite, the latter the most frequently observed structures for CZTS. X-ray and Neutron studies have demonstrated that the quaternary compound CZTS, crystallizes in the kesterite structure (I-4) [37], [38]. The "disordered" kesterite structure associated with space group (I-42m) was first observed by *Schorr* [39]. In this phase Cu and Zn cations intermix in the Cu-Zn layers (z=1/4, 3/4) of stoichiometric CZTS [39], see Figure1 a. The critical temperature for the phase transition from the ordered to disordered kesterite is reported to be in the range T_c = 480-560 K [18], [40], [41]. These temperatures are all below the annealing treatments under which CZTS is usually grown (720-830 K). Therefore, disordered kesterite will form initially, and ordering among Cu and Zn can only be controlled during the cooling process.

Moreover, CZTS films are grown in Cu-poor, Zn-rich conditions to obtain high-efficiency devices [42], [43]. The off-stoichiometric CZTS maintains the kesterite-type structure with variations in the lattice parameters due to the altering composition and the cation disorder [44]. The pure-phase kesterite phase only exists in a narrow area of the ZnS-CuS_2-SnS_2 phase diagram [45], [46]. Thus, secondary phases tend to form in the off-stoichiometric films, for instance, ZnS with a face-centered cubic crystal structure (F-43m), Figure 1 b). The two structures are closely related: doubling the a, b, or c axis of the cubic structure of the ZnS yields a unit cell corresponding to kesterite and with nearly identical lattice parameters, see Table 1.

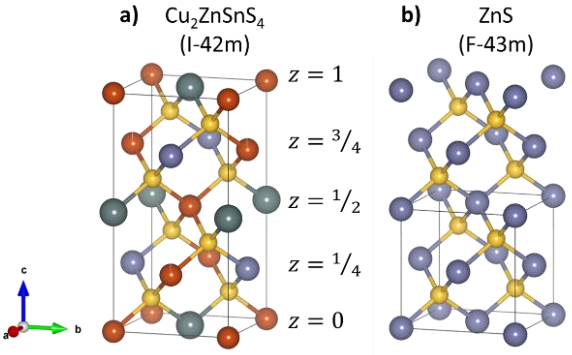

Figure 1. a) Kesterite crystal structure. b) Sphalerite crystal structure (two unit cells are depicted, only one is marked). (orange: Cu, lilla: Zn, gray: Sn, yellow: S). The crystal structures were drawn with the VESTA computer program [47].

Table 1. Lattice parameters of ZnS and CZTS.

Phase	Space group	Unit cell parameters	ICSD No.	Reference
ZnS	F-43m	a, b, c = 5.4340 Å α, β, γ = 90º	77090	[48]
		a, b, c = 5.4032 Å α, β, γ = 90º	230703	[49]
Cu_2ZnSnS_4	I-4	a, b= 5.4337 Å c= 10.8392 Å α, β, γ = 90º	239674	[18]
	I-42m	a, b= 5.4326 Å c= 10.8445 Å α, β, γ = 90º	239684	

4 3DXRD methodology

4.1 3DXRD geometry and formalism

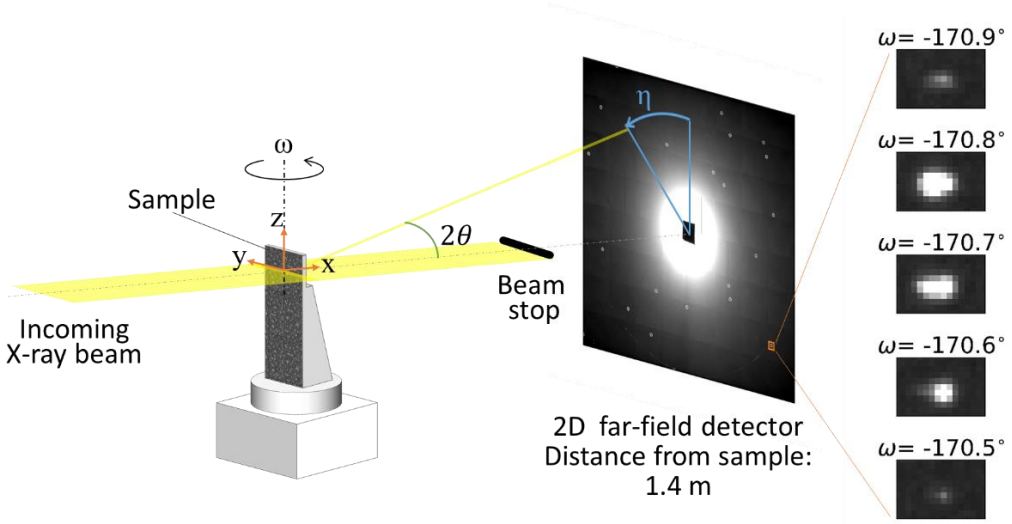

Figure 2. Sketch of the 3DXRD experimental geometry. The laboratory coordinate system is defined. The diffracted beam for a reflection from some grain is characterized by the rotation angle ω, the Bragg diffraction angle θ, and the azimuthal angle η. The evolution of a diffraction spot associated with a given grain reflection, framed in an orange box on the detector, is shown as function of ω: it appears at -170.9° and disappears at -170.5°.

3DXRD is a well-established tool for non-destructive characterization of grains in 3D. Based on the use of a monochromatic beam from a synchrotron source, the experimental geometry is sketched in Figure 2. Similar to the rotation method, diffraction images are acquired while rotating the sample around an axis (ω) perpendicular to the incoming beam. It images the intensity of the diffraction spots originating from the individual grains. Figures 2 displays a stack of recorded diffraction images for a small rotation range, showing the evolution of the intensity

within a region of interest comprising the diffraction spot from one reflection. Typically, a focused line beam is used, thereby characterizing one slice in the sample. To provide 3D information, the sample is then and translated along z, and the data acquisition is repeated. In this way, one characterizes multiple slices that correspond to consecutive z-positions in the sample. In the far-field version of 3DXRD, which is of interest here, the sample-detector distance is relatively large (tens of centimeters to meters), and the size of the detector pixels (a few hundred μm) similar to the size of the sample. This geometry is optimized for high angular resolution.

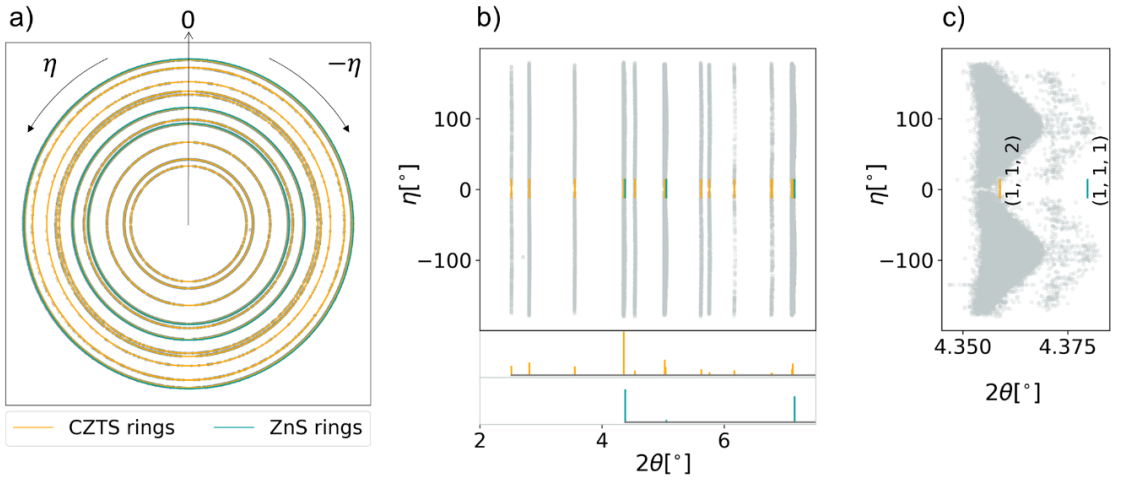

Figure 3 a) Plot of the position of the diffraction spots on the detector (sum over all ω) and b) corresponding plot of the azimuthal angle, η, vs. the two-theta angle (2θ) of the diffraction spots. In both cases the lines related to the two phases CZTS and ZnS are identified. c) Zoom in on the overlapping CZTS (112) ring and the ZnS (111) ring.

For the relation between experimental observables (position of diffraction peaks on the detector and corresponding rotation angle ω) and reciprocal space, we shall follow the FABLE conventions [50]. Figure 3 shows a plot of the position of all the harvested reflections from all the slices and their azimuthal angle η, according to the FABLE protocols. Let Gl be the reciprocal lattice vector corresponding to lattice planes (h,k,l) in a particular grain of interest, as defined in the laboratory system (see Figure 2). Let Gs be the same diffraction vector defined in the sample system – fixed with respect to the sample. The diffraction condition is fulfilled when

$$\vec{G}_l = \boldsymbol{\Omega}\vec{G}_s = \boldsymbol{\Omega U B}\begin{pmatrix} h \\ k \\ l \end{pmatrix} = \left|\vec{G}\right|\begin{pmatrix} -sin(\theta) \\ -cos(\theta)\,sin(\eta) \\ cos(\theta)\,cos(\eta) \end{pmatrix}. \qquad (1)$$

Here **Ω** is the rotation matrix corresponding to rotation around the ω-axis, **U** is a matrix representing the orientation of a grain of interest, (θ, η) are polar coordinates characterizing the direction of the diffracted beam, see Figure 2, and $\left|\vec{G}\right| = \frac{2\sin(\theta)}{\lambda} = \frac{1}{d}$ is given from Bragg's law,

with d representing the spacing between crystallographic planes. **B** is a matrix that comprises information about the unit cell as expressed by reciprocal lattice constants (a*,b*,c*, α^*, β^*, γ^*):

$$\boldsymbol{B} = \begin{pmatrix} \boldsymbol{a^*} & \boldsymbol{b^* cos(\gamma^*)} & \boldsymbol{c^* cos(\beta^*)} \\ \mathbf{0} & \boldsymbol{b^* sin(\gamma^*)} & \boldsymbol{-c^* sin(\beta^*) cos(\alpha)} \\ \mathbf{0} & \mathbf{0} & \boldsymbol{c^* sin(\beta^*) sin(\alpha)} \end{pmatrix} \text{ with } \boldsymbol{cos(\alpha)} = \frac{\boldsymbol{cos(\beta^*)\, cos(\gamma^*) - cos(\alpha^*)}}{\boldsymbol{sin(\beta^*) sin(\gamma^*)}}. \quad (2)$$

As usual in crystallography, the matrix $\mathbf{A} = (\mathbf{B}^{-1})^T$, where $(\ldots)^T$ symbolizes transposing, comprises the corresponding information about the direct space unit cell of the grain of interest, expressed by the direct space lattice constants (a, b, c, α, β, γ). Notably, the matrix inverse of $(\mathbf{UB})^{-1}$ gives the real space unit cell vectors $(\vec{a}, \vec{b}, \vec{c})$ of the grain in the sample frame.

The grain elastic strain can be expressed in terms of the unit cell of a reference (unstrained) crystal $\mathbf{A}_0$ and a strained crystal **A**. We determine the deformation gradient tensor of the grain as:

$$\boldsymbol{F^g = A A_0^{-1} = (B_0 B^{-1})^T}. \quad (3)$$

For the small strain levels of relevance to this study and in the absence of rotation, the infinitesimal strain tensor **ε** is applicable and is, by definition, given by the symmetric tensor

$$\varepsilon_{ij} = \frac{1}{2}\left(F^g{}_{ij} + F^g{}_{ji}\right) - I_{ij} \quad (4)$$

where **I** is the identity matrix. Ultimately the strain is transformed in the sample coordinate system by applying the orientation of the grain:

$$\boldsymbol{\varepsilon_{sample} = U \cdot \varepsilon_{grain} \cdot U^T} \quad (5)$$

4.2 Conventional 3DXRD data analysis and its relation to polycrystalline photovoltaic materials

3DXRD methods are usually applied to studies of polycrystalline materials. It requires knowing the space group and unit cell lattice parameters for the unstrained material (that is, with a known matrix $\mathbf{B}_0$). The position of diffraction spots on the detector are given by the grain orientation with only small perturbations due to strain. In this case, one may initially assume that all grains are associated with the undistorted matrix $\mathbf{B}_0$. The process of identifying grains, multigrain indexing, then becomes a question of identifying orientations, **U**, that complies with Eq. (1), for a set of known (h,k,l) indices. As a result, the reflections determined are sorted into groups, where each group represents one grain. The main limitation is the overlap of diffraction spots. For inorganic materials exhibiting weak textures, up to around 3000 grains can be indexed [28] from a single rotation scan. Our approach is to utilize a line beam that limits the number of simultaneously illuminated grains to avoid spot overlaps.

Following this indexing step, all the tools of single-crystal crystallography can be applied to each grain. The relative grain volume can be estimated from the integrated intensities of the assigned reflections. A least-square fit can be performed to determine all nine **U** and **B** components, by

minimizing the angular distance between the predicted reflections, cf. Eq. (1), and the experimentally determined ones. Next the strain tensor can be determined from $\underline{\mathbf{B}}$ by Eqs. (3)-(4), where the grain unit cell, determined during indexing, is compared to an unstrained reference $\mathbf{B_0}$ [26]. When required, crystal structure refinement can also be used to optimize the position of the atoms within the unit cell – with a quality in the results that can match that of refinement based on single-crystal diffraction [51], [28].

In principle, the 3DXRD formalism, as expressed by Eq. (1), allows for indexing without any *prior* information by operating in the 9D space, spanned by **U** and **B**. In this way, 3DXRD could handle any number of arbitrary unknown phases, strained or unstrained. However, brute force procedures are too slow to be operational. A general-purpose method involving searching only in 3D has been suggested [36], but this algorithm still lacks a sufficiently robust software implementation. In this work, phase identification from a database search could provide sufficiently accurate for the unit cell parameters of the phases in the sample.

The polycrystalline photovoltaic materials, and particularly the kesterite solar cell, pose a special challenge as several complications are present simultaneously:

- Several phases are present, and some might not be known *a priori*.
- Some phases may exhibit a doubling of the unit cell in one direction, and their lattice parameters give rise to 2θ-angles that are nearly indistinguishable.
- Twins may appear, leading to a large fraction of reflections being shared by more than one grain.
- The specimens are subject to mechanical stress, originating in the thin film preparation.
- The grains are sub-micron in size leading to signal to noise ratios (S/N) in the diffraction data.

These CZTS data comprise additional information, as the doubling of a unit cell leads to superstructure peaks. These may, however, be weak, and spurious peaks from other phases can cause unexpected overlaps.

In the following, we present an approach that overcomes these challenges and generates a list of grains. Each grain is associated with an orientation, a size, and a phase related to a unit cell. The unit cell parameters represent a strained state, caused by stoichiometry changes and an externally imposed mechanical strain. We demonstrate how to calculate an overall strain for the film and subtract it from the oriented unit cells of the grains.

In section 4.3, we present our approach to indexing the grains and identifying their unstrained unit cells. Section 4.4 describes how to exploit the results for the statistical description of phases, grains size distributions, stresses, and texture with a special focus on potential twin relations.

In an initial exploratory phase, we discovered that a data analysis based on the existence of two phases, a cubic and a tetragonal, was consistent with the data. Figure 3b displays the lines associated with the cubic and tetragonal phases. Hence, we shall assume two phases in the following.

4.3 Identifying grains and their crystal structure.

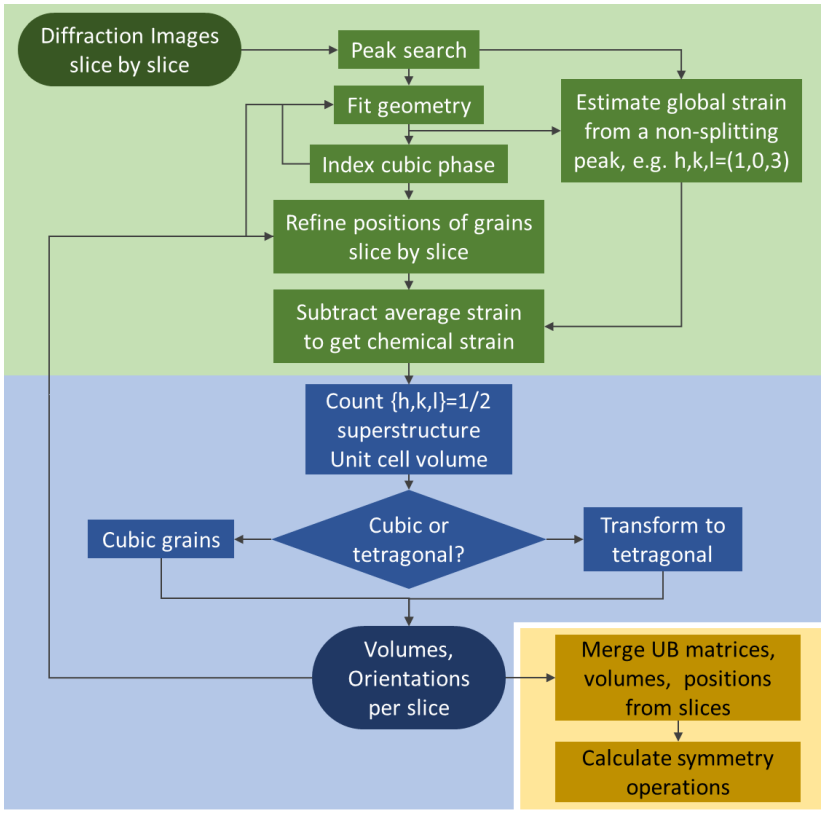

Figure 4. Flow diagram of the data analysis pipeline for indexing grains and identifying their unstrained unit cells.

The data analysis pipeline used is sketched in Figure 4. It is structured in three parts. Its implementation is based on existing 3DXRD software, throughout, primarily the ImageD11 software [52].

In the first part, the experimental data from different slices of the sample (different z-positions) are analyzed independently. For each slice, initially, a background is subtracted from the raw images, and the diffraction spots are identified ("peak search"). Based on the statistics of these reflections, several global parameters related to the experimental setup are refined, including wavelength, sample-to-detector distance, and tilts of the detector. We assume all grains belong to the same phase with a cubic symmetry and an "average" lattice constant, a_0^*, corresponding to a common $\mathbf{B}_0 = a_0^* \mathbf{I}$. Excluding superstructure peaks and using only diffraction spots positioned at 2θ angles, corresponding to the cubic phase (the three green lines marked in Figure 3b), grains are found by the classical monophase 3DXRD indexing program ImageD11. The result is a list of grains, each with an associated $(\mathbf{UB})^{-1}$ matrix and a list of reflections.

Next, we assume that the mechanical stress gives rise to comparable strains in the grains if asserted in the sample coordinate system. The grain strain can then be expressed in terms of an

"average" contribution and a residual that is specific to the grain. The average strain tensor of the film may be determined in several ways. The approach used here is to focus on the diffraction spots belonging to a specific (hkl) family. For each diffraction spot, *i*, we can determine the shift in 2θ position, $\Delta 2\theta^i_{hkl}$. The corresponding normalized scattering vector in the sample system is $\vec{n}_i = \overrightarrow{G_s{}^i}/|G_s|$. From the differentiation of Bragg's law, the 2θ shift corresponds to an axial strain (a strain in the direction $\vec{n}_i$) of

$$\varepsilon^i{}_{hkl} = \frac{\Delta d_{hkl}}{d^0{}_{hkl}} = -\Delta\theta^i_{hkl}\, cot\, \theta^0{}_{hkl} \tag{6}$$

Here $2\theta^0{}_{\mathrm{hkl}}$ is the average two-theta angle of the (hkl) Debye-Scherrer ring. By definition,

$$\varepsilon^i{}_{hkl} = \begin{pmatrix} n^i_x & n^i_y & n^i_z \end{pmatrix} \begin{pmatrix} \varepsilon_{11} & \varepsilon_{12} & \varepsilon_{13} \\ \varepsilon_{12} & \varepsilon_{22} & \varepsilon_{23} \\ \varepsilon_{13} & \varepsilon_{23} & \varepsilon_{33} \end{pmatrix} \begin{pmatrix} n^i_x \\ n^i_y \\ n^i_z \end{pmatrix}. \tag{7}$$

From this follows that the average strain tensor elements for the hkl ring, ε_{ij}, can be determined by a linear least-squares fit of experimental data to Eqs. (6) and (7). Let the resulting matrix be $\boldsymbol{\varepsilon}^{\mathrm{mat}}$. Subsequently, for each grain, $\boldsymbol{\varepsilon}^{\mathrm{mat}}$ is subtracted to correct the unit cell parameters and obtain the "strain-free" lattice parameters.

$$(\boldsymbol{UB})_0 = (\boldsymbol{I} + \boldsymbol{\varepsilon}^{mat}) \cdot \boldsymbol{UB} \tag{8}$$

Next, the grain strain tensor is calculated applying Eq. (4) and the obtained "strain-free" unit cell as the unstrained reference. Then, we calculate the stress tensor using Hook's law

$$\sigma_{ij} = C_{ijkl}\varepsilon_{hkl}. \tag{9}$$

Subsequently, the stress in the film is obtained by transforming the grain into the sample reference system.

$$\boldsymbol{\sigma}_{sample} = \boldsymbol{U} \cdot \boldsymbol{\sigma}_{grain} \cdot \boldsymbol{U}^T \tag{10}$$

From here on, we will adopt Voigt's notation to simplify the index of the tensor components, where index ij=[11 22 33 23 13 12] becomes i=[1 2 3 4 5 6]. We have chosen the elastic constants given in [17] because the converged lattice parameters agree with our experimental data. Other calculations report similar numbers [16], [53]-[56].

In the second part, the superstructure peaks are taken into consideration. These appear at positions in the reciprocal space that corresponds to a doubling of the direct space unit cell. To study this systematically, for each grain, we form the supercell $(2\vec{a}, 2\vec{b}, 2\vec{c})$ in direct space, a doubling in all directions of the unit cell $(\vec{a}, \vec{b}, \vec{c})$. The reciprocal space unit cell is correspondingly halved in all directions. A search is now performed within the full set of reflections from the original peak search of reflections positioned at the nodal points of the supercell. The reflections appearing with an odd number in any of the three directions are "superstructure peaks"; they do not belong

to the original cell. Searching for grains with a double unit cell in the $\vec{a}$ direction, the number of reflections appearing at (h, 2k, 2l) with h odd is compared to the number of reflections assigned to the supercell. If the ratio is above a certain threshold, defined by S/N and spurious background, the grain is defined to have a double cell with the preferred axis along $\vec{a}$. Likewise, searches are performed on unit cells that are doubled along $\vec{b}$ or $\vec{c}$. It is generally observed that the shortest unit cell lattice and the axis with odd reflections coincide. No occurrence is found of cells being doubled in more than one direction.

Figure 5 shows a plot of the ratio of the number of superstructure diffraction spots to the total number of diffraction spots for a given grain as a function of the derived grain volume. For large grains, most the weak diffraction spots at low scattering angles from the superstructure are recorded. Hence, it is straightforward to classify a grain as tetragonal or cubic based on the existence of superstructure peaks. As expected, with a decreasing grain volume, more of the superstructure peaks become too faint to be recorded. For relatively small grains with few or no superstructure reflections, the distinction between tetragonal or cubic was therefore based on the unit cell geometry. This classification scheme turns out to be very robust.

For grains that are classified as tetragonal, the shortest axis is doubled. Moreover, the unit cell axes were permuted, such that this short axis becomes the $\vec{c}$-axis.

The (illuminated) volume of the grain, assuming proportionality of the volume with the reflection intensities, is given by Eq. (11), where $\sum \bar{I}_g$ is the sum of the average intensities of all indexed grains, and V_{sample} is the illuminated sample volume.

$$V_{grain} = \frac{\bar{I}_{grain}}{\sum \bar{I}_g} \times V_{sample} \tag{11}$$

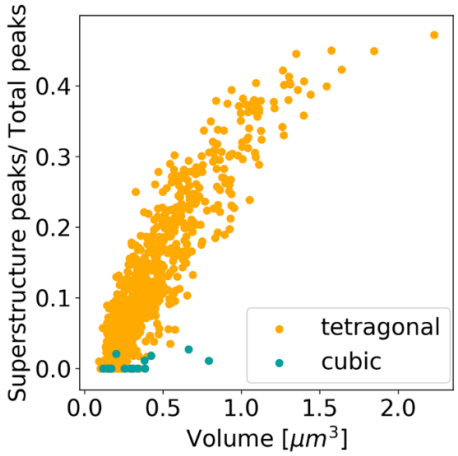

Figure 5. The ratio of the superstructure peaks to the total number of peaks for a given grain is compared to the grain volume.

In the third part of the flow diagram, the slices are combined. Grains in neighboring slices with a similar $(\mathbf{UB})^{-1}$ within given tolerances are considered identical. For these, the weighted average

of $(\mathbf{UB})^{-1}$ by the integrated intensities is determined. Moreover, the (sub) volumes determined in the different slices are added. Following this, for each grain, a final optimization step is performed. Here all parameters in $(\mathbf{UB})^{-1}$ and the 3D center-of-mass position of the grain (which will cause minor translations of diffraction peaks not described by Eq. 1) are refined.

The result of the data analysis is, therefore, a division of the grains into two "phases": one with no cell doubling and with a unit cell that is close to cubic, and another with a unit cell that is close to a tetragonal unit cell with unit cell parameters (a, a, 2a, 90°, 90°, 90°). We shall term these the "cubic" phase associated with ZnS and the "tetragonal phase" associated with CZTS. Each grain is associated with an orientation, **U**, a **B** matrix, a center-of-mass position, and a list of reflections. Moreover, we have determined the average strain tensor within the (illuminated part of the) sample.

4.4 Statistics on the structural and mechanical properties of the grain ensemble

As already stated, once the grains have been identified, their properties can be subject to statistical analysis for understanding both average properties and the heterogeneity within the sample. The local texture (within the volume studied) can be derived from the grain orientations. The grain sizes and their distribution can be determined from the integrated intensities. Strain components and their distributions can be derived via Eqs. (3)-(4), changes in stoichiometry may be inferred directly from changes in unit cell parameters.

The spatial resolution of far-field 3DXRD did not allow us to identify neighboring grains, and therefore their misorientation angle is not accessible. But *twins* can be identified from angular relationships. In practice, reflections can be shared among grains because of coincidental overlap or due to the presence of twin relationships between grains, so thresholds must be introduced in the data analysis. Notably, twin relationships may also exist between the tetragonal and the cubic phase.

We calculate the number of shared reflections between grains by computing the scattering vectors of each grain to look for overlapping of Bragg peaks. Using equation (1), the error of the computed hkl should be below ~0.02 to be considered as part of the grain. We confirm the twin relation among pairs with 30% of reflections overlapping, if the pair has a certain misorientation angle associated to a symmetry operation.

When comparing a pair of grains, we compute a natural lattice mismatch via the deformation gradient tensor $\boldsymbol{F}$. Based on Eq. (3), here we utilize the reciprocal lattice of a grain $(\boldsymbol{UB})_n$, considered as the reference lattice that has been deformed by the inverse transpose of $\boldsymbol{F}$ when compared to grain m, whose reciprocal lattice is $(\boldsymbol{UB})_m$.

$$\boldsymbol{F} = (\boldsymbol{UB})_m{}^{-T} \cdot (\boldsymbol{UB})_n{}^{T} \tag{12}$$

Following conventions in the field of continuum mechanics, we perform a polar decomposition of $\boldsymbol{F}$ to produce a pure rotation $\boldsymbol{R}$ and a pure stretch tensor $\boldsymbol{U}_s$, the right stretch tensor (not to be confused with **U**-rotation matrix in 3DXRD)

$$\boldsymbol{F} = \boldsymbol{R} \cdot \boldsymbol{U}_s \tag{13}$$

Next we calculate the Biot strain tensor Eq. (14), which is equivalent to the infinitesimal strain tensor in the absence of rotations. The overall strain magnitude is given by the Euclidean norm of the Biot strain tensor $\|E\|$.

$$\boldsymbol{E} = \boldsymbol{U}_s - \boldsymbol{I} \tag{14}$$

This rotation matrix $\boldsymbol{R}$, is used to determine the angle and axis of rotation between the two grains being compared. The equivalent symmetry operations are applied to the reference grain, calculating the strain magnitude. The symmetry transformation with the lowest strain value describes the misorientation angle between two grains, where the lattices are also well matched. For the tetragonal structure, eight transformations are possible, whereas the cubic structure allows 24.

5 Experimental

5.1 Sample description and preparation

The investigated kesterite solar cell architecture consists of a stack of layers deposited on a molybdenum coated soda-lime glass substrate (Mo-SLG). The CZTS absorber layer is fabricated by pulsed laser deposition (PLD) and annealed in a high-temperature sulfurized atmosphere to form the polycrystalline kesterite film (~400 nm thick). The subsequent coatings are a CdS buffer layer (60 nm), an intrinsic ZnO window layer (50 nm), an Indium Tin Oxide (ITO) contact layer (200 nm), and an MgF2 anti-reflection coating (100 nm). The fabrication details can be found in [57].

We cut a 40 (W) x 300 (H) µm2 piece of the solar cell, as shown schematically in Figure 6a. To maximize the signal to noise ratio of the diffracted intensity originating from the 1 µm sized grains, we reduced the 1 mm thickness of the Mo-SLG by mechanical polishing and milling by a focused ion beam (FIB) down to 4 µm thickness (see Figure 6b).

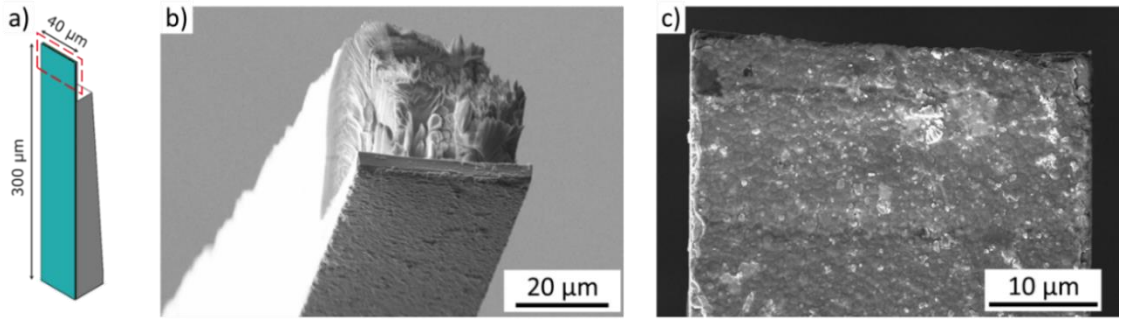

Figure 6. a) Dimensions of the cut piece of the kesterite CZTS solar cell. The red box is where the scans of the slices are measured. b) SEM image of the tip of the sample. c) Front view of the solar cell.

5.2 3DXRD experiment

The experiment was carried out at the Advanced Photon Source synchrotron at the 1-ID beamline. A monochromatic X-ray beam (52 keV) focused to a size of 1.5 µm (FWHM) (V) x 200 µm (H)

illuminated the solar cell parallel to its normal plane. The range of oscillation was ω ϵ [-180°, 180°] with a step size of Δω=0.1°. A GE Revolution 41RT flat-panel detector (2048 x 2048 pixels, 200 µm pixel pitch) recorded the diffraction images. The acquisition time per slice was about 1.4 hours with 1.2 s per frame. The translation step along the z-axis was 1 µm, capturing an overlap of 0.5 µm between slices. A standard LaB_6 powder (NIST SRM 660c) was used for the initial calibration of the geometry of the set-up.

6 Results

Following the procedure outlined above, a total of 597 grains were identified, 582 tetragonal and 15 cubic. As a figure-of-merit we note that 33% of the diffraction spots identified by the peak search were assigned to these grains. It is possible to identify more grains, but they will be associated with larger errors.

6.1 Averaged strain and stress in the sample and the grains.

Shown in Figure 7a is the variation of the 2θ angle with the azimuthal angle, η, and with the rotation angle, ω, for all reflections in the (103) lattice plane. We define the reference angle $2\theta^0{}_{103}$ as the average angle. There is a systematic displacement of the 2θ angle with both η and ω, which we attribute to an external stress field. Hence, we can determine a strain tensor, corresponding to this external stress, using the fitting procedure formulated in Eqs. (6)-(7).

The average strain tensor elements for each of the 7 slices obtained by this least-square approximation are listed in Table 2. By subtracting the strain in the tetragonal and cubic grains, we can observe the improvement of the lattice parameters in both phases, as the distributions of the corrected lattice parameters become narrower (see Figure 7b, c).

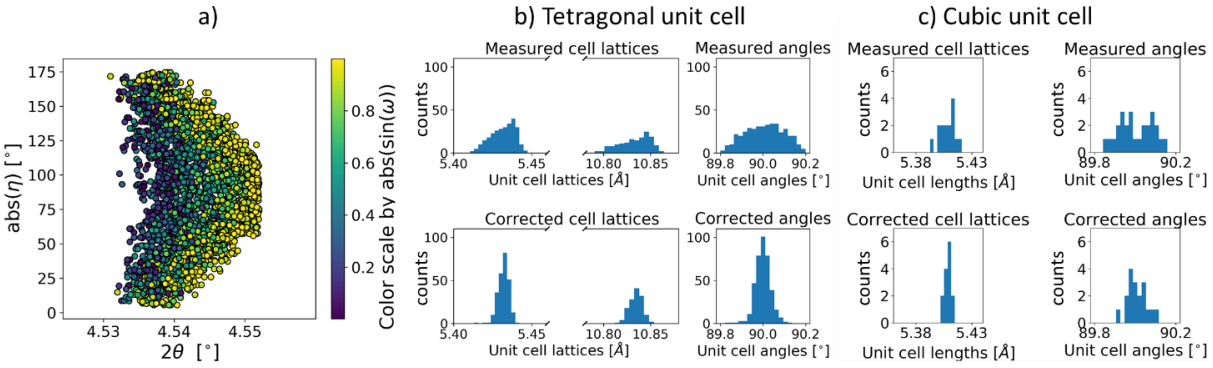

Figure 7. a) Absolute azimuthal angle vs. 2θ angle of the diffraction spots in the (103) plane; the colors symbolize the corresponding ω-position. b) Distribution of lattice parameters for the tetragonal grains; c) Distribution of lattice parameters for the cubic grains. In both b) and c) the term the "measured" denotes the original data while the term "corrected" are the results after subtracting the effect of an external stress acting on the film.

Subsequently, for each grain we can derive its strain tensor elements using the corrected unit cells as the reference unstrained state and Eqs. (3)-(4). Figure 8a defines the elements of the strain tensor in the tetragonal crystal structure. The normal strains directions of ε_1, ε_2, ε_3 are

perpendicular to the (100), (010), (001) planes, whereas the shear strains ε_4, ε_5, and ε_6 are coplanar to the planes where the normal strain is applied. The shear strains are in equilibrium, implying that ε_4: $\varepsilon_{23}= \varepsilon_{32}$, ε_5: $\varepsilon_{13}=\varepsilon_{31}$, ε_6: $\varepsilon_{12}= \varepsilon_{21}$, and therefore they appear in two planes. Figure 8b shows the resulting correlation between the normal strain components ε_1 and ε_3. We observe the typical behavior of a deformed object where an increasing strain along the a-lattice will result in a decreasing strain along the c-lattice. The slope is determined to be -0.83 by a linear fit to the data. However, we also note a substantial scatter in these data, caused by grain-grain interactions.

Next, we use Eq. (9) and the corresponding elastic constants to calculate the stress components for each grain. Histograms of these components are shown in Fig 8c for the tetragonal phase. The normal stress along the a-direction σ_1 has a slightly right-skewed distribution suggesting predominant compressive stresses, whereas the normal stresses along b (σ_2) and c (σ_3) directions have left-skewed distributions that correspond to tensile stresses. The shear stress σ_4 has an almost normal distribution, whereas σ_5 has a bimodal distribution, and σ_6 a left-skewed one.

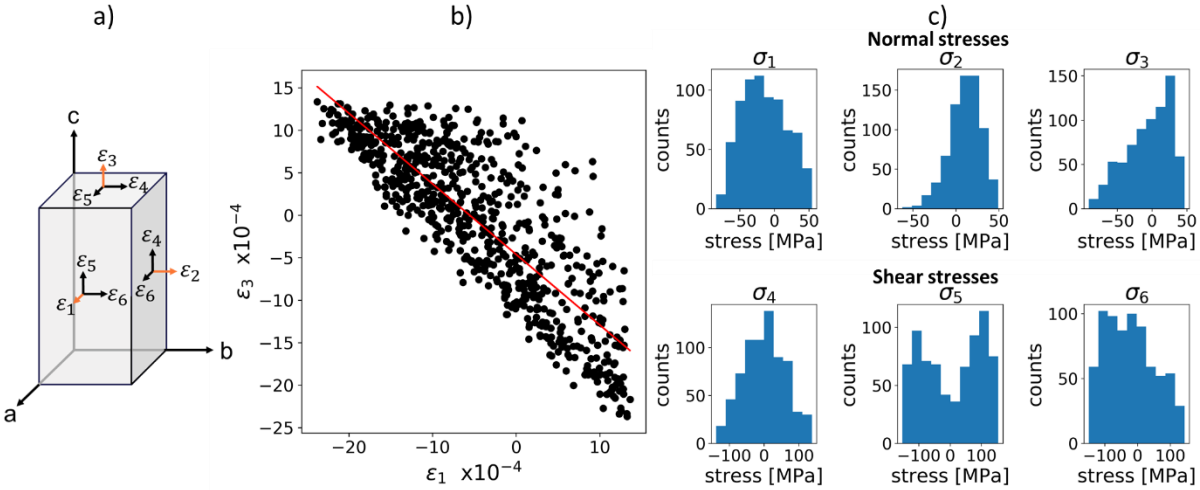

Figure 8. a) Definition of strain components within the tetragonal grain unit cell. b) Plot of the normal strain ε_3 vs. ε_1 with a best fit to a linear regression. c) Histograms of the corresponding stress components in the grain unit cell. All the retrieved tetragonal grains are represented in b and c.

We can now calculate the macroscopic stresses in the sample by averaging over the grains while taking into consideration their orientation. The results are listed for each slice in Table 3 and displayed in Figure 9a. We visualize the normal stresses σ_1, σ_2, and σ_3 along the x-, y-, and z-axes correspondingly. The shear stresses are coplanar to the planes where the normal stresses are applied. Similar to the strain depiction, the shear stresses appear in two planes as they are in equilibrium, meaning that σ_4: $\sigma_{23}=\sigma_{32}$, σ_5: $\sigma_{13}=\sigma_{31}$, and σ_6: $\sigma_{12}= \sigma_{21}$.

The film shows a compressive strain in the normal direction of the film plane that corresponds to an averaged compressive stress of -144.7 MPa. The corresponding tensile strain within the film plane results in an average stress of 53.6 MPa along the y-axis and 81.9 MPa along the z-axis (Figure 9). The shear strains ε_4 and ε_5 are zero within experimental error. On the other hand, the

non-zero component $\varepsilon_{6,}$ coplanar to the (xz)- and the (yz)-planes, is associated with a compressive shear stress σ_6 = -38.1 MPa. This can be explained by a misalignment of the sample in the diffractometer.

Table 2. The ε^{mat} strain tensor components per slice for the tetragonal phase obtained from the 2θ angle displacements (Eq. (7)).

Strain component	Slice 1 Value $[\times 10^{-4}]$	Slice 2 Value $[\times 10^{-4}]$	Slice 3 Value $[\times 10^{-4}]$	Slice 4 Value $[\times 10^{-4}]$	Slice 5 Value $[\times 10^{-4}]$	Slice 6 Value $[\times 10^{-4}]$	Slice 7 Value $[\times 10^{-4}]$	Average Strain $[\times 10^{-4}]$
ε_1	-19.1	-20.5	-20.8	-22.1	-22.2	-22.5	-21.0	-21.2
ε_2	8.4	9.6	8.0	8.6	8.5	7.3	7.7	8.3
ε_3	10.5	11.7	13.1	11.8	12.8	13.3	13.7	12.4
ε_4	-0.3	-0.3	-0.3	-0.4	-0.2	0.4	0.4	-0.1
ε_5	-0.8	0.8	1.3	1.1	1.4	-0.0	0.4	0.6
ε_6	-5.6	-5.5	-4.9	-5.2	-5.0	-6.3	-5.4	-5.4

Table 3. The average stress tensor components per slice obtained after calculating grain stresses (Eq.(10)).

Stress component	Slice 1 Value [MPa]	Slice 2 Value [MPa]	Slice 3 Value [MPa]	Slice 4 Value [MPa]	Slice 5 Value [MPa]	Slice 6 Value [MPa]	Slice 7 Value [MPa]	Average Stress [MPa]
σ_1	-132.5	-134.8	-138.0	-156.2	-151.6	-156.1	-144.0	-144.7
σ_2	54.1	68.2	54.8	50.2	52.2	38.9	57.0	53.6
σ_3	73.4	82.1	92.0	72.7	80.4	79.5	93.3	81.9
σ_4	-5.7	-4.4	-2.6	-3.2	-2.9	1.5	5.0	-1.8
σ_5	-4.5	7.4	7.6	6.0	6.7	1.9	4.1	4.2
σ_6	-39.1	-38.4	-37.4	-35.3	-34.0	-44.4	-38.4	-38.1

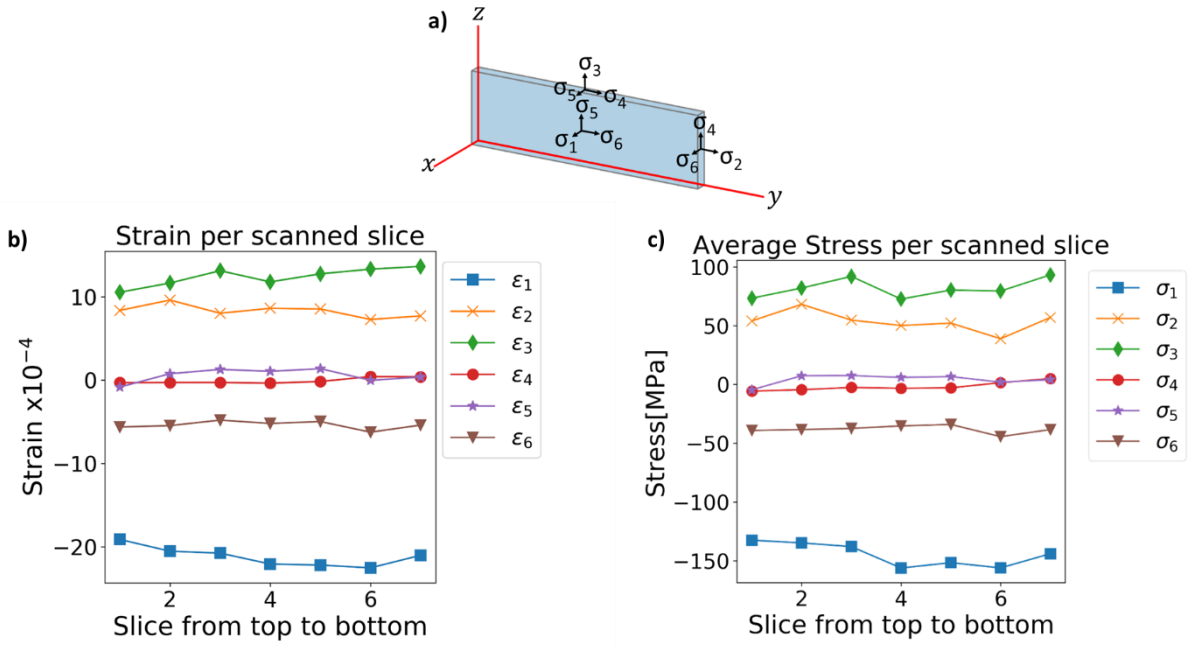

Figure 9. a) Definition of the stress components with reference to one of the measured slices. b) strain and c) stress components, per scanned slice from the tip of the CZTS solar cell (slice 1) downwards.

6.2 Grain size distribution and orientations

The grain volumes were derived using Eq. (11). The histogram for the tetragonal phase shown in Fig 10 a) and b) are consistent with a log-normal size distribution with a cut-off at lower radii due to thresholding of the intensities. The grain size is 0.32 ±0.26 μm^3, and the corresponding radius 0.47 ±0.18 μm (see Figure 10a, b). The radius is obtained assuming a cylindrical volume for the CZTS grain with a height of 0.45 μm, the film thickness. For the cubic grains, the grain statistics is scarce. The volume is 0.25 ±0.16 μm^3, Figure 10c), and the corresponding equivalent-sphere radius is 0.43 ±0.13 μm, (see Figure 10d).

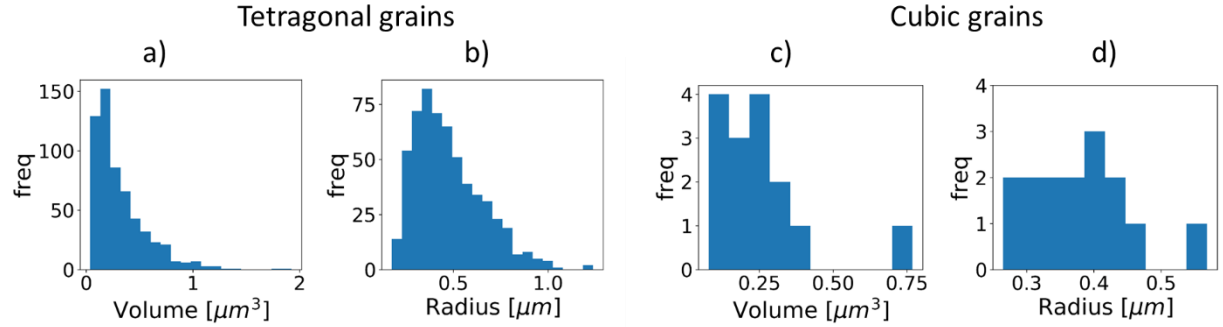

Figure 10. Histograms for the tetragonal grains: a) volume, b) radius. Histograms for the cubic grains: c) volume, d) radius.

The orientation distribution functions were computed using the MTEX MATLAB toolbox and a 5° resolution [58]. The pole figures of the tetragonal grains for the planes {100}, {110}, {001} and {112} are shown in Figure 11, with the yz-plane being the film plane on the diffractometer. The pole figures for the cubic grains are not shown because of poor grain statistics (15 grains).

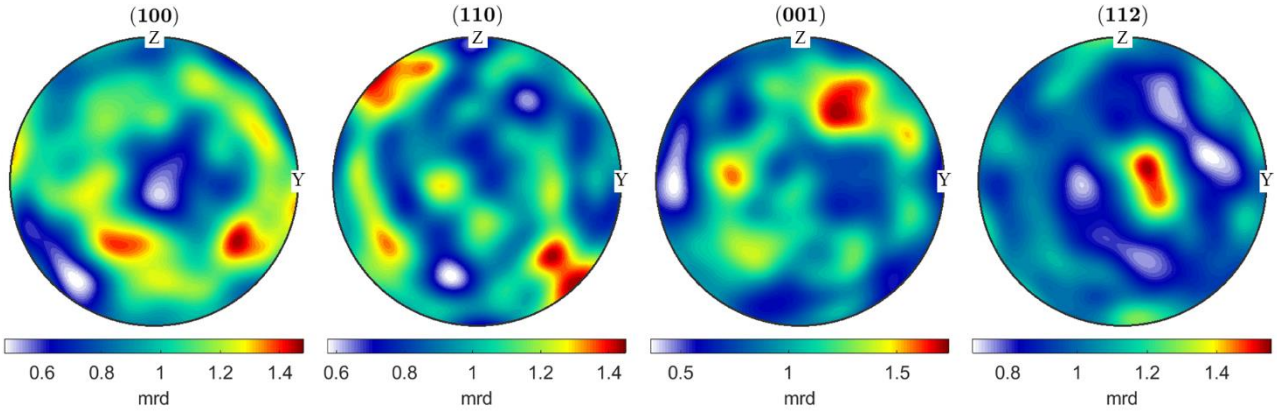

Figure 11. Pole figures of the tetragonal grains in multiples of random distribution (mrd).

6.3 Twin boundaries

Twin boundaries are often described with the quantity Σ, which is defined by the ratio between the area enclosed by a unit cell of the coincident lattice sites and the standard unit cell.

To identify twins among the tetragonal grains a search was performed for pairs of grains sharing 30% of the reflections or more. We find that the misorientation angles of these in all cases correspond to one of four values, corresponding to the symmetry operations with the minimum strain between the compared grains.

120 twin pairs were identified. Their resulting misorientation angles are shown in Figure 12a-d.The most frequent type of grain boundary is identified as Σ3, characterized by a rotation of 70.53° and the corresponding symmetrically equivalent misorientation angles 109.47°, 131.81°, and 180°. Σ3 boundaries are also detected by EBSD in chalcopyrite thin films [59]. Our measurements deviate from the mentioned angles due to the tetragonal distortion c/2a< 1 in the kesterite structure. We report the average rotation angles, the corresponding rotation axis and the transformed lattice plane in Table 4.

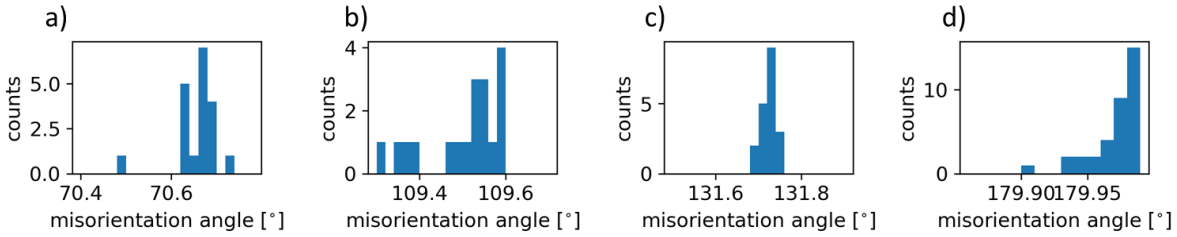

Figure 12. Distribution of the misorientation angles for pairs of CZTS grains sharing 30% of their reflections. These fall in four groups around a) 70.66°, b) 109.50°, c) 131.73°, and d)179.98°.

Table 4. Total counts of Σ3 boundaries according to the rotation angle

Rotation angle	Rotation axis	Transformed plane	No. twinned pairs	twinned grains/ total tetragonal grains × 100 [%]
70.65°	$<110>_{tetra}$	$\{110\}_{tetra}$	19	6.5
109.50°	$<110>_{tetra}$	$\{110\}_{tetra}$	4	1.4
	$<201>_{tetra}$	$\{102\}_{tetra}$	14	4.8
131.73°	$<401>_{tetra}$	$\{101\}_{tetra}$	19	6.5
179.98°	$<201>_{tetra}$	$\{112\}_{tetra}$	39	13.4
	$<111>_{tetra}$	$\{114\}_{tetra}$	25	8.6
		Total	120	41.2

Among the cubic grains, only one pair of twinned grains was found with a rotation of 180°-$<211>_{cubic}$ transforming the plane $(211)_{cubic}$. This transformation corresponds to a Σ3 twin boundary. The equivalent symmetric transformation is the Σ3 60°-$<111>_{cubic}$, typically found in the diamond-type structure [59].

Special orientation relationships between grains of the different phases were not considered.

7 Discussion

7.1 The kesterite solar cell

Identification of secondary phases. The 3DXRD analysis of the CZTS absorber layer revealed the presence of the ZnS phase representing 2.5% of the total number of grains in the film. This small amount of ZnS is not detrimental to CZTS devices. However, when present in large amounts, it can block the charge transport or increase the series resistance in the solar cell [60].

A similar value has been measured in a sputtered CZTS film with 3.1% of ZnS by X-ray absorption near-edge spectroscopy (XANES) at the sulfur K-edge [61]. A co-sputtered CZTS film, also measured by XANES, yielded 10.5% of ZnS [61]. These measurements are within the ZnS limit detection in XANES of 3% [24].

Film averaged stress. The stress and strain components vary slightly between slices with an average standard error of 2.23 MPa. These almost constant values are a testament to the robustness of the 3DXRD method.

Comparing to literature, Johnson *et al.* consider the formation of a biaxial tensile thermal stress at the Mo/CZTS interface during annealing as a result of the Mo deposition stress and the thermal expansion mismatch stresses [62]. In their study, wafer curvature measurements show compressive deposition stresses of about -400 MPa to -38MPa for optimized Mo sputtering deposition, and a compressive deposition stress of about -100 MPa for CZTS by co-sputtering. The normal tensile stresses over the PLD-CZTS film plane agree with the biaxial tensile stresses of the co-sputtered CZTS, although the compressive normal element and the shear components

are missing in their model. Moreover, our calculated stresses are in the same order of magnitude as their deposition stresses.

In addition to the thermal stresses inflicted during annealing, we can also consider the entangled combination of the chemical distortion caused by the off-stoichiometric composition of the film and the inflicted mechanical deformation through the cutting of the solar cell and the removal of the glass through mechanical polishing. Likewise, FIB etching could have introduced artifacts such as ion implantation and structural damage [63], [64]. Unfortunately, sample preparation is unavoidable as the 5 mm thick amorphous glass substrate causes a background that buries the signal of the grains.

Grain averaged stress and strain. At the grain level, the slope derived from linear fitting of the normal strain components ε_1 and ε_3 shown in Fig 8b, -0.83, is larger than the biaxial relaxation coefficient of -1.23 reported by Li *et al.* [16]. The forces along the c-axis are set to zero in their model, whereas our stress measurements have shown non-zero elements. The same study by Li *et al.* calculated an increase in the bandgap with the increase of compressive biaxial strain for ε_1 above -1.5% and a decrease for ε_1 below -1.5%. Our ε_1 strain values oscillate between compressive and tensile strain in a range of $[-25; 20]\times10^{-4}$, which implies that the bandgap is not homogeneous among the grains. The overall bandgap of the film is the result of contributions from all of these grain bandgaps. We also note that the strain is on the order of 10^{-4}, which agrees with the strains measured in $CuInSe_2$ thin-film solar cells [65].

Grain properties. The standard error of the grain variations in angle, length and volume among the measured tetragonal unit cell parameters is 0.008°, 8.8×10^{-4} Å, and 0.012 $Å^3$ respectively, demonstrating a high accuracy in the 3DXRD measurements.

The estimation of the grain size based on the intensities of the reflections agrees with the scale shown in the SEM image (Figure 6c). The grain volumes of CZTS grains are larger than those of the ZnS grains.

The main conclusion from the texture analysis is that the <112> poles are preferably aligned to the normal direction of the film, whereas a faint discontinuous ring in the same pole figure could indicate a weak fiber texture. Moreover, the poles <001> and <001> are almost aligned parallel to the surface of the film. This out-of-plane (112) fiber texture has also been observed in a co-sputtered CZTS film [66]. The link between this texture and efficiency is not clearly established, but many studies report the (112) preferred orientation in CZTS films deposited by PLD [67]. In CIGS films, a (200)/(204) preferred orientations yields higher efficiencies than CIGS films with (112) orientations [68].

Twin boundaries. The six variants of Σ3-type twin boundaries have also been observed with electron microscopy in CIGS, CGS, and CIS solar cells [59]. Σ3 boundaries have lower defect density compared to random grain boundaries according to electron-beam scattering diffraction (EBSD) and cathodoluminescence (CL) measurements [69].

The formation energies of Σ3 are low, and hence they are common in CZTS films. In our results, 41.2% of the total number of grains are Σ3 twins. The most frequent twin operation is the Σ3{112} that corresponds to the 180° around <221>. Characterization of grain Σ3 {112} twin

boundaries in CIGS has been done extensively, revealing a rather benign electronic behavior [69]. Additionally, the formation of Cu vacancies and In_{Ga} antisite defects in Σ3 {112} have been experimentally confirmed [70]. Similarly, one could expect the development of defects in CZTS Σ3{112} twin boundaries. In a theoretical study by Wong et al. [71], Σ3{112} grain boundaries are constructed with Zn_{Cu} and Sn_{Zn} defects based on anion-anion terminations. Such grain boundaries are detrimental and can acts as seeds for secondary phases. According to this model, we could speculate that ZnS grains might be lying close to the Σ3{112} twin boundaries. Moreover, first principle calculations have predicted Cu-poor anion terminated (-1-1-2) surfaces to situate V_{Cu} defects, which are benign for the solar cell performance [72].

7.2 3DXRD limitations and new horizons

This paper demonstrates that far-field 3DXRD is suitable for providing comprehensive statistical information about the ensemble of grains in the absorber layer. However, the position of the grain is not resolved. In outlook, one can make mapping of grains in 3D using the 3DXRD scanning modality that employs a smaller X-ray beam (200 nm) and records diffraction patterns at each yz-position of the sample [73]-[75]. Thus, grain positions and strain maps with a higher resolution can be achieved [76]. A drawback with scanning techniques is that the acquisition time increases. However, the next generation of synchrotron sources, such as the Extremely Brilliant Source, EBS, in Grenoble, which was successfully put into operation in Summer 2020, promises an increase in the data acquisition speed of all types of 3DXRD modalities by a factor of 10-50. Moreover, preliminary results on a new full field modality known as High-resolution 3DXRD suggests that 300 nm spatial resolution is within reach [32].

In outlook, combining scanning 3DXRD with X-ray Beam Induced Current (XBIC) and X-ray fluorescence (XRF) could reveal the relation between microstructure and photovoltaics properties of the device and localized elemental composition. By performing *in-operando* studies implementing the mentioned techniques, we could analyse the effects of grain boundaries on PV properties and identify elemental clusters that tend to populate the grain boundaries for passivation. These studies could improve current models for thin-film optimization [71], [77], [78].

8 Conclusion

We have characterized the microstructure of a PLD-deposited CZTS absorber layer buried within the stack of layers that constitute a full solar cell device. We demonstrate that 3DXRD can distinguish between phases with nearly identical unit cell parameters. As a result, we found 597 grains; 582 were identified as tetragonal and 15 as cubic. We extracted the strain and stress components both at the sample and at the grain level. We provided extensive statistics of the tetragonal and cubic grains, including the number of grains, sizes, orientations, and twin boundaries of each phase and discussed the relevance of this information for CZTS design.

More generally, the most common photovoltaic thin-film materials are chalcogenides with cubic and tetragonal structures. Structural characterization of these with traditional methods is

hampered by the same issues as CZTS. Hence, we propose that the 3DXRD methodology may be applied to index grains of other absorber materials such as CdTe (F-43m) and CIGS (I-42d).

9 Acknowledgements

This study was supported by the H2020 European Research Council through the SEEWHI Consolidator grant, ERC-2015-CoG-681881. We acknowledge a travel grant for synchrotron experiments by DANSCATT. We thank Sara Engberg, Andrea Crovetto, Prof. Jørgen Schou and Prof Xiaojing Hao for providing the sample and fruitful discussions. Special thanks are due to Ebtisam Abdellahi for helping with sample preparation and to Henning Osholm Sørensen and Innokenty Kantor for advice on multigrain crystallography. We thank Jonathan Almer, Jun-Sang Park, and Hemant Sharma for their support during the experiment. HFP acknowledge support from the PMP Advanced grant, ERC-2020-Adv-885022 and from the Danish ESS lighthouse on hard materials in 3D, SOLID. This research used resources of the Advanced Photon Source, a U.S. Department of Energy (DOE) Office of Science User Facility, operated for the DOE Office of Science by Argonne National Laboratory under Contract No. DE-AC02-06CH11357.

10 References

[1] First Solar, “First Solar Achieves Efficiency, Durability Milestones,” Presse Release Details, 2015. [Online]. Available: https://investor.firstsolar.com/news/press-release-details/2015/First-Solar-Achieves-Efficiency-Durability-Milestones/default.aspx.

[2] M. Nakamura, K. Yamaguchi, Y. Kimoto, Y. Yasaki, T. Kato, and H. Sugimoto, “Cd-Free Cu (In , Ga)(Se , S) 2 Thin-Film Solar Cell With Record Efficiency of 23 . 35 %,” vol. 9, no. 6, pp. 1863–1867, 2019.

[3] C. Yan et al., “Cu2ZnSnS4 solar cells with over 10% power conversion efficiency enabled by heterojunction heat treatment,” Nat. Energy, vol. 3, no. 9, pp. 764–772, 2018, doi: 10.1038/s41560-018-0206-0.

[4] D. H. Son et al., “Effect of solid-H2S gas reactions on CZTSSe thin film growth and photovoltaic properties of a 12.62% efficiency device,” J. Mater. Chem. A, vol. 7, no. 44, pp. 25279–25289, 2019, doi: 10.1039/c9ta08310c.

[5] W. Shockley and H. J. Queisser, “Detailed balance limit of efficiency of p-n junction solar cells,” J. Appl. Phys., vol. 32, no. 3, pp. 510–519, 1961, doi: 10.1063/1.1736034.

[6] J. D. Major, “Grain boundaries in CdTe thin film solar cells: A review,” Semicond. Sci. Technol., vol. 31, no. 9, 2016, doi: 10.1088/0268-1242/31/9/093001.

[7] S. Siebentritt, M. Igalson, C. Persson, and S. Lany, “The electronic structure of chalcopyrites - Bands, point defects and grain boundaries,” Prog. Photovoltaics Res. Appl., vol. 18, no. 6, pp. 390–410, 2010, doi: 10.1002/pip.936.

[8] J. B. Li, V. Chawla, and B. M. Clemens, “Investigating the role of grain boundaries in CZTS and CZTSSe thin film solar cells with scanning probe microscopy,” Adv. Mater., vol. 24, no. 6, pp. 720–723, 2012, doi: 10.1002/adma.201103470.

[9] A. Polman, M. Knight, E. C. Garnett, B. Ehrler, and W. C. Sinke, “Photovoltaic materials: Present efficiencies and future challenges,” Science (80-.)., vol. 352, no. 6283, pp. 1–10, 2016, doi: 10.1126/science.aad4424.

[10] B. G. Mendis, M. C. J. Goodman, J. D. Major, A. A. Taylor, K. Durose, and D. P. Halliday, “The role of secondary phase precipitation on grain boundary electrical activity in Cu 2 ZnSnS 4 (CZTS) photovoltaic absorber layer material,” J. Appl. Phys., vol. 112, no. 12, p. 124508, Dec. 2012, doi: 10.1063/1.4769738.

[11] D. M. Berg and P. J. Dale, “Kesterites: Equilibria and Secondary Phase Identification,” in Copper Zinc Tin Sulfide-Based Thin-Film Solar Cells, Chichester, UK: John Wiley & Sons Ltd, 2015, pp. 107–132.

[12] L. Grenet, M. A. A. Suzon, F. Emieux, and F. Roux, “Analysis of Failure Modes in Kesterite Solar Cells,” ACS Appl. Energy Mater., vol. 1, no. 5, pp. 2103–2113, May 2018, doi: 10.1021/acsaem.8b00194.

[13] Q. Cao et al., “Defects in Cu(In,Ga)Se 2 chalcopyrite semiconductors: A comparative study of material properties, defect states, and photovoltaic performance,” Adv. Energy Mater., vol. 1, no. 5, pp. 845–853, 2011, doi: 10.1002/aenm.201100344.

[14] M. A. Contreras et al., “Defect chalcopyrite Cu(In1-xGax)3Se5 materials and high-Ga-content Cu(In,Ga)Se2-based solar cells,” Conf. Rec. IEEE Photovolt. Spec. Conf., pp. 809–812, 1996.

[15] C. V. Thompson and R. Carel, “Stress and grain growth in thin films,” J. Mech. Phys. Solids, vol. 44, no. 5, pp. 657–673, 1996, doi: 10.1016/0022-5096(96)00022-1.

[16] C. R. Li et al., “Electronic and optical properties of kesterite Cu2ZnSnS 4 under in-plane biaxial strains: First-principles calculations,” Phys. Lett. Sect. A Gen. At. Solid State Phys., vol. 377, no. 37, pp. 2398–2402, 2013, doi: 10.1016/j.physleta.2013.06.046.

[17] M. Jamiati, B. Khoshnevisan, and M. Mohammadi, “Second- and third-order elastic constants of kesterite CZTS and its electronic and optical properties under various strain rates,” Energy Sources, Part A Recover. Util. Environ. Eff., vol. 40, no. 8, pp. 977–986, Apr. 2018, doi: 10.1080/15567036.2018.1468509.

[18] A. Ritscher, M. Hoelzel, and M. Lerch, “The order-disorder transition in Cu2ZnSnS4 - A neutron scattering investigation,” J. Solid State Chem., vol. 238, pp. 68–73, 2016, doi: 10.1016/j.jssc.2016.03.013.

[19] J. Zhang et al., “Grain boundary mobilities in polycrystals,” Acta Mater., vol. 191, pp. 211–220, 2020, doi: 10.1016/j.actamat.2020.03.044.

[20] J. Orloff, M. Utlaut, and L. Swanson, High Resolution Focused Ion Beams: FIB and its Applications. Boston, MA: Springer US, 2003.

[21] J. Tao et al., Laser Ablation, vol. 28, no. 2. Berlin, Heidelberg: Springer Berlin Heidelberg, 1994.

[22] D. M. Berg et al., “Discrimination and detection limits of secondary phases in Cu2ZnSnS4 using X-ray diffraction and Raman spectroscopy,” Thin Solid Films, vol. 569, no. C, pp. 113–123, 2014, doi: 10.1016/j.tsf.2014.08.028.

[23] G. Fevola et al., “Resonant x-ray ptychographic nanotomography of kesterite solar cells,” Phys. Rev. Res., vol. 2, no. 1, 2020, doi: 10.1103/physrevresearch.2.013378.

[24] J. Just, D. Lützenkirchen-Hecht, R. Frahm, S. Schorr, and T. Unold, “Determination of secondary phases in kesterite Cu2ZnSnS4 thin films by x-ray absorption near edge structure analysis,” Appl. Phys. Lett., vol. 99, no. 2011, p. 262105, 2011, doi: 10.1063/1.3671994.

[25] E. M. Lauridsen, S. Schmidt, R. M. Suter, and H. F. Poulsen, “Tracking: a method for structural characterization of grains in powders or polycrystals,” J. Appl. Crystallogr., vol. 34, no. 6, pp. 744–750, Dec. 2001, doi: 10.1107/S0021889801014170.

[26] H. F. Poulsen et al., “Three-dimensional maps of grain boundaries and the stress state of individual grains in polycrystals and powders,” J. Appl. Crystallogr., vol. 34, no. 6, pp. 751–756, 2001, doi: 10.1107/S0021889801014273.

[27] J. Oddershede, Sø. Schmidt, H. F. Poulsen, H. O. Srensen, J. Wright, and W. Reimers, “Determining grain resolved stresses in polycrystalline materials using three-dimensional X-ray diffraction,” J. Appl. Crystallogr., vol. 43, no. 3, pp. 539–549, 2010, doi: 10.1107/S0021889810012963.

[28] J. V. Bernier, N. R. Barton, U. Lienert, and M. P. Miller, “Far-field high-energy diffraction microscopy: A tool for intergranular orientation and strain analysis,” J. Strain Anal. Eng. Des., vol. 46, no. 7, pp. 527–547, 2011, doi: 10.1177/0309324711405761.

[29] H. O. Sørensen et al., “Multigrain crystallography,” Zeitschrift für Krist., vol. 227, no. 1, pp. 63–78, Jan. 2012, doi: 10.1524/zkri.2012.1438.

[30] H. Sharma, R. M. Huizenga, and S. E. Offerman, “A fast methodology to determine the characteristics of thousands of grains using three-dimensional X-ray diffraction. II. Volume, centre-of-mass position, crystallographic orientation and strain state of grains,” J. Appl. Crystallogr., vol. 45, no. 4, pp. 705–718, 2012, doi: 10.1107/S0021889812025599.

[31] S. F. Li and R. M. Suter, “Adaptive reconstruction method for three-dimensional orientation imaging,” J. Appl. Crystallogr., vol. 46, no. 2, pp. 512–524, 2013, doi: 10.1107/S0021889813005268.

[32] H. F. Poulsen, “Multi scale hard x-ray microscopy,” Curr. Opin. Solid State Mater. Sci., vol. 24, no. 2, p. 100820, 2020, doi: 10.1016/j.cossms.2020.100820.

[33] S. E. Offerman et al., “Grain nucleation and growth during phase transformations,” Science (80-.)., vol. 298, no. 5595, pp. 1003–1005, 2002, doi: 10.1126/science.1076681.

[34] G. L. Wu and D. J. Jensen, “In-situ measurement of annealing kinetics of individual bulk grains in nanostructured aluminium,” Philos. Mag., vol. 92, no. 25–27, pp. 3381–3391, 2012, doi: 10.1080/14786435.2012.711494.

[35] C. D. M. Kutsal, H.F. Poulsen, G. Winther, H.O. Sorensen, “High resolution 3DXRD: 3D mapping of deformed metal microstructures,” (In Rev., 2020.

[36] C. Wejdemann and H. F. Poulsen, “Multigrain indexing of unknown multiphase materials,” J. Appl. Crystallogr., vol. 49, no. 2, pp. 616–621, Apr. 2016, doi: 10.1107/S1600576716003691.

[37] S. Schorr, H.-J. Hoebler, and M. Tovar, “A neutron diffraction study of the stannite-kesterite solid solution series,” Eur. J. Mineral., vol. 19, no. 1, pp. 65–73, 2007, doi: 10.1127/0935-1221/2007/0019-0065.

[38] A. Lafond, L. Choubrac, C. Guillot-Deudon, P. Fertey, M. Evain, and S. Jobic, “X-ray resonant single-crystal diffraction technique, a powerful tool to investigate the kesterite structure of the photovoltaic Cu2ZnSnS 4 compound,” Acta Crystallogr. Sect. B Struct. Sci. Cryst. Eng. Mater., vol. 70, no. 2, pp. 390–394, 2014, doi: 10.1107/S2052520614003138.

[39] S. Schorr, “The crystal structure of kesterite type compounds: A neutron and X-ray diffraction study,” Sol. Energy Mater. Sol. Cells, vol. 95, no. 6, pp. 1482–1488, 2011, doi: 10.1016/j.solmat.2011.01.002.

[40] J. J. S. Scragg, L. Choubrac, A. Lafond, T. Ericson, and C. Platzer-Björkman, “A low-temperature order-disorder transition in Cu2ZnSnS4 thin films,” Appl. Phys. Lett., vol. 104, no. 4, pp. 2–6, 2014, doi: 10.1063/1.4863685.

[41] C. J. Bosson, M. T. Birch, D. P. Halliday, K. S. Knight, A. S. Gibbs, and P. D. Hatton, “Cation disorder and phase transitions in the structurally complex solar cell material Cu 2 ZnSnS 4,” J. Mater. Chem. A, vol. 5, no. 32, pp. 16672–16680, 2017, doi: 10.1039/C7TA03603E.

[42] H. Katagiri, K. Jimbo, M. Tahara, H. Araki, and K. Oishi, “The influence of the composition ratio on CZTS-based thin film solar cells,” in Materials Research Society Symposium Proceedings, 2010, doi: 10.1557/proc-1165-m04-01.

[43] T. Mise, S. Tajima, T. Fukano, K. Higuchi, and H. Katagiri, “Influence of chemical composition on the properties of directly coevaporated Cu-Zn-Sn-S-based thin films and solar cells,” Jpn. J. Appl. Phys., vol. 55, no. 1, 2016, doi: 10.7567/JJAP.55.012303.

[44] L. E. Valle Rios, K. Neldner, G. Gurieva, and S. Schorr, “Existence of off-stoichiometric single phase kesterite,” J. Alloys Compd., vol. 657, pp. 408–413, 2016, doi: 10.1016/j.jallcom.2015.09.198.

[45] A. Nagoya, R. Asahi, R. Wahl, and G. Kresse, “Defect formation and phase stability of Cu2 ZnSnS4 photovoltaic material,” Phys. Rev. B - Condens. Matter Mater. Phys., vol. 81, no. 11, pp. 1–4, 2010, doi: 10.1103/PhysRevB.81.113202.

[46] S. Chen, A. Walsh, X. G. Gong, and S. H. Wei, “Classification of lattice defects in the kesterite Cu2ZnSnS 4 and Cu2ZnSnSe4 earth-abundant solar cell absorbers,” Adv. Mater., vol. 25, no. 11, pp. 1522–1539, 2013, doi: 10.1002/adma.201203146.

[47] K. Momma and F. Izumi, “VESTA 3 for three-dimensional visualization of crystal, volumetric and morphology data,” J. Appl. Crystallogr., vol. 44, no. 6, pp. 1272–1276, 2011, doi: 10.1107/S0021889811038970.

[48] M. K. Rabadanov, A. A. Loshmanov, and Y. V. Shaldin, “Anharmonic thermal vibrations of atoms in crystals with sphalerite structure-GaP, ZnS, ZnSe, and ZnTe: High-temperature x-ray structure studies,” Crystallogr. Reports, vol. 42, no. 4, pp. 592–602, 1997, doi: 10.1134/1.170655.

[49] B. Thiodjio Sendja, D. Tchana Kamgne, G. Aquilanti, L. Olivi, and J. R. Plaisier, “Low-range thermal investigation of zincblende-type ZnS by combined extended X-ray absorption fine structure and X-ray diffraction techniques,” Phys. B Condens. Matter, vol. 545, no. June, pp. 481–490, 2018, doi: 10.1016/j.physb.2018.06.005.

[50] FABLE, “Fully automated beam line experiment.” [Online]. Available: https://sourceforge.net/p/fable/wiki/Home/. [Accessed: 04-Nov-2020].

[51] G. B. M. Vaughan, S. Schmidt, and H. F. Poulsen, “Multicrystal approach to crystal structure solution and refinement,” Zeitschrift fur Kristallographie, vol. 219, no. 12. De Gruyter, pp. 813–825, 01-Dec-2004, doi: 10.1524/zkri.219.12.813.55870.

[52] “FABLE-3DXRD/ImageD11: ImageD11 is a python code for identifying individual grains in spotty area detector X-ray diffraction image.” [Online]. Available: https://github.com/FABLE-3DXRD/ImageD11. [Accessed: 17-Nov-2020].

[53] I. Camps, J. Coutinho, M. Mir, A. F. D. Cunha, M. J. Rayson, and P. R. Briddon, “Elastic and optical properties of Cu 2SZnSn(Se xS 1S x) 4S alloys: Density functional calculations,” Semicond. Sci. Technol., vol. 27, no. 11, 2012, doi: 10.1088/0268-1242/27/11/115001.

[54] P. P. Gunaicha, S. Gangam, J. L. Roehl, and S. V. Khare, “Structural, energetic and elastic properties of Cu2ZnSn(SxSe1-x)4 (x=1, 0.75, 0.5, 0.25, 0) alloys from first-principles computations,” Sol. Energy, vol. 102, pp. 276–281, 2014, doi: 10.1016/j.solener.2014.01.015.

[55] Y. Zhao, D. Li, and Z. Liu, “Structural and elastic DFT study of four structures for Cu2ZnSnS4under high pressure,” J. Alloys Compd., vol. 696, pp. 86–95, 2017, doi: 10.1016/j.jallcom.2016.11.091.

[56] Z. Zhao and X. Zhao, “Electronic, optical, and mechanical properties of Cu2ZnSnS4 with four crystal structures,” J. Semicond., vol. 36, no. 8, 2015, doi: 10.1088/1674-4926/36/8/083004.

[57] A. Cazzaniga et al., “Ultra-thin Cu2ZnSnS4 solar cell by pulsed laser deposition,” Sol. Energy Mater. Sol. Cells, vol. 166, pp. 91–99, Jul. 2017, doi: 10.1016/j.solmat.2017.03.002.

[58] F. Bachmann, R. Hielscher, and H. Schaeben, “Texture analysis with MTEX- Free and open source software toolbox,” in Solid State Phenomena, 2010, vol. 160, pp. 63–68, doi: 10.4028/www.scientific.net/SSP.160.63.

[59] D. Abou-Ras, S. Schorr, and H. W. Schock, “Grain-size distributions and grain boundaries of chalcopyrite-type thin films,” J. Appl. Crystallogr., vol. 40, no. 5, pp. 841–848, Oct. 2007, doi: 10.1107/S0021889807032220.

[60] S. Siebentritt, “Why are kesterite solar cells not 20% efficient?,” Thin Solid Films, vol. 535, no. 1, pp. 1–4, 2013, doi: 10.1016/j.tsf.2012.12.089.

[61] J. Just, D. Luetzenkirchen-Hecht, O. Mueller, R. Frahm, and T. Unold, “Depth distribution of secondary phases in kesterite Cu 2 ZnSnS 4 by angle-resolved X-ray absorption spectroscopy,” APL Mater., vol. 5, no. 12, p. 126106, Dec. 2017, doi: 10.1063/1.5000306.

[62] J. L. Johnson et al., “Effects of 2nd phases, stress, and Na at the Mo/Cu 2ZnSnS4 interface,” Mater. Res. Soc. Symp. Proc., vol. 1268, no. May 2014, pp. 85–90, 2010, doi: 10.1557/proc-1268-ee03-03.

[63] V. Ray, J. Obona, S. Sharang, L. Rotkina, E. Chang, and K. Tolua, “Optimizing gas-assisted processes for Ga and Xe FIB circuit edit application,” Conf. Proc. from Int. Symp. Test. Fail. Anal., no. November, pp. 397–401, 2016.

[64] R. P. Babu, S. Irukuvarghula, A. Harte, and M. Preuss, “Nature of gallium focused ion beam induced phase transformation in 316L austenitic stainless steel,” Acta Mater., vol. 120, pp. 391–402, 2016, doi: 10.1016/j.actamat.2016.08.008.

[65] N. Schäfer et al., “Microstrain distributions in polycrystalline thin films measured by X-ray microdiffraction,” J. Appl. Crystallogr., vol. 49, pp. 632–635, 2016, doi: 10.1107/S1600576716003204.

[66] W. M. M. Hlaing OO, J. L. L. Johnson, a. Bhatia, E. a. A. Lund, M. M. M. Nowell, and M. a. a. Scarpulla, “Grain Size and Texture of Cu2ZnSnS4 Thin Films Synthesized by Cosputtering Binary Sulfides and Annealing: Effects of Processing Conditions and Sodium,” J. Electron. Mater., vol. 40, no. 11, pp. 2214–2221, 2011, doi: 10.1007/s11664-011-1729-3.

[67] S. A. Vanalakar et al., “A review on pulsed laser deposited CZTS thin films for solar cell applications,” J. Alloys Compd., vol. 619, pp. 109–121, 2015, doi: 10.1016/j.jallcom.2014.09.018.

[68] S. Chaisitsak, A. Yamada, and M. Konagai, “Preferred orientation control of Cu(In1-x Gax)Se2 (x ≈ 0.28) thin films and its influence on solar cell characteristics,” Japanese J. Appl. Physics, Part 1 Regul. Pap. Short Notes Rev. Pap., vol. 41, no. 2 A, pp. 507–513, 2002, doi: 10.1143/jjap.41.507.

[69] D. Abou-Ras et al., “Grain-boundary types in chalcopyrite-type thin films and their correlations with film texture and electrical properties,” Thin Solid Films, vol. 517, no. 7, pp. 2545–2549, 2009, doi: 10.1016/j.tsf.2008.11.044.

[70] M. Kawamura, T. Yamada, N. Suyama, A. Yamada, and M. Konagai, “Grain boundary evaluation of Cu(In1-xGax)Se 2solar cells,” Jpn. J. Appl. Phys., vol. 49, no. 6 PART 1, pp. 0623011–0623013, 2010, doi: 10.1143/JJAP.49.062301.

[71] M. Wong, K. Tse, and J. Zhu, “New Types of CZTS Σ3 {112} Grain Boundaries: Algorithms to Passivation,” J. Phys. Chem. C, vol. 122, no. 14, pp. 7759–7770, 2018, doi: 10.1021/acs.jpcc.8b00811.

[72] P. Xu, S. Chen, B. Huang, H. J. Xiang, X. G. Gong, and S. H. Wei, “Stability and electronic structure of Cu2ZnSnS4 surfaces: First-principles study,” Phys. Rev. B - Condens. Matter Mater. Phys., vol. 88, no. 4, pp. 1–8, 2013, doi: 10.1103/PhysRevB.88.045427.

[73] Y. Hayashi, Y. Hirose, and Y. Seno, “Polycrystal orientation mapping using scanning three-dimensional X-ray diffraction microscopy,” J. Appl. Crystallogr., vol. 48, pp. 1094–1101, 2015, doi: 10.1107/S1600576715009899.

[74] Y. Hayashi, D. Setoyama, and Y. Seno, “Scanning three-dimensional X-ray diffraction microscopy with a high-energy microbeam at SPring-8,” Mater. Sci. Forum, vol. 905 MSF, pp. 157–164, 2017, doi: 10.4028/www.scientific.net/MSF.905.157.

[75] J. Hektor et al., “Scanning 3DXRD measurement of grain growth, stress, and formation of Cu 6 Sn 5 around a tin whisker during heat treatment,” Materials (Basel)., vol. 12, no. 3, pp. 1–16, 2019, doi: 10.3390/ma12030446.

[76] N. A. Henningsson, S. A. Hall, J. P. Wright, and J. Hektor, “Reconstructing intragranular strain fields in polycrystalline materials from scanning 3DXRD data,” J. Appl. Crystallogr., vol. 53, pp. 314–325, 2020, doi: 10.1107/S1600576720001016.

[77] C. Y. Liu, Z. M. Li, H. Y. Gu, S. Y. Chen, H. Xiang, and X. G. Gong, “Sodium Passivation of the Grain Boundaries in CuInSe2 and Cu2ZnSnS4 for High-Efficiency Solar Cells,” Adv. Energy Mater., vol. 7, no. 8, 2017, doi: 10.1002/aenm.201601457.

[78] B. G. Mendis, M. C. J. Goodman, J. D. Major, A. A. Taylor, K. Durose, and D. P. Halliday, “The role of secondary phase precipitation on grain boundary electrical activity in Cu 2 ZnSnS 4 (CZTS) photovoltaic absorber layer material,” J. Appl. Phys., vol. 112, no. 12, p. 124508, 2012, doi: 10.1063/1.4769738.

3.2 SCANNING 3DXRD MEASUREMENTS OF STRAIN AND GRAIN ORIENTATIONS OF THE ABSORBER LAYER OF A CZTS SOLAR CELL

3.2.1 Introduction

We propose scanning 3DXRD to analyze the microstructure of the absorber layer. This method offers a higher spatial resolution than the line beam approach form APS, allowing the reconstruction of a grain map. Scanning 3DXRD [127] utilizes a focused nano-beam that illuminates a small part of the sample. It is necessary to scan along two translational and one rotational axis. While measurements are time-consuming, the gain in spatial resolution allows the observation of the variations of strain and orientation in 3D dimensions. Another advantage of scanning 3DXRD is the use of high energies (ranges 50-100 keV). The high energy ensures the penetration of the beam through the sample and generates more condensed diffraction angles on the detector, increasing the number of the recorded diffraction peaks.

We aim to identify the crystallographic phases in the absorber layer of the solar cell and map neighbouring grains to determine their position and variations in orientations and strains from one grain to another.

3.2.2 Sample description

The investigated sample consists of a CZTS solar cell, and its fabrication is described in [82]. The solar cell comprises a stack of layers deposited on a soda-lime glass (SGL) substrate. The first layer is molybdenum, followed by the absorber layer Cu_2ZnSnS_4 (CZTS), and the subsequent top layers: ZnO, CdS, Al:ZnO, MgF_2. The absorber layer is formed through two steps. First, the precursor materials are deposited by Pulsed Laser Deposition (PLD) on the Mo-SLG substrate. Secondly, the as-deposited film is annealed at 560 °C in a sulfur atmosphere.

We cut one piece of the device (0.8 mm × 0.5 mm) and decrease the substrate thickness from 1 mm to about 13-15 µm by mechanical polishing (see Figure 3.1). The thinned substrate generates less background noise than a thick one improving the signal-to-noise ratio for the experiment.

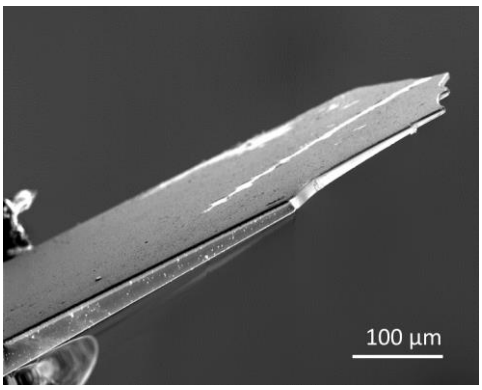

Figure 3.1. SEM image of the sample showing the thickness gradient of the SLG substrate

3.2.3 Experiment description

In addition to the conventional 3DXRD layout, the scanning 3DXRD setup requires a focused pencil beam that illuminates one part of the sample and a translation stage that moves the sample in the (yz) plane laboratory system (see Figure 3.2).

The sample is mounted on a rotation stage and illuminated by an X-ray nano-focused beam (40 keV, 300 nm x 300 nm). Diffraction spots from lattice planes that fulfil the Bragg condition are recorded on the detector. To probe the complete crystal structure within the illuminated volume, the sample is rotated in the range ω= [-180°, 180°] in steps of 1°. The rotation follows a clockwise and anticlockwise intercalation, measuring diffraction patterns at each ω-angle. The specimen is translated in the y-direction by steps of 0.25 µm collecting rotation scans at 180 consecutive y-positions. The overall experiment took about 15 hours.

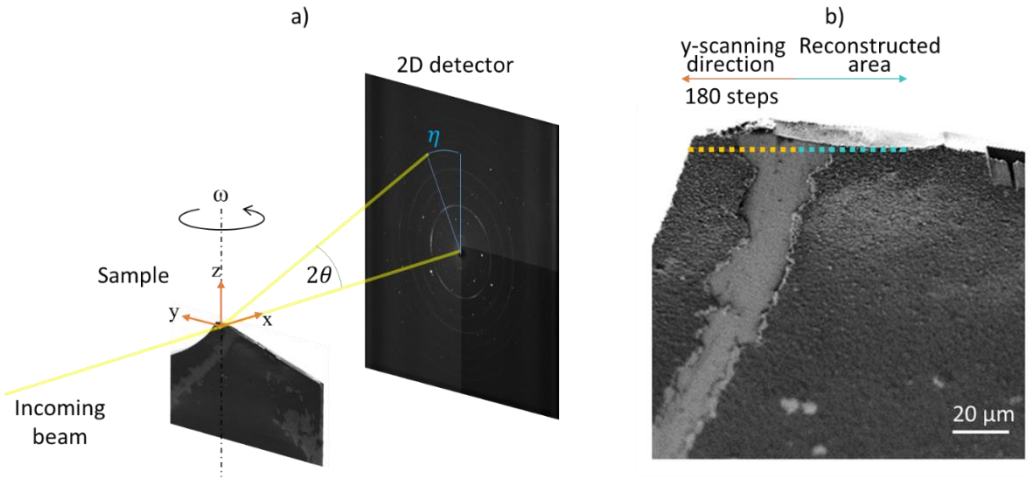

Figure 3.2. a) 3DXRD setup using a focused nano-beam. The sample is scanned in the y-direction from a central position towards the edge, collecting diffraction patterns of 360° rotation angles at each y-position. The diffraction peaks on the detector are determined by the angles (2θ, η). b) SEM image of the sample showcasing the y-scanning positions and the reconstructed area recovered by the rotation scans.

3.2.4 Data analysis

The grain shape and position can be reconstructed using a filtered back-projection from the sinogram of the total intensity of the diffraction peaks belonging to each grain. The reconstruction is repeated for all grains at all y-positions, resulting in the grain map of the sample.

The orientations of the grains are calculated based on the approach described by Hayashi (2015). It consists of tracking the illuminated point Q (x_s, y_s), located somewhere in the sample, in the combined y-ω scans. The point Q is occupied by one grain, and their associated diffraction images can be extracted from the y-ω scans when Δy is infinitesimal and satisfies the following equation:

$$Y(\omega) = ({x_s}^2 + {y_s}^2)^{1/2}\, cos[\omega + tan^{-1}(y_s/x_s)]. \quad (3.1)$$

The extracted diffraction data is analyzed using a collection of scripts developed at ESRF [128] and the indexing program ImageD11 [129]. The outcome is a grain in the form of the $(\mathbf{UB})^{-1}$ matrix per voxel Q.

3.2.5 Results and discussion

The sinogram and the reconstruction of one grain are shown in Figure 3.3. The sinogram represents the sum of the intensities of the diffraction peaks that belong to the specific grain. The intensity corresponds to a diffracting lattice plane (hkl) at the y-position of the beam.

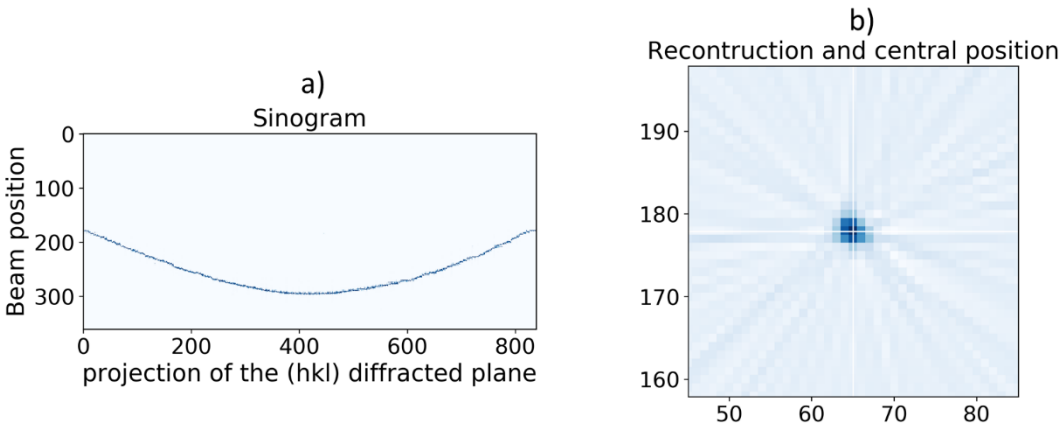

Figure 3.3. a) Sinogram corresponding to a grain. b) Reconstructed shape of the grain and determination of the central grain position.

The grain map reconstruction is displayed in Figure 3.4. At the top, the grains are coloured by their labels to distinguish one grain from another. At the bottom, the grains are

reconstructed according to the projections in the sinograms, as shown in Figure 3.3. The x-axis indicates the scan at the y-position with a unit size of 0.25 µm (the step size of the scan).

At the y-location while executing the rotation scan, one grain in the sample is always illuminated, but neighbouring grains come in and out of the beam. Therefore it is possible to recover contributions along the y-axis of non-scanned positions. From the 180 scanned positions, it was possible to reconstruct the other complementary 180 positions. Hence, 360 positions were reconstructed. The estimated distance covered is 90 µm. The absence of grains in the middle coincides with the gap shown in Figure 3.2b.

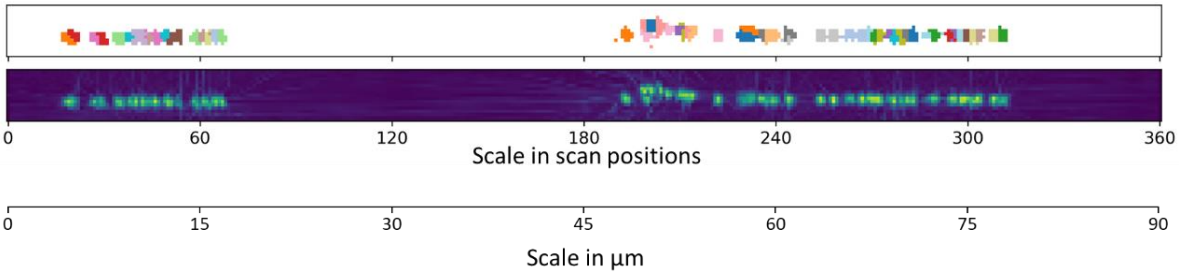

Figure 3.4. Grain map reconstruction. Top: the grains are coloured by their label. Bottom: reconstruction of the shape and central positions of the grains.

As shown in Figure 2.11 in section 2.4.4.2, the histogram of the reflections identifies CZTS, the expected overlapping Cu_2SnS_3, and ZnS, and the top layers, indium tin oxide, and molybdenum. We index with the tetragonal phase, kesterite, as most of the reflections agree with this phase.

After indexing the reflections in the scans, we identify 59 grains that belong to the kesterite phase. We calculate the misorientation angle between two neighbouring grains by calculating the pure rotation $\mathbf{U}_s$ of the polar decomposition of the deformation tensor **F**. The details of the calculation are explained in section 2.4.7 of this thesis. For each pair, the symmetry operations are applied. In the case of the tetragonal kesterite phase, eight transformations are possible. The normal strain tensor for each symmetry operation determines the smallest lattice mismatch between the grains, ultimately selecting the twin relation among the eight possible combinations. The most common misorientation angles are 70.53°, 109.47°, 131.81°, and 180°. These angles are characteristic of Σ3 twin boundaries and are displayed in Figure 3.5.

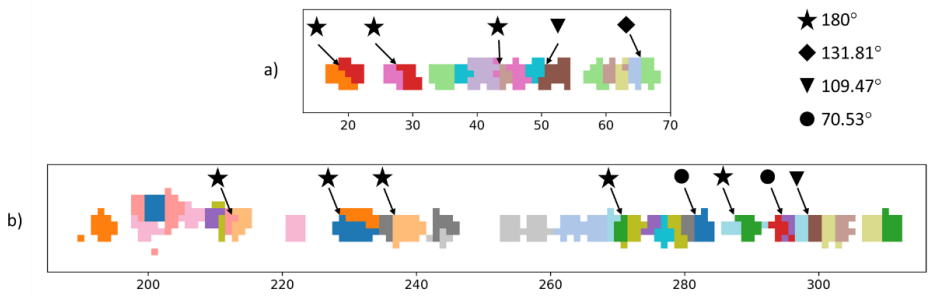

Figure 3.5. a) Left side and b) right side of the grain map coloured by the grain label, showing the locations of the Σ3 boundaries.

Moreover, we calculate the strain in the grain and in the sample reference systems using the average of the indexed grain unit cell parameters as the reference cell. The details of the strain calculation are explained in section 2.4.6.2 of this thesis.

Figure 3.6 shows the distributions of the strain components. At the grain level, we notice that the strain component ε_1 along the a-axis is predominantly tensile. The strain component ε_2 along the b-axis is tensile by looking at the slightly left-skewed distribution, whereas the strain ε_3 along the c-axis is tensile and compressive according to the bimodal distribution (see Figure 3.6 c-h). The shear strain components have a unimodal distribution with no indication of a predominant tensile or compressive effect.

In the sample reference system (Figure 3.6 i-n), the distribution of the strain components in ε_1 is bimodal, where the first mode corresponds to the compressive strain. Strain ε_2 has a left-skewed distribution, whereas ε_3 and the shear strains have an almost normal distribution within a range of [-25; 25] $\times 10^{-4}$.

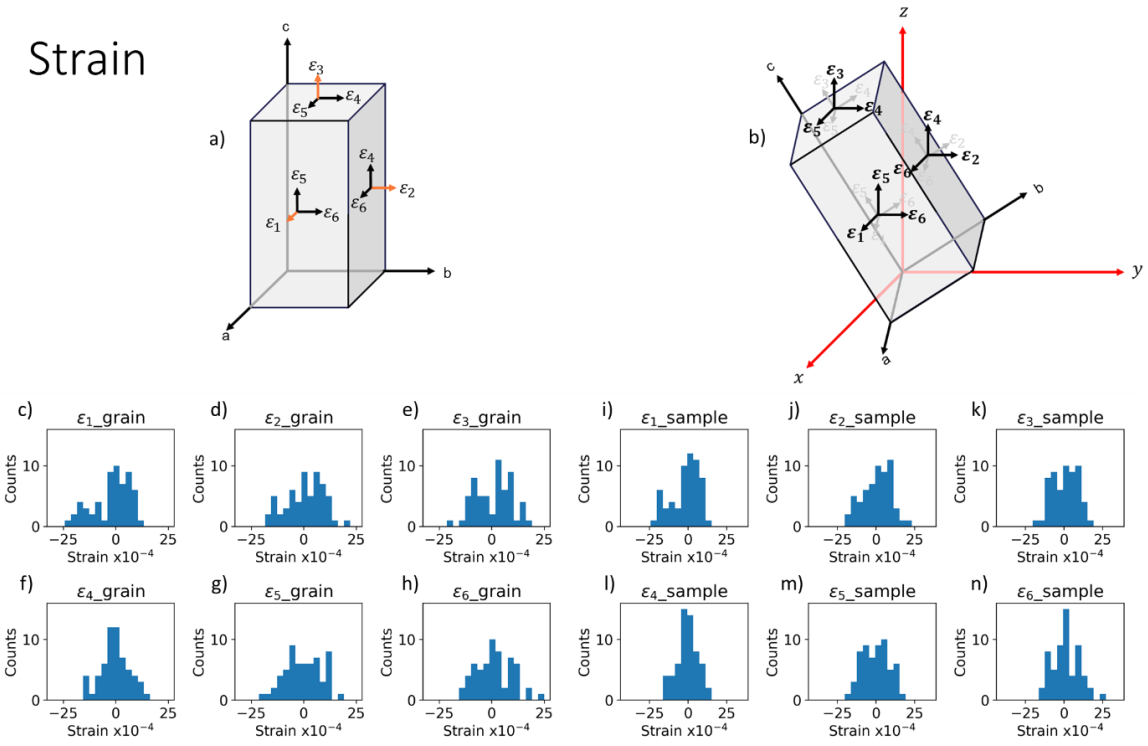

Figure 3.6. Illustration of the strain components a) in the grain and b) in the sample. Histograms of the strain components in the grain reference system (c-h) and in the sample reference system (i-n).

Using Hook's law described in section 2.4.6.3 of this thesis, we compute the stress elements in the grain and in the sample references system. The distributions of these components are displayed in Figure 3.7.

At the grain level (Figure 3.7 c-h), similarly to the strain trends, we observe tensile stresses for σ_1 and σ_2 along the a and b axes, whereas the stress σ_3 along the c-axis is compressive. At the sample level (Figure 3.7 i-n), all the stress components span over [-100,100] MPa. No predominant tensile or compressive stress is observed.

The sample for the ESRF test and the sample for the APS experiment were taken from the same specimen, a PLD CZTS solar cell divided into different subcells. However, the findings are surprisingly contrasting between both samples. The strain in the APS sample was evident and could be observed from the displacement of the diffraction spots. As a result, compressive stress along the film plane normal and tensile stresses along the film plane were found.

The ESRF sample did not show the strain effect as in the APS experiment. We suspect that the sample treatment for this particular experiment inflicted less mechanical stress while reducing the substrate thickness to 15 µm. On the other hand, the sample prepared for APS

was additionally milled by FIB removing the glass at the tip to 4µm thick. This is almost double the thickness of the overall stack of layers in the solar cell. With such a thin substrate, the tip of the sample is more sensitive to external stresses than the sample with a thicker substrate.

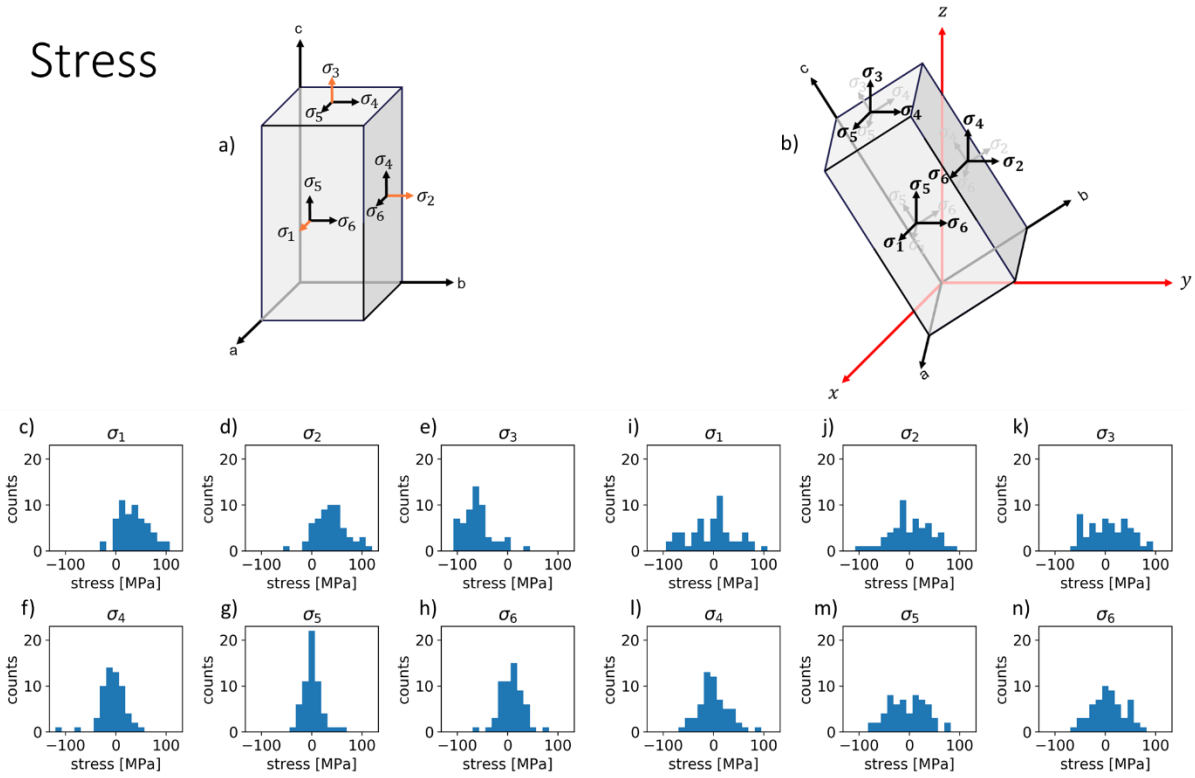

Figure 3.7. Illustration of the stress components a) in the grain and b) in the sample. Histograms of the stress components in the grain reference system (c-h) and in the sample reference system (i-n).

3.2.6 Conclusions and perspectives for further analysis

In summary, we identified 59 grains that correspond to the CZTS phase. We have reconstructed the corresponding grain map and recognized the Σ3 twin boundaries between the grains. We have calculated the strain in the grains and in the sample. We noticed that the strain effect is not as pronounced as in the sample tested at APS, even though both samples come from the same specimen.

This test shows the advantages of implementing scanning 3DXRD for the characterization of the thin-film microstructure. For this test, we resolved one line scan, but raster scans in the (yz)-plane can reveal more grains and details of the microstructure, improving the quality of the map. This technique is continuously improving, finding different fields of applications.

For example, measuring the grain growth of a tin whisker [130] and reconstructions of the intragranular strain fields [131]. Moreover, the upgrade of the storage ring at ESRF will allow faster experiments with higher resolution.

For further analysis, we can potentially isolate one grain dataset that includes the intensities of the reflections and the corresponding (hkl) planes. With this dataset, one can perform the crystal structure refinement to locate the coordinates of atoms.

Further experiments could study the annealing experiments stages of CZTS films or any other chalcogenide thin-film solar cell such as CIGS and CdTe. Scanning 3DXRD combined with X-ray fluorescence could also reveal the elemental composition at the grain boundaries. *In operando* studies could also measure the current transport in the solar cell and their correlation with the film structural properties combining scanning-3DXRD with X-ray Beam Induced Current measurements [132].

3.3 MICROSTRUCTURE OF AG-ALLOYED CZTS

3DXRD Experiment at APS, beamline 1-ID (November 2018)

3.3.1 Introduction

The incorporation of Ag to CZTS thin-films has been studied in recent years [133]–[136]. It started as a strategy to overcome the low V_{oc} in CZTS solar cells associated with the Cu_{Zn} antisite defect. Partially replacing Cu with Ag could reduce the number of Cu_{Zn} antisite defects [137]. Moreover, an increase in the grain size has been observed, representing a change in the microstructure of the material [135], [137].

In this study, we analyze the structural properties of the grains in an (Ag, $Cu)_2ZnSnS_4$ (ACZTS) polycrystalline thin-film through 3DXRD.

3.3.2 Sample description

We investigate a sample that consists of a soda-lime substrate coated with a molybdenum layer and ACZTS. The top layers were not applied. The absorber layer was deposited on Mo-SLG via PLD with a target of sulfide precursors and a silver content of Ag/(Cu+Ag) ≈10%. Then, the film was annealed at 600 ºC.

We follow a similar sample preparation procedure as for the PLD-CZTS solar cell. We cut a piece of approximately 35 µm wide and 500 µm in length (see Figure 3.8a). Moreover, we reduce the substrate thickness by mechanical polishing to improve the signal to noise ratio. The thinnest part at the tip of the sample is further milled with a Focused Ion Beam (FIB). Through this process, some parts peeled off given the poor adherence of the film. It can be observed in Figure 3.8b, where a third of the tip is seen to have delaminated.

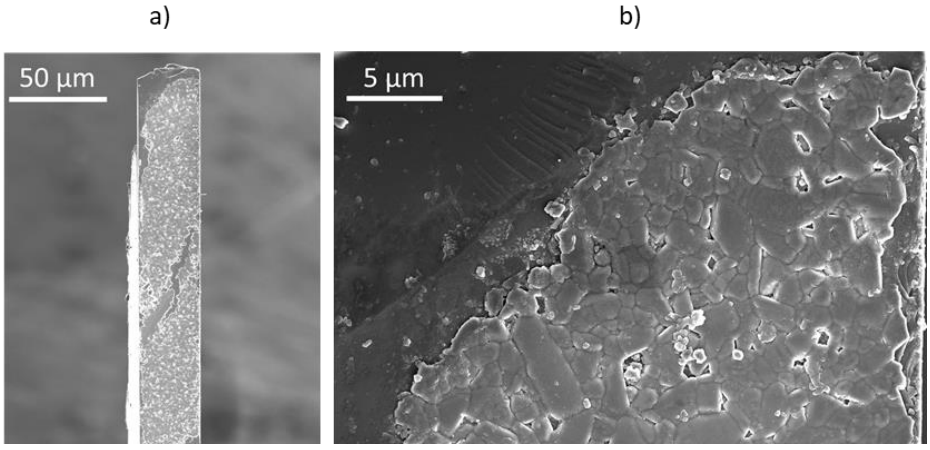

Figure 3.8. SEM images: a) Sample overview, b) Top view of the ACZTS film around the scanned area.

3.3.3 Experimental description

The experimental setup is the same implemented for the measurements of the PLD-CZTS solar cell depicted in section 3.1 of this thesis. Similar to the PLD-CZTS solar cell measurements, we scanned seven slices along the z-axis with a step size of 1 µm.

The tip of the sample was illuminated with a monochromatic beam (52 keV, 1.5 µm (V) x 200 µm (H)). The normal to the film plane is parallel to the beam. A far-field detector (2048 x 2048 pixels, 200 µm pixel pitch) records the diffraction pattern while rotating the sample in a range of -180° to 180° with a step of 0.1° and an exposure time of 1.2 s per frame. A total of 3600 images per slice are obtained during an overall 9-hour scan. Moreover, we measure the standard powder LaB_6 to fit the detector parameters (sample-detector distance and tilts).

3.3.4 Data Analysis

In a preliminary assessment, we investigate the phases in the film. Figure 3.9 depicts the azimuthal angle η and the Bragg angle, 2θ of the reflections. An attempted Le Bail fitting has been performed using Topas6 [138] to provide an approximate determination of unit cell parameters (a=5.463 Å; c=10.847 Å). We referred to this phase as the fitted-ACZTS. Compared to the CZTS unit cell (a=5.43373 Å, c=10.8392 Å, [47]), the a and b lattice constants increase by 0.5%, whereas the c-lattice expands less than 0.1%. As a consequence, the rings (200)/(004) and (220)/(204) are also more separated than in the CZTS diffraction patterns (see Figure 3.9).

Each slice is analyzed individually. The reflections are indexed with the cubic phase applied for the PLD-CZTS solar cell (a=5.43) by the program ImageD11 [129]. We index the reflections in the planes $(112)_{tetragonal}$, $(200)/(204)_{tetragonal}$ and $(220)/(204)_{tetragonal}$, equivalent to the face-centered rings $(111)_{cubic}$, $(200)_{cubic}$, $(220)_{cubic}$, respectively. The outcome is a list per slice of the cubic grains with a minimum of 30 peaks and an hkl tolerance of 0.02.

Next, the cubic grains are converted into tetragonal, described in section 2.4.4.4 of this thesis. All grains were matched to a tetragonal structure. Following the conversion of the indexed "as-cubic" grains to the tetragonal structure, we refine the parameters of the grains and collect all the corresponding superstructure reflections per grain. Subsequently, the grain size and the twin relations are calculated as explained in section 2.4.5 and section 2.4.7 of this thesis.

The merging of the grains appearing in multiple slices is not completed. Therefore, we present the results per slice.

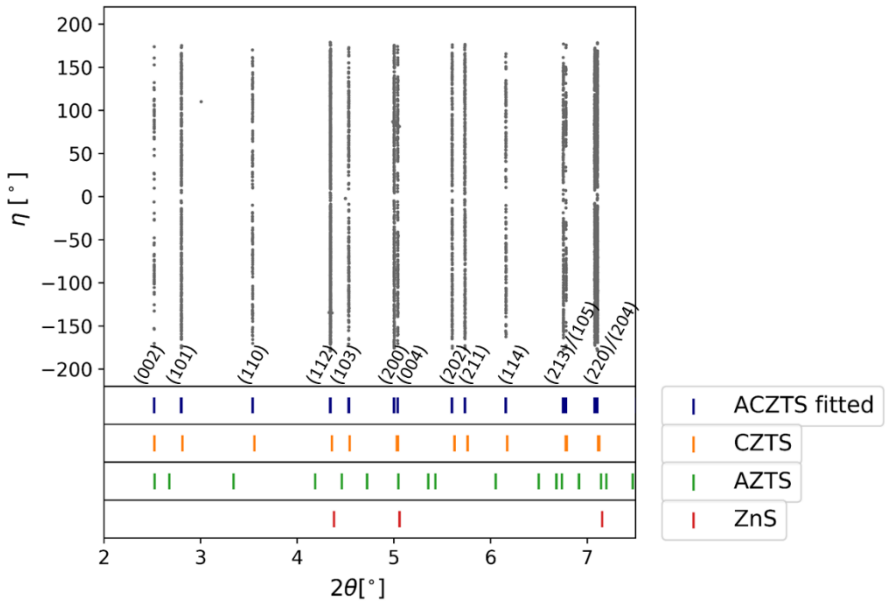

Figure 3.9. Azimuthal angles vs the two-theta angles of the diffraction spots corresponding to slice 1. The lines related to the fitted-AZCTS, CZTS, AZTS, and ZnS phases are shown.

3.3.5 Preliminary results and discussion

We report the number of grains found per layer in Table 3.1. Moreover, the number of peaks assigned to transformed tetragonal grains has increased from the limit imposed during indexing as the superstructure peaks are now included. The percentage of the reflections assigned to the grains is also reported together with the average unit cell parameters and the average unit cell volume.

Overall, on average, 37% of the reflections from all the datasets have been indexed. Unindexed reflections could belong to unidentified grains, which were rejected because of the tolerances during indexing. We observe that the unit cell lattice parameters are almost constant through the slices and agree with the fitted-ACZTS unit cell.

Additionally, we notice that the reflections of this dataset are not displaced, indicating the absence of strain. From slice 1, Figure 3.10a shows a minimum variation of the two-theta angle, 2θ, with the azimuthal angle, η, and with the rotation angle, ω, for all reflections in the (103) lattice plane.

The strain components, calculated from the diffraction data, as explained in section 2.4.6.1 of this thesis, have values in the order of 10^{-6} and 10^{-5}. When removing the calculated strain from the grains, the lattice parameters do not change severely. Figure 3.10(b-e) shows the distribution of the unit cell parameters measured and the “strain-free” unit cells. There is no

major change in the values of the unit cell values, disproving any possible strain in the ACZTS sample. Therefore, we can discard any strain effect on the sample.

Table 3.1. Results per slice indicating the number of retrieved grains and the corresponding unit cell parameters.

Slice	*No. grains*	*Min. peaks per grain*	*%indexed peaks*	*Average unit cell parameters ± standard error [Å]*	*Average unit cell volume ± standard error [Å³]*
1	49	68	29.1	a=5.4627 ± 0.0001 b=5.4629 ± 0.0001 c=10.8445 ± 0.0003	323.504 ± 0.012
2	63	65	36.6	a=5.4615 ± 0.0002 b= 5.4624 ± 0.0001 c=10.8455 ± 0.0003	323.549 ± 0.009
3	62	62	34.6	a=5.4615 ± 0.0002 b=5.4626 ± 0.0002 c=10.8452 ± 0.0004	323.552 ± 0.011
4	75	48	39.6	a=5.4612 ± 0.0005 b=5.4617 ± 0.0005 c=10.8453 ± 0.0006	323.485 ± 0.055
5	81	66	41.5	a=5.4614 ± 0.0002 b=5.4619 ± 0.0004 c=10.8458 ± 0.0007	323.527 ± 0.009
6	80	65	40.1	a=5.4614 ± 0.0002 b=5.4620 ± 0.0002 c=10.8448 ± 0.0004	323.503 ± 0.008
7	66	66	36.9	a=5.4615 ± 0.0001 b=5.4621 ± 0.0002 c=10.8446 ± 0.0003	323.509 ± 0.010
Total	476				

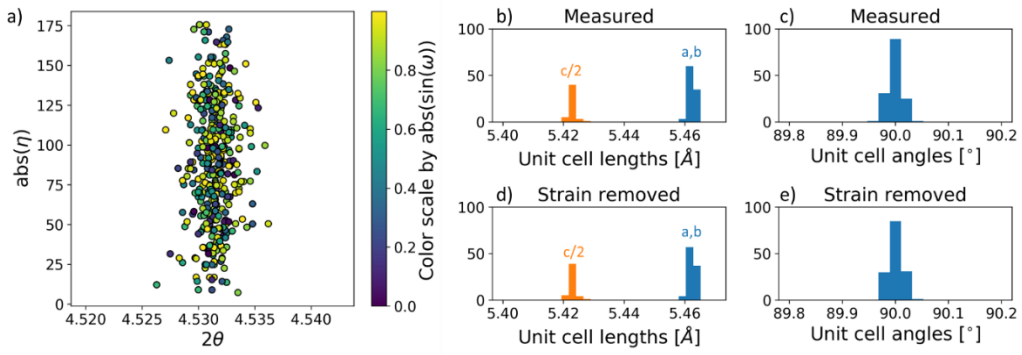

Figure 3.10. a) Absolute azimuthal angle vs two-theta angle of the diffraction spots in the (103) plane; the colours symbolize the variation of the ω-position. b) distribution of measured lattice parameters; c) distribution of measured unit cell angles; d) distribution of "strain-free" lattice parameters, d) distribution of "strain free" unit cell angles.

Moreover, we can only estimate a partial grain volume based on the reflections per slice. We estimate the real grain volume during the merging of the slices by considering all the grain reflections from the slices where the corresponding grain is located.

Figure 3.11 shows the distribution of the grain volume and grain radius per slice. The average volume is 0.380 µm^3, with a standard deviation of 0.322 µm^3. The average radius equivalent to a cylinder of height 0.5 µm (the film thickness) is 0.448 µm with a standard deviation of 0.203 µm. This size is smaller than the displayed in b, characterized by 1-3 µm grains. The grains are constrained by the vertical beam size (1.5 µm), which explains why the radius values for most of the grains are below 1 µm.

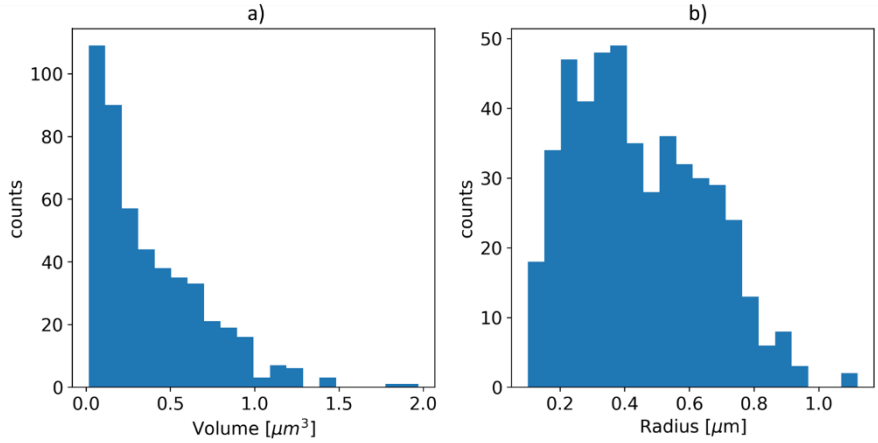

Figure 3.11 a) Grain volume b) Grain radius.

Concerning twin boundaries, we observe misorientation angles that correspond to Σ3 boundaries, characterized by the misorientation angle 70.53°, and the symmetrically equivalent misorientation angles 109.47°, 131.81°, and 180°. These angles are calculated and reported by [26] based on the tetragonal structure of CIGS (I-42d). Besides the Σ3-70.53°, their results also reveal Σ3-60°. However, ACZTS only has the former misorientation angle.

The reported angles in Table 3.2 deviate from the angles in [26] because of the tetragonal distortion c/2a<1. Here, we report the average misorientation angles per slice. The frequency of the Σ3-type boundaries is shown in Figure 3.12, where the misorientation angle 180° is the most recurrent with rotation axes $<111>_{tetragonal}$ and $<221>_{tetragonal}$.

In contrast to the studied PLD-CZTS solar cell with 41.2% of twins, the frequency of twin boundaries in ACZTS is higher with nearly 54%. Besides, the Σ3 - 131.56° - $<401>_{tetragonal}$ and Σ3 109.52° - $<201>_{tetragonal}$ are also more frequent than in CZTS.

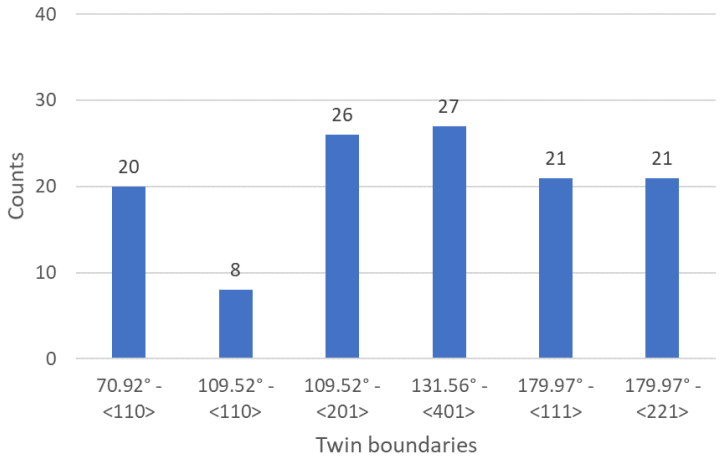

Figure 3.12.Frequency of Σ3 type boundaries

Table 3.2 Results of the type of Σ3 type boundaries per slice

Σ3 \ Slice	1	2	3	4	5	6	7	Total of twin pairs	twinned grains/ total grains × 100 [%]
70.92° - <110>	1	2	5	3	4	2	3	20	8.8
109.52° - <110>	1	0	0	2	3	1	1	8	3.5
109.52° - <201>	1	2	5	5	6	4	3	26	11.4
131.56° - <401>	5	4	1	2	7	5	3	27	11.8
179.97° - <111>	3	2	2	4	2	5	3	21	9.2
179.97° - <221>	2	3	3	6	1	4	2	21	9.2
Total	13	13	16	22	23	21	15	123	53.9

3.3.6 Conclusions and perspectives for further analysis

We indexed 456 grains that correspond to the ACZTS phase, from which 54% are twins. These numbers can change as the grains appearing in adjacent slices are merged, and the twin relations with other grains are recalculated. We apply the same methodology that was implemented for the PLD-CZTS solar cell. By following the same procedure, we show the adaptability of the precedent analysis. Also, we did not detect secondary phases nor strain.

As the merging procedure of the slices is not completed, we could only provide the partial volume of the grains, which are within the beam size limit. To calculate the volume, we could follow the strategy of adding the volumes as it was done for the PLD-CZTS solar cell. However, ACZTS grains are larger than CZTS grains, and therefore, one should consider the variations of the grain volume through the z-slices. After analyzing this transition, one can create a model that allows merging the volume accordingly.

3.4 PERSPECTIVES FOR THE CRYSTAL STRUCTURE REFINEMENT OF CZTS GRAINS

Structure refinements of individual grains have been achieved in the past for polycrystalline materials and powders [139]. From the ensemble of identified grains by 3DXRD, we can select one grain to be studied individually as a single-crystal. The assigned reflections to this grain can be used to refine the crystal structure and assess the position of the atoms in the unit cell.

The crystal structure of CZTS has been defined as kesterite (I-4) [49], [140], but because of the cation disorder of Cu^{+} and Zn^{2+} in the 2c and 2d Wyckoff position, CZTS has also been appointed to a modified stannite-type structure (I-42m) [141], also referred to as disordered kesterite. In this structure, Cu^{+} and Zn^{2+} occupy the 4d Wyckoff position (see Figure 3.13). However, the Cu^{+} and Zn^{2+} cations have very similar atomic X-ray scattering factors. Therefore, assessing the degree of disorder (atom occupancies) between these two atoms cannot be determined nor refined by conventional X-ray Diffraction. The refinement of the atom positions and occupancies of the CZTS crystal structure has only been achieved by neutron [46] or X-ray resonant anomalous crystal Diffraction [44]. Moreover, the transition from order to disordered kesterite has been studied by neutron scattering analysis [47], [142].

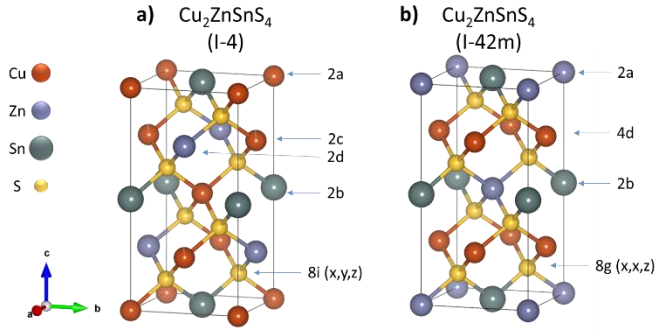

Figure 3.13. The crystal structure for a) kesterite and b) disordered kesterite. The crystal structures were drawn with the VESTA computer program [53].

We have isolated the reflections of one grain and pursue its structural refinement in collaboration with Assoc. Prof. Anders Ø. Madsen from the University of Copenhagen. The obtained refined crystal structure is compared with the examined structures by Ritscher *et al.* [47]. Their study investigated the order-disorder transition in stoichiometric CZTS annealed at different temperatures in the range of 473 - 623 K, employing neutron diffraction [47]. They concluded that the critical temperature corresponding to the transition from order to disordered kesterite is 552 K ±2 K. This temperature is far below the annealing temperature

of the CZTS films (833 K). Hence, one would expect that the refined crystal structure of the grain corresponds to the disordered kesterite.

They also provide detailed information of their refinements in the supplementary material, and their crystal structures have been included in the ICSD collection. We examine the crystallographic information files of the prospect samples, focusing on the sulfur positions, the bond lengths of the Cu (2c) - S, and the occupancies of the Cu (2c). We aim at finding a correlation between the extracted information and our refined structure that can reveal some evidence about the Cu/Zn occupancies and thereby about the order/disorder in the structure of our grain.

We present the approach for normalizing the intensities of our grain and the followed refinement method. Finally, we compare the refined structure of the grain with the published crystal structures.

3.4.1 Normalization of the intensities of the grain dataset.

From the collected diffraction data at APS, we identify the reflections using an intensity threshold of 200 arb. units. Their intensity, detector positions, Bragg angle 2θ, azimuth angle η, and rotation angle ω (around the z-axis) are saved into a list used by the ImageD11 software to index and assign the reflections to the grains. The details of the indexing are explained in section 3.1 of this thesis.

We select a candidate grain from the first scanned slice with 220 reflections. Moreover, the reflections are not shared with any other grain from the actual slice or adjacent slices.

We correct the intensity of the reflections for the Lorentz and polarization factors, as described in [139], using equation (3.2), where k is the crystal scale factor. The definition of the Lorentz factor is given by equation (3.3), where 2θ is the Bragg angle, and η is the azimuthal angle measured in the plane of the image with respect to the rotation axis. Subsequently, the polarization factor is defined in equation (3.4), where p=1 is the degree of horizontal polarization, and η' is the azimuthal angle with respect to the horizontal plane.

$$k|F|^2 = \frac{I}{LP} \tag{3.2}$$

$$L = \frac{1}{sin(2\theta)|sin^2(\eta)|} \tag{3.3}$$

$$P = \frac{1}{2}[1 + cos^2(2\theta) - p\ cos(2\eta')sin^2(2\theta)] \tag{3.4}$$

The intensity standard errors σ^2 are calculated using equation (3.5), where σ_m is the machine error set to 0.05. It represents analogue-digital noise, re-absorption, etc.

$$\sigma^2_{k|F|} = \frac{(I + \sigma_m^2 I^2)^{1/2}}{LP} \tag{3.5}$$

Finally, an ASCII file with the miller indices h, k, l, the corresponding intensity, and standard error is obtained.

Figure 3.14a shows the normalized intensity of the reflections of the selected grain and the 2θ angle positions. Moreover, Figure 3.14b shows the variation of the intensities while rotating the sample. We observe a drop in the intensity values at ω=-100°. This discrepancy is also recognized during the refinement, with large inconsistencies of the intensity values between equivalent reflections.

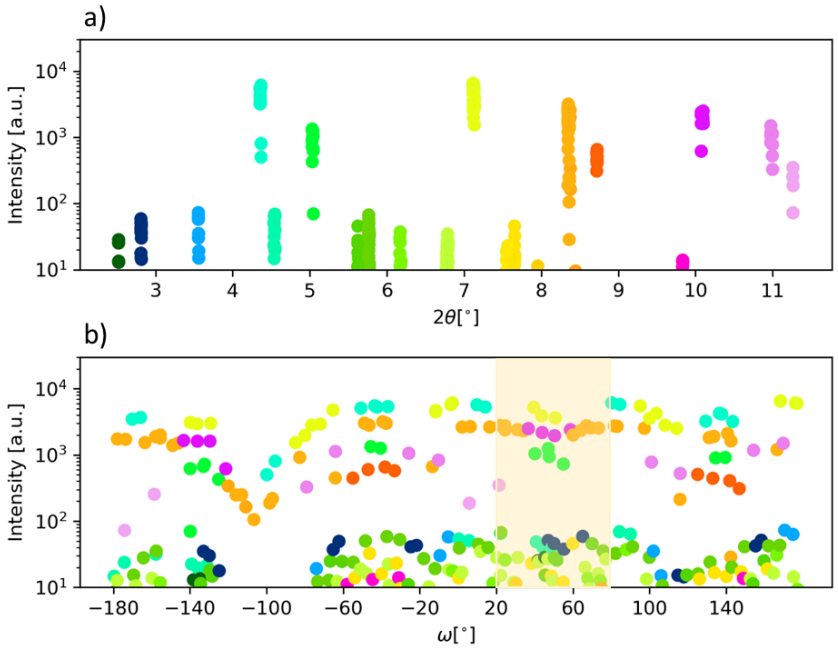

Figure 3.14. The intensity of the reflections coloured by the (hkl) lattice plane in correspondence to a) the 2θ angle, b) the rotation angle ω. The shadowed area corresponds to the range where the reflections are taken for refinement.

3.4.2 Crystal structure refinement

It is common in single-crystal diffraction to apply a data-collection strategy that scans a certain range of the scattering space, ensuring that all unique reflections are collected, including certain redundancy. The present data were collected in a 360° sweep of the ω-

angle. Nonetheless, the deviations in intensities prompt us to choose a smaller subset corresponding to the 20°-80°. This fragment still corresponds to a full set of data, but with a better internal agreement between symmetry-equivalent reflections than what was observed for the full dataset.

The model was refined against the reflections within the space group I-4 without introducing any disorder. The starting model was obtained from Ritscher *et al*. In a least-squares refinement using the program Shelxl [143], the sulfur atom position and an isotropic displacement parameter, common to all atoms, were refined against 33 unique reflections, giving an agreement index R1 = 0.167. Attempts to refine atomic occupancies and/or individual atomic displacement parameters failed, probably due to the aforementioned low data quality.

The results of the refinement are listed in Table 3.3.

Table 3.3. Refined structural parameters of the isolated grain.

Atom	Wyckoff	x	y	z	Occ.	Uiso
Cu1	2a	0	0	0	1	0.01
Cu2	2c	0	1/2	1/4	1	0.01
Zn1	2d	0	1/2	3/4	1	0.01
Sn1	2b	0	0	1/2	1	0.01
S1	8g	0.752	0.746	0.875	1	0.01

3.4.3 Correlations with the ICSD compounds

Certainly, without resonant scattering information, conventional XRD cannot distinguish between Cu and Zn, thereby refining the relative occupancies of Zn and Cu at the 2c and 2d sites. However, we can still compare our results with the studied structures by Ritscher *et al.* and hypothesize whether our grain has an ordered or disordered kesterite structure.

First, we look at the sulfur positions in the 12 published structures listed in Table 3.4. In Figure 3.15(a-c), we plot the sulfur positions as a function of the annealing temperature of the samples. We observe a linear trend in all the coordinates before the transition temperature. We depict this trend with an arbitrary line to ease its visualization. Nevertheless, not all the data points agree with this trend, and some samples remain as outliers. Only for the sulfur z-coordinate, we observe this linearity before the sample approaches the temperature transition. After that, by ignoring N5 and N8 (I-42m), the points oscillate around z=0.874.

The sulfur coordinates of the refined grain are shown in green. The x coordinate aligns with the x-coordinate of the N8 (I-4) and N9 (I-4) samples. Both samples were synthesized above the disorder/order transition temperature and were refined with both space groups, (I-4) and (I-42m). The y-coordinate is far from the range of the samples' coordinates, so it is not easy to draw any correlation. Even the low-temperature samples (N1-N7) have a much higher y-coordinate. For the z-coordinate, our refined grain could relate to the N9 (I-4) and N8 (I-42m) samples, as both are above the transition temperature and the z-coordinate discrepancy is ±0.001Å.

Next, the bond lengths between the 2a and 4d positions of the copper and the 8g and 8i positions of the sulfur are listed in Table 3.5. The bond lengths of Zn (2c) – (8g) have the same value as Cu(2c)-S(8g) as this is the shared site between Cu and Zn, only the occupancies vary following Zn(2c) = (1-Cu(2c)). Therefore, they are not shown here.

In Figure 3.15d, we draft the Cu(2c) –S(8g) bond lengths according to the Cu(2c) occupancies in the kesterite structure. The bond length of the Cu(4d) –S(8i) vs the Cu(4d) occupancy of the disordered kesterite is also depicted. In this graph, we represent the bond length of the refinement of our grain as the green line as the occupancy cannot be accurately determined. Most of the Cu(2c) –S(8g) bond lengths in the (I-4) group are below 2.343Å, except for the N6 sample. The Cu(4d) –S(8i) bond lengths in the (I-42m) group are above this value, as well as our refined grain's bond length.

Based on these observations, we resolve that our grain has a disordered kesterite structure (I-42m), which agrees with the hypothesis that the film grains are likely to adopt this structure because of the high annealing temperature. The N8 and N9 samples refined with this structure have occupancies of 0.5, which could very well describe the occupancies in our grain crystal structure.

Table 3.4. The sulfur coordinates taken from the supplementary information [47].

Sample	T(K)	ICSD	Space group	a,b [Å]	c[Å]	Wyckoff	Sx	Sy	Sz
N1	473	239674	I -4	5.43373	10.8392	8 g	0.7584	0.7576	0.8726
N2	493	239675	I -4	5.43358	10.8383	8 g	0.7567	0.7563	0.8732
N3	503	239676	I -4	5.43321	10.8417	8 g	0.753	0.76	0.87
N4	513	239677	I -4	5.43382	10.8373	8 g	0.757	0.758	0.874
N5	523	239678	I -4	5.4326	10.8433	8 g	0.746	0.754	0.8759
N6	533	239679	I -4	5.43355	10.8397	8 g	0.7599	0.7551	0.8742
N7	543	239680	I -4	5.4327	10.8447	8 g	0.747	0.7557	0.8741
N8 (I-4)	553	239681	I -4	5.43339	10.842	8 g	0.752	0.7586	0.874
N8(I-42m)	553	239682	I -4 2 m	5.43344	10.8421	8 i	0.7566	0.7566	0.876
N9(I-4)	623	239683	I -4	5.43256	10.8446	8 g	0.752	0.7583	0.8741
N9(I-42m)	623	239684	I -4 2 m	5.43259	10.8445	8 i	0.756	0.756	0.8737
N10	473	239685	I -4	5.43341	10.8376	8 g	0.75	0.7588	0.8738
N10(ordered)*	473	239686	I -4	5.43336	10.8377	8 g	0.753	0.7589	0.8724

*N10 undergoes a second annealing step at 473K for two extra weeks

Table 3.5. The calculated bond lengths of Cu(2c)-S (8g) and Cu(4d)-S(8i) and their occupancies.

Sample	T(K)	Space group	Cu(2c) - S(8g)	Cu(4d) - S(8i)	Occ. Cu(2c)	Occ. Cu(4d)
N1	473	I -4	2.339		0.95	
N2	493	I -4	2.341		0.95	
N3	503	I -4	2.334		0.93	
N4	513	I -4	2.342		0.93	
N5	523	I -4	2.331		0.89	
N6	533	I -4	2.362		0.82	
N7	543	I -4	2.324		0.70	
N8 (I-4)	553	I -4	2.324		0.50	
N8 (I-42m)	553	I -4 2 m		2.358		0.502
N9 (I-4)	623	I -4	2.326		0.51	
N9 (I-42m)	623	I -4 2 m		2.343		0.505
N10	473	I -4	2.316		1.01	
N10 (ordered)*	473	I -4		2.316		0.99

*N10 undergoes a second annealing step at 473K for two extra weeks

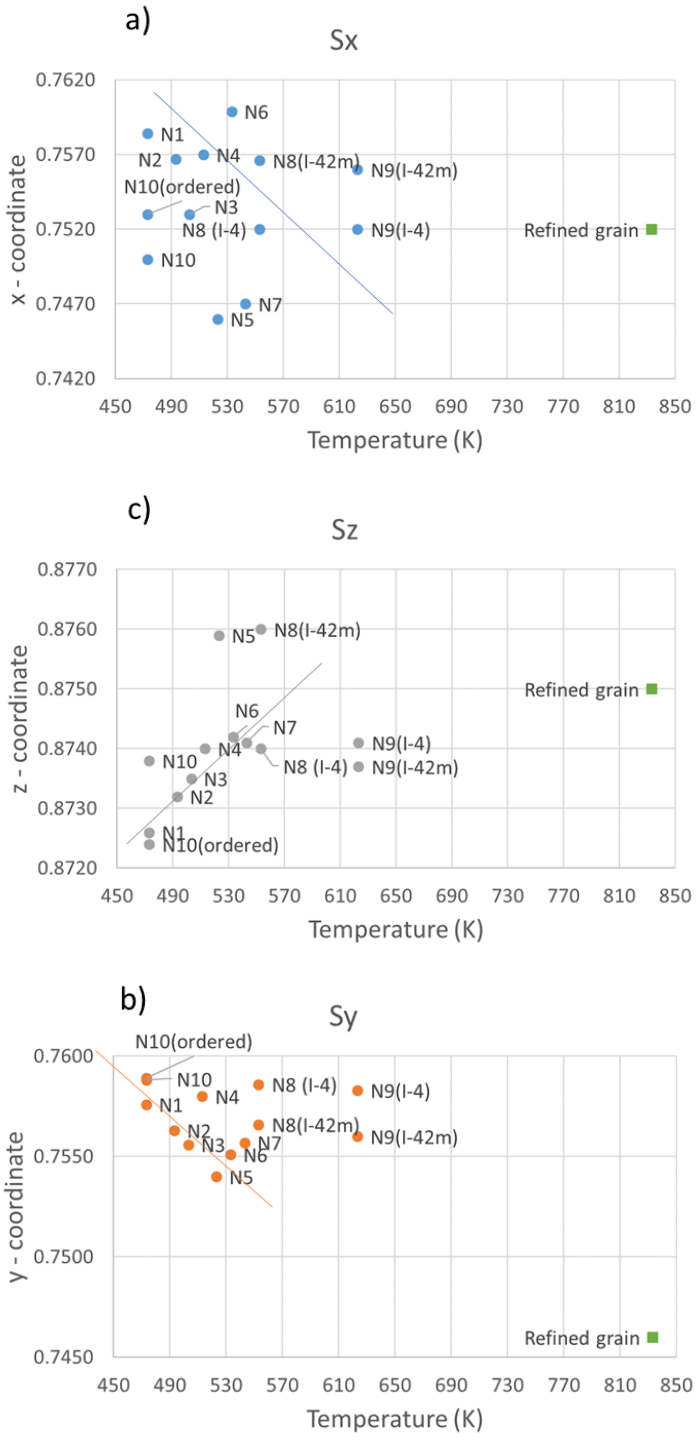

Figure 3.15. Position of the Sulfur atom according to the annealing temperature of the sample: a) x-coordinate, b) y-coordinate, c) z-coordinate.

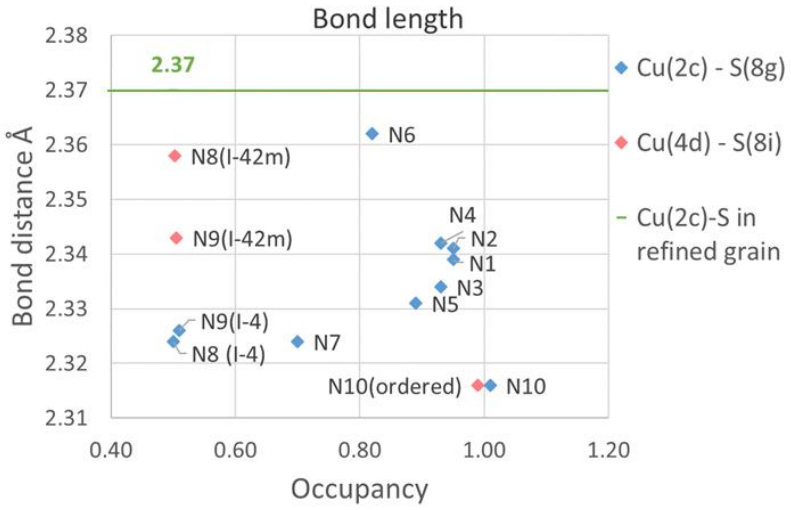

Figure 3.16. The bond length between the Cu(2c) and the S(8g) in ordered kesterite and Cu(4d) and S(8i) in disordered kesterite according to their occupancy

3.4.4 Summary and outlook

We have compared the results of our refinement with the structures from Ritscher's investigation. We resolve that our grain has the I-42m structure based on the bond length 2.37 Å between the Cu (4d) and S(8i). We can thereby infer that the occupancies in the grain crystal structure must be close to 0.5, as it is reported in Ritscher's refinements. Although we cannot determine the atom occupancies directly, we can still determine the bond lengths between the atoms.

The application of refinement methods is constrained by the quality of the data and the number of reflections. In our case, the inconsistency in the intensity of the equivalent reflections did not allow us to use the whole dataset. Nevertheless, we overcome this constraint by selecting a subset of the reflections.

A similar approach could be taken for the rest of the grains. However, many grains have twins sharing reflections between them. It requires more sophisticated tools to achieve the structure refinement in twin cases.

Another potential dataset to perform the crystal structure refinement is isolating the reflections of one grain from the ESRF data. In a first trial, we have extracted the diffraction images corresponding to a grain and its diffracted spots. After that, the images were input to CrysAlis, software commonly used for single crystal diffraction, to obtain a better integration of the reflections' intensities. However, CrysAlis could not index the reflections according to the grain orientation matrix and the unit cell established by ImageD11, the polycrystalline

indexing software. Additionally, twinned reflections appeared in the images. The results were inconclusive.

On the other hand, we can follow the approach presented in this section. We would need to extract the list of intensities from the sinogram and establish a method for integrating and normalizing the intensities. Moreover, selecting a grain without twinned reflections would also facilitate the structure refinement.

3.5 3DXRD ANALYSIS OF A CIGS ABSORBER LAYER

3DXRD Experiment at APS, beamline 1-ID (November 2018)

3.5.1 Introduction

$Cu(In, Ga)Se_2$ (CIGS) solar cells have reached 23.35% efficiency [144], becoming the lead technology among the chalcogenide thin-films. The absorber layer is typically fabricated through a three-stage co-evaporation process. Through this process, a $Cu(In, Ga)_5Se_8$ phase forms, then a $Cu(In, Ga)_3Se_5$ phase, and finally, the CIGS phase [145], [146]. However, precipitates of the $Cu(In, Ga)_3Se_5$ phase may remain as shown in Neutron diffraction experiments [147]. These copper-poor precipitates appear at the surface of the CIGS films with n-type conductivity when Ga-content<0.3% [145]. Cu-poor CIGS compounds form buried pn-junctions reducing interfacial defect density and suppressing interfacial recombination processes [148].

In this study, we use 3DXRD to identify the different crystallographic phases of CIGS and analyze the microstructure of the absorber layer. We compare the obtained X-ray diffraction pattern to the available CIGS structures reported in the Inorganic Crystal Structure Database (ICSD). We index the reflections to obtain the grain orientations and verify possible twin relations between grains that share reflections.

3.5.2 Crystallographic aspects of CIGS and its defective derivatives

The crystal structure of $Cu(In_{1-x}Ga_x)Se_2$ has been studied in bulk as a powder and as a single crystal to understand the structural variations of the x=Ga/(Ga+In) ratio. It has been concluded that CIGS adopts the tetragonal chalcopyrite structure (I-42d). Moreover, the tetragonal lattice parameters decrease as the Ga-content increases, with Ga^+ replacing In^+ on the same crystallographic site. Furthermore, copper-poor compounds with stoichiometry $Cu_{1-z}(In_{0.5}Ga_{0.5})_{1+z/3}Se_2$ show a lower symmetry with space group (I-42m) [141], [149], [150].

3.5.3 Sample description

We investigate a sample with a device structure consisting of a polyimide substrate coated by a Mo back contact (500 nm). The CIGS layer (2.5-3 µm) is coated via co-evaporation described by [151]. The cell is completed by adding a CdS buffer layer (20-50 nm), then a window layer ZnO:Al (250 nm), followed by a metal grid as front contacts, and finally, a MgF_2 anti-reflective coating.

We peeled off a flake from the device, avoiding the metal grids, and glued it to a flattened nickel wire (Figure 3.17a). A focused Ga^+ beam milled the tip to an approximate 40 µm wide and 70 µm height (Figure 3.17b, c). It would be desirable to use a different beam source instead of Ga^+ since Ga^+ can be implanted and generate structural damage in the absorber layer [152][153]. However, the crossbeam microscope at DTU Energy is only equipped with a Ga^+ beam source.

3.5.4 Experiment description

The experimental setup is the same implemented for the analysis of the PLD- CZTS solar cell depicted in section 3.1 of this thesis. The sample was illuminated with a monochromatic beam (52 keV, 1.2 µm (V) x 200 µm (H)). The normal to the film plane is parallel to the beam. A far-field detector records the diffraction pattern while rotating the sample in a range of -180° to 180° with a step of 0.1° and an exposure time of 0.8 s per frame. A total of 3600 images are obtained during the one hour scan. Moreover, we measure the standard powder LaB_6 to fit the detector parameters (sample-detector distance and tilts).

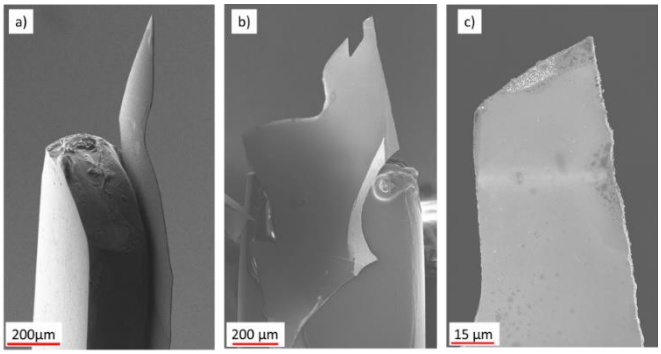

Figure 3.17. a) Flake of CIGS sample glued to Ni-wire before FIB milling. b) SEM image after FIB milling and after being exposed to the X-ray beam at APS. c) The lighter grey area suggests the position where the X-ray line beam was focused.

3.5.5 Data Analysis

A peak search procedure through the diffraction images collects the reflections with an intensity above the threshold values 200, 500, and 1000 arb. units. After collecting the reflections from the diffraction patterns (Figure 3.18a), we obtain a list containing the reflection detector coordinates (Figure 3.18b), the rotation angle ω, the Bragg angle 2θ, and the azimuthal angle η (Figure 3.18c). Then, we calculate the scattering vectors in the 3D reciprocal space, as shown in Figure 3.18d.

ImageD11 indexes the reflections and assigns them to a determined orientation (a grain). In a preliminary assessment, the following three different tetragonal cells could fit the two-theta positions in the diffraction pattern: a stoichiometric CIGS and two Cu-poor compounds with stoichiometry $Cu_{1-z}(In_{0.5}Ga_{0.5})_{1+z/3}Se_2$ with z=0.4 and z=0.7:

- "CIGS" (I-42d): a=5.6959 Å, c=11.3362 Å (ICSD No.190356)
- "CIGS, z=0.4" (I-42m): a=5.6501 Å, c=11.1486 Å (ICSD No.214512)
- "CIGS, z=0.7" (I-42m): a=5.6660 Å, c=11.2725 Å (ICSD No. 247514)

We index one phase at a time following the order in the above list. We sort the grain reflections, and finally, we perform symmetry operations among grains that share reflections to verify any possible twin relations.

We determine the volume following the methodology described in section 2.4.5 of this thesis. The twin relations are computed based on the right pure-rotation R, and the right stretch-tensor U_s derived from the polar decomposition of the deformation tensor F. The details of these calculations are explained in section 2.4.7 of this thesis.

3.5.6 Results and discussion

Preliminary assessment

A high-resolution powder diffraction pattern is obtained by plotting a histogram of the 2θ positions, weighted by the intensity of the reflections (Figure 3.19a). The reflections are distributed in bins with a width of 0.001° within a range of two-theta= [2°, 12°]. The most prominent peaks correspond to planes (112), (220)/(204), (312)/(116), and (303)/(215). It appears that all these planes are composed of three peaks. We feature the plane (112) in Figure 3.19b, as well as the planes (220)/(204) in Figure 3.19c. We compare the two-theta positions with the phases from the Inorganic Crystal Structures Database (ICSD). Those that agree most with the mentioned planes are listed in Table 3.6 and shown in Figure 3.19.

A preliminary assessment of the possible phases in the sample reveals that the chalcopyrite structure (I-42d) is present. Despite the fact that the superstructure reflections of the Cu-poor CIGS compounds are absent, these compounds corresponding to the space group (I-42m) could still be present. This is because the planes (002), (110), and (114) may be neglected during the peak search if their intensities are below the established thresholds.

As observed in Figure 3.19, the phases that coincide with the planes (112) and (220)/(204) are the phases with ICSD collection number 190576, 247514, and 247512.

According to the reference [154], the 190576 crystal structure is chalcopyrite and correlates to an initially stoichiometric composition sample $CuGa_{0.5}In_{0.5}Se_2$ with a final (Ga, Se)-rich

and (Cu, In)-poor composition. We refer to this phase as the chalcopyrite CIGS or simply CIGS.

The 247514 and 247512 crystal structures are reported as "modified-stannite" structures with stoichiometry $Cu_{1-z}(In_{0.5}Ga_{0.5})_{1+z/3}Se_2$, where z represents the copper deficiency ratio [150]. These phases have ratio z=0.4 and z=0.7, respectively. Therefore, we refer to them as "CIGS, z=0.4" and "CIGS, z=0.7".

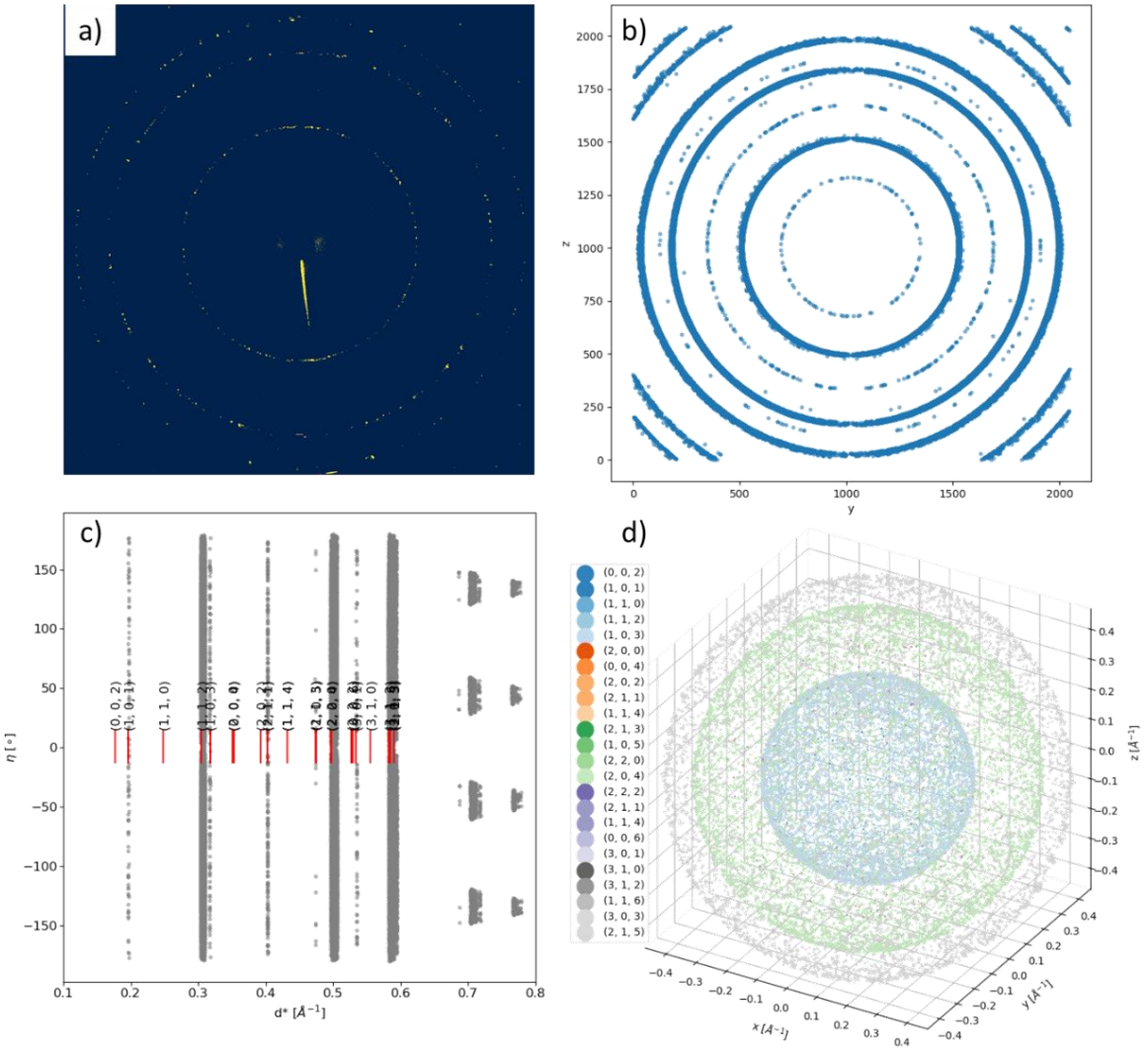

Figure 3.18 a) Sum of 100 diffraction patterns corresponding to 10 degrees rotation. b) Plot showing the position of the diffraction spots on the detector. c) Azimuthal projection of the diffraction spots and the position of the rings using structure ICSD-190356 $Cu_{0.89}(In_{0.48}Ga_{0.52})Se_2$. d) Scattering vectors in reciprocal space.

Table 3.6. Crystallographic phases from the ICSD database that match the diffraction pattern and ordered according to decreasing unit cell volume

Chemical Structure	Space group	Lattice parameters a=b, c [Å]	Unit cell volume	ICSD	Reference
$Cu_{0.89}(In_{0.48}Ga_{0.52})Se_2$	I-42d	a=5.6959, c=11.3362	367.78	190356	[155]
$Cu_{0.87}(In_{0.46}Ga_{0.54})Se_2$	I-42d	a=5.6924, c=11.3124	366.56	190350	
$Cu_{0.96}(In_{0.44}Ga_{0.56})Se_2$	I-42d	a=5.6864, c=11.2963	365.27	190357	
$Cu(Ga_{0.5}In_{0.5})Se_2$	I-42d	a=5.6847, c=11.2817	364.58	169230	[156]
$Cu_{0.815}In_{1.48}Ga_{0.9}Se_4$ $Cu(In_{0.6}Ga_{0.4})_3Se_5$*	I-42m	a=5.663, c=11.304	362.51	181414	[157]
$Cu_{0.6}(Ga_{0.5}In_{0.5})_{1.133}Se_2$	I-42m	a=5.666, c=11.2725	361.89	247514	[150]
$Cu_{0.835}In_{1.23}Ga_{1.24}Se_4$ $Cu(In_{0.5}Ga_{0.5})_3Se_5$*	I-42m	a=5.637, c= 11.241	357.19	181415	[157]
$Cu(Ga_{0.82}In_{0.18})Se_2$	I-42d	a=5.6501, c=11.14862	355.9	247512	[150]
$Cu_{0.25}(Ga_{0.5}In_{0.5})_{1.25}Se_2$	I-42m	a=5.6166, c=11.214	353.76	247517	

*initial sample composition

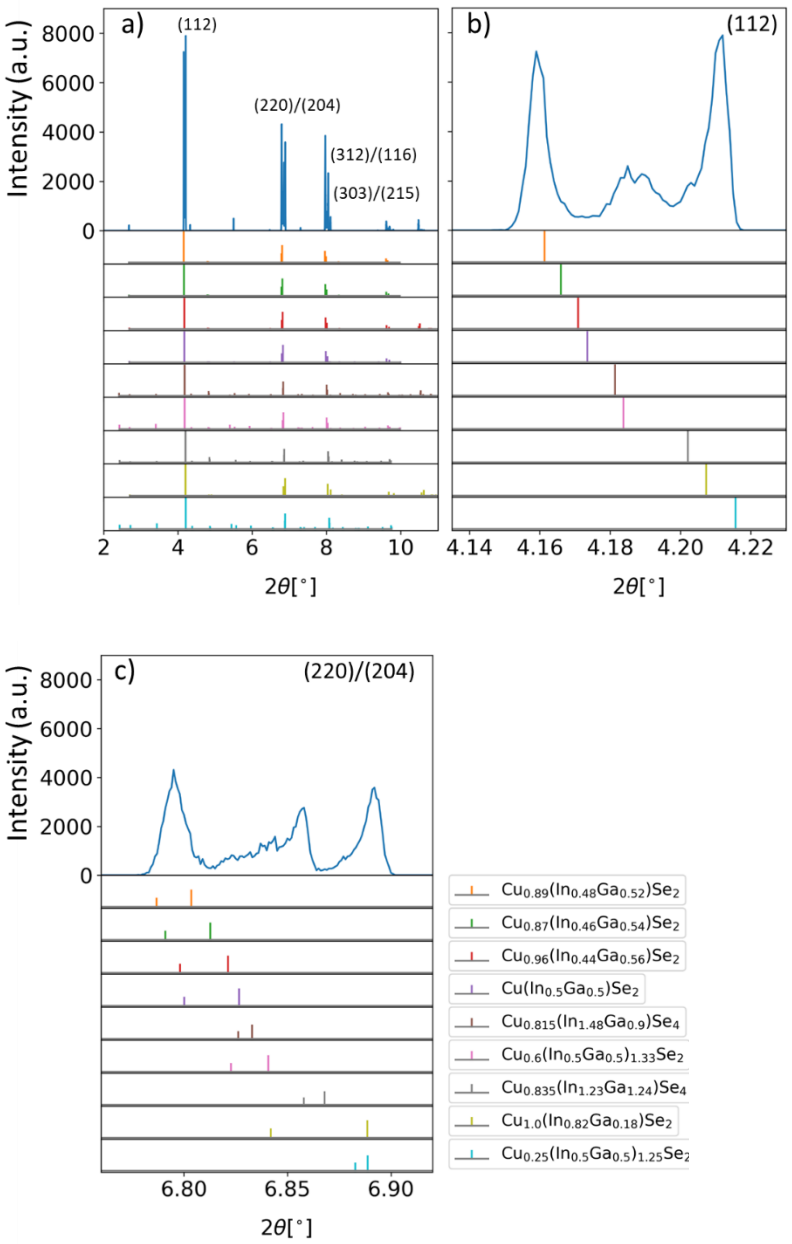

Figure 3.19 a) Histogram of 2θ positions weighted by the intensity of the reflections. b) Zoom in on the plane (112), and c) Zoom in on the plane (220)/(204). Below the histograms, the most likely phases are illustrated.

Indexing

We start the indexing of the reflections based on the three identified phases from the preliminary assessment. ImageD11 can index one phase at a time, so the indexing is done in three rounds. In the first round, we index the reflections with the CIGS phase. We identify 84 grains with more than 54 reflections per grain. The second turn corresponds to the "CIGS,

z=0.4". We find 23 grains with more than 68 reflections per grain. Finally, the "CIGS, z=0.7" phase is indexed, collecting 50 grains with more than 64 reflections per grain.

After the three indexing rounds, only 30% of the reflections are assigned to grains from a total of 48426 reflections (See Figure 3.20b). This indicates that more grains are to be found, but they can be ignored if they do not pass the threshold of the number of reflections per grain above 50. This is not optimal for small grains, whose faint reflections are missing due to the peak search, and thus, they will be indexed with a low number of reflections.

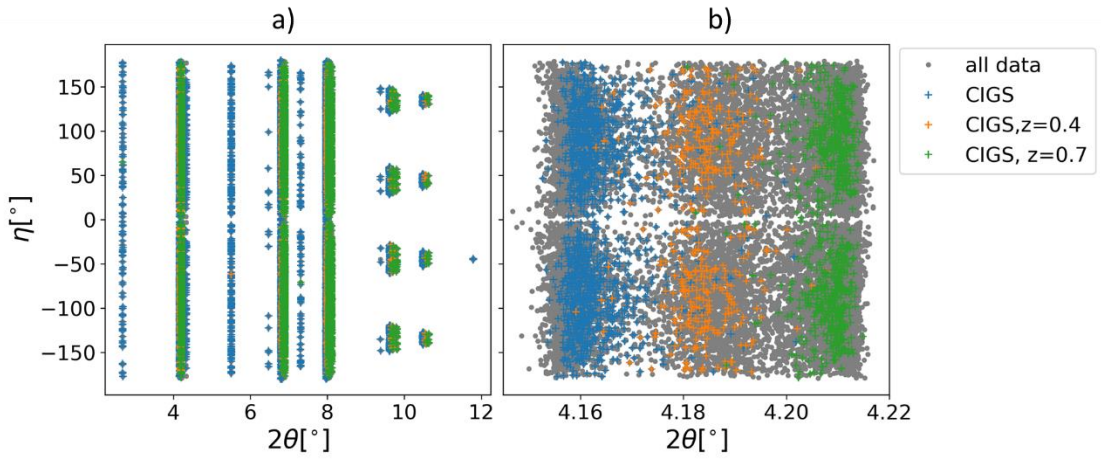

Figure 3.20 a) Plot of the η angle vs 2θ angle of the indexed reflections and b) Zoom in on the plane (112).

Grain size distribution

Here, we present the calculated grain volume (Figure 3.21a). We also estimate the corresponding equivalent-sphere radius for the grains obtained from each indexing process (Figure 3.21b). The average grain volume and radius are given in Table 3.7. The radius is obtained assuming a cylindrical volume for the CIGS grain with a height of 2 µm, the film thickness.

Overall, the "CIGS, z=0.7" and "CIGS, z=0.4" phases have larger grains than the CIGS. Twinning could explain the differences in the grain volumes. When calculating the volume of twinned grains, the intensities of the shared reflections are not taken into account in the calculations. Most CIGS grains are twinned, whereas the other phases have fewer cases of twinning.

The average grain sizes reported by Abou-Ras *et al.* for CIGS grown by rapid thermal processing are in the range of 0.47-0.73 µm [26]. We have measured slightly larger grains in our CIGS sample, on average, 0.74 µm accounting for the three phases. Moreover, we observe a similar log-normal distribution, as described in [26].

Table 3.7 Average grain volume and radius for each phase

Phase	Number of grains	Average Grain volume (µm^3)	Average grain radius (µm)
CIGS	84	1.43	0.66
CIGS, z=0.4	23	4.94	0.98
CIGS, z=0.7	50	2.30	0.77
Total	157	2.22	0.74

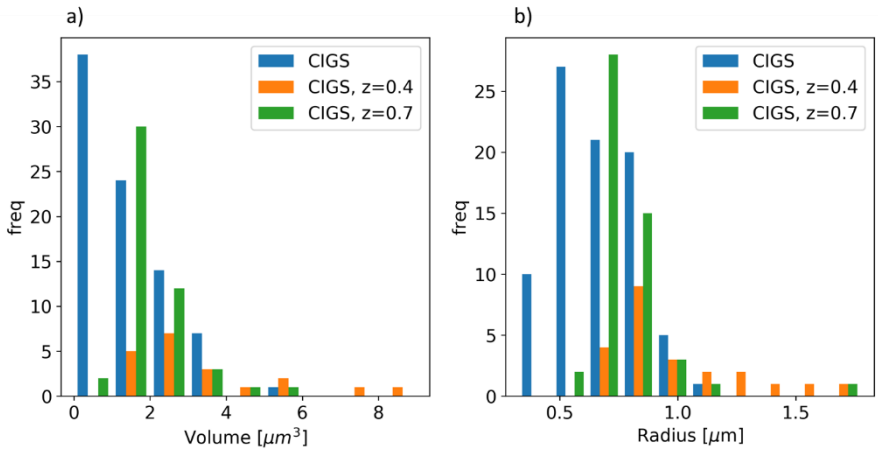

Figure 3.21. a)Volume and b) radius of grains for each indexing process.

Twinning

For CIGS, the observed types of twinning are Σ3 characterized by rotation angles around 60° and 70.53°, and Σ9 twin boundaries with the misorientation angle 39°. For the Cu-poor phases, "CIGS, z=0.4" has Σ3-60° and Σ3-70.53° twin boundaries, whereas "CIGS, z=0.7" only has Σ3-70.5°.

We estimate the proportion of twinning among the phases by dividing the number of twins by the total grains of the corresponding phase. CIGS has the highest proportion of twinning with 82%, followed by "CIGS, z=0.7" with 34%, and "CIGS, z=0.4" with 26%.

Overall, Σ3-70.53° twin boundaries are the most frequent type among the twinned grains (see Figure 3.22). We found that some grains have multiple twin operations, which can be different. For example, grain 3 and 37 have a Σ3-70.53° twin boundary, whereas grain 3 and 83 have Σ3-60°. However, we did not compare grains across phases; therefore, twinning between phases should not be discarded.

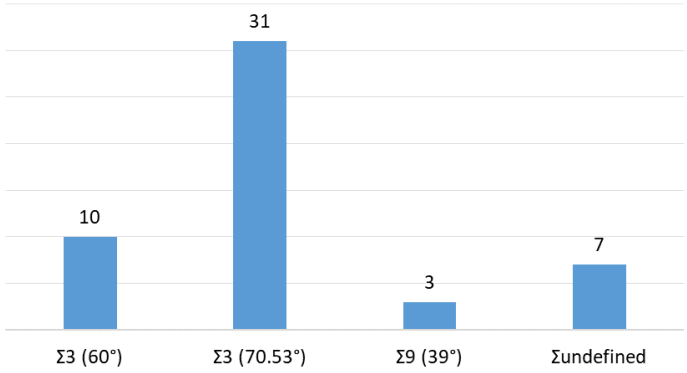

Figure 3.22 Distribution of twin boundaries in the scanned area

These types of twin boundaries have already been observed by EBSD, [26] [158], reporting the symmetrically equivalent misorientations. The misorientations symmetrically equivalent identified in our sample are reported in Table 3.8. We also found symmetry relations, which share misorientation angles similar to the ones in Σ9 (96.3°, 141.1°, 152.9°, 179.9°), but the smallest angles in the different cases were 67.1° and 89.95° instead of the 39°. Additionally, an unidentified twin boundary with a rotation angle of 120° and axis [221] perpendicular to (112) is also observed. These cases are labelled as Σunidentified in Figure 3.22.

Table 3.8 Misorientations symmetrically equivalent

Σ3	**Σ3**	**Σ9**
60° - <221>	**70.53° - <110>**	**39° - <110>**
70.53° - <201>	109.4° - <110>	96.37° - <101>
131.78° - <101>	109.4° - <201>	141.08° - <110>
131.81° - <210>[1]	131.67° - <401>	152.91° - <801>
146.53° - <223>	179.58° - <111>	179.86° - <441>
146.53° - <621>	179.99° - <221>	179.97° - <112>
179.86°-<241>		

[1]From [26], not observed here.

The calculated list of twinned grains can be found in Table 3.9. The chalcopyrite and the modified-stannite structures have a tetragonal deformation with a ratio c/a ≈ 2. Therefore, the angles in Table 3.9 deviate from the corresponding rotation angles by 0.01°, and the twin boundaries can be referred to as (near) Σ3.

Table 3.9 List of twinned grains with the corresponding percentage of shared reflections (%npks), twin operation (rotation angle, rotation axis [uvw], and transformed plane (hkl)).

Phase	*g1*	*g2*	*%shared reflections*	*angle*	*u*	*v*	*w*	*(h*	*k*	*l)*	*sigma*
CIGS	12	76	6	70.38	0	-2	1	0	-1	2	Σ3 (60deg)
CIGS	43	63	14	70.57	2	0	-1	1	0	-2	Σ3 (60deg)
CIGS	5	19	11	70.59	0	2	1	0	1	2	Σ3 (60deg)
CIGS, z=0.4	98	105	3	131.78	0	1	1	0	1	4	Σ3 (60deg)
CIGS	17	31	6	146.46	-2	-2	3	-1	-1	3	Σ3 (60deg)
CIGS	14	33	5	146.52	-6	-2	-1	-3	-1	-2	Σ3 (60deg)
CIGS	9	62	7	146.53	-2	2	-3	-1	1	-3	Σ3 (60deg)
CIGS	3	83	7	146.62	-6	-2	1	-3	-1	2	Σ3 (60deg)
CIGS	60	76	2	179.74	2	4	-1	1	2	-2	Σ3 (60deg)
CIGS	9	34	11	179.98	2	-4	-1	1	-2	-2	Σ3 (60deg)
CIGS	42	74	20	70.54	1	-1	0	1	-1	0	Σ3 (70deg)
CIGS	0	4	27	70.57	-1	1	0	-1	1	0	Σ3 (70deg)
CIGS	21	54	30	70.63	-1	-1	0	-1	-1	0	Σ3 (70deg)
CIGS	10	71	10	70.75	-1	1	0	-1	1	0	Σ3 (70deg)
CIGS, z=0.7	119	143	10	71.06	1	-1	0	1	-1	0	Σ3 (70deg)
CIGS, z=0.7	112	147	10	108.87	-1	1	0	-1	1	0	Σ3 (70deg)
CIGS, z=0.7	112	135	10	108.96	-1	1	0	-1	1	0	Σ3 (70deg)
CIGS, z=0.7	115	146	10	109.00	1	-1	0	1	-1	0	Σ3 (70deg)
CIGS	18	53	23	109.34	1	1	0	1	1	0	Σ3 (70deg)
CIGS	41	64	24	109.43	-1	1	0	-1	1	0	Σ3 (70deg)
CIGS	5	51	33	109.46	1	1	0	1	1	0	Σ3 (70deg)
CIGS	16	29	18	109.51	-1	1	0	-1	1	0	Σ3 (70deg)
CIGS	16	26	28	109.52	-1	-1	0	-1	-1	0	Σ3 (70deg)
CIGS, z=0.7	116	123	4	109.61	-2	0	1	-1	0	2	Σ3 (70deg)
CIGS, z=0.7	118	141	9	109.77	0	-2	-1	0	-1	-2	Σ3 (70deg)
CIGS, z=0.7	112	145	7	109.90	0	2	1	0	1	2	Σ3 (70deg)
CIGS, z=0.7	132	139	8	131.42	-4	0	-1	-1	0	-1	Σ3 (70deg)
CIGS, z=0.7	108	153	10	131.46	0	-4	-1	0	-1	-1	Σ3 (70deg)
CIGS	31	82	30	131.68	0	4	1	0	1	1	Σ3 (70deg)
CIGS	2	70	18	131.72	0	-4	1	0	-1	1	Σ3 (70deg)
CIGS	35	80	24	131.72	0	4	1	0	1	1	Σ3 (70deg)
CIGS, z=0.4	84	87	7	131.74	-4	0	-1	-1	0	-1	Σ3 (70deg)
CIGS	15	75	23	131.77	-4	0	1	-1	0	1	Σ3 (70deg)
CIGS	32	38	19	131.85	0	-4	1	0	-1	1	Σ3 (70deg)
CIGS	4	44	8	179.79	-1	1	1	-1	1	4	Σ3 (70deg)
CIGS	13	23	32	179.93	1	-1	1	1	-1	4	Σ3 (70deg)
CIGS, z=0.4	85	88	7	179.93	1	-1	1	1	-1	4	Σ3 (70deg)
CIGS	3	37	17	179.94	-1	1	1	-1	1	-4	Σ3 (70deg)
CIGS	1	7	17	179.98	2	-2	-1	1	-1	-2	Σ3 (70deg)
CIGS	15	55	17	179.99	1	1	-1	1	1	-4	Σ3 (70deg)
CIGS, z=0.7	128	129	10	180.00	1	-1	-1	1	-1	-4	Σ3 (70deg)
CIGS	26	29	6	140.97	1	-1	0	1	-1	0	Σ9 (39 deg)
CIGS	34	62	2	152.85	8	0	-1	2	0	-1	Σ9 (39 deg)
CIGS	38	73	2	179.98	-1	-1	2	-1	-1	8	Σ9 (39 deg)

Table 3.9. (Continued).

Phase	*g1*	*g2*	*%shared reflections*	*angle*	*u*	*v*	*w*	*(h*	*k*	*l)*	*sigma*
CIGS	19	51	2	123.60	-2	4	-3	-1	2	-6	Σundefined
CIGS	17	82	2	152.78	-3	2	-1	3	2	-4	Σundefined
CIGS	40	58	3	96.22	1	2	0	1	2	0	Σundefined
CIGS	0	44	4	123.79	3	1	-1	3	1	-4	Σundefined
CIGS	55	75	6	179.88	1	2	1	1	2	4	Σundefined
CIGS	67	68	2	179.99	-2	-1	1	-2	-1	4	Σundefined
CIGS	12	60	2	120.41	-2	-2	-1	-1	-1	-2	Σundefined

3.5.7 Conclusions and perspectives for further analysis

We have identified three phases, the chalcopyrite CIGS and the modified-stannite "CIGS, z=04" and "CIGS, z=0.7". We have found 157 grains with an average volume of 2.22 μm^3 and a sphere-equivalent radius of 0.74 µm. The number of grains corresponds to 30% of the indexed reflections indicating that more grains could be recovered. However, the faint superstructure peaks are missing, and therefore grains are identified with a lower number of reflections than the theoretically expected number. A more robust indexing strategy involving one phase and relaxed tolerances could evaluate the rest of the reflections. Moreover, the peak search routine could use another segmentation method to find more of the faint superstructure peaks. Experimentally, a longer exposure time could improve the signal of the spurious diffraction spots.

CIGS has the highest proportion of twinning with 82%, followed by "CIGS, z=0.7" with 34%, and "CIGS, z=0.4" with 26%. Overall, Σ3-70.53° twin boundaries are the most frequent type among the twinned grains. We did not calculate the Σ value of the unidentified transformations. This could be done by dividing the area enclosed by a unit cell of the coincidence sites and the standard unit cell to associate "Σ unidentified" with the corresponding twin boundary. Moreover, one could compare grains across phases to find if they are twin related.

Further analysis with 3DXRD data includes the texture of the absorber layer, average grain strain, and structure refinement of the grain unit cell parameters. The grain orientation could be used to investigate the texture of the film by plotting the pole figures. Strain analysis at the grain level and the sample level can potentially be conducted. Additionally, one could proceed with the grain structure refinement if the grain has a sufficient number of reflections and the intensities of the equivalent reflections are consistent.

3.6 3DXRD MEASUREMENTS ON CZTS FABRICATED BY DIFFERENT DEPOSITION METHODS

3DXRD Experiment at Spring-8, beamline BL20XU (July 2019)

3.6.1 Introduction

The fabrication of CZTS films typically follows two steps, the deposition of precursors and the annealing for CZTS formation and grain growth. In these two single steps, many parameters can vary and influence the final film microstructure. From the deposition method to the annealing conditions, there are many variables to control the film growth.

At DTU Photonics, CZTS is deposited by PLD using a sulfur-based target and recently an oxide-based target. Moreover, the sputtering of sulfur precursors is also investigated. A third fabrication method by solution-processed nanoparticles is developed using oxide precursors provided by Haldor Topsoe.

Each deposited film undergoes an annealing step, which has been optimized according to the deposition method. For example, the annealing process of a PLD film does not yield the same film quality if it is annealed following the conditions for a sputtered film. Therefore, we only compare the microstructure of optimized annealed films. We can obtain the grain volumes, orientations, twin relations, and strain from each film and compare these properties among the fabrication methods.

Moreover, we take films deposited by spin coating of the solution-processed nanoparticles, which have been annealed at 600° for 10 minutes and 60 minutes. The annealing steps featured in our study can unveil the kinetics that leads to the formation of CZTS, from precursors to the quaternary compound, along with the intermediate phases. We can analyze the average size from both deposition stages, the grain orientations, and variations on the phases appearing in the film.

3.6.2 Description of the samples

The studied samples are thin-films composed of CZTS that constitute the absorber layer of solar cells. These films are deposited via three different methods:

- Spin coating of solution-processed nanoparticles (Cu-Zn-Sn-O slurry with binder and solvent)
- PLD (from oxide and a sulfide target)
- Sputtering from binary compounds

The absorber layer is deposited on a soda-lime glass substrate coated with Molybdenum (Mo-SLG). The film annealing process promotes the formation and grain growth of the CZTS. The list of the samples and the corresponding SEM images are featured in section 2.3.3.1.

We have cut a strip from the samples with dimensions 50 - 70 µm wide and 1.5 - 2 mm in length and polished the glass to reduce the glass thickness, as shown in Figure 3.23. The tip is further milled by FIB to achieve a width of 10 µm and a glass thickness of 4 µm (see Figure 3.23(b-d)).

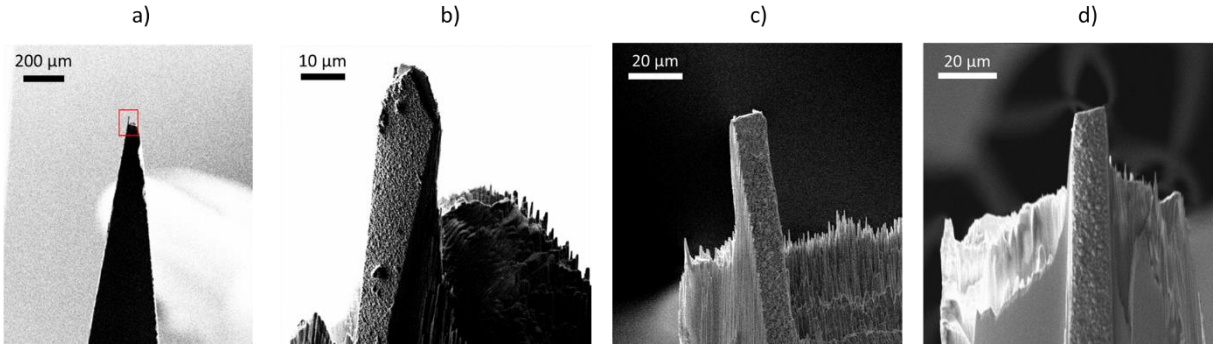

Figure 3.23. SEM images of the sample preparation by FIB. a) General shape of the cut piece. b) Tip of the sputtered film. Tip of the solution-processed: c) annealed for 60 min, d) annealed for 10 min.

Unfortunately, the adherence of the PLD films was weak, and flakes would peel off easily while polishing the glass. We decided to take a flake of these films and use the FIB at the tip of the sample to achieve the 10 µm width, as shown in Figure 3.24.

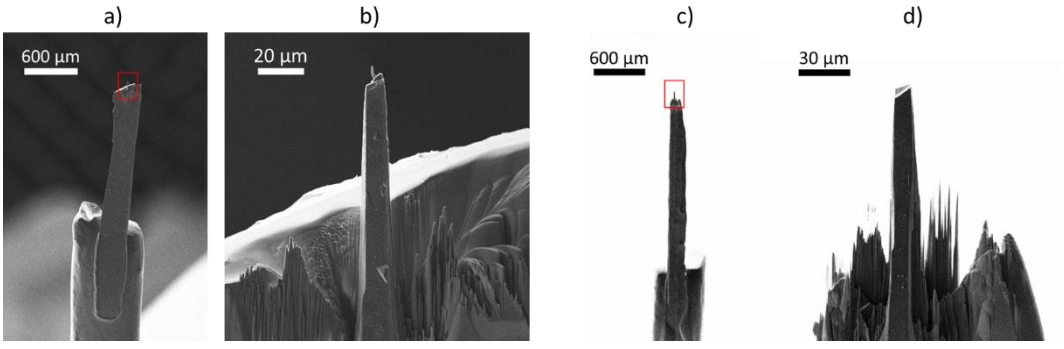

Figure 3.24. SEM images of the PLD sample preparation. a) PLD-oxides flake. b) Tip of the PLD-oxides flake milled by FIB. c) PLD-sulfides flake. d) Tip of the PLD-sulfides flake milled by FIB

3.6.3 Experimental details

We perform room temperature 3DXRD and CT measurements of each sample at beamline BL20XU of the synchrotron radiation facility SPring-8.

A monochromatic box beam (25 keV, 11.3 µm (V) x 19.2 µm (H)) illuminates the sample. We collect the diffraction images with an imaging detector (Hamamatsu C11440-22) in the far-field regime while rotating the samples 360° in 0.1° steps. We record the diffraction patterns at three different distances. At a close range, we aim to capture as many rings in the detector as possible. In the far range, we emphasize the inner rings of the diffraction pattern. We use a long exposure time to recover weak reflections and a short exposure time to avoid pixels saturation. Additionally, we measure the standard powder LaB_6 to calibrate the distance between the sample and the detector.

In Table 3.10. We tabulate the diffraction scans measured for each sample, the sample detector distance, and the exposure time.

Table 3.10. Matrix of the scans per sample, exposure time, and sample-detector distance.

Sample/Distance	**D=33.8 mm**	**D=68.8 mm**	**D3= 94.6 mm**
Nano_10 (oxides)	200 ms, 2000 ms	200 ms, 3125 ms	5000 ms
Nano_60 (oxides)	200 ms, 2000 ms	2000 ms	5000 ms
Sputtered-sulfides	500 ms	1000 ms	
PLD-sulfides	200 ms, 2000 ms		200 ms, 3500 ms
PLD-oxides	200 ms, 2000 ms		200 ms, 3500 ms

3.6.4 Comparison of diffraction patterns and azimuthal integration at different distances

This section inspects the diffraction images of the solution-processed CZTS sample annealed for 60 min at 600 °C. The diffraction images in Figure 3.25 are created using the maximum intensity found in any single frame from a set of 600 images. The 600 images correspond to a rotation of 60°. The images have been acquired at three distances. The azimuthal projection of the diffraction patterns is also shown to visualize the variations of the number of rings, here plotted as lines, and the 2θ range. The integration of the intensity along the azimuthal angle forms a 1D diffraction pattern from which we can do a preliminary fitting of the crystallographic phases in the sample.

As we move the detector away from the sample, the number of complete recorded rings decreases, with the covered 2θ range. We can observe that most of the rings fit the CZTS phase, but potentially ZnS could be present. The molybdenum rings are characterized by continuous and diffuse lines, whereas the CZTS rings are spotty with discrete reflections visible. The Mo signal will not be collected during the peak search as there are no obvious diffraction spots. On the other hand, the azimuthal integration includes the Mo-signal, which overlaps with the (114)-plane of CZTS. We also notice a decrease of the (200)/(004) planes' intensities from the azimuthal integration in Figure 3.25a to the azimuthal integration in Figure 3.25b. We do not know the source of this change as the sample remains in the same position, and the rotation starts at the same angle at every scan.

Based on these observations, a 3DXRD analysis of the diffraction patterns recorded at a distance of 33.8 mm with a short exposure time could lead to the recovery of the largest grains in the films, but the differentiation between CZTS and ZnS could be difficult to achieve. The diffraction patterns at a distance of 68.8 mm and 94.6 mm offer a better angular resolution, and the distinction between CZTS and ZnS should be possible.

Long exposure time patterns improve the intensity of the weak superstructure diffraction spots and small grains' diffraction spots. However, the detector pixels of the more intense diffraction spots could be saturated, challenging the determination of the grain volume. The pattern with long exposure time can be indexed to retrieve the grain orientations, including small grains. Grains with saturated peaks, expectedly the main reflections, can be searched in the patterns with short exposure time to recover those intensities. A normalization strategy of these intensities from these two patterns should also be considered.

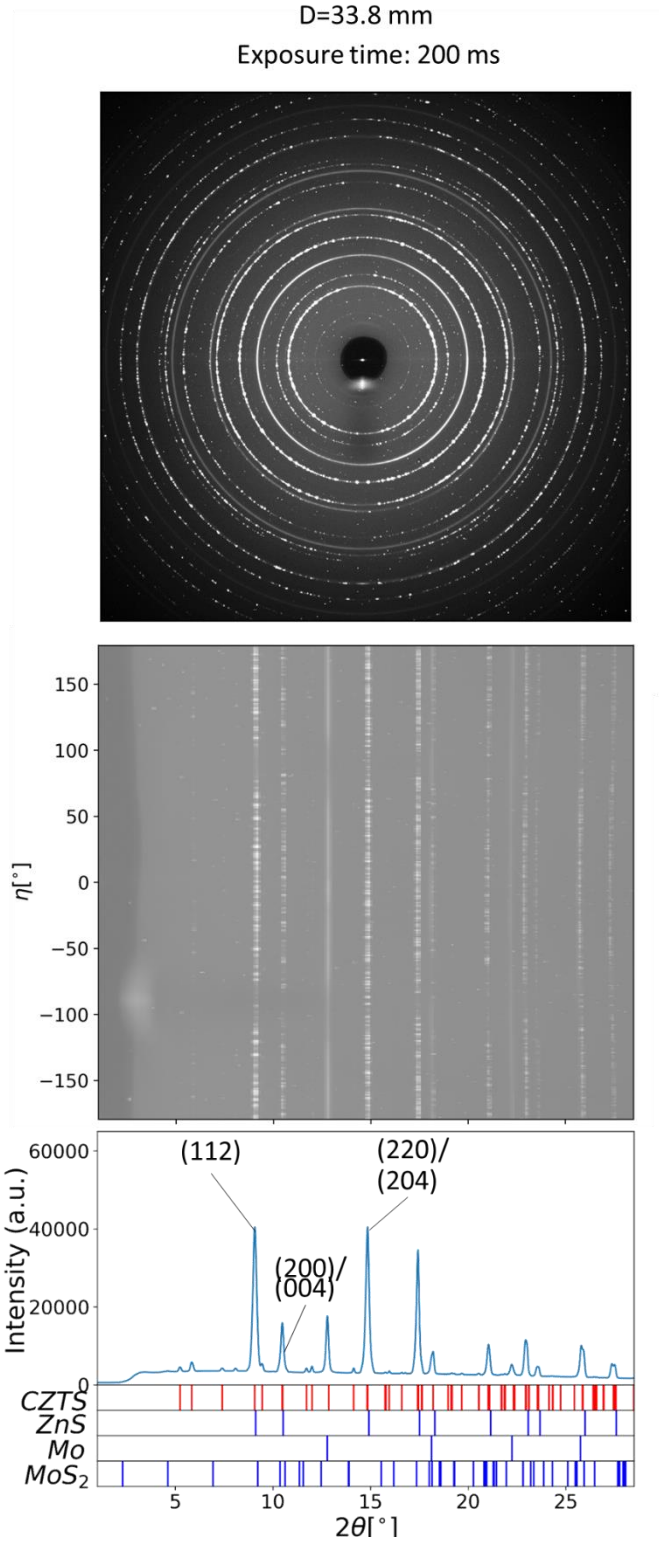

Figure 3.25. Stack of 600 diffraction images, azimuthal projection, and azimuthal integration in 1D at three sample-detector distances 33.8 mm

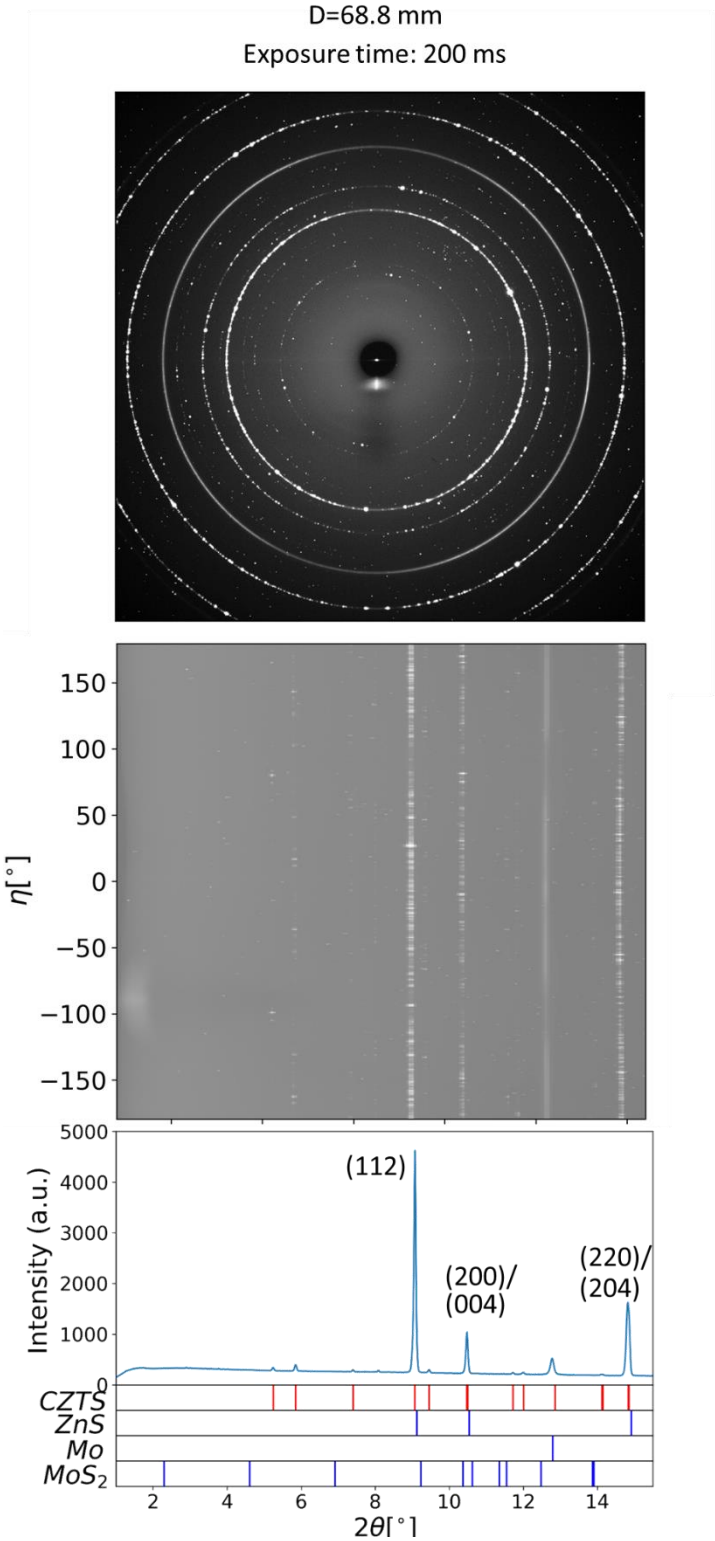

Figure 3.26. Stack of 600 diffraction images, azimuthal projection, and azimuthal integration in 1D at three sample-detector distances 68.8 mm.

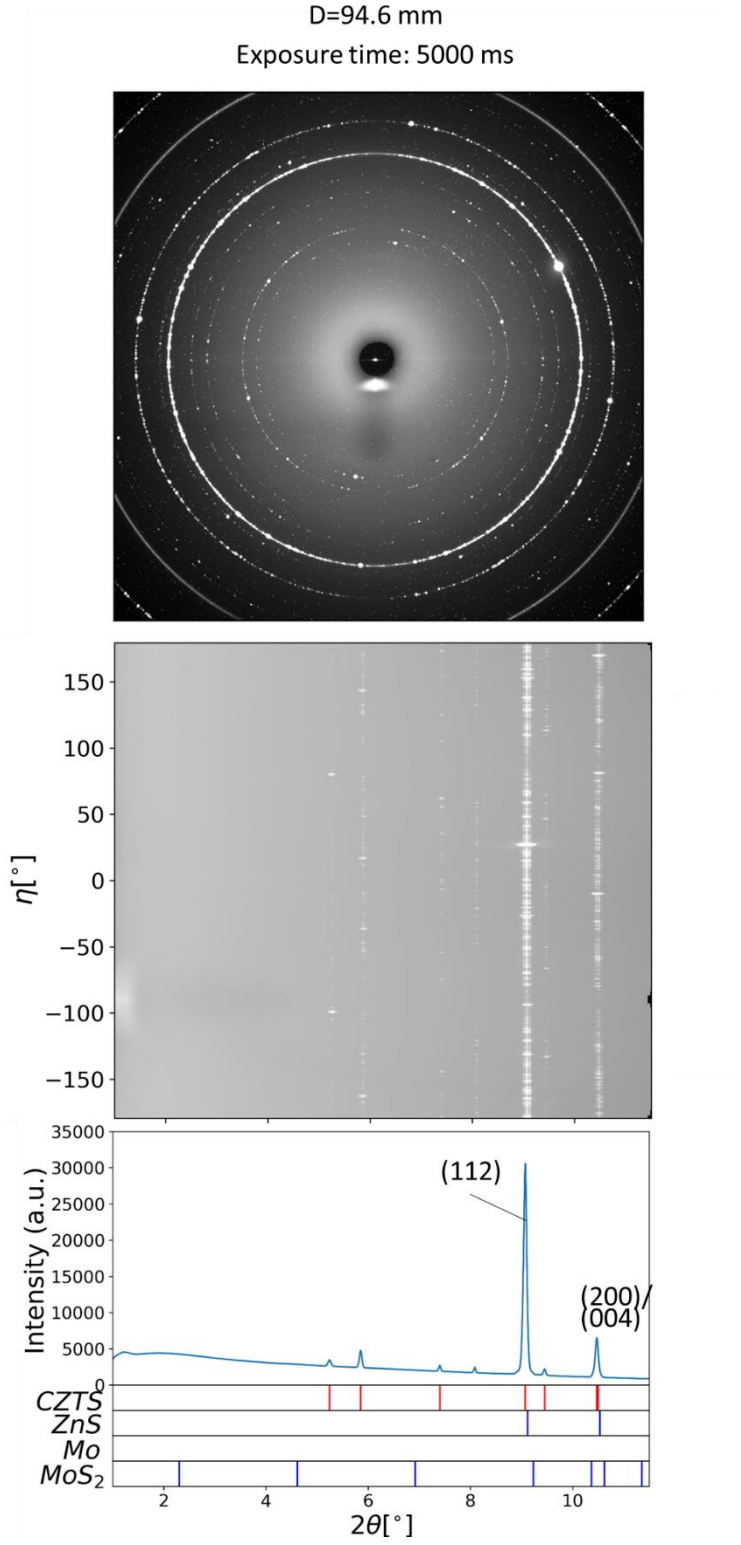

Figure 3.27. stack of 600 diffraction images, azimuthal projection, and azimuthal integration in 1D at three sample-detector distances 94.6 mm.

3.6.5 An alternative peak search algorithm

Preliminary attempts for peak searching using the threshold procedure could not overcome the noisy background in the diffraction images. Jonathan Wright, the scientist at ESRF, supplied an alternative method to segment the diffraction images. The proposed alternative to the peak search algorithm is the separation of peaks by the local maxima and the subtraction of a dynamic background, which uses Gaussian filters to remove hot pixels. The peaks in the diffraction images are labelled without merging them in 3D. Therefore, the indexing is not completed.

Figure 3.28 depicts the Bragg angles and the corresponding intensities of the PLD-CZTS film deposited using the sulfides target. The reflections were collected by implementing the new algorithm. We identify the planes associated with the CZTS phase. However, a persistent background is still present. We need a strategy to collect the peaks effectively.

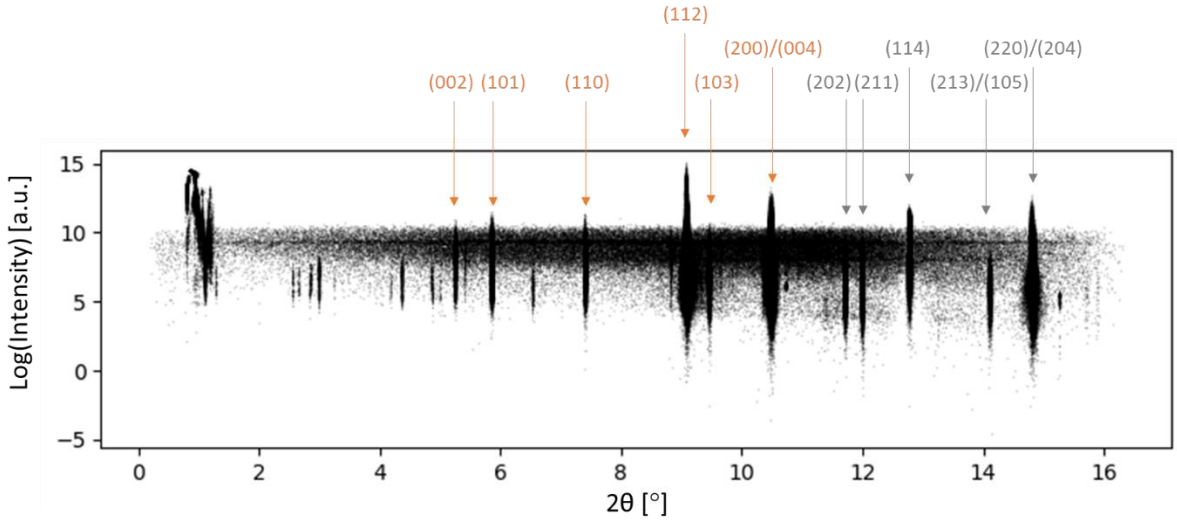

Figure 3.28. 2θ angle vs intensity of the diffraction spots for the PLD-sulfides thin-film. The diffraction patterns were recorded at 94.6 mm with an exposure time of 5000 ms. The planes in orange correspond to the complete ring in the detector.

3.6.6 Expected results

This experiment aims to acquire statistical information about the grains (orientation, volumes) and identify secondary phases. In contrast to the line-beam scan at APS, the box-beam records all the diffraction spots in one scan. Hence, we can directly estimate the volumes without worrying about merging the partial intensities from grains appearing in different scanned slices.

From the five measured samples, we have identified three potential study cases:

A. Comparison of the three deposition methods.
   We can analyze the properties of the grains of the fully annealed films deposited via solution process (oxides) vs PLD from an oxide target and sputter from binary sulfide compounds vs PLD form a sulfide target.

B. Comparison of the grain properties from the two PLD samples
   The PLD deposited sample utilizing the sulfur target can be compared with the grown film deposited by the oxides target.

C. Analysis of the annealing process of the solution process method.
   We can study the intermediate (10 min) and the last instance (60 min) of the solution-processed samples.

4 Discussion

3DXRD enabled us to characterize the microstructure of different absorber layers of thin-film solar cells, such as CZTS, ACZTS, and CIGS. We obtained grain sizes, orientations, twin boundaries, and strain in the grain and film. Moreover, it was also possible to identify and quantify secondary phases in some of the films.

Some of these structural properties can hamper the performance of the solar cell. Therefore, one needs to identify the type of defects associated with the film microstructure. For example, secondary phases have different bandgaps reducing the volume of the material with the ideal bandgap and consequently decreasing the short circuit current [97]. Moreover, low bandgap materials can limit the open-circuit voltage, whereas wide bandgap materials can block the transport or increase the series resistance in the film [159]. Besides, grain boundaries between the main and secondary phases can trap carriers or act as resistive barriers depending on their bandgaps [97]. Another type of grain boundary is the twin boundaries, whose role is still debated in the kesterite community, whereas it was determined neutral in chalcopyrites [160],[161].

Furthermore, we have attempted the crystal structure refinement of one CZTS grain. The reflections of this grain were extracted from the 3DXRD data, creating a single crystal diffraction dataset. We have described an approach to assess whether the CZTS grain has an ordered or disordered kesterite structure by comparing the refined structure with published Neutron Diffraction data [47].

Many polycrystalline materials are multiphase materials, and CZTS is not the exception. For this reason, we have tested a multigrain indexing algorithm that can identify all the phases in the material with no *a priori* knowledge of them. Using simulated 3DXRD data, we were able to identify CZTS and the secondary phases.

4.1 MICROSTRUCTURE IN THE CONTEXT OF SOLAR CELLS

First, let us discuss the relationship between the microstructure and the photovoltaic properties of the absorber layers for the samples studied in this thesis, starting with the CZTS solar cell measured at APS. This sample is compared with the results of the ESRF measurements and the ACZTS microstructure. Next, we discuss the approach taken for the crystal structure refinement of a CZTS grain from the APS data. Coming up are the results of a chalcopyrite CIGS solar cell. Finally, we recount the expected findings of the 3DXRD measurements at Spring-8.

PLD CZTS solar cell (section 3.1). We estimated 2.5% of ZnS in the absorber layer from a total of 597 identified grains. This small amount does not hinder the solar cell performance. However, ZnS has a wide bandgap that can block charge transport in large amounts or increase series resistance [159].

We have also observed a weak fibre (112) texture. Similarly, Hlang Oo *et al*. identified the fibre (112) texture in co-sputtered CZTS [95]. The (112) preferred orientation of CZTS films is frequently reported and identified by the highest intensity of the (112)-plane in the diffraction patterns. The film texture arises from the growth competition between different crystallographic directions. For CZTS films, the <112> direction seems to grow faster, hence the preference of this axis to be perpendicular to the film plane, creating the fibre texture. Other possible implications of the fibre texture are the minimisation of surface energy and elastic strain energy [162].

Besides, 41% of the grains are twins. We have encountered Σ3 twin boundary and its six equivalent misorientation angles. This type of boundary has low formation energy and therefore forms easily in the absorber layer. The influence of this type of twin boundary is still open for debate as the experimental work to assess the grain boundaries' electronic properties is missing. On the other hand, theoretical studies have predicted a benign behaviour in anion terminated (-1-1-2) surfaces hosting V_{Cu} [163]. Another study concluded that an anion terminated (-1-1-2) surface hosting Zn_{Cu} and Sn_{Zn} defects can form incoherent grain boundaries with detrimental secondary phases [98].

Moreover, the absorber layer shows a significant strain effect that is appreciated in the displacement of the Bragg angles in the diffraction patterns. The strain correlates with a compressive stress normal to the film and in-plane tensile stress over the film. These findings disagree with the conventional biaxial in-plane stress model, typically used for thin-films, where the stress normal to the film is zero [100]. In contrast to this model, 3DXRD also revealed non-zero shear stresses along the planes (xz) and (yz).

The origin of the film stress can be attributed to intrinsic stresses produced during the deposition and annealing (thermal expansion). It has been observed that a tensile stress in a co-sputtered CZTS film develops during annealing as a result of the Mo deposition stress and thermal expansion [100]. In the same study, they optimized the back contact deposition, improving the adherence of the absorber layer [100]. Additionally, extrinsic stress due to the mechanical polishing and the FIB milling of the sample can also contribute to the strain effect observed in this sample.

A similar strain-stress correlation is observed at the grain level, where a compressive strain along the a-axis of the unit cell induces a tensile strain in the b and c-axis. These strain components will also produce normal compressive stress along the a-axis and tensile stress

along the b and c-axis. Non-zero shear components are calculated, contradicting the biaxial in-plane strain model. The implications of strain for the bandgap of the material have been studied by theoretical calculations, where a reduction of the bandgap is due to a tensile biaxial in-plane strain. In contrast, a compressive strain increases the bandgap [16], [17]. A triaxial model has been studied on ZnO films, where a tensile strain along a, b, and c axes is simultaneously applied. They observed that the bandgap increases under compressive strain but decreases under tensile strain [164]. As described for ZnO, a different strain model could be established to observe the bandgap variations when applying a 3D strain tensor on CZTS.

PLD CZTS solar cell grain map (section 3.2). We implemented the scanning 3DXRD modality available at ESRF, reconstructing a map of aligned grains at the top edge of the sample. We identified the CZTS phase with no trace of ZnS. The expected Σ3 twin boundaries were identified and located on the grain map. The strain and stress in the grain and the sample did not reveal any predominant tensile or compressive stress.

Comparison of the APS sample and the ESRF sample. As we compare the PLD CZTS solar cell results from APS and the grain map of the PLD CZTS solar cell measured at ESRF, we observe that the sample tested the ESRF did not show the strain effect that was revealed in the APS experiment. We suspect that the sample treatment for the ESRF test inflicted less mechanical stress while reducing the substrate thickness to 15 µm. On the other hand, the sample prepared for APS was additionally milled by FIB, removing the glass at the tip to 4 µm thick. This is almost double the thickness of the overall stack of layers in the solar cell. The milled tip of the sample can be compared to a cantilever where forces act on the unfixed end. This could explain why the strain is more remarkable in one of the samples, even though both come from the same specimen.

PLD ACZTS absorber layer (section 3.3). The identified grains have unit cells with larger lattice parameters than the CZTS. This is due to the inclusion of Ag with larger ionic radii modifying the distance between the atoms. Another notable property of this sample is the large grain size revealed in the SEM images. However, we could only calculate partial grain volumes constrained by the vertical beam dimension (1.5 µm). We expect that the merging of the different slices will result in larger grain volumes and grain radius, and hence the number of grains will decrease as grains appearing in multiple slices will be consolidated as one. We also encountered the Σ3 boundaries in 54% of the grains from a total of 476 grains. The nature of the Σ3 boundaries in ACZTS has not been studied. Σ3 boundaries are a predominant feature in the ACZTS microstructure. Hence experimental methods should be considered to assess their electronic properties.

Correlations between ACZTS and CZTS. Based on the number of identified grains and twin boundaries in both films, the density of Σ3-type boundaries is higher in ACZTS than in CZTS. One could expect that the share of twin boundaries increases in ACZTS because the

number of grains decreases when merging the slices, whereas the number of twin boundaries is preserved. Twins usually form in stressed thin-films to reduce the elastic (misfit) strain energy [165]. Both films were deposited via PLD. However, the CZTS solar cell was annealed at 560 °C, whereas the ACZTS film was annealed at 600 °C. Ag-doping is expected to increase the stress by lattice strain, as we have observed the unit cell lattices are increased by Ag-incorporation. We suspect the residual stress in the film, generated during PLD deposition and the Ag-doping, may be relaxed during the annealing step by twinning with the low energy Σ3-type boundary. Such behaviour was observed in (ZnO:B) thin-films, where Boron doping increases the film tensile stress [166].

Crystal refinement of CZTS grains (section 3.4). Certainly, without resonant scattering information, conventional XRD cannot distinguish between Cu and Zn, thereby refining the relative occupancies of Zn and Cu at the 2c and 2d sites. Under the assumptions that the film has been annealed above the order-disorder transition temperature, and considering the Cu(2c) –S bond lengths, the associated occupancies, and the sulfur atom positions from the published crystal information data in [47], we assign the grain crystal structure to that of disordered kesterite. The disordered kesterite structure is characterized by the intrinsic antisite defects Cu_{Zn} and Zn_{Cu} distributed in sites 2c and 2d. According to theoretical models, Cu_{Zn} defects together with copper vacancies V_{Cu} are responsible for the intrinsic p-type conductivity, whereas a high population of [V_{Cu} + Zn_{Cu}] clusters facilitate the separation of photo-generated electron-hole pairs [167].

Co-evaporated CIGS solar cell (section 3.5). We have identified the stoichiometric CIGS and two phases corresponding to the Cu-poor compounds. These compounds appear inevitably during the co-evaporation process and are associated with a beneficial role [148]. We have also identified Σ3 and Σ9 twin boundaries. According to Abou-Ras *et al.*, Σ9 boundaries are a geometric consequence of the high concentration of Σ3 boundaries in the film[158]. Further experimental studies determined that Σ3 {112} boundaries are cation-Se terminated boundaries and allocate V_{Cu}^{-} and In_{Cu}^{2+} point defects [168]. They are not considered to affect the electrical and optoelectronic of the film. For Σ9 twins, they behave as a neutral barrier tunnelled through by the majority carriers, explaining the benign behaviour of the grain boundaries [161].

Comparison of different deposition methods of the CZTS absorber layer (section 3.6). The design of the experiment envisions comparative studies between the fabrications employed at DTU Photonics. The processing conditions affect the final microstructure, as well as the optical and electronic properties. Here, we can compare the stresses in the films, secondary phases, and grain sizes. We also propose an analysis of the microstructure of PLD CZTS films from different targets (oxides and sulfides) [83]. According to this study, oxide films develop rough films and form $Sn_2(S_2O_4)_2$. However, no reports on grain boundaries nor

strain have been published. Ultimately, the contrast of the two annealing stages corresponding to a solution-processed CZTS can reveal the evolution of the microstructure with this fabrication method.

Multigrain crystallography (section 2.5). CZTS thin-film is a multiphase material whose phases are difficult to identify. An alternative indexing algorithm, Multigrain, has shown promising results identifying the secondary phases of CZTS on simulated 3DXRD data. This algorithm can speed up the analysis of thin-film solar cells.

In line with the objectives of this thesis, we were able to characterize the microstructure of thin-film solar cells. We have shown the robustness of 3DXRD as a technique to achieve a comprehensive analysis of the absorber layer, describing the film texture, strain, and individual grain properties. We foresee that 3DXRD can advance the understanding of other polycrystalline thin-films in different fields.

4.2 WHY DO THESE RESULTS MATTER?

Photovoltaic thin-film technologies are a sustainable solution to fulfil the increasing global electricity demand. Especially for the inexpensive, non-toxic, earth-abundant semiconductor CZTS, the road is still long as their efficiencies are about 11%. One way to optimize the device performance can be achieved by controlling the fabrication of the absorber layer. The diverse processing conditions dictate the final microstructure and determine the optoelectronic and electric properties of the film. We have proven that 3DXRD is useful to study microstructures and enables us to understand and improve the film fabrication processes. 3DXRD is a non-destructive technique that does not require smooth surfaces or vacuum environments. Ultimately, the scanning modality can be applied to generate a grain map with the position of the grains.

The absorber layer microstructure can warn us about the possible physical mechanisms that occur in the film. For example, the secondary phases are linked to bandgap variations. Also, the type of grain boundaries and their associated defects can benefit or hamper solar cell efficiency. The lattice strain in the grain can affect the material bandgap, whereas film stress developed from growth mechanisms or external forces can also explain mechanical properties (adherence, elasticity). 3DXRD results provide 3D strain tensors that can support models of the CZTS mechanical and elastic properties. Moreover, the texture can suggest the growth mechanisms, as the orientation can be correlated with the minimisation of surface energy or elastic strain energy [22].

The application of 3DXRD to microstructure analysis can be extended to any chalcogenide and any polycrystalline material with grains around 1 μm, as demonstrated by analyzing a CIGS film. Moreover, we have utilized the same data analysis of the CZTS solar cell to the

ACZTS absorber film, showing the flexibility of the methodology for materials with cubic and tetragonal crystal structures.

4.3 LIMITATIONS

One constraint for applying 3DXRD is the grain size. We estimate the low limit of about 0.2 μm grain size (the minimal size calculated from our measurements). Also, such a small grain size will challenge the determination of the grain centre of mass. We would need a detector with infinitesimal pixel size and a large area, which does not exist. An alternative solution is the application of High-resolution 3DXRD, a technique compatible with the existing instruments. In addition to the conventional 3DXRD setup, it requires the translation of a high-resolution detector to record the η and θ angles over the Debye-Scherrer rings. Once the diffraction images are stitched together, a high-resolution diffraction pattern can be indexed by the 3DXRD software. The scanning 3DXRD modality, in which the sample is translated, is also available at ESRF, where the reconstruction of the map can resolve grains within the size of the beam (200 nm).

Another limitation concerning the kesterite solar cell analysis is that identifying the ternary phase Cu_2SnS_3 (I-42m) remains ambitious. Cu_2SnS_3 has the same space group as disordered kesterite and similar their unit cell parameters, creating undiscernible diffraction patterns. Additionally, 3DXRD cannot determine the Cu/Zn disorder in kesterite. Unless a resonant modality is applied, the assessment of the Cu and Zn occupancies cannot be solved. The comparative approach with the refined structures from a neutron study [47] described in this thesis could guide us to a closer determination of the refined crystal structure.

One should be critical by setting the parameters to index the reflections. The tolerance should distinguish between matching peaks from other peaks located in close proximity. Large tolerances and a low number of peaks could create fake grains. The predicament of setting the tolerances for small grains in thin-films is that grains with small volume will be assigned a low number of reflections. Also, for twinned grains sharing reflections, one grain will be appointed the shared reflections, whereas the other grain will only keep the complementary ones. For small grains, additional strategies are required to accept or reject the grain. For example, by indexing the APS data with a cubic phase, we retrieved most of the grains as we only used the most intense overlapping rings, i.e. (112)/(111), (200). Then, we evaluate whether the grain is cubic or tetragonal based on the unit cell and the lattice parameters, among other criteria.

The density of peaks on the data could also pose a problem for specimens with secondary phases and twinning. We can minimize the quantity of the reflections to avoid spot overlap

by probing reduced areas as we did at APS. In case the beam size cannot be reduced, one might instead decrease the sample size.

The substrate thickness is another issue when collecting 3DXRD measurements. The amorphous soda-lime glass generates a background that buries the signal of the diffracted beam. A thinner substrate would be suitable for the measurements but not for the fabrication processes, as it could easily break during the annealing process or just by manipulation. Moreover, it is known that the diffusion of Na into the film from SLG enhances the film crystallinity and grain growth. A thin substrate could curtail this mechanism.

Alternatively, to avoid probing the glass, one could place the sample with the normal to the film parallel to the rotation axis. At PETRA III, the nano-focus scattering beamline P03 can be adapted for scanning 3DXRD experiments. We started a collaboration with a PhD student who is setting a high-precision rotation table to allow 3DXRD measurements. Unfortunately, the pandemic crisis prevented us from participating in the beamtime. Nevertheless, we are aware that data were collected, and the analysis is in progress.

Nonetheless, we have demonstrated a solid case where 3DXRD can provide an extensive report about the thin-film microstructure. Based on the kesterite solar cell case, we were able to showcase two different modalities of 3DXRD.

5 Conclusion

This research aimed to identify secondary phases in CZTS thin-films and describe the grain properties in the absorber layer by employing 3DXRD. Based on the analysis of a PLD CZTS solar cell, we can conclude that 3DXRD is a robust technique for characterizing polycrystalline thin-films. Far-field 3DXRD can be applied to obtain a statistical analysis of the film microstructure, whereas the scanning modality can provide a grain map with the corresponding grain locations, orientations, and strains.

We summarize our findings:

- For the particular case of PLD-CZTS measured at APS, the film microstructure consists of 2.5% of the secondary phase ZnS, 41.2% of twins with grain boundary type Σ3, grains with sizes below 1 μm, and a weak (112) fibre texture. We also obtained 3D strain tensors of the grains and the film.
- In contrast to these findings, the PLD-CZTS solar cell studied by scanning 3DXRD did not reveal any secondary phase nor any strain effect. We attribute this discrepancy to the different cutting procedures which might have inflicted major stress in the APS sample.
- An ACZTS film (measured at APS) was analyzed, showing a higher density of Σ3 twin boundaries than the PLD-CZTS solar cell. We associate the twin boundary formation with stress relaxation from the Ag-doping and deposition processes.
- We refined a CZTS grain from the APS data assigned to the disordered kesterite structure by establishing a correlation with neutron experimental data.
- Also, we identified two Cu-poor phases and the chalcopyrite phase in a co-evaporated CIGS film. The twin boundaries Σ3 and Σ9 and their equivalent misorientation angles were also identified.
- We measured samples fabricated by three different deposition methods measured at Spring-8. A brief inspection of the data was done. We advise a different segmentation procedure given the low signal to noise ratio of the diffraction images.
- An alternative indexing algorithm was implemented to identify crystallographic phases in multiphase materials, showing promising results on simulations of CZTS and secondary phases.

In general, other types of polycrystalline thin-films could benefit from the microstructural characterization by 3DXRD.

6 Outlook

In outlook, the crystal refinement of a crystal from the ESRF data can be done by CrysAlis. Unfortunately, we ran out of time to achieve conclusive results. Furthermore, the Multigrain algorithm could potentially be tested on one of the 3DXRD datasets from this thesis.

Other experiments employing 3DXRD can include the strain analysis of thin-films deposited on flexible substrates. Additionally, the effect of the microstructure of degraded solar cells could also be studied.

Further research is required to establish a direct correlation between microstructure and the electronic properties of the solar cell. Analogous to the combined EBSD and Electron Beam Induced Current (EBIC) studies, we could implement multimodal experiments with simultaneous measurements of the X-ray Beam Induced Current (XBIC). Moreover, one could record the X-ray Fluorescence (XRF) signal during a scanning 3DXRD experiment. This could resolve the elemental composition of the sample and detect the typical accumulations of Na in grain boundaries.

With the new upgrades in synchrotron facilities, such as the Extremely Brilliant Source, EBS, at ESRF in Grenoble, experiments can be done faster. This could allow *in situ* annealing experiments to follow the microstructure evolution of thin-films and growth mechanisms. *In operando* experiments could study if any strain is induced while the solar cell is active.

Bibliography

[1] International Energy Agency, “World Energy Outlook 2018: Highlights,” vol. 32, no. 0, pp. 23–28, 2018, doi: 10.1787/weo-2018-2-en.

[2] K. L. Chopra, P. D. Paulson, and V. Dutta, “Thin-film solar cells: an overview,” *Prog. Photovoltaics Res. Appl.*, vol. 12, no. 23, pp. 69–92, 2004, doi: 10.1002/pip.541.

[3] A. Shah, “Photovoltaic Technology: The Case for Thin-Film Solar Cells,” *Science (80-.).*, vol. 285, no. 5428, pp. 692–698, Jul. 1999, doi: 10.1126/science.285.5428.692.

[4] R. Aninat, L. E. Quesada-Rubio, E. Sanchez-Cortezon, and J. M. Delgado-Sanchez, “Mapping and comparison of the shortcomings of kesterite absorber layers, and how they could affect industrial scalability,” *Thin Solid Films*, vol. 633, pp. 146–150, 2017, doi: 10.1016/j.tsf.2016.10.007.

[5] L. Grenet, M. A. A. Suzon, F. Emieux, and F. Roux, “Analysis of Failure Modes in Kesterite Solar Cells,” *ACS Appl. Energy Mater.*, vol. 1, no. 5, pp. 2103–2113, May 2018, doi: 10.1021/acsaem.8b00194.

[6] N. Schäfer *et al.*, “Microstrain distribution mapping on CuInSe2 thin films by means of electron backscatter diffraction, X-ray diffraction, and Raman microspectroscopy,” *Ultramicroscopy*, vol. 169, pp. 89–97, 2016, doi: 10.1016/j.ultramic.2016.07.001.

[7] S. O. Mbam, S. E. Nwonu, O. A. Orelaja, U. S. Nwigwe, and X.-F. Gou, “Thin-film coating; historical evolution, conventional deposition technologies, stress-state micro/nano-level measurement/models and prospects projection: a critical review,” *Mater. Res. Express*, vol. 6, no. 12, p. 122001, Nov. 2019, doi: 10.1088/2053-1591/ab52cd.

[8] “Triclinic - Crystal structure - Wikipedia/ Original PNGs by DrBob, traced in Inkscape by User:Stannered - Crystal structure, distributed under a CC BY-SA 3.0 license.” [Online]. Available: https://en.wikipedia.org/wiki/Crystal_structure#/media/File:Triclinic.svg. [Accessed: 04-Dec-2020].

[9] “Tetragonal, body-centered - Crystal structure - Wikipedia/Original PNGs by User:Rocha, traced in Inkscape by User:Stannered - Crystal structure, distributed under a CC BY-SA 3.0 license.” [Online]. Available: https://en.wikipedia.org/wiki/Crystal_structure#/media/File:Tetragonal-body-centered.svg. [Accessed: 04-Dec-2020].

[10] “Cubic, face-centered - Crystal structure - Wikipedia/ Original PNGs by Daniel Mayer and DrBob, traced in Inkscape by User: Stannered - Cubic, face-centered.png: Lattice face centered, distributed under a CC BY-SA 3.0 license.” [Online]. Available:

https://en.wikipedia.org/wiki/Crystal_structure#/media/File:Cubic-face-centered.svg. [Accessed: 04-Dec-2020].

[11] J. Humphreys, G. S. Rohrer, and A. Rollett, “The Growth and Stability of Cellular Microstructures,” in *Recrystallization and Related Annealing Phenomena*, Elsevier, 2017, pp. 361–373.

[12] T. Michely and J. Krug, *Islands, Mounds and Atoms*, vol. 42, no. 45. Berlin, Heidelberg: Springer Berlin Heidelberg, 2004.

[13] J. W. Dini, “Properties of coatings: Comparisons of electroplated, physical vapor deposited, chemical vapor deposited, and plasma sprayed coatings,” *Mater. Manuf. Process.*, vol. 12, no. 3, pp. 437–472, 1997, doi: 10.1080/10426919708935157.

[14] H. J. Frost, “Microstructural evolution in thin films,” *Mater. Charact.*, vol. 32, no. 4, pp. 257–273, 1994, doi: 10.1016/1044-5803(94)90102-3.

[15] K. Barmak *et al.*, “Grain growth and the puzzle of its stagnation in thin films: The curious tale of a tail and an ear,” *Prog. Mater. Sci.*, vol. 58, no. 7, pp. 987–1055, 2013, doi: 10.1016/j.pmatsci.2013.03.004.

[16] W. J. Yin, Y. Wu, R. Noufi, M. Al-Jassim, and Y. Yan, “Defect segregation at grain boundary and its impact on photovoltaic performance of CuInSe2,” *Appl. Phys. Lett.*, vol. 102, no. 19, pp. 2–6, 2013, doi: 10.1063/1.4804606.

[17] I. Petrov, P. B. Barna, L. Hultman, and J. E. Greene, “Microstructural evolution during film growth,” *J. Vac. Sci. Technol. A Vacuum, Surfaces, Film.*, vol. 21, no. 5, pp. S117–S128, 2003, doi: 10.1116/1.1601610.

[18] P. B. Barna and M. Adamik, “Fundamental structure forming phenomena of polycrystalline films and the structure zone models,” *Thin Solid Films*, vol. 317, no. 1–2, pp. 27–33, 1998, doi: 10.1016/S0040-6090(97)00503-8.

[19] J. Humphreys, G. S. Rohrer, and A. Rollett, “The Structure and Energy of Grain Boundaries,” in *Recrystallization and Related Annealing Phenomena*, Elsevier, 2017, pp. 109–143.

[20] W. Neumann and K. Benz, “Characterization of Crystals,” in *Introduction to Crystal Growth and Characterization*, Weinheim, Germany: Wiley-VCH Verlag GmbH & Co. KGaA, 2014, pp. 301–414.

[21] J. Zhang *et al.*, “Grain boundary mobilities in polycrystals,” *Acta Mater.*, vol. 191, pp. 211–220, 2020, doi: 10.1016/j.actamat.2020.03.044.

[22] C. V. Thompson and R. Carel, “Stress and grain growth in thin films,” *J. Mech. Phys. Solids*, vol. 44, no. 5, pp. 657–673, 1996, doi: 10.1016/0022-5096(96)00022-1.

[23] D. Liu and P. E. J. Flewitt, “Chapter 5. Raman measurements of stress in films and coatings,” in *Spectroscopic Properties of Inorganic and Organometallic Compounds*, vol. 45, no. January, 2014, pp. 141–177.

[24] H. R. Moutinho, R. G. Dhere, M. J. Romero, C.-S. Jiang, B. To, and M. M. Al-Jassim, “Electron backscatter diffraction of CdTe thin films: Effects of CdCl2 treatment,” *J. Vac. Sci. Technol. A Vacuum, Surfaces, Film.*, vol. 26, no. 4, pp. 1068–1073, 2008, doi: 10.1116/1.2841523.

[25] H. Li, X. X. Liu, Y. S. Lin, B. Yang, and Z. M. Du, “Enhanced electrical properties at boundaries including twin boundaries of polycrystalline CdTe thin-film solar cells,” *Phys. Chem. Chem. Phys.*, vol. 17, no. 17, pp. 11150–11155, 2015, doi: 10.1039/c5cp00564g.

[26] D. Abou-Ras, S. Schorr, and H. W. Schock, “Grain-size distributions and grain boundaries of chalcopyrite-type thin films,” *J. Appl. Crystallogr.*, vol. 40, no. 5, pp. 841–848, Oct. 2007, doi: 10.1107/S0021889807032220.

[27] D. Abou-Ras *et al.*, “Electron backscatter diffraction: An important tool for analyses of structure-property relationships in thin-film solar cells,” *Jom*, vol. 65, no. 9, pp. 1222–1228, 2013, doi: 10.1007/s11837-013-0685-1.

[28] NREL, “Champion Photovoltaic Module Efficiency Chart,” *NREL Publications Database*, 2020. [Online]. Available: https://www.nrel.gov/pv/module-efficiency.html.

[29] D. E. Carlson and C. R. Wronski, “Amorphous silicon solar cell,” *Appl. Phys. Lett.*, vol. 28, no. 11, pp. 671–673, 1976, doi: 10.1063/1.88617.

[30] M. Stuckelberger, R. Biron, N. Wyrsch, F. J. Haug, and C. Ballif, “Review: Progress in solar cells from hydrogenated amorphous silicon,” *Renew. Sustain. Energy Rev.*, vol. 76, no. January, pp. 1497–1523, 2017, doi: 10.1016/j.rser.2016.11.190.

[31] M. A. Green, “Self-consistent optical parameters of intrinsic silicon at 300 K including temperature coefficients,” *Sol. Energy Mater. Sol. Cells*, vol. 92, no. 11, pp. 1305–1310, 2008, doi: 10.1016/j.solmat.2008.06.009.

[32] M. A. Green, E. D. Dunlop, J. Hohl-Ebinger, M. Yoshita, N. Kopidakis, and X. Hao, “Solar cell efficiency tables (version 56),” *Prog. Photovoltaics Res. Appl.*, vol. 28, no. 7, pp. 629–638, 2020, doi: 10.1002/pip.3303.

[33] T. A. M. Fiducia *et al.*, “Understanding the role of selenium in defect passivation for highly efficient selenium-alloyed cadmium telluride solar cells,” *Nat. Energy*, vol. 4, no. 6, pp. 504–511, 2019, doi: 10.1038/s41560-019-0389-z.

[34] H. R. Moutinho, M. M. Al-Jassim, D. H. Levi, P. C. Dippo, and L. L. Kazmerski, “Effects of CdCl2 treatment on the recrystallization and electro-optical properties of

CdTe thin films," *J. Vac. Sci. Technol. A Vacuum, Surfaces, Film.*, vol. 16, no. 3, pp. 1251–1257, 1998, doi: 10.1116/1.581269.

[35] J. Luschitz *et al.*, "CdTe thin film solar cells: Interrelation of nucleation, structure, and performance," *Thin Solid Films*, vol. 517, no. 7, pp. 2125–2131, 2009, doi: 10.1016/j.tsf.2008.10.075.

[36] C.-J. Tong and K. P. McKenna, "Passivating Grain Boundaries in Polycrystalline CdTe," *J. Phys. Chem. C*, vol. 123, no. 39, pp. 23882–23889, Oct. 2019, doi: 10.1021/acs.jpcc.9b08373.

[37] A. Kowsar *et al.*, "Progress in major thin-film solar cells: Growth technologies, layer materials and efficiencies," *Int. J. Renew. Energy Res.*, vol. 9, no. 2, pp. 579–597, 2019.

[38] L. Kronik, D. Cahen, and H. W. Schock, "Effects of sodium on polycrystalline Cu(In,Ga)Se2 and its solar cell performance," *Adv. Mater.*, vol. 10, no. 1, pp. 31–36, 1998, doi: 10.1002/(sici)1521-4095(199801)10:1<31::aid-adma31>3.0.co;2-3.

[39] D. Abou-Ras, J. Gibmeier, G. Nolze, A. Gholinia, and P. Konijnenberg, "On the capability of revealing the pseudosymmetry of the chalcopyrite-type crystal structure," *Cryst. Res. Technol.*, vol. 43, no. 3, pp. 234–239, 2008, doi: 10.1002/crat.200711082.

[40] S. Chaisitsak, A. Yamada, and M. Konagai, "Preferred orientation control of Cu(In1-x Gax)Se2 (x ≈ 0.28) thin films and its influence on solar cell characteristics," *Japanese J. Appl. Physics, Part 1 Regul. Pap. Short Notes Rev. Pap.*, vol. 41, no. 2 A, pp. 507–513, 2002, doi: 10.1143/jjap.41.507.

[41] K. Ito and T. Nakazawa, "Electrical and Optical Properties of Stannite-Type Quarternary Semiconductor Thin Films," *Jpn. J. Appl. Phys.*, vol. 27, pp. 2094–2097, 1988, doi: 10.1143/JJAP.27.2094.

[42] R. Nitsche, D. F. Sargent, and P. Wild, "Crystal growth of quaternary 122464 chalcogenides by iodine vapor transport," *J. Cryst. Growth*, vol. 1, no. 1, pp. 52–53, 1967, doi: 10.1016/0022-0248(67)90009-7.

[43] L. Choubrac, a Lafond, Y. Moëlo, and S. Jobic, "Structure flexibility of the Cu2ZnSnS4 absorber in low cost photovoltaic cells: from the stoichiometric to the Cu-poor compounds (Supporting info)," pp. 3346–3348, 2012.

[44] A. Lafond, L. Choubrac, C. Guillot-Deudon, P. Fertey, M. Evain, and S. Jobic, "X-ray resonant single-crystal diffraction technique, a powerful tool to investigate the kesterite structure of the photovoltaic Cu2ZnSnS 4 compound," *Acta Crystallogr. Sect. B Struct. Sci. Cryst. Eng. Mater.*, vol. 70, no. 2, pp. 390–394, 2014, doi: 10.1107/S2052520614003138.

[45] P. Bonazzi, L. Bindi, G. P. Bernardini, and S. Menchetti, "A model for the mechanism

of incorporation of Cu, Fe and Zn in the stannite - K??sterite series, Cu2FeSnS4 - Cu2ZnSnS4," *Can. Mineral.*, vol. 41, no. 3, pp. 639–647, 2003, doi: 10.2113/gscanmin.41.3.639.

[46] S. Schorr, "The crystal structure of kesterite type compounds: A neutron and X-ray diffraction study," *Sol. Energy Mater. Sol. Cells*, vol. 95, no. 6, pp. 1482–1488, 2011, doi: 10.1016/j.solmat.2011.01.002.

[47] A. Ritscher, M. Hoelzel, and M. Lerch, "The order-disorder transition in Cu2ZnSnS4 - A neutron scattering investigation," *J. Solid State Chem.*, vol. 238, pp. 68–73, 2016, doi: 10.1016/j.jssc.2016.03.013.

[48] H. Nozaki, T. Fukano, S. Ohta, Y. Seno, H. Katagiri, and K. Jimbo, "Crystal structure determination of solar cell materials: Cu2ZnSnS4 thin films using X-ray anomalous dispersion," *J. Alloys Compd.*, vol. 524, pp. 22–25, 2012, doi: 10.1016/j.jallcom.2012.01.134.

[49] J. Paier, R. Asahi, A. Nagoya, and G. Kresse, "Cu2 ZnSnS4 as a potential photovoltaic material: A hybrid Hartree-Fock density functional theory study," *Phys. Rev. B - Condens. Matter Mater. Phys.*, vol. 79, no. 11, pp. 1–8, 2009, doi: 10.1103/PhysRevB.79.115126.

[50] S. Chen, A. Walsh, Y. Luo, J. H. Yang, X. G. Gong, and S. H. Wei, "Wurtzite-derived polytypes of kesterite and stannite quaternary chalcogenide semiconductors," *Phys. Rev. B - Condens. Matter Mater. Phys.*, vol. 82, no. 19, pp. 1–8, 2010, doi: 10.1103/PhysRevB.82.195203.

[51] T. Gürel, C. Sevik, and T. ÇağIn, "Characterization of vibrational and mechanical properties of quaternary compounds Cu2ZnSnS4 and Cu2ZnSnSe4 in kesterite and stannite structures," *Phys. Rev. B - Condens. Matter Mater. Phys.*, vol. 84, no. 20, pp. 1–7, 2011, doi: 10.1103/PhysRevB.84.205201.

[52] S. Schorr, "Crystallographic Aspects of Cu 2 ZnSnS 4 (CZTS)," in *Copper Zinc Tin Sulfide-Based Thin-Film Solar Cells*, K. Ito, Ed. Chichester, UK: John Wiley & Sons Ltd, 2015, pp. 53–74.

[53] K. Momma and F. Izumi, "VESTA 3 for three-dimensional visualization of crystal, volumetric and morphology data," *J. Appl. Crystallogr.*, vol. 44, no. 6, pp. 1272–1276, 2011, doi: 10.1107/S0021889811038970.

[54] D. M. Berg and P. J. Dale, "Kesterites: Equilibria and Secondary Phase Identification," in *Copper Zinc Tin Sulfide-Based Thin-Film Solar Cells*, Chichester, UK: John Wiley & Sons Ltd, 2015, pp. 107–132.

[55] I. D. Olekseyuk, I. V. Dudchak, and L. V. Piskach, "Phase equilibria in the Cu2S–ZnS–SnS2 system," *J. Alloys Compd.*, vol. 368, no. 1–2, pp. 135–143, Apr. 2004, doi: 10.1016/j.jallcom.2003.08.084.

[56] S. V. Bagul, S. D. Chavhan, and R. Sharma, “Growth and characterization of CuxS (x=1.0, 1.76, and 2.0) thin films grown by solution growth technique (SGT),” *J. Phys. Chem. Solids*, vol. 68, no. 9, pp. 1623–1629, 2007, doi: 10.1016/j.jpcs.2007.03.053.

[57] D. M. Berg *et al.*, “Discrimination and detection limits of secondary phases in Cu2ZnSnS4 using X-ray diffraction and Raman spectroscopy,” *Thin Solid Films*, vol. 569, no. C, pp. 113–123, 2014, doi: 10.1016/j.tsf.2014.08.028.

[58] A. Lafond, L. L. Choubrac, C. Guillot-Deudon, P. Deniard, and S. Jobic, “Crystal structures of photovoltaic chalcogenides, an intricate puzzle to solve: The cases of CIGSe and CZTS materials,” *Zeitschrift fur Anorg. und Allg. Chemie*, vol. 638, no. 15, pp. 2571–2577, 2012, doi: 10.1002/zaac.201200279.

[59] T. M. Ng *et al.*, “Optoelectronic and spectroscopic characterization of vapour-transport grown Cu2ZnSnS4 single crystals,” *J. Mater. Chem. A*, vol. 5, no. 3, pp. 1192–1200, 2017, doi: 10.1039/c6ta09817g.

[60] A. Ritscher, J. Just, O. Dolotko, S. Schorr, and M. Lerch, “A mechanochemical route to single phase Cu2ZnSnS4powder,” *J. Alloys Compd.*, vol. 670, no. 82, pp. 289–296, 2016, doi: 10.1016/j.jallcom.2016.02.058.

[61] M. Hamdi, A. Lafond, C. Guillot-Deudon, F. Hlel, M. Gargouri, and S. Jobic, “Crystal chemistry and optical investigations of the Cu2Zn(Sn,Si)S4series for photovoltaic applications,” *J. Solid State Chem.*, vol. 220, pp. 232–237, 2014, doi: 10.1016/j.jssc.2014.08.030.

[62] M. Onoda, X. A. Chen, A. Sato, and H. Wada, “Crystal structure and twinning of monoclinic Cu2SnS3,” *Mater. Res. Bull.*, vol. 35, no. 9, pp. 1563–1570, 2000, doi: 10.1016/S0025-5408(00)00347-0.

[63] T. Nomura, T. Maeda, K. Takei, M. Morihama, and T. Wada, “Crystal structures and band-gap energies of Cu2Sn(S,Se)3 (0≤ x ≤1.0) solid solution,” *Phys. Status Solidi Curr. Top. Solid State Phys.*, vol. 10, no. 7–8, pp. 1093–1097, 2013, doi: 10.1002/pssc.201200867.

[64] X. Chen, H. Wada, A. Sato, and M. Mieno, “Synthesis, Electrical Conductivity, and Crystal Structure of Cu4Sn7S16and Structure Refinement of Cu2SnS3,” *J. Solid State Chem.*, vol. 139, no. 1, pp. 144–151, 1998, doi: 10.1006/jssc.1998.7822.

[65] Y. Goto *et al.*, “Enhanced thermoelectric figure of merit in stannite-kuramite solid solutions Cu2+xFe1-xSnS4-y (x = 0-1) with anisotropy lowering,” *Inorg. Chem.*, vol. 52, no. 17, pp. 9861–9866, 2013, doi: 10.1021/ic401310c.

[66] P. a R. S. Jaulmes, “Cuivre-Etain-Sou fre,” *Society*, vol. IV, no. Ii, pp. 540–542, 1976.

[67] A. Choudhury *et al.*, “New insights into the structure, chemistry, and properties of Cu4SnS4,” *J. Solid State Chem.*, vol. 253, no. May, pp. 192–201, 2017, doi:

10.1016/j.jssc.2017.05.033.

[68] M. Dogguy, S. Jaulmes, P. Laruelle, and J. Rivet, “Structure du sulfure de cuivre et d’Etain CuSn3.75S8,” *Acta Crystallogr. Sect. B Struct. Crystallogr. Cryst. Chem.*, vol. 38, no. 7, pp. 2014–2016, 1982, doi: 10.1107/S0567740882007778.

[69] X. –. Chen, H. Wada, and a Sato, “Preparation, crystal structure and electrical properties of Cu4SnS6,” *Mater. Res. Bull.*, vol. 34, no. 2, pp. 239–247, 1999, doi: 10.1016/S0025-5408(99)00013-6.

[70] J. P. F. Jemetio, P. Zhou, and H. Kleinke, “Crystal structure, electronic structure and thermoelectric properties of Cu4Sn7S16,” *J. Alloys Compd.*, vol. 417, no. 1–2, pp. 55–59, 2006, doi: 10.1016/j.jallcom.2005.09.030.

[71] M. K. Rabadanov, A. A. Loshmanov, and Y. V. Shaldin, “Anharmonic thermal vibrations of atoms in crystals with sphalerite structure-GaP, ZnS, ZnSe, and ZnTe: High-temperature x-ray structure studies,” *Crystallogr. Reports*, vol. 42, no. 4, pp. 592–602, 1997, doi: 10.1134/1.170655.

[72] B. Thiodjio Sendja, D. Tchana Kamgne, G. Aquilanti, L. Olivi, and J. R. Plaisier, “Low-range thermal investigation of zincblende-type ZnS by combined extended X-ray absorption fine structure and X-ray diffraction techniques,” *Phys. B Condens. Matter*, vol. 545, no. June, pp. 481–490, 2018, doi: 10.1016/j.physb.2018.06.005.

[73] E. H. Kisi and M. M. Elcombe, “u Parameters for the Wurtzite structure of ZnS and ZnO using powder neutron diffraction,” *Acta Crystallogr. Sect. C Cryst. Struct. Commun.*, vol. 45, no. 12, pp. 1867–1870, 1989, doi: 10.1107/S0108270189004269.

[74] R. M. Hazen and L. W. Finger, “The crystal structures and compressibilities of layer minerals at high pressure. II. Phlogopite and chlorite,” *Am. Mineral.*, vol. 63, pp. 293–296, 1978.

[75] M. Filsø, E. Eikeland, J. Zhang, S. R. Madsen, and B. B. Iversen, “Atomic and electronic structure transformations in SnS2 at high pressures: A joint single crystal X-ray diffraction and DFT study,” *Dalt. Trans.*, vol. 45, no. 9, pp. 3798–3805, 2016, doi: 10.1039/c5dt04532k.

[76] H. Wiedemeier and H. G. Von Schnering, “Refinement of the structures of GeS, GeSe, SnS and SnSe,” *Zeitschrift fur Krist. - New Cryst. Struct.*, vol. 148, no. 3–4, pp. 295–303, 1978, doi: 10.1524/zkri.1978.148.3-4.295.

[77] T. P. J. . S. H. . Von Chattopadhyay, “Neutron Diffraction Study of The Structural Phase Transition in SnS and SnSe,” *J. Phys. Chem. Solids*, vol. 47, pp. 879–885, 1986, doi: 10.1016/0022-3697(86)90059-4.

[78] H. T. Evans, “The crystal structures of low chalcocite and djurleite,” *Zeitschrift fur Krist. - New Cryst. Struct.*, vol. 150, no. 1–4, pp. 299–320, 1979, doi:

10.1524/zkri.1979.150.1-4.299.

[79] G. Will, E. Hinze, and A. R. M. Abdelrahman, “Crystal structure analysis and refinement of digenite, Cu1.8S, in the temperature range 20 to 500 C under controlled sulfur partial pressure,” *Eur. J. Mineral.*, vol. 14, no. 3, pp. 591–598, Jun. 2002, doi: 10.1127/0935-1221/2002/0014-0591.

[80] K. Yamamoto and S. Kashida, “X-ray study of the average structures of Cu2Se and Cu1.8S in the room temperature and the high temperature phases,” *J. Solid State Chem.*, vol. 93, no. 1, pp. 202–211, 1991, doi: 10.1016/0022-4596(91)90289-T.

[81] H. J. Gotsis, a C. Barnes, and P. Strange, “Experimental and theoretical investigation of the crystal structure of CuS,” *J. Phys. Condens. Matter*, vol. 4, no. 50, pp. 10461–10468, 1992, doi: 10.1088/0953-8984/4/50/034.

[82] A. Cazzaniga *et al.*, “Ultra-thin Cu2ZnSnS4 solar cell by pulsed laser deposition,” *Sol. Energy Mater. Sol. Cells*, vol. 166, pp. 91–99, Jul. 2017, doi: 10.1016/j.solmat.2017.03.002.

[83] M. Gansukh *et al.*, “Oxide route for production of Cu2ZnSnS4 solar cells by pulsed laser deposition,” *Sol. Energy Mater. Sol. Cells*, vol. 215, no. March, 2020, doi: 10.1016/j.solmat.2020.110605.

[84] J. Schou *et al.*, “Pulsed laser deposition of chalcogenide sulfides from multi- and single-component targets: the non-stoichiometric material transfer,” *Appl. Phys. A Mater. Sci. Process.*, vol. 124, no. 1, pp. 1–7, 2018, doi: 10.1007/s00339-017-1475-3.

[85] R. B. Ettlinger *et al.*, “Formation of copper tin sulfide films by pulsed laser deposition at 248 and 355 nm,” *Appl. Phys. A Mater. Sci. Process.*, vol. 122, no. 4, pp. 1–10, 2016, doi: 10.1007/s00339-016-9939-4.

[86] A. Cazzaniga *et al.*, “Ultra-thin Cu 2 ZnSnS 4 solar cell by pulsed laser deposition,” *Sol. Energy Mater. Sol. Cells*, vol. 166, no. January, pp. 91–99, Jul. 2017, doi: 10.1016/j.solmat.2017.03.002.

[87] F. Martinho *et al.*, “Persistent Double-Layer Formation in Kesterite Solar Cells: A Critical Review,” *ACS Appl. Mater. Interfaces*, vol. 12, no. 35, pp. 39405–39424, Sep. 2020, doi: 10.1021/acsami.0c10068.

[88] N. Mirbagheri *et al.*, “Synthesis of ligand-free CZTS nanoparticles via a facile hot injection route,” *Nanotechnology*, vol. 27, no. 18, p. 185603, 2016, doi: 10.1088/0957-4484/27/18/185603.

[89] S. Engberg, J. Symonowicz, J. Schou, S. Canulescu, and K. M. Ø. Jensen, “Characterization of Cu2ZnSnS4 Particles Obtained by the Hot-Injection Method,” *ACS Omega*, vol. 5, no. 18, pp. 10501–10509, 2020, doi: 10.1021/acsomega.0c00657.

[90] Y. Yan, C. S. Jiang, R. Noufi, S. H. Wei, H. R. Moutinho, and M. M. Al-Jassim, "Electrically benign behavior of grain boundaries in polycrystalline CuInSe2 films," *Phys. Rev. Lett.*, vol. 99, no. 23, pp. 2–5, 2007, doi: 10.1103/PhysRevLett.99.235504.

[91] W. Li, Y. Ma, S. Yang, J. Gong, S. Zhang, and X. Xiao, "Nanoscopic study of the compositions, structures, and electronic properties of grain boundaries in Cu(InGa)Se2 photovoltaic thin films," *Nano Energy*, vol. 33, no. January, pp. 157–167, 2017, doi: 10.1016/j.nanoen.2017.01.041.

[92] Y. Yan *et al.*, "Physics of grain boundaries in polycrystalline photovoltaic semiconductors," *J. Appl. Phys.*, vol. 117, no. 11, 2015, doi: 10.1063/1.4913833.

[93] J. B. Li, V. Chawla, and B. M. Clemens, "Investigating the role of grain boundaries in CZTS and CZTSSe thin film solar cells with scanning probe microscopy," *Adv. Mater.*, vol. 24, no. 6, pp. 720–723, 2012, doi: 10.1002/adma.201103470.

[94] D. Abou-Ras *et al.*, "Grain-boundary types in chalcopyrite-type thin films and their correlations with film texture and electrical properties," *Thin Solid Films*, vol. 517, no. 7, pp. 2545–2549, 2009, doi: 10.1016/j.tsf.2008.11.044.

[95] W. M. HLAING Oo, J. L. Johnson, A. Bhatia, E. A. Lund, M. M. Nowell, and M. A. Scarpulla, "Grain Size and Texture of Cu2ZnSnS4 Thin Films Synthesized by Cosputtering Binary Sulfides and Annealing: Effects of Processing Conditions and Sodium," *J. Electron. Mater.*, vol. 40, no. 11, pp. 2214–2221, Nov. 2011, doi: 10.1007/s11664-011-1729-3.

[96] J. B. Li, V. Chawla, and B. M. Clemens, "Investigating the role of grain boundaries in CZTS and CZTSSe thin film solar cells with scanning probe microscopy," *Adv. Mater.*, vol. 24, no. 6, pp. 720–723, 2012, doi: 10.1002/adma.201103470.

[97] B. G. Mendis, M. C. J. Goodman, J. D. Major, A. A. Taylor, K. Durose, and D. P. Halliday, "The role of secondary phase precipitation on grain boundary electrical activity in Cu_2ZnSnS_4 (CZTS) photovoltaic absorber layer material," *J. Appl. Phys.*, vol. 112, no. 12, p. 124508, 2012, doi: 10.1063/1.4769738.

[98] M. Wong, K. Tse, and J. Zhu, "New Types of CZTS Σ3 {112} Grain Boundaries: Algorithms to Passivation," *J. Phys. Chem. C*, vol. 122, no. 14, pp. 7759–7770, 2018, doi: 10.1021/acs.jpcc.8b00811.

[99] A. Weber *et al.*, "Texture inheritance in thin-film growth of Cu2ZnSnS4," *Appl. Phys. Lett.*, vol. 95, no. 4, p. 041904, Jul. 2009, doi: 10.1063/1.3192357.

[100] J. L. Johnson *et al.*, "Effects of 2nd phases, stress, and Na at the Mo/Cu 2ZnSnS4 interface," *Mater. Res. Soc. Symp. Proc.*, vol. 1268, no. May 2014, pp. 85–90, 2010, doi: 10.1557/proc-1268-ee03-03.

[101] P. P. Gunaicha, S. Gangam, J. L. Roehl, and S. V. Khare, "Structural, energetic and

elastic properties of Cu2ZnSn(SxSe1-x)4 (x=1, 0.75, 0.5, 0.25, 0) alloys from first-principles computations," *Sol. Energy*, vol. 102, pp. 276–281, 2014, doi: 10.1016/j.solener.2014.01.015.

[102] C. R. Li *et al.*, "Electronic and optical properties of kesterite Cu2ZnSnS 4 under in-plane biaxial strains: First-principles calculations," *Phys. Lett. Sect. A Gen. At. Solid State Phys.*, vol. 377, no. 37, pp. 2398–2402, 2013, doi: 10.1016/j.physleta.2013.06.046.

[103] M. Jamiati, B. Khoshnevisan, and M. Mohammadi, "Second- and third-order elastic constants of kesterite CZTS and its electronic and optical properties under various strain rates," *Energy Sources, Part A Recover. Util. Environ. Eff.*, vol. 40, no. 8, pp. 977–986, Apr. 2018, doi: 10.1080/15567036.2018.1468509.

[104] P. Willmott, *An Introduction to Synchrotron Radiation*. 2011.

[105] H. F. Poulsen *et al.*, "Applications of high-energy synchrotron radiation for structural studies of polycrystalline materials," *J. Synchrotron Radiat.*, vol. 4, no. 3, pp. 147–154, 1997, doi: 10.1107/S0909049597002021.

[106] H. F. Poulsen, "An introduction to three-dimensional X-ray diffraction microscopy," *J. Appl. Crystallogr.*, vol. 45, no. 6, pp. 1084–1097, Dec. 2012, doi: 10.1107/S0021889812039143.

[107] H. O. Sørensen *et al.*, "Multigrain crystallography," *Zeitschrift für Krist.*, vol. 227, no. 1, pp. 63–78, Jan. 2012, doi: 10.1524/zkri.2012.1438.

[108] H. F. Poulsen, "Multi scale hard x-ray microscopy," *Curr. Opin. Solid State Mater. Sci.*, vol. 24, no. 2, p. 100820, 2020, doi: 10.1016/j.cossms.2020.100820.

[109] A. Lyckegaard, E. M. Lauridsen, W. Ludwig, R. W. Fonda, and H. F. Poulsen, "On the use of laguerre tessellations for representations of 3D grain structures," *Adv. Eng. Mater.*, vol. 13, no. 3, pp. 165–170, 2011, doi: 10.1002/adem.201000258.

[110] H. Poulsen, *Three-Dimensional X-Ray Diffraction Microscopy*, vol. 205. Berlin, Heidelberg: Springer Berlin Heidelberg, 2004.

[111] FABLE, "Fully automated beam line experiment." [Online]. Available: https://sourceforge.net/p/fable/wiki/Home/. [Accessed: 04-Nov-2020].

[112] S. Schmidt, "GrainSpotter: A fast and robust polycrystalline indexing algorithm," *J. Appl. Crystallogr.*, vol. 47, no. 1, pp. 276–284, 2014, doi: 10.1107/S1600576713030185.

[113] MIDAS, "MIDAS: Microstructural Identification using Diffraction Analysis Software." [Online]. Available: https://github.com/marinerhemant/MIDAS. [Accessed: 04-Nov-2020].

[114] H. Sharma, R. M. Huizenga, and S. E. Offerman, “A fast methodology to determine the characteristics of thousands of grains using three-dimensional X-ray diffraction. I. Overlapping diffraction peaks and parameters of the experimental setup,” *J. Appl. Crystallogr.*, vol. 45, no. 4, pp. 693–704, 2012, doi: 10.1107/S0021889812025563.

[115] H. Sharma, R. M. Huizenga, and S. E. Offerman, “A fast methodology to determine the characteristics of thousands of grains using three-dimensional X-ray diffraction. II. Volume, centre-of-mass position, crystallographic orientation and strain state of grains,” *J. Appl. Crystallogr.*, vol. 45, no. 4, pp. 705–718, 2012, doi: 10.1107/S0021889812025599.

[116] D. E. Boyce and J. V Bernier, “heXRD: Modular, Open Source Software for the Analysis of High Energy X-Ray Diffraction Data,” 2013.

[117] J. V. Bernier, N. R. Barton, U. Lienert, and M. P. Miller, “Far-field high-energy diffraction microscopy: A tool for intergranular orientation and strain analysis,” *J. Strain Anal. Eng. Des.*, vol. 46, no. 7, pp. 527–547, 2011, doi: 10.1177/0309324711405761.

[118] “Peaksearching — ImageD11 1.7.0 documentation.” [Online]. Available: https://pythonhosted.org/ImageD11/peaksearching.html. [Accessed: 09-Nov-2020].

[119] L. Margulies, T. Lorentzen, H. F. Poulsen, and T. Leffers, “Strain tensor development in a single grain in the bulk of a polycrystal under loading,” *Acta Mater.*, vol. 50, no. 7, pp. 1771–1779, 2002, doi: 10.1016/S1359-6454(02)00028-9.

[120] “ImageD11/DeformationGradientTensor.ipynb.” [Online]. Available: https://github.com/FABLE-3DXRD/ImageD11/blob/master/docs/DeformationGradientTensor.ipynb. [Accessed: 16-Nov-2020].

[121] C. Wejdemann and H. F. Poulsen, “Multigrain indexing of unknown multiphase materials,” *J. Appl. Crystallogr.*, vol. 49, no. 2, pp. 616–621, Apr. 2016, doi: 10.1107/S1600576716003691.

[122] A. J. M. Duisenberg, “Indexing in single-crystal diffractometry with an obstinate list of reflections,” *J. Appl. Crystallogr.*, vol. 25, no. pt 2, pp. 92–96, Apr. 1992, doi: 10.1107/S0021889891010634.

[123] H. O. Sørensen, “PolyXSim,” 2006. [Online]. Available: https://sourceforge.net/p/fable/wiki/PolyXSim/. [Accessed: 04-Nov-2020].

[124] C. Giacovazzo *et al.*, *Fundamentals of Crystallography*. Oxford University Press, 2013.

[125] G. Will, E. Hinze, and A. R. M. Abdelrahman, “Crystal structure analysis and refinement of digenite, Cu$_{1.8}$S, in the temperature range 20 to 500 °C under

controlled sulfur partial pressure," *Eur. J. Mineral.*, vol. 14, no. 3, pp. 591–598, 2002, doi: 10.1127/0935-1221/2002/0014-0591.

[126] S. Del Bucchia, J. C. Jumas, and M. Maurin, "Contribution à l'étude de composés sulfurés d'étain(II): affinement de la structure de SnS," *Acta Crystallogr. Sect. B Struct. Crystallogr. Cryst. Chem.*, vol. 37, no. 10, pp. 1903–1905, Oct. 1981, doi: 10.1107/S0567740881007528.

[127] Y. Hayashi, Y. Hirose, and Y. Seno, "Polycrystal orientation mapping using scanning three-dimensional X-ray diffraction microscopy," *J. Appl. Crystallogr.*, vol. 48, pp. 1094–1101, 2015, doi: 10.1107/S1600576715009899.

[128] "FABLE-3DXRD/S3DXRD: Scanning 3DXRD scripts." [Online]. Available: https://github.com/FABLE-3DXRD/S3DXRD. [Accessed: 01-Dec-2020].

[129] "FABLE-3DXRD/ImageD11: ImageD11 is a python code for identifying individual grains in spotty area detector X-ray diffraction image." [Online]. Available: https://github.com/FABLE-3DXRD/ImageD11. [Accessed: 17-Nov-2020].

[130] J. Hektor *et al.*, "Scanning 3DXRD measurement of grain growth, stress, and formation of Cu 6 Sn 5 around a tin whisker during heat treatment," *Materials (Basel).*, vol. 12, no. 3, pp. 1–16, 2019, doi: 10.3390/ma12030446.

[131] N. A. Henningsson, S. A. Hall, J. P. Wright, and J. Hektor, "Reconstructing intragranular strain fields in polycrystalline materials from scanning 3DXRD data," *J. Appl. Crystallogr.*, vol. 53, pp. 314–325, 2020, doi: 10.1107/S1600576720001016.

[132] M. Stuckelberger *et al.*, "Latest developments in the x-ray based characterization of thin-film solar cells," *2015 IEEE 42nd Photovolt. Spec. Conf. PVSC 2015*, 2015, doi: 10.1109/PVSC.2015.7355592.

[133] W. Li, X. Liu, H. Cui, S. Huang, and X. Hao, "The role of Ag in (Ag,Cu)2ZnSnS4 thin film for solar cell application," *J. Alloys Compd.*, vol. 625, pp. 277–283, 2015, doi: 10.1016/j.jallcom.2014.11.136.

[134] Z. K. Yuan *et al.*, "Engineering Solar Cell Absorbers by Exploring the Band Alignment and Defect Disparity: The Case of Cu- and Ag-Based Kesterite Compounds," *Adv. Funct. Mater.*, vol. 25, no. 43, pp. 6733–6743, 2015, doi: 10.1002/adfm.201502272.

[135] A. Guchhait *et al.*, "Enhancement of Open-Circuit Voltage of Solution-Processed Cu2ZnSnS4 Solar Cells with 7.2% Efficiency by Incorporation of Silver," *ACS Energy Lett.*, vol. 1, no. 6, pp. 1256–1261, 2016, doi: 10.1021/acsenergylett.6b00509.

[136] G. Sai Gautam, T. P. Senftle, and E. A. Carter, "Understanding the Effects of Cd and Ag Doping in Cu 2 ZnSnS 4 Solar Cells," *Chem. Mater.*, vol. 30, no. 14, pp. 4543–4555, 2018, doi: 10.1021/acs.chemmater.8b00677.

[137] T. H. Nguyen *et al.*, "Structural and Solar Cell Properties of a Ag-Containing Cu2ZnSnS4 Thin Film Derived from Spray Pyrolysis," *ACS Appl. Mater. Interfaces*, vol. 10, no. 6, pp. 5455–5463, 2018, doi: 10.1021/acsami.7b14929.

[138] A. A. Coelho, "TOPAS and TOPAS-Academic: An optimization program integrating computer algebra and crystallographic objects written in C++: An," *J. Appl. Crystallogr.*, vol. 51, no. 1, pp. 210–218, 2018, doi: 10.1107/S1600576718000183.

[139] S. Schmidt, H. F. Poulsen, and G. B. M. Vaughan, "Structural refinements of the individual grains within polycrystals and powders," *J. Appl. Crystallogr.*, vol. 36, no. 2, pp. 326–332, 2003, doi: 10.1107/S0021889803002383.

[140] S. Schorr, H.-J. Hoebler, and M. Tovar, "A neutron diffraction study of the stannite-kesterite solid solution series," *Eur. J. Mineral.*, vol. 19, no. 1, pp. 65–73, 2007, doi: 10.1127/0935-1221/2007/0019-0065.

[141] A. Lafond, L. Choubrac, C. Guillot-Deudon, P. Deniard, and S. Jobic, "Crystal structures of photovoltaic chalcogenides, an intricate puzzle to solve: The cases of CIGSe and CZTS materials," *Zeitschrift fur Anorg. und Allg. Chemie*, vol. 638, no. 15, pp. 2571–2577, 2012, doi: 10.1002/zaac.201200279.

[142] C. J. Bosson, M. T. Birch, D. P. Halliday, K. S. Knight, A. S. Gibbs, and P. D. Hatton, "Cation disorder and phase transitions in the structurally complex solar cell material Cu 2 ZnSnS 4," *J. Mater. Chem. A*, vol. 5, no. 32, pp. 16672–16680, 2017, doi: 10.1039/C7TA03603E.

[143] G. M. Sheldrick, "Crystal structure refinement with SHELXL," *Acta Crystallogr. Sect. C Struct. Chem.*, vol. 71, no. Md, pp. 3–8, 2015, doi: 10.1107/S2053229614024218.

[144] M. A. Green, E. D. Dunlop, J. Hohl-Ebinger, M. Yoshita, N. Kopidakis, and A. W. Y. Ho-Baillie, "Solar cell efficiency tables (Version 55)," *Prog. Photovoltaics Res. Appl.*, vol. 28, no. 1, pp. 3–15, Jan. 2020, doi: 10.1002/pip.3228.

[145] M. A. Contreras *et al.*, "Defect chalcopyrite Cu(In1-xGax)3Se5 materials and high-Ga-content Cu(In,Ga)Se2-based solar cells," *Conf. Rec. IEEE Photovolt. Spec. Conf.*, pp. 809–812, 1996.

[146] E. Haubold *et al.*, "Short-range versus long-range structure in Cu(In,Ga)Se2, Cu(In,Ga)3Se5, and Cu(In,Ga)5Se8," *J. Alloys Compd.*, vol. 774, pp. 803–812, 2019, doi: 10.1016/j.jallcom.2018.10.026.

[147] C. Stephan, D. Greiner, S. Schorr, and C. A. Kaufmann, "The influence of sodium on the point defect characteristics in off stoichiometric CuInSe2," *J. Phys. Chem. Solids*, vol. 98, pp. 309–315, 2016, doi: 10.1016/j.jpcs.2016.07.022.

[148] Y. Cho *et al.*, "Recombination in Cu(In,Ga)Se2 thin-film solar cells containing ordered vacancy compound phases," *Thin Solid Films*, vol. 546, pp. 358–361, 2013,

doi: 10.1016/j.tsf.2013.04.078.

[149] M. Souilah, X. Rocquefelte, A. Lafond, C. Guillot-Deudon, J. P. Morniroli, and J. Kessler, “Crystal structure re-investigation in wide band gap CIGSe compounds,” *Thin Solid Films*, vol. 517, no. 7, pp. 2145–2148, 2009, doi: 10.1016/j.tsf.2008.10.077.

[150] M. Souilah, A. Lafond, C. Guillot-Deudon, S. Harel, and M. Evain, “Structural investigation of the Cu2SeIn2Se 3Ga2Se3 phase diagram, X-ray photoemission and optical properties of the Cu1-z(In0.5Ga 0.5)1z/3Se2 compounds,” *J. Solid State Chem.*, vol. 183, no. 10, pp. 2274–2280, 2010, doi: 10.1016/j.jssc.2010.08.014.

[151] E. Avancini *et al.*, “Impact of compositional grading and overall Cu deficiency on the near-infrared response in Cu(In, Ga)Se2 solar cells,” *Prog. Photovoltaics Res. Appl.*, vol. 25, no. 3, pp. 233–241, Mar. 2017, doi: 10.1002/pip.2850.

[152] V. Ray, J. Obona, S. Sharang, L. Rotkina, E. Chang, and K. Tolua, “Optimizing gas-assisted processes for Ga and Xe FIB circuit edit application,” *Conf. Proc. from Int. Symp. Test. Fail. Anal.*, no. November, pp. 397–401, 2016.

[153] A. M. Korsunsky *et al.*, “Quantifying eigenstrain distributions induced by focused ion beam damage in silicon,” *Mater. Lett.*, vol. 185, pp. 47–49, 2016, doi: 10.1016/j.matlet.2016.08.111.

[154] R. Díaz, T. Martín, J. M. Merino, M. León, J. L. Martín de Vidales, and F. Rueda, “Composition effects on structural and optical infrared properties of CuIn0.5Ga0.5Se2,” *J. Appl. Phys.*, vol. 88, no. 4, pp. 1776–1783, Aug. 2000, doi: 10.1063/1.1303063.

[155] R. Díaz, T. Martín, J. M. Merino, M. León, J. L. Martín De Vidales, and F. Rueda, “Composition effects on structural and optical infrared properties of CuIn0.5Ga0.5Se2,” *J. Appl. Phys.*, vol. 88, no. 4, pp. 1776–1783, 2000, doi: 10.1063/1.1303063.

[156] E. J. Friedrich, R. Fernández-Ruiz, J. M. Merino, and M. León, “ X-ray diffraction data and Rietveld refinement of CuGa x In 1- x Se 2 (x =0.15 and 0.50) ,” *Powder Diffr.*, vol. 25, no. 3, pp. 253–257, 2010, doi: 10.1154/1.3478374.

[157] S. Lehmann *et al.*, “Long-range structure of Cu(InxGa1-x)3Se5 A complementary neutron and anomalous x-ray diffraction study,” *J. Appl. Phys.*, vol. 109, no. 1, 2011, doi: 10.1063/1.3524183.

[158] D. Abou-Ras *et al.*, “Grain-boundary character distribution and correlations with electrical and optoelectronic properties of CuInSe2 thin films,” *Acta Mater.*, vol. 118, pp. 244–252, Oct. 2016, doi: 10.1016/j.actamat.2016.07.042.

[159] S. Siebentritt, “Why are kesterite solar cells not 20% efficient?,” *Thin Solid Films*, vol. 535, no. 1, pp. 1–4, 2013, doi: 10.1016/j.tsf.2012.12.089.

[160] S. Siebentritt, S. Sadewasser, M. Wimmer, C. Leendertz, T. Eisenbarth, and M. C. Lux-Steiner, “Evidence for a neutral grain-boundary barrier in chalcopyrites,” *Phys. Rev. Lett.*, vol. 97, no. 14, pp. 1–4, 2006, doi: 10.1103/PhysRevLett.97.146601.

[161] M. Hafemeister, S. Siebentritt, J. Albert, M. C. Lux-Steiner, and S. Sadewasser, “Large neutral barrier at grain boundaries in chalcopyrite thin films,” *Phys. Rev. Lett.*, vol. 104, no. 19, pp. 14–17, 2010, doi: 10.1103/PhysRevLett.104.196602.

[162] C. V. Thompson, “Grain growth in thin films,” *Annu. Rev. Mater. Sci.*, vol. 20, no. 1, pp. 245–268, 1990, doi: 10.1146/annurev.ms.20.080190.001333.

[163] P. Xu, S. Chen, B. Huang, H. J. Xiang, X. G. Gong, and S. H. Wei, “Stability and electronic structure of Cu2ZnSnS4 surfaces: First-principles study,” *Phys. Rev. B - Condens. Matter Mater. Phys.*, vol. 88, no. 4, pp. 1–8, 2013, doi: 10.1103/PhysRevB.88.045427.

[164] G. Qin, G. Zhang, J. Yang, G. Yu, H. Fu, and F. Ji, “Electronic band Gap of ZnO under triaxial strain,” *J. Wuhan Univ. Technol. Sci. Ed.*, vol. 28, no. 1, pp. 48–51, Feb. 2013, doi: 10.1007/s11595-013-0638-0.

[165] N. Sridhar, J. M. Rickman, and D. J. Srolovitz, “Twinning in thin films—I. Elastic analysis,” *Acta Mater.*, vol. 44, no. 10, pp. 4085–4096, Oct. 1996, doi: 10.1016/S1359-6454(96)00058-4.

[166] M. L. Addonizio and C. Diletto, “Doping influence on intrinsic stress and carrier mobility of LP-MOCVD-deposited ZnO:B thin films,” *Sol. Energy Mater. Sol. Cells*, vol. 92, no. 11, pp. 1488–1494, 2008, doi: 10.1016/j.solmat.2008.06.013.

[167] S. Chen, A. Walsh, X. G. Gong, and S. H. Wei, “Classification of lattice defects in the kesterite Cu2ZnSnS 4 and Cu2ZnSnSe4 earth-abundant solar cell absorbers,” *Adv. Mater.*, vol. 25, no. 11, pp. 1522–1539, 2013, doi: 10.1002/adma.201203146.

[168] D. Abou-Ras, B. Schaffer, M. Schaffer, S. S. Schmidt, R. Caballero, and T. Unold, “Direct insight into grain boundary reconstruction in polycrystalline Cu(In,Ga)Se 2 with atomic resolution,” *Phys. Rev. Lett.*, vol. 108, no. 7, pp. 1–5, 2012, doi: 10.1103/PhysRevLett.108.075502.

Annex I. Conference Posters

3D Multigrain Crystallography for detection and discrimination of secondary phases in Cu_2ZnSnS_4 for thin film solar cell applications

M. Mar Lucas[1], H.F. Poulsen[2], J.W. Andreasen[1]

[1] DTU Energy, Technical University of Denmark, Frederiksborgvej 399, 4000 Roskilde, Denmark.

[2] DTU Physics, Technical University of Denmark, Fysikvej, bldg. 311, 2800 Kgs. Lyngby, Denmark.

1. Motivation

Solar cells are an excellent option to supply the increasing demand of energy. We need the most efficient and sustainable technology with a low energy payback time. Thin film solar cells require less material than c-Si, and Cu_2ZnSnS_4 (CZTS) is a promising absorber material for thin film solar cells.

2. What is CZTS?

Properties

- Earth abundant and non-toxic
- Direct Band gap: 1.5 eV
- High absorption coefficient: $1{\cdot}10^4$ cm^{-1}
- P-type semiconductor
- Synthesis:
  1. Deposition of precursors (PLD, Sputtering) or CZTS nanoparticles
  2. Annealing SnS(g), S(g)
     - Cu-poor and Zn-rich stoichiometry

The Challenge

Common characterization techniques are not good enough to distinguish nor quantify the most common phases without destroying the sample. [2]

Phase diagram of the Cu_2S-SnS_2-ZnS system at 400°C. [1]

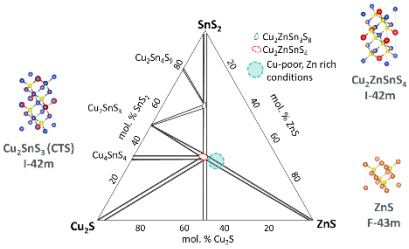

- X-ray Powder Diffraction Pattern

Bragg peaks overlapping from CZTS, Cu_2SnS_3 (CTS) and ZnS

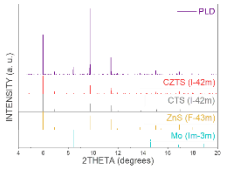

Secondary phases

- They are detrimental to the electrical performance of the device.
- Crystallographic structures of most common phases:

Phase	Space group	Lattice parameters	Reduced Unit cell lattice parameters
Cu_2ZnSnS_4	I-42m	a,b=5.43344; c=10.8421 α,β,γ=90°	a,b=5.433; c=6.644 α,β=114.13 γ=90°
Cu_2SnS_3	I-42m	a,b=5.413 c=10.824 α,β,γ=90°	a,b=5.413; c=6.629 α,β=114.1° γ=90°
ZnS	F-43m	a,b,c=5.433 α,β,γ=90°	a,b,c=3.842 α,β,γ=60°

The sample

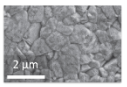

- Annealed CZTS PLD thin film. [4]

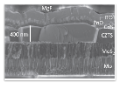

Cross section of CZTS solar cell. [4]

3. Multigrain Crystallography

The Technique

- Application of 3DXRD methods [3] to recover grain properties such as volumes, positions and orientations, size of the grains, strain and stress analysis.
- Indexing of the diffraction pattern from hundreds of simultaneously illuminated grains of different or same, known or unknown phases.

3DXRD setup

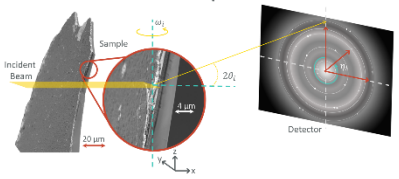

Simulation

- 3DXRD diffraction patterns of **30** grains of CZTS, CTS(tetragonal), ZnS were created by the program PolyXSim, (Sørensen, 2006).

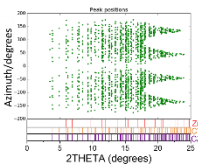

Parameters	Value
Distance to detector	160 mm
Detector	Channel size: 50 x 50 µm No. channels: 2048 x 2048
ω range [ω_{start} ; ω_{stop}]	[0°; 180°]
ω step	0.5°
Wavelength	0.32628 Å
Grain size	50 µm

- Multigrain Indexing algorithm from Xnovo:
  - ✓ List of the grains that were found with corresponding list of indexed reflections
  - ✓ Proposed reduced unit cell, lattice parameters and orientation matrix

Multigrain Indexing algorithm

Lattice planes, defined by a distance d* and a direction u, which comprise a maximum density of experimentally observed reflections. [5]

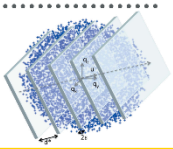

Preliminary analysis and results

- The lattice parameters of the proposed unit cell are correlated to those of the actual phases.
- Multigrain Indexing algorithm fully extracted 30 grains and phases could be assigned accordingly the proposed lattice parameters with less than 0.008% average error in lattice parameters.

Average error of lattice parameters in %

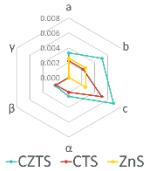

4. Next Steps

In development...

- Multigrain crystallography approach has the potential to be an integral part of solar cell research.
- Ideally, it can differentiate between CZTS and its secondary phases as these have different space groups that can be resolved in 3D reciprocal space.

Outlook

- Characterize quantitatively the phases in CZTS films and provide the volume fraction of each phase within a illuminated area.
- Apply multigrain indexing algorithm to retrieve a larger number of grains.
- Structural refinement of the individual grains and its dynamics within the bulk.

Acknowledgements

- Xnovotech, Nanna Wahlberg

References

1. Olekseyuk, I. D., et. al., J. Alloys Compd. 368, 135–143, (2004).
2. Berg, D. M. et al., Thin Solid Films 569, 113–123, (2014).
3. A. Cazzaniga et al., Sol. Energy Mater. Sol. Cells, 166, 91–99, (2017).
4. Poulsen, H. F., J. Appl. Crystallogr. 45, 1084–1097 (2012).
5. Wejdemann, C., Poulsen H. F., J. Appl. Crystallogr. 49, 616–621, (2016).
6. Polyxsim: https://sourceforge.net/p/fable/wiki/PolyXSim/

DTU Energy
Department of Energy Conversion and Storage

Characterization of the crystallographic phases in Cu_2ZnSnS_4 thin film solar cells

Mariana Mar Lucas[1], Henning Friis Poulsen[2], Jens Wenzel Andreasen[1].
[1] DTU Energy, Technical University of Denmark, Frederiksborgvej 399, 4000 Roskilde, Denmark.
[2] DTU Physics, Technical University of Denmark, Fysikvej, 2800 Kgs. Lyngby, Denmark.

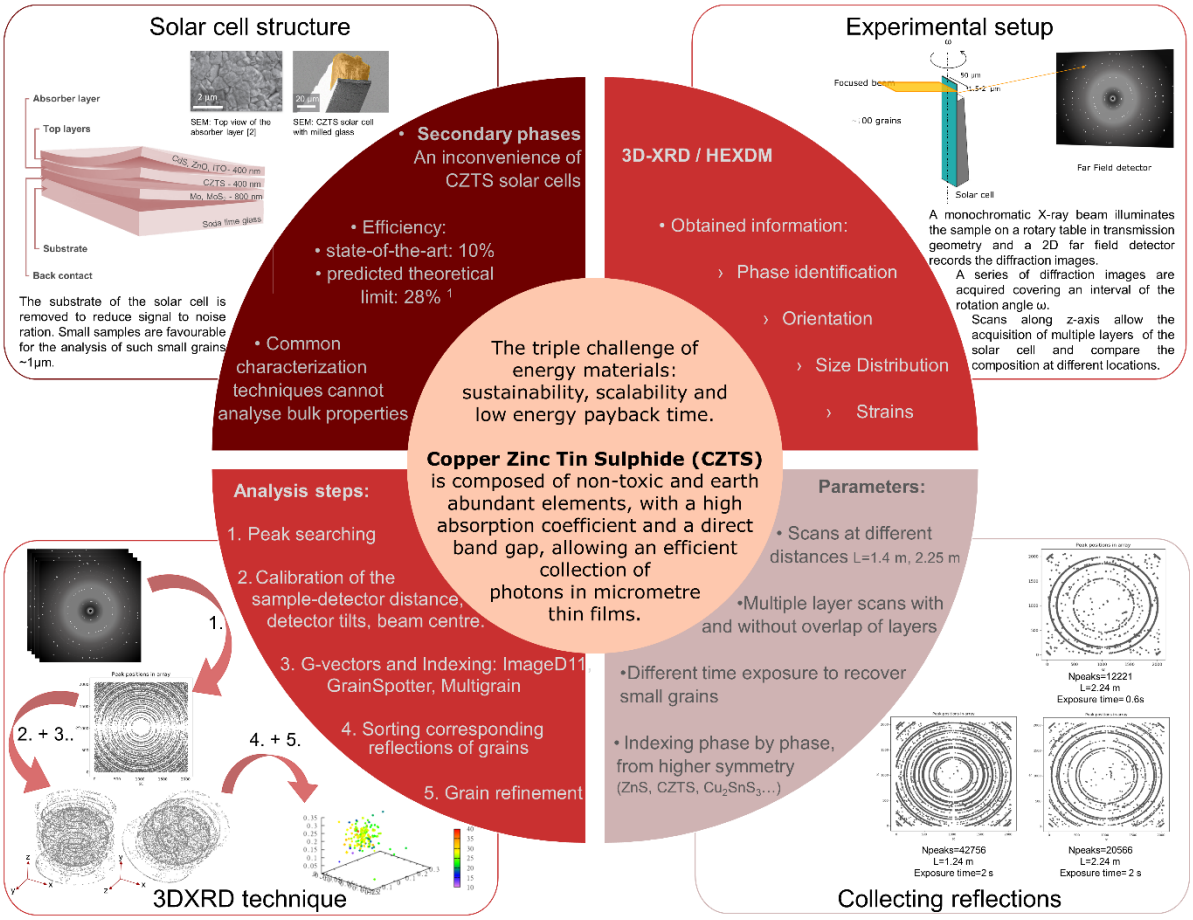

Discussion

› Similarity of the crystal structures of secondary phases (ZnS, Cu_2SnS_3).
› Overlapping of reflections
› Determining the threshold for recovering small grains with lower intensities.
› Multigrain algorithm for indexing unknown phases.

Conclusions

› 3D-XRD analysis allows an insight into the crystallographic bulk properties that cannot be deduced without destroying the sample.

Future Work

› Apply multigrain indexing algorithm to retrieve a larger number of grains.
› Structural refinement of the individual grains
› Study of the formation and grain growth of CZTS and secondary phases

Acknowledgements:

› Jonathan Almer, APS.
› Peter Kenesei, APS.
› Jonathan Wright, ESRF.
› Peter Stanley, Tiago Ramos

References
1. Wallace, S. K., ACS Energy Lett. 2, 776–779 (2017).
2. A. Cazzaniga et al., Sol. Energy Mater. Sol. Cells, 166, 91–99, (2017).
3. Poulsen, H. F., J. Appl. Crystallogr. 45, 1084–1097 (2012).
4. Wejdemann, C., Poulsen H. F., J. Appl. Crystallogr. 49, 616–621, (2016).
5. FABLE packages including ImageD11: https://github.com/FABLE-3DXRD

Identification of secondary phases in thin film solar cells by 3DXRD and multigrain crystallography

M. Mar Lucas[(1)], M. Gansukh[(2)], S. Canulescu[(2)], S. Engberg[(2)], T. Ramos[(1)], P. S. Jørgensen[(1)], P. Kenesei[(3)], J. Wright[(4)], H.F. Poulsen[(5)], J. W. Andreasen[(1)]

(1) DTU Energy, Technical University of Denmark, Frederiksborgvej 399, 4000 Roskilde, Denmark.
(2) DTU Photonics, Technical University of Denmark, , Frederiksborgvej 399, 4000 Roskilde, Denmark.
(3) Advance Photon Source, Argonne National Laboratory, 9700 S. Cass Avenue Lemont, IL 60439, USA.
(4) European Synchrotron Radiation Facility, 71, Avenue des Martyrs, CS 40220, 38043 Grenoble, France.
(5) DTU Physics, Technical University of Denmark, Fysikvej, 2800 Kgs. Lyngby, Denmark.

jewa@dtu.dk

Here, we present advances in Three-Dimensional X-ray Diffraction (3DXRD)[1] for the analysis of submicron size quaternary polycrystalline thin film solar cells.

3DXRD was used to identify crystallographic phases in photovoltaic thin films. One target system used for these investigations is Cu_2ZnSnS_4 (CZTS)[2], a promising material for 3rd generation solar cells. CZTS is a polycrystalline material and through its formation process, secondary phases arise. These phases cannot be identified with conventional methods such as powder diffraction. Hence, the motivation to apply 3DXRD to reveal the structural properties, texture and their effect on the solar cell efficiency.

We have performed 3DXRD experiments at APS beamline 1-ID and at beamline BL20XU at Spring-8. We first demonstrate that we can index the grains that constitute the absorber layer and thereby identify the crystallographic phases and orientations. Next, we map the crystal growth dynamics of the annealing process of CZTS. Finally, we present the status on reconstructing a 3D grain map of a CZTS thin film solar cell through scanning 3DXRD, providing the size, location, and orientation of each individual grain and allowing a grain boundary study of such system. We discuss the potential use for other materials and the limitations of the method.

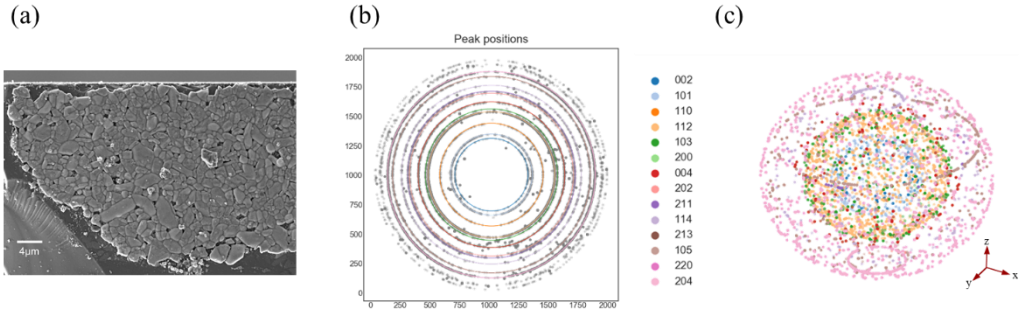

Fig. 1. (a) SEM image of a silver-doped CZTS thin film accompanied by its (b) harvested diffraction spots from 3DXRD represented in 2D. (c) Scattering vectors in 3D in the reciprocal space. Each colour label represents the powder rings associated with the crystal lattices of CZTS.

1. Poulsen, H. F.. J. Appl. Cryst. 45, 1084–1097 (2012).
2. Wallace, S. K., Mitzi, D. B. & Walsh, A. ACS Energy Lett. 2, 776–779 (2017).

DTU

DTU Energy
Department of energy conversion and storage

Analysis of polycrystalline Ag-alloyed Cu_2ZnSnS_4 by 3DXRD

M. Mar Lucas[1], P. S. Jørgensen[1], T. Ramos[1], M. Gansukh[2], S. Canulescu[2], H.F. Poulsen[3], J. W. Andreasen[1]

[1] DTU Energy, Technical University of Denmark, Frederiksborgvej 399, 4000 Roskilde, Denmark.
[2] Department of Photonics Engineering, Technical University of Denmark, Frederiksborgvej 399, 4000 Roskilde, Denmark .
[3] DTU Physics, Technical University of Denmark, Fysikvej, 2800 Kgs. Lyngby, Denmark.

1. Background

Polycrystalline $(Ag,Cu)_2ZnSnS_4$, or ACZTS, can be used as the absorber layer in thin film solar cells. The addition of silver reduces antisite defect density and band tailing, and it increases the grain size[1].

We applied **3DXRD²** to study the structural properties of the grains in the film.

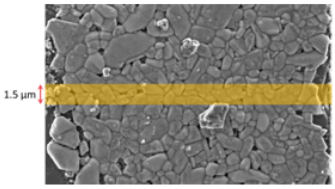

Fig. 1 The film is made via pulse laser deposition on a soda lime glass substrate coated with molybdenum and has Ag/(Cu+Ag)≈10%. It undergoes an annealing process at 600°C. The yellow band illustrates the approximate area illuminated by the beam.

2. Experimental

A monochromatic X-ray beam (52keV) focused to a size of 1.5 µm (V) x 200 µ (H) illuminates the sample in transmission geometry. The sample rotates over 360° in steps of 0.1° while a 2D far field detector records the diffraction images. The acquisition time of the data was about 2 hours with 1 s per frame. The experiment was carried out at the Advanced Photon Source synchrotron at the 1-ID beamline.

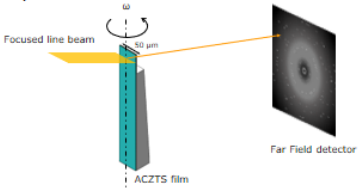

Fig. 2 The sample substrate was removed to improve signal to noise ratio.

3. Analysis

- Peaks are found in the raw images using a thresholding algorithm.
- We obtained a list of reflections containing the **spot position** on the detector, the corresponding **omega angle**, **intensity**, calculated **two-theta** angle and **azimuthal** angle. (Fig. 3a)
- A histogram of the two-theta and intensities is used to assess the cell parameters of the ACZTS and find other possible secondary phases. (Fig.3b) An attempted Le Bail fitting has been performed using Topas6[3] to provide an approximate determination of unit cell parameters (a, b=5.463272; c=10.847371, α,β,γ=90°)
- Indexing: We selected the rings with the strongest peaks to determine orientations of possible grains. ImageD11[4] calculates the angle between a peak in the first ring and all of the peaks in the second and compares the computed values from the unit cell parameters. Only grains with a number of reflections above 200 are selected.

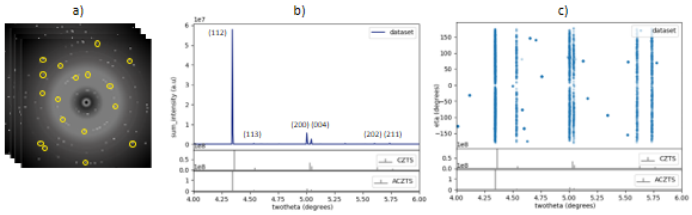

Fig. 3 a) Example of raw images indicating spots above certain threshold, b) histogram of the two-theta weighted by the sum of the peak intensity, c) azimuthal position of the reflections, superstructure planes such as (103) and the splitting of (200)/(004) of the tetragonal phase can be clearly observed in contrast to b).

4. Results

- 25 grains indexed with more than 200 reflections. (Fig. 4)
- ACZTS lattice parameters have changed due to the addition of Ag.
- The average of the unit cell parameters of the grains are:

a [Å]	b [Å]	c [Å]	α [°]	β [°]	γ [°]
5.4645	5.4647	10.8493	89.9987	90.0015	89.9986

- Other secondary phases were not observed.
- The center of mass of the grains cannot be precisely resolved since the grain size (1µm) is smaller than the detector pixel size (200 µm x 200 µm).

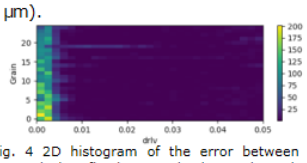

Fig. 4 2D histogram of the error between the theoretical reflections and observed peaks of each individual grain. Most grains have reflections with an error< 0.01

5. Outlook

- 3DXRD offers a high angular resolution, and allows the indexation of the reflections to individual grains.
- We can obtain statistical information about the orientation of the grains and structure parameters.
- Work in progress: scanning-3DXRD experiment with a smaller beam and a detector with a smaller pixel size allows an analysis grain by grain, and thus identify secondary phases for the case of CZTS solar cells.

Acknowledgements

- Jonathan Almer, APS.
- Peter Kenesei, APS.
- Jonathan Wright, ESRF.

References
1. Sai Gautam, Chem. Mater. 30, 4543-4555 (2018).
2. Poulsen, H. F., J. Appl. Crystallogr. 45, 1084-1097 (2012).
3. Coelho, A., J. Appl. Crystallogr. 51, 210-218 (2018).
4. ImageD11: https://github.com/FABLE-3DXRD

Poster ID PS01-05

Analysis of polycrystalline Ag-alloyed Cu_2ZnSnS_4 by 3DXRD

MARIANA MAR LUCAS, TECHNICAL UNIVERSITY OF DENMARK

SEEWHI

Project summary

- **$(Ag,Cu)_2ZnSnS_4$**, (**ACZTS**), can be used as the absorber layer in thin film solar cells. Ag reduces antisite defect density and band tailing, and it increases the grain size[1]
- We applied **3DXRD**[2] to study the **structural properties** of polycrystalline ACZTS thin film.

Fig. 1 Annealed ACZTS (T= 600ºC) film by Pulsed laser deposition (PLD) on Mo-SLG, **Ag/(Cu+Ag)≈10%**.

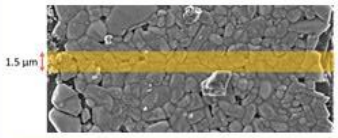

Fig. 2 3DXRD setup

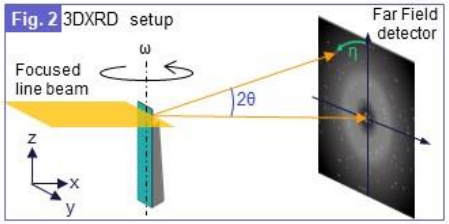

Fig. 3 Diffraction patterns

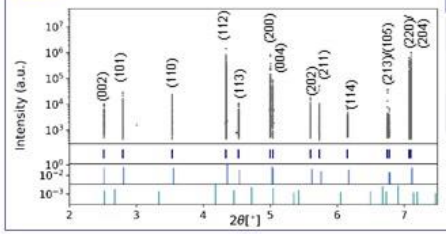

Phase	a, b [Å]	c [Å]	α,β,γ [°]
Ag-CZTS fitted by TOPAS6[3]	5.4632	10.8474	90
Cu_2ZnSnS_4 (ICSD-239674)	5.43373	10.8392	90
Ag_2ZnSnS_4 (ICSD-605734)..	5.786	10.829	90

Fig. 4 Indexing by ImageD11[4]. Retrieving orientations for 45 grains. Grain radius (<1µm), detector pixel size (200 µm x 200 µm).

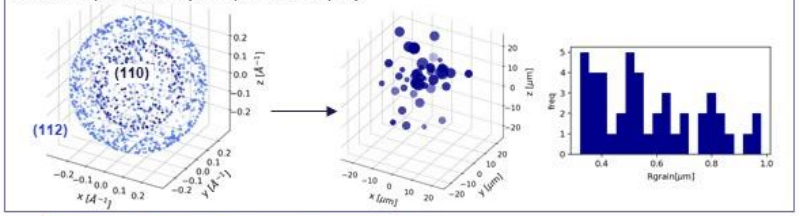

Project impact

- 3DXRD give us access to statistical information about the **orientation, size, strain** of the grains and their **structural parameters**.

Co-authors / Institutions

P. S. Jørgensen - DTU Energy, Technical University of Denmark
M. Gansukh; S. Canulescu - Department of Photonics Engineering, Technical University of Denmark.
J. Wright - European Synchrotron Radiation Facility
H.F. Poulsen - DTU Physics, Technical University of Denmark.
J. W. Andreasen - DTU Energy, Technical University of Denmark

erc European Research Council

DanScatt

References

(1) Sai Gautam, Chem. Mater. 30, 4543–4555 (2018).
(2) Poulsen, H. F., J. Appl. Crystallogr. 45, 1084–1097 (2012)
(3) Coehlo, A., J. Appl. Crystallogr. 51, 210-218 (2018).
(4) ImageD11: https://github.com/FABLE-3DXRD

3DXRD is a non-destructive technique that provides structural characterization of thin film solar cells